Forschungsbericht 2025-36

Mitigation of Internal and External Antenna Interactions for Multiband Remote-Sensing Applications

Diego Lorente Catalán

Deutsches Zentrum für Luft- und Raumfahrt
Institut für Hochfrequenztechnik und Radarsysteme
Oberpfaffenhofen

DLR Deutsches Zentrum für Luft- und Raumfahrt

Forschungsbericht 2025-36

Mitigation of Internal and External Antenna Interactions for Multiband Remote-Sensing Applications

Diego Lorente Catalán

Deutsches Zentrum für Luft- und Raumfahrt
Institut für Hochfrequenztechnik und Radarsysteme
Oberpfaffenhofen

320 Seiten
224 Bilder
50 Tabellen
116 Literaturstellen

Deutsches Zentrum
DLR für Luft- und Raumfahrt

Herausgeber:

Deutsches Zentrum
für Luft- und Raumfahrt e. V.
Wissenschaftliche Information
Linder Höhe
D-51147 Köln

ISSN 1434-8454
ISRN DLR-FB-2025-36
Erscheinungsjahr 2025
DOI: 10.57676/qx4s-sm16

SAR, Antenne, Phased-Array, Kopplung, Kreuzpolarisation, flache Bauweise, SIW, CPW, Flugzeuggestützer Sensor, Antennenträger, EBG

Diego LORENTE CATALÁN
DLR, Institut für Hochfrequenztechnik und Radarsysteme, Oberpfaffenhofen

Reduzierung interner und externer Antenneninteraktionen für Multiband-Fernerkundungsanwendungen

Dissertation Universidad Politécnica de Valencia (UPV)

Das Synthetische Apertur Radar (SAR) hat sich zu einem der wichtigsten Bereiche der Fernerkundung entwickelt. SAR liefert hochauflösende Bildgebungsdaten, was es zu einem hervorragenden Forschungsinstrument für Umweltstudien in Bereichen wie Rodung, Gletscher- und Katastrophenüberwachung sowie für die Ozeanographie, Landwirtschaft oder Verkehrsbeobachtung macht.

Genauer gesagt führt die steigende Nachfrage nach SAR-Anwendungen zusammen mit fortschrittlichen Radarkonzepten, wie Multiple-Input Multiple-Output (MIMO) oder Digital Beamforming (DBF)-Methoden, zu immer anspruchsvolleren Anforderungen an SAR-Systeme. Diese zunehmende Komplexität von SAR-Sensoren der nächsten Generation wirkt sich direkt auf die Spezifikationen des Antennen-Radar-Frontends aus.

Die Leistungsfähigkeit des Antennensystems hängt von seinen internen Interaktionen ab, die durch die elektrischen Eigenschaften bestimmt werden, die jeder Antennensensor naturgemäß besitzt. Diese intrinsischen elektromagnetischen Effekte stehen in engem Zusammenhang und führen in der Regel zu einem Design-Kompromiss: effiziente Nutzung der Antennenapertur bei gleichzeitig verringertem Elementabstand und hoher Isolation, Unterdrückung von Kreuzpolarisation bei dual-polarisierten Antennen, Bandbreitensteigerung und Kompaktbauweise, robuste Signalzuführung bei flachen Antennenkonstruktionen usw.

Eine verbesserte Antennenleistung für SAR-Systeme der nächsten Generation erfordert Methoden, um diese inhärenten Einschränkungen zu überwinden. Dies wird insbesondere bei luft- und weltraumgestützten Anwendungen zu einer anspruchsvolleren Aufgabe, bei denen ein hoher Integrationsgrad erforderlich ist. Um die hohen elektrischen Anforderungen zukünftiger SAR-Sensoren zu erfüllen, werden daher neuartige Techniken benötigt, um beispielsweise die Antennenkopplung zu verringern, die Kreuzpolarisation zu verbessern oder robuste Speisestrukturen zu realisieren.

In dieser Dissertation wird eine neuartige, flache, dual-polarisierte, mehrschichtige L-Band-Phased-Array-Antenne für luftgestützte SAR-Anwendungen entwickelt, gefertigt und vermessen. Das vorgeschlagene Design nutzt die verfügbare Antennenapertur am Flugzeug mittels abgeschnittener Resonanzhohlräume, um die Isolation zwischen den Antennenelementen zu verbessern, bei gleichzeitig geringem Elementabstand von $0.48\lambda_0$. Dadurch wird die Anzahl der Array-Elemente maximiert, was eine präzisere Formung des Antennenstrahlungsdiagramms für Beamforming-Anwendungen ermöglicht. Das vorgestellte Design erreicht eine Antennenbandbreite von nahezu 20% und gemessene Kreuzpolarisation-Unterdrückungswerte von 35 dB, bei gleichzeitig flacher, kosteneffizienter und kompakter Bauweise.

Gleichzeitig wird in dieser Arbeit eine robuste und äußerst kompakte Speisenetzwerk-Topologie im X-Band vorgestellt, die auf der Substrate Integrated Waveguide (SIW)-Technologie mit Coplanar Waveguide (CPW)-Anregung basiert. In diesem Zusammenhang wird zudem ein neuer ultrabreitbandiger, gewichteter V-Slot-CPW-SIW-Übergang mit verbesserten Eigenschaften bei hohen Frequenzen vorgestellt.

Abschließend wird die Gesamtleistung des SAR-Systems auch durch die Wechselwirkung der abgestrahlten Wellen mit der Umgebung der Antenne beeinflusst. Der Rahmen dieser Dissertation werden daher auch die Auswirkungen solcher externen Wechselwirkungen in verschiedenen praktischen Antennenszenarien analysiert. Darüber hinaus werden in dieser Arbeit Methoden zur Reduzierung dieser Einflüsse vorgestellt, unter anderem durch den Einsatz von Electromagnetic Bandgaps (EBGs), um eine unabhängigere Antennenleistung zu erzielen – weitgehend unabhängig von der jeweiligen Umgebung.

SAR, antenna, phased array, coupling, cross-polarization, low-profile, SIW, CPW, airborne sensor, antenna carrier, EBG

(Published in English)

Diego LORENTE CATALÁN
German Aerospace Center (DLR), Microwaves and Radar Institute, Oberpfaffenhofen

Mitigation of Internal and External Antenna Interactions for Multiband Remote-Sensing Applications

Doctoral Thesis Universidad Politécnica de Valencia (UPV)

Synthetic Aperture Radar (SAR) has become one of the most important fields of remote-sensing. SAR provides high-resolution imaging data, which makes it an excellent scope of research for environmental studies such as deforestation, glacier and disasters monitoring, as well as for oceanography, agriculture or traffic observations.
Precisely, the rising demand of SAR applications along with enhanced radar concepts, such as Multiple-Input Multiple Output (MIMO) or Digital Beamforming (DBF) methods, lead to more demanding SAR system requirements. Such increasing complexity of next-generation SAR sensors has a direct impact on the antenna radar front-end specifications.
The antenna system performance is dependent on its internal interactions, given by the electrical characteristics that are inherent to any antenna sensor. These intrinsic electromagnetic limitations are strongly related and they usually lead to a trade-off design: efficient exploitation of the antenna aperture size with reduced array interelement spacing and high isolation, cross-polarization suppression in dual-polarized antennas, bandwidth enhancement and compaction, feeding robustness in low-profile solutions, etc.
Enhanced antenna performance for next-generation SAR systems requires methods to overcome these inherent limitations, which becomes a more demanding task for airborne and spaceborne applications, in which a high degree of integration is also required. Thus, in order to fulfill the demanding electrical requirements of upcoming SAR sensors, novel techniques to mitigate the antenna coupling, to improve the cross-polarization levels or to achieve robust feeding topologies, among others, are needed.
In this PhD dissertation, a novel low-profile dual-polarized multilayer phased array L-band antenna for airborne SAR applications is designed, manufactured and measured. The proposed design exploits the antenna aperture size on the aircraft by means of truncated cavities, in order to improve the array element isolation along with a tight interelement spacing of $0.48\lambda_0$. This way, the number of array elements is maximized, thus allowing to shape more accurately the antenna radiation pattern for beamforming applications. The presented design achieves an antenna bandwidth of almost 20% and measured cross-polarization suppression levels of 35 dB, while keeping a low-profile, cost-effective and compact antenna solution.
At the same time this work presents a robust and extremely compact feeding network topology in X-band, based on Substrate Integrated Waveguide (SIW) technology with coplanar waveguide (CPW) excitation. In this framework, a new ultra-wideband tapered V-Slot CPW-SIW transition with enhanced high frequency band performance is also presented.
Lastly, the final SAR system performance is also determined by the interaction of the radiated waves with the antenna environment. The scope of this PhD thesis also analyzes the impact of such external interactions in different practical antenna scenarios. Besides, this dissertation proposes methods to deal with them by means of Electromagnetic Bandgaps (EBGs), in order to achieve a more independent antenna performance regardless its environment.

Mitigation of Internal and External Antenna Interactions for Multiband Remote-Sensing Applications

A thesis submitted in fulfillment of the requirements for the degree of Doctor of Philosophy.
Submitted doctoral thesis by Diego Lorente Catalán
Date of submission: 11.6.2025

1. Supervisor: Héctor Esteban González (UPV)
2. Supervisor: Vicente E. Boria Esbert (UPV)
3. Advisor: Markus Limbach (DLR)

Universidad Politécnica de Valencia

Valencia, June 2025

UNIVERSITAT POLITÈCNICA DE VALÈNCIA

Deutsches Zentrum für Luft- und Raumfahrt
German Aerospace Center

Mitigation of Internal and External Antenna Interactions for Multiband Remote-Sensing Applications

Submitted doctoral thesis by Diego Lorente Catalán

Date of submission: 11.6.2025

Universidad Politécnica de Valencia

Valencia, June 2025

To my parents and my brother

"Any sufficiently advanced technology is indistinguishable from magic"
Arthur C. Clarke

Acknowledgements

I would like to express my sincere gratitude to those who have helped me and accompanied me along this journey.

First of all, I would like to thank my university supervisors Héctor Esteban González and Vicente Boria Esbert for their guidance and support. For enriching this work with fruitful discussions and for showing me that knowledge and humbleness are compatible with each other.

I am also really grateful to my supervisor at DLR, Markus Limbach. For his kindness and unlimited patience, and for teaching me what a group leader should become.

Thank you to all my closest colleagues at DLR, Alicja, Tobias, Fairouz and Michael, for creating such a special atmosphere at work everyday that made me want to come to the office with a smile. Many thanks also to Bernd Gabler, for his effort and commitment during the countless measurements at the Compact Test Range and for his company during lunch time. I should not forget to mention the workshop's colleagues, Christoph, Ullrich and Peter, and thank them for their cooperation and engagement.

I would also like to thank my family, especially my parents, José Vicente and Amparo, for their unconditional support, and my brother Pablo, for becoming the strongest example of resilience that I know. Thank you also to my girlfriend, Giulia, for being the best partner of this journey called life, and for inspiring me to become a better person.

Last but not least, I also want to thank all my friends and people, that directly or indirectly supported me in good and bad times, and gave me the encouragement enough to make this work possible.

Abstract

Synthetic Aperture Radar (SAR) has become one of the most important fields of remote-sensing. SAR provides high-resolution imaging data, which makes it an excellent scope of research for environmental studies such as deforestation, glacier and disasters monitoring, as well as for oceanography, agriculture or traffic observations.

Precisely, the rising demand of SAR applications along with enhanced radar concepts, such as Multiple-Input Multiple Output (MIMO) or Digital Beamforming (DBF) methods, lead to more demanding SAR system requirements. Such increasing complexity of next-generation SAR sensors has a direct impact on the antenna radar front-end specifications.

The antenna system performance is dependent on its internal interactions, given by the electrical characteristics that are inherent to any antenna sensor. These intrinsic electromagnetic limitations are strongly related and they usually lead to a trade-off design: efficient exploitation of the antenna aperture size with reduced array interelement spacing and high isolation, cross-polarization suppression in dual-polarized antennas, bandwidth enhancement and compaction, feeding robustness in low-profile solutions, etc.

Enhanced antenna performance for next generation SAR systems requires methods to overcome these inherent limitations, which becomes a more demanding task for airborne and spaceborne applications, in which a high degree of integration is also required. Thus, in order to fulfill the demanding electrical requirements of upcoming SAR sensors, novel techniques to mitigate the antenna coupling, to improve the cross-polarization levels or to achieve robust feeding topologies, among others, are needed.

In this PhD dissertation, a novel low-profile dual-polarized multilayer phased array L-band antenna for airborne SAR applications is designed, manufactured and measured. The proposed design exploits the antenna aperture size on the aircraft by means of truncated cavities, in order to improve the array element isolation along with a tight interelement spacing of $0.48\lambda_0$. This way, the number of array elements is maximized, thus allowing to shape more accurately the antenna radiation pattern for beamforming applications. The presented design achieves an antenna bandwidth of almost 20% and measured cross-polarization suppression levels of 35 dB, while keeping a low-profile, cost-effective and compact antenna solution.

At the same time this work presents a robust and extremely compact feeding network

topology in X-band, based on Substrate Integrated Waveguide (SIW) technology with coplanar waveguide (CPW) excitation. In this framework, a new ultra-wideband tapered V-Slot CPW-SIW transition with enhanced high frequency band performance is also presented.

Lastly, the final SAR system performance is also determined by the interaction of the radiated waves with the antenna environment. For airborne applications, the antenna is mounted on an aerodynamic holding platform or antenna carrier that is attached sideways or under the aircraft. The electromagnetic waves, due to their inherent propagation nature, interact with the surrounding structures, arising multipath, scattering and diffraction effects, that can severely degrade the antenna radiation pattern.

The scope of this PhD thesis also analyzes the impact of such external interactions in different practical antenna scenarios. Besides, this dissertation proposes methods to deal with them by means of Electromagnetic Bandgaps (EBGs), in order to achieve a more independent antenna performance regardless its environment.

Keywords: Synthetic Aperture Radar (SAR), antenna, phased array, coupling, cross-polarization, low-profile, substrate integrated waveguide (SIW), coplanar waveguide (CPW), airborne sensor, antenna carrier, electromagnetic bandgap (EBG)

Resumen

El radar de apertura sintética (SAR) se ha convertido en uno de los campos más importantes de la detección a distancia. SAR proporciona imágenes de alta resolución, lo que lo convierte en un excelente medio de investigación en el ámbito de estudios medioambientales para el control de la deforestación, glaciares y monitorización de desastres naturales, así como para aplicaciones oceonográficas y marítimas, agricultura y observaciones de tráfico.

Precisamente, la creciente demanda de aplicaciones SAR junto con conceptos de radar mejorados, como métodos MIMO (Multiple-Input Multiple-Output) o DBF (Digital Beamforming), hacen que los requisitos de los sistemas SAR sean más exigentes. Esta creciente complejidad de los sensores SAR de nueva generación tiene un impacto directo en las especificaciones de la antena del radar.

Las prestaciones finales de la antena vienen determinadas por sus interacciones internas, que son características eléctricas inherentes a cualquier sistema de antenas. Estas limitaciones electromagnéticas intrínsecas suelen estar fuertemente interrelacionadas y normalmente llevan a un compromiso en el diseño: por ejemplo, un aprovechamiento eficiente de la apertura de la antena junto con un reducido espaciado entre elementos de un array y alta isolación entre ellos, la reducción de la polarización cruzada en antenas de polarización dual, la mejora del ancho de banda junto a miniaturización, robustez para lidiar con tolerancias de fabricación en redes de alimentación compactas, etc.

La mejora en las prestaciones eléctricas de la antena para sistemas SAR de nueva generación requiere de métodos para superar estas limitaciones inherentes, lo que se convierte en una tarea aún más exigente para aplicaciones aerotransportadas y espaciales, donde un alto nivel de integración es necesario. De esta manera, para cumplir con los requisitos eléctricos de los futuros sensores SAR, se necesitan técnicas novedosas para mitigar el acoplamiento de antenas, mejorar los niveles de polarización cruzada, o conseguir topologías de alimentación robustas, entre otros.

En esta tesis doctoral se ha diseñado, fabricado y medido una nueva phased array antena planar multicapa de polarización lineal dual y alta integración en banda L para aplicaciones SAR aerotransportadas. El diseño propuesto aprovecha el limitado tamaño de la apertura de la antena en el avión usando cavidades truncadas, con el fin de mejorar

el aislamiento de los elementos del array, permitiendo así un espaciado entre elementos de $0.48\lambda_0$. De este modo se maximiza el número de elementos del array, lo que permite conformar con mayor precisión el diagrama de radiación de la antena. El diseño propuesto proporciona un ancho de banda de casi 20% así como niveles de supresión de polarización cruzada medidos de 35 dB, manteniendo una solución de antena compacta.

Al mismo tiempo, en este trabajo se presenta una topología de red de alimentación robusta y extremadamente compacta, en banda X, basada en la tecnología de guía de ondas integrada en sustrato (SIW) con excitación en guía de ondas coplanar (CPW). En este marco, también se propone una nueva transición CPW-SIW cónica en V de banda ultraancha y con prestaciones mejoradas en el margen de frecuencias más altas.

Por último, el funcionamiento final del sistema SAR también viene determinado por la interacción de las ondas radiadas con el entorno de la antena. En aplicaciones aerotransportadas, la antena se instala en una plataforma aerodinámica de sujeción, o portaantenas, que suele montarse lateralmente o debajo de la aeronave. Debido a su naturaleza inherente de propagación, las ondas electromagnéticas interactúan con las estructuras adyacentes, dando lugar a efectos de multicamino, dispersión y difracción, que pueden degradar considerablemente las características de radiación de la antena.

En el ámbito de esta tesis doctoral también se analiza el impacto de dichas interacciones externas en diferentes escenarios prácticos de antenas aerotransportadas para aplicaciones SAR. Además, también se proponen métodos para mitigar dicho impacto por medio de Electromagnetic Bandgaps (EBGs) con el fin de lograr unas prestaciones de la antena que sean independientes de su entorno.

Resum

El radar d'obertura sintètica (SAR) s'ha convertit en un dels camps més importants de la detecció a distància. SAR proporciona imatges d'alta resolució, la qual cosa ho convertix en un excel·lent mitjà d'investigació en l'àmbit d'estudis mediambientals per al control de la desforestació, glaceres i monitoratge de desastres naturals, així com per a aplicacions oceanogràfiques i marítimes, agricultura i observacions de trànsit.

Precisament, la creixent demanda d'aplicacions SAR juntament amb conceptes de radar millorats, com a mètodes MIMO (Multiple-Input Multiple-Output) o DBF (Digital Beamforming), fan que els requisits dels sistemes SAR siguen més exigents. Esta creixent complexitat dels sensors SAR de nova generació té un impacte directe en les especificacions de l'antena del radar.

Les prestacions finals de l'antena venen determinades per les seues interaccions internes, que són característiques elèctriques inherents a qualsevol sistema d'antenes. Estes limitacions electromagnètiques intrínseques solen estar fortament interrelacionades i normalment porten a un compromís en el disseny: per exemple, un aprofitament eficient de l'obertura de l'antena juntament amb un reduït espaiat entre elements d'un array i alta isolació entre ells, la reducció de la polarització creuada en antenes de polarització dual, millorar l'ample de banda i la miniaturització, robustesa per a bregar amb toleràncies de fabricació en xarxes d'alimentació compactes, etc.

La millora en les prestacions elèctriques de l'antena per a sistemes SAR de nova generació requerix de mètodes per a superar estes limitacions inherents, la qual cosa es convertix en una tasca encara més exigent per a aplicacions aerotransportades i espacials, on un alt nivell d'integració és necessari. D'esta manera, per a complir amb els requisits elèctrics dels futurs sensors SAR, es necessiten tècniques noves per a mitigar l'acoblament d'antenes, millorar els nivells de polarització creuada, o aconseguir topologies d'alimentació robustes, entre altres.

En esta tesi doctoral s'ha dissenyat, fabricat i mesurat una nova phased array antena planar multicapa de polarització lineal dual i alta integració en banda L per a aplicacions SAR aerotransportades. El disseny proposat aprofita la limitada grandària de l'obertura de l'antena en l'avió usant cavitats truncades, amb la finalitat de millorar l'aïllament dels elements de l'array, permetent així un espaiat entre elements de $0.48\lambda_0$. D'aquesta manera

es maximitza el nombre d'elements de l'array, la qual cosa permet conformar amb major precisió el diagrama de radiació de l'antena. El disseny proposat proporciona un ample de banda de quasi 20% així com nivells de supressió de polarització creuada mesurats de 35 dB, mantenint una solució d'antena compacta.

Al mateix temps, en este treball es presenta una topologia de xarxa d'alimentació robusta i extremadament compacta, en banda X, basada en la tecnologia de guia d'ones integrada en substrat (SIW) amb excitació en guia d'ones coplanar (CPW). En este marc, també es proposa una nova transició CPW-SIW cònica en V de banda ultraampla i amb prestacions millorades en el marge de freqüències més altes.

Finalment, el funcionament final del sistema SAR també ve determinat per la interacció de les ones radiades amb l'entorn de l'antena. En aplicacions aerotransportades, l'antena s'instal·la en una plataforma aerodinàmica de subjecció, o portaantenes, que sol muntar-se lateralment o davall de l'aeronau. A causa de la seua naturalesa inherent de propagació, les ones electromagnètiques interactuen amb les estructures adjacents, donant lloc a l'efecte de multicamí, dispersió i difracció, que poden degradar considerablement les característiques de radiació de l'antena.

En l'àmbit d'esta tesi doctoral també s'analitza l'impacte d'aquestes interaccions externes en diferents escenaris pràctics d'antenes aerotransportades per a aplicacions SAR. A més, també es proposen mètodes per a mitigar este impacte per mitjà de Electromagnetic Bandgaps (EBGs) amb la finalitat d'aconseguir unes prestacions de l'antena que siguen independents del seu entorn.

Acronyms

CATR	Compact Antenna Test Rage
CPW	Coplanar Waveguide
CTR	Compact Test Rage
DBF	Digital Beamforming
DBF-SAR	Digital Beamforming Synthetic Aperture Radar
DEM	Digital Elevation Model
DFWG	Dielectric Filled Rectangular Waveguide
DGS	Defected Ground Structure
DLR	Deutsches Zentrum für Luft- und Raumfahrt (German Aerospace Center)
EBG	Electromagnetic Bandgap
ESIW	Empty Substrate Integrated Waveguide
FMCW	Frequency Modulated Continuous Wave
GCPW	Grounded Coplanar Waveguide
HIS	High Impedance Surface
HPBW	Half-Power Beamwidth
LOS	Line-of-Sight
MIMO	Multiple-Input Multiple-Output
NESZ	Noise Equivalent Sigma Zero
PBC	Periodic Boundary Condition
PEC	Perfect Electrical Conductor
PMC	Perfect Magnetic Conductor
PML	Perfect Matched Layer
RADAR	Radar Detection and Ranging
RAM	Receive Antenna Module
RAR	Real Aperture Radar
RCS	Radar Cross Section
SAR	Synthetic Aperture Radar
SLAR	Side Looking Airborne Radar
SIW	Substrate Integrated Waveguide

SMA	Sub Miniature Version A
SMP	Sub Miniature Push-on
TE	Transversal Electric
TEM	Transversal Electromagnetic
TM	Transversal Magnetic
TRL	Thru-Reflect-Line
VNA	Vector Network Analyzer
WG	Waveguide

Symbols

Lower Case Latin Symbols

Symbol	Unit	Description
a	m	waveguide width
a_{d}	m	dielectric filled waveguide width
a_{eff}	m	effective dielectric filled waveguide width
a_{siw}	m	SIW line width
b	m	waveguide height
b_{d}	m	dielectric filled waveguide width
c	m/s	speed of light in a medium
d_{a}	m	array interelement spacing
d_{az}	m	antenna length in azimuth
d_{e}	m	patch to patch edge distance
d_{f}	m	connector footprint diameter
d_{center}	m	diameter center via SIW power divider
d_{offset}	m	connector position
d_{sep}	m	separation output ports SIW power divider
d_{shift}	m	position center via SIW power divider
d_{via}	m	via diameter
d_{x}	m	array interelement spacing in x-axis
d_{y}	m	array interelement spacing in y-axis
d_line	m	microstrip line separation from EBG structure
$d(\theta, \varphi)$	-	antenna radiation pattern
$edge\_l$	m	slot edge length
$edge\_w$	m	slot edge width
f_{c}	Hz	waveguide cut-off frequency
$f_{c_{mn}}$	Hz	waveguide cut-off frequency of mode mn
f_{D}	Hz	Doppler frequency
$f_{\mathrm{D}}^{\mathrm{max}}$	Hz	maximum Doppler frequency
f_{e}	Hz	frequency of received pulses by a moving observer

f_{max}	Hz	higher frequency of operation
f_{min}	Hz	lower frequency of operation
f_{s}	Hz	frequency of transmitted pulses
f_0	Hz	central frequency of operation
g	m	separation distance between unit cells
h	m	substrate thickness
h_{feed1}	m	feed substrate 1 thickness
h_{feed2}	m	feed substrate 2 thickness
h_{foam1}	m	foam 1 layer thickness
h_{foam2}	m	foam 2 layer thickness
h_{foam3}	m	foam 3 layer thickness
h_{p1}	m	substrate patch 1 thickness
h_{p2}	m	substrate patch 2 thickness
h_1	m	substrate patch thickness
h_2	m	feeding substrate thickness
ini_line	m	GCPW feeding line length
k	m^{-1}	wavenumber
k_{x}	m^{-1}	wavenumber in x-direction
k_{y}	m^{-1}	wavenumber in y-direction
k_{z}	m^{-1}	wavenumber in z-direction
k_0	m^{-1}	wavenumber in free-space
l_{H}	m	feeding line length horizontal polarization
l_{V}	m	feeding line length vertical polarization
$line1\_l$	m	end line 1 length
$line1\_in$	m	input feeding line length 1
$line2\_l$	m	end line 2 length
$line2\_in$	m	input feeding line length 2
$line1\_w$	m	line 1 width
$line2\_w$	m	line 2 width
m	m	metallization thickness
p	m	vias separation
p_{g}	m	unti cell periodicity
$patch1\_l$	m	patch 1 length
$patch2\_l$	m	patch 2 length
$patch1\_w$	m	patch 1 width
$patch2\_w$	m	patch 2 width
$r(\theta, \varphi)$	-	angle dependent slant range function
r	m	radial distance

r_0	m	slant range at closest approach
r_{tx}	m	range distance in transmission
r_{rx}	m	range distance in reception
r_{via}	m	via radius
s	m	CPW line gap
s_{a}	-	azimuth signal
$slot\_l$	m	GCPW-SIW transition slot length
$slot\_offset1$	m	slot 1 offset
$slot\_offset2$	m	slot 2 offset
$slot\_sep$	m	geometrical parameter GCPW-SIW transition
$slot\_w$	m	GCPW-SIW transition slot width
$slot1\_l$	m	slot 1 length
$slot2\_l$	m	slot 2 length
$slot1\_w$	m	slot 1 width
$slot2\_w$	m	slot 2 width
$swath\_width$	m	width of the illuminated footprint on the ground
$t(\theta, \varphi)$	-	antenna radiation pattern in terms of power
v_ini	m	geometrical parameter GCPW-SIW V-Slot transition
v_l	m	geometrical parameter GCPW-SIW V-Slot transition
v_p	m	geometrical parameter GCPW-SIW V-Slot transition
v_w	m	geometrical parameter GCPW-SIW V-Slot transition
v_w2	m	geometrical parameter GCPW-SIW V-Slot transition
v_{p}	m/s	radar platform velocity
v_{ph}	m/s	phase velocity
v_{sep}	m	vias separation in GCPW line
w	m	CPW line width
$wall\_l$	m	wall length
$wall\_th$	m	wall thickness

Capital Latin Symbols

Symbol	Unit	Description
A_{i}	-	amplitude weighting antenna element i
$A_{\mathrm{i}}^{\mathrm{H}}$	-	amplitude in azimuth antenna element i for the horizontal polarization
$A_{\mathrm{i}}^{\mathrm{H}}$	-	amplitude in azimuth antenna element i for the vertical polarization
A_{cell}	m^2	resolution cell
A_{eff}	m^2	antenna effective aperture
A_{m}	-	Antenna elements amplitude along row m of x-axis in planar arrays
A_{n}	-	Antenna elements amplitude along row n of y-axis in planar arrays
$A_{\mathrm{rx}}^{\mathrm{eff}}$	m^2	antenna effective aperture in reception
A_{s}	m^2	antenna physical area
AF	-	array factor
B_{D}	Hz	Doppler bandwidth
B_{r}	Hz	radar bandwidth
BW	Hz	antenna bandwidth
C	F	capacitance
D	m	antenna dimension
D_{max}	m	maximum directivity
$D(\theta, \varphi)$	-	antenna directivity as a function of spherical coordinates
$E(\theta, \varphi)$	V/m	radiated electric field
E_{i}	V/m	incident electric field
$E_{\mathrm{i}}^{\mathrm{H}}$	-	amplitude at the elevation row i and horizontal polarization
$E_{\mathrm{i}}^{\mathrm{V}}$	-	amplitude at the elevation row i and vertical polarization
E_{r}	V/m	reflected electric field
E_{θ}	V/m	radiated electric field in θ direction
E_{φ}	V/m	radiated electric field in φ direction
F	-	receiver figure noise
G,G_{max}	-	antenna gain in maximum radiation direction
G_{tx}	-	antenna gain in transmission
G_{rx}	-	antenna gain in reception
$G(\theta, \varphi)$	-	antenna gain as a function of spherical coordinates
$H(\theta, \varphi)$	A/m	radiated magnetic field
H_i	-	horizontal polarization excitation port antenna element i
H_{θ}	A/m	radiated magnetic field in θ direction
H_{φ}	A/m	radiated magnetic field in φ direction
I_{mn}	-	Array element mn excitation

I_{m}^{x}	-	Antenna elements exctitation along row m of x-axis in planar arrays
I_{n}	-	Array element n excitation
I_{n}^{y}	-	Antenna elements exctitation along row n of y-axis in planar arrays
$K(\theta, \varphi)$	W/sr	radiation intensity
L	H	inductance
L_1	m	back-to-back transition length 13.1 mm
L_2	m	back-to-back transition length 26.2 mm
L_{GCPW}	m	length of the GCPW section
L_{ap}	m	aperture length
L_{p}	m	microstrip patch length
L_{path}	-	atmospheric and receiver losses
L_{pd}	m	SIW power divider length
L_{tr}	m	length of the transition section
L_{sa}	m	synthetic aperture length
L_{SIW}	m	length of the SIW section
N_{az}	-	number of integrated pulses
$NESZ$	-	noise equivalent sigma zero
P_{avg}	W	average power
P_{in}	W/m^2	power density of the received plane wave
P_{iso}	W/m^2	power density of an insotropic radiator
P_{peak}	W	peak power
$P(\theta, \varphi)$	W/m^2	power density
PRF	Hz	pulse repetition frequency
PRI	s	pulse repetition interval
R_{Ω}	Ω	antenna internal loss resistance at its terminals
R_{a}	Ω	resistance of the antenna input impedance
R_{F}	m	far-field distance measured from antenna
R_{far}	m	far range distance
R_{near}	m	near range distance
R_{r}	Ω	antenna radiation resistance at its terminals
SNR	-	signal-to-noise ratio
T_{obs}	s	illumination time
T_{s}	k	receiver noise temperature
V_i	-	vertical polarization excitation port antenna element i
W	mm	microstrip line width
W_{Ω}	W	dissipated power due to antenna losses
W_{in}	W	power delivered to the antenna
W_{g}	W	power delivered by the generator

W_{p}	m	microstrip patch width // EBG metallic patch width
W_{pd}	m	SIW power divider width
W_{rad}	W	antenna radiated power
$W_{\mathrm{rad}}^{\mathrm{iso}}$	W	total radiated power of an isotropic radiator
W_{rx}	W	received power
X_{a}	Ω	reactance of the antenna input impedance
Z_0	Ω	line impedance
Z_{a}	Ω	antenna input impedance
Z_{g}	Ω	generator impedance
Z_{s}	Ω	surface impedance

Greek Symbols

Symbol	Unit	Description
α	rad // -	progressive phase difference in linear arrays // attenuation constant
α_{x}	rad	progressive phase difference along x-axis in planar arrays
$\alpha_{\mathrm{i}}^{\mathrm{H}}$	rad	phase at the elevation row i for the horizontal polarization
$\alpha_{\mathrm{i}}^{\mathrm{V}}$	rad	phase at the elevation row i for the vertical polarization
β	rad/m	propagation constant
β_{H}	rad/m	propagation constant of the feeding line for the horizontal polarization
β_{V}	rad/m	propagation constant of the feeding line for the vertical polarization
β_{y}	rad	progressive phase difference between along y-axis in planar arrays
δ_{a}	m	azimuth resolution in SLAR systems
δ_{sa}	m	azimuth resolution in SAR systems
δ_{sd}	m	skin depth
δ_{r}	m	slant range resolution
δ_{rg}	m	ground range resolution
Δf_{D}	Hz	Doppler frequency variation
Δl	m	patch length variation
Δr	m	increased distance from pulse to pulse
Δt	s	total time delay
Δt_{e}	s	time interval between pulses by a moving observer
Δt_{s}	s	temporal separation between pulses
Δw	m	patch width variation
$\Delta\alpha$	rad	angular resolution
$\Delta\varphi$	rad	phase difference // angular resolution
ε_{r}	-	dielectric permittivity
$\varepsilon_{\mathrm{eff}}$	-	effective dielectric permittivity
$\varepsilon_{\mathrm{r}_1}$	-	patch substrate dielectric permittivity
$\varepsilon_{\mathrm{r}_2}$	-	feeding substrate dielectric permittivity
λ	m	operation wavelength
λ_0	m	wavelength in free space
λ_g	m	guided wavelength
$\lambda_{\mathrm{g}}^{\mathrm{H}}$	m	guided wavelength feeding microstrip line horizontal polarization
$\lambda_{\mathrm{g}}^{\mathrm{V}}$	m	guided wavelength feeding microstrip line vertical polarization
μ_{eff}	-	effective magnetic permeability
μ_{r}	-	magnetic permeability
ω	rad/s	angular frequency

ρ_{rad}	-	radiation losses
σ	S/m	conductivity
σ_0	-	normalized backscattering coefficient
τ_{p}	s	pulse duration
θ_{D}	rad	depression angle
θ_{l}	rad	look angle
θ_{i}	rad	incident angle
Θ_{a}	rad	half-power beamwidth in azimuth
Θ_{e}	rad	half-power beamwidth in elevation
Θ_{sa}	rad	half-power beamwidth of the synthetic aperture
φ_{a}	rad	azimuth phase
φ_{H}	rad	feeding phase microstrip line horizontal polarization
φ_{V}	rad	feeding phase microstrip line vertical polarization
φ_{scatt}	rad	scattering phase
φ_i	rad	phase coefficient antenna element i
φ_{V}	rad	feeding phase microstrip line vertical polarization
η	Ω	intrinsic impedance
η_0	Ω	free-space propagation impedance
η_{ap}	-	antenna aperture efficiency
η_{eff}	-	total antenna efficiency

Mathematical and Physical Constants

Symbol	Value	Unit	Description
c_0	$2.997925 \cdot 10^8$	m/s	speed of light in vacuum
e	2.718281	-	Euler number
j	$\sqrt{-1}$	-	complex constant
k	$1.3800649 \cdot 10^{-23}$	J/K	Boltzmann constant
π	3.141519	-	pi
ε_0	$8.854 \cdot 10^{-12}$	F/m	permittivity in vacuum
μ_0	$4\pi \cdot 10^{-7}$	N/A^2	magnetic permeability in vacuum

List of Figures

List of Tables

Contents

1. Introduction

Remote-sensing is a scientific method of detecting and acquiring information about an object, area or phenomenon from a given distance with dedicated instruments. One of the most well-known methods of remote-sensing is radar. Radar (RAdio Detecting And Ranging) was invented in 1904 by the German engineer Christian Hülsmeyer for ship detection applications [1]. The radar principle is based on the transmission of an electromagnetic wave, and the measurement of the received backscattering signal produced by the wave reflection on the target. Thus, knowing the propagation speed of light, the distance to the target can be determined.

Unlike passive sensors, radar systems dispose of its own illumination source providing day and night imaging capability, nearly weather independent, that became a complementary method to optical sensors. Radar sensors were intensively developed during World War II for surveillance and defense applications. Consequently, the first Side-Looking Airborne Radars (SLAR) appeared in the 1950s [2], allowing radar imaging from flying platforms.

To overcome the inherent limitations of airborne side-looking radars regarding the trade-off between antenna size and azimuth resolution, Carl Wiley established in 1951 the principles of Synthetic Aperture Radar (SAR) [3]. As its name implies, SAR synthesizes a larger effective antenna aperture, by means of sequential acquisition of radar pulses received with a shorter antenna as the sensor moves along its flight track. Thus, the radar resolution capabilities are enhanced, providing high resolution distance-independent imaging data.

Due to its operation possibilities, Synthetic Aperture Radar has become one of the most important methods of remote-sensing. Exploiting the electrical properties of the electromagnetic waves, SAR covers a wide range of application areas. By means of interferometry and phase information, SAR sensors are used for terrain topography studies creating digital elevation models [4], as well as disaster monitoring such as volcanoes or earthquakes. SAR systems make use of the polarization diversity to identify different scattering mechanisms and thus measure vegetation, soil moisture [5] or snow properties [6] and their changes over time, among other applications. Furthermore, taking advantage of the penetrating capabilities of the electromagnetic waves at lower frequencies,

SAR allows to perform forest density analysis and forest height estimation by means of tomography [7, 8], as well as subsurface imaging [9].

This broad scope of research makes SAR one of the most relevant remote-sensing techniques nowadays, with an increasingly interest not only among the scientific community but also for defense and commercial activities. Some examples of the outstanding remote-sensing capabilites achieved with SAR spaceborne sensors can be seen in Figure 1.1.

1.1. Motivation and State-of-the-Art

The rising interest in Earth monitoring for environmental studies and global warming effects has boosted the demand for SAR sensors. This public awareness can be seen in all the spaceborne missions launched in the last years, such as TerraSAR-X and TanDEM-X [10], Sentinel-1 [11], PAZ [12] or Biomass [13]. Upcoming spaceborne sensors such as Tandem-L [14] reaffirm this trend.

At the same time, this increasing demand of SAR systems also leads to the development of new radar concepts, enhancing the SAR capabilities to achieve high-resolution imaging across larger image swaths by means of Digital Beamforming (DBF) techniques [15], Multiple-Input Multiple-Output (MIMO) methods [16] or new SAR imaging modes [17].

To support the technological advancements of next-generation spaceborne SAR systems, airborne SAR sensors become an essential scope of research [18]. Due to their versatility, they are considered to study new radar techniques, to experiment with novel signal processing algorithms and to develop and test state-of-the-art components and hardware.

Precisely, the development of upcoming SAR systems with enhanced radar capabilities leads to an increasing sensor complexity, and thus more demanding electrical specifications are required. Such requirements have a direct impact in the radar antenna design, that plays a key role in the final SAR performance. The radiation properties of the antenna can strongly determine the quality of the final delivered radar image after processing. Figures 1.2 and 1.3 show how different radiation pattern characteristics such as a high side lobe level and lower nadir suppression, respectively, can influence the SAR image quality.

Thus, in order to meet the required antenna performance to fulfill next-generation SAR sensor specifications, new design methods to overcome the inherent limitations related to the antenna internal interactions are needed. However, this aim presents a scientific challenge, since most of the antenna parameters are strongly correlated leading to design trade-offs.

Due to the side-looking operation of SAR along with novel digital beamforming concepts [19], or new advanced imaging modes such as ScanSAR or Spotlight [20], phased

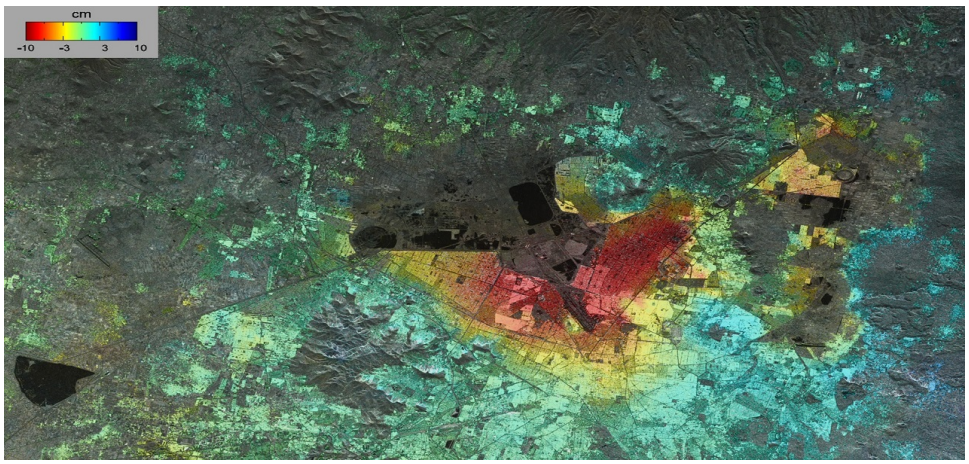

(a)

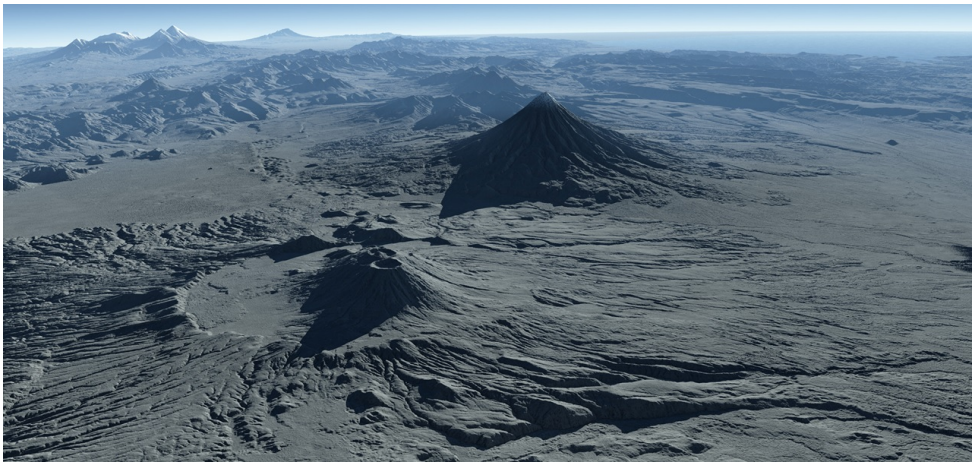

(b)

Figure 1.1.: SAR imaging data acquired from German spaceborne missions TerraSAR and TanDEM-X: (a) Subsidence in Mexico City during the dry season (over 3 months) due to ground water pumping (b) Digital elevation model of the Kamchatka peninsula in Russia.

array antennas with enhanced scanning capabilities are required for upcoming sensors. Maximizing the density of array elements allows a higher versatility to shape the radiation pattern accurately. However, the antenna aperture size is usually limited for practical

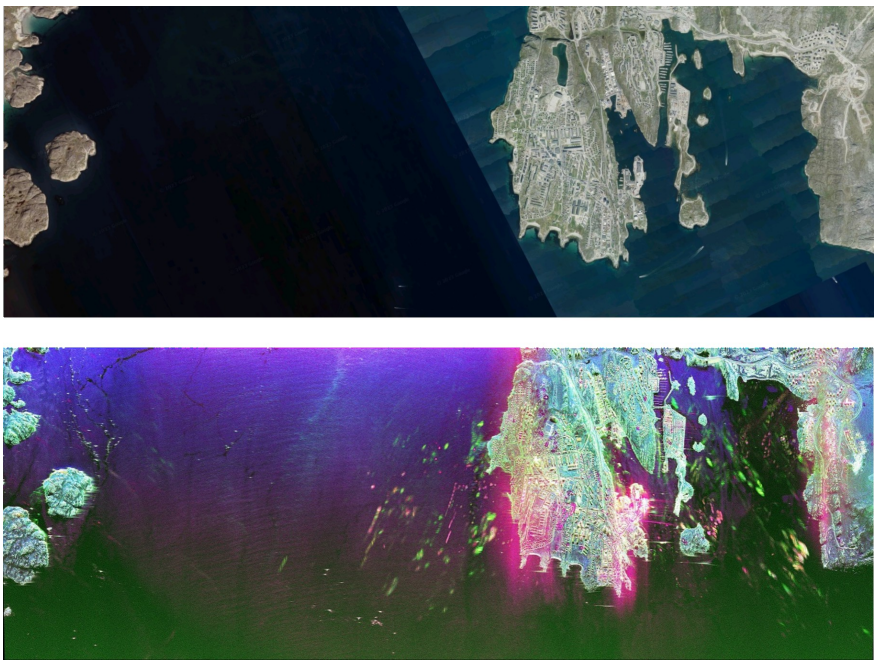

Figure 1.2.: Comparison between Google Maps and DLR airborne F-SAR acquisition of Nuuk (Greenland). After post-processing, the effect of a high side lobe level is displayed in the SAR image in form of bright green dots. The shining red area comes from the signal saturation of the A/D converter.

reasons which involves a considerable compaction effort. Furthermore, this task becomes more demanding for lower frequencies operation as well as for spaceborne, airborne and UAV applications [21], due to the limited available space for the antenna installation [22]. Dealing with these constraints can involve the use of multiband antennas [23] or innovative low-profile array configurations with novel feeding topologies [24]. At the same time, compaction techniques usually have a negative impact in the antenna bandwidth, preventing the wideband specification of next-generation SAR sensors.

Alternatively, the beamforming capabilities of the SAR antenna system can be improved by the reduction of the interelement spacing between array elements. Thereby, the number of antenna elements can be increased, thus exploiting more efficiently the limited antenna aperture size available in most flying-platform sensors. Typical SAR array antennas usually make use of interelement spacings greater than $0.5\lambda_0$ [23, 25–30]. Considering a closer disposal of array elements involves methods to mitigate the interelement coupling in order

to improve the antenna element-to-element isolation.

Well-known approaches to reduce the interelement coupling in array applications consider metamaterial structures. For instance, Electromagnetic Bandgaps (EBGs) suppress the propagation of surface waves, thus enhancing the element isolation [31]. Nevertheless, multilayer stacked antenna configurations make its implementation difficult, especially if materials with low dielectric permittivity like foam are used. In addition, the repetition pattern of EBG unit-cells demands greater spacings, preventing their application in arrays with a tight disposition of antenna elements.

Other solutions such as Defected Ground Structures (DGS) [32] are not suitable for aperture coupling feeding antennas, due to the inherent modification of the ground plane where the apertures can cause spurious radiation and field distortion of the feeding lines.

Thus, other isolation techniques have to be considered such as cavity assemblies where the array element is inserted within a closed structure of electric walls [33]. However, this solution leads to a bandwidth reduction due to its resonant nature. In addition, its mechanical realization for planar arrays is demanding if foam layers are used, since soft materials prevent the implementation of electric walls by means of vias or metal posts (wet etching process).

Furthermore, polarimetric SAR systems make use of the polarization diversity to identify scattering mechanisms. For such applications, dual-linear polarized antennas are required. Thereby, in order to enhance the polarization purity and improve the retrieval of information, different approaches to maximize the cross-polarization suppression of SAR antennas are used [34–36]. The emergence of new antenna solutions and feeding configurations to fulfill the former requirements, also involves the research of novel techniques to reduce the cross-polarization level of upcoming SAR antenna systems.

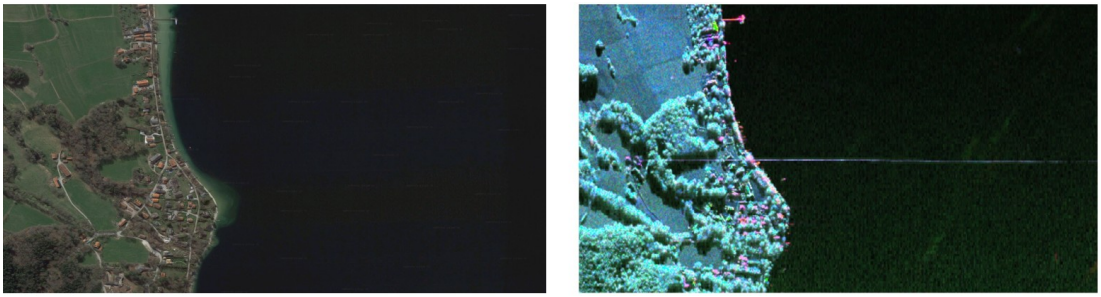

Figure 1.3.: Comparison between Google Maps and DLR airborne F-SAR acquisition of lake Stanberg (Germany). The effect of a insufficient nadir suppression in antenna radiation pattern is displayed in the SAR image as a continuous bright line.

This way, new design challenges arise in order to meet all the aforementioned specifications and to overcome the intrinsic limitations of the antenna internal interactions.

The scope of this thesis is to present novel antenna solutions for next-generation polarimetric airborne SAR applications, that involve new methods and techniques to deal with the former antenna internal interactions, leading to a direct enhancement of the final SAR sensor performance.

Thus, this dissertation presents the design of a low-profile multilayer L-band dual-polarized phased array antenna with beam steering in elevation. The proposed design maximizes the number of array elements to enhance the beamforming capabilities of the SAR system, by means of truncated cavities to improve the antenna isolation along with a reduced interelement spacing of $0.48\lambda_0$. In addition, the cross-polarization suppression of the antenna is improved by a novel 90° element sequential rotation approach, achieving measured cross-polarization discrimination values of 35 dB. At the same time, the antenna provides beam steering in elevation, enhanced side lobe level better than 20 dB and achieves a bandwidth of almost 20%.

Furthermore, this thesis introduces a low-profile feeding network in CPW-SIW technology in X-band with enhanced robustness against feeding tolerances. The proposed feeding configuration, based on three geometrical variations of balanced power dividers, allows to excite different antenna module arrangements to achieve several beamforming operations in elevation and azimuth. At the same time, the presented design provides a very compact solution by allowing stacked-up configurations along with the use of extremely high permittivity substrates. In the scope of this work, a novel ultrawideband tapered V-Slot CPW-SIW transition with improved performance for higher frequencies has been also developed.

Last but not least, the final antenna performance is also determined by the external interactions arisen between the antenna and its environment. Due to the inherent radiation nature of the electromagnetic waves, the electric fields interact with the antenna surrounding structures resulting in multipath, diffraction and scattering effects that can severely degrade the antenna radiation pattern. Figure 1.4 shows how a given antenna sitting position can influence the radiation pattern leading to a pattern distortion, as it can been seen in some areas of the antenna carrier used on the DLR airborne SAR sensor F-SAR [37].

Thus, the extension of this dissertation also includes the analysis and methods to mitigate the external interactions. Some well-known methods to reduce the multipath effect are based on choke-rings [38] around the antenna, especially for communication applications. Alternative low-profile approaches make use of planar metamaterials to synthesize High Impedance Surface (HIS) grounds in order to reduce the induced surface currents by means of surface waves suppression [39] or the synthesis of microwave absorbers [40].

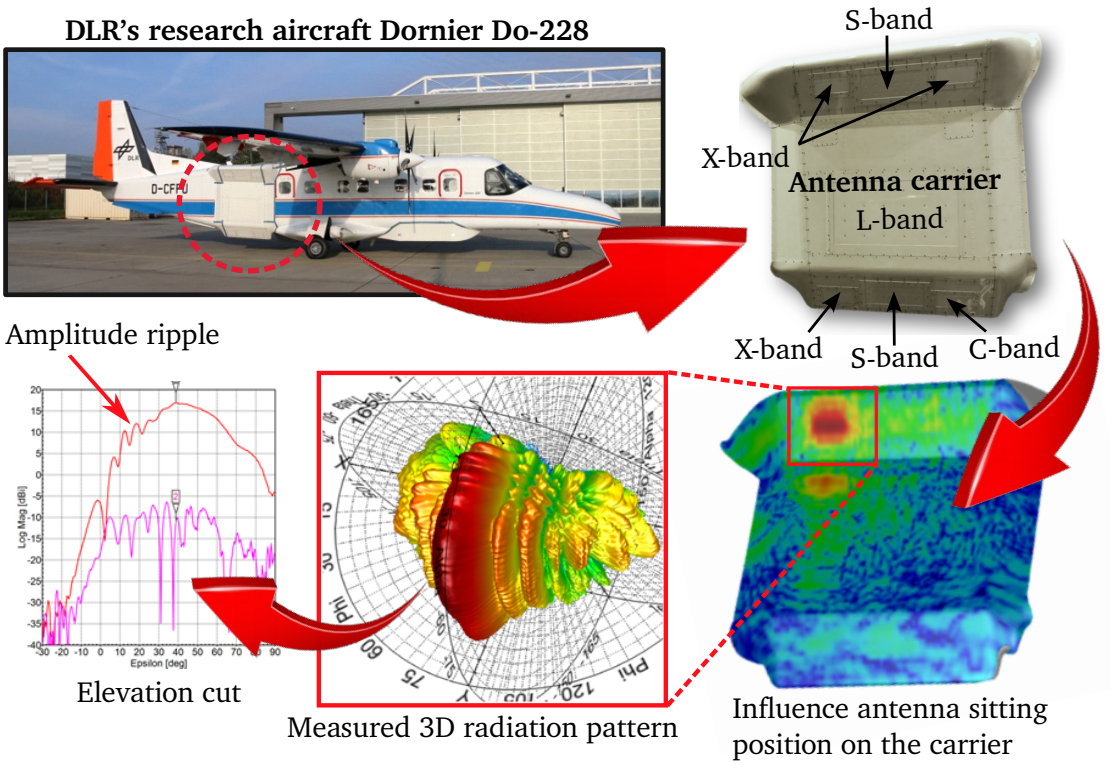

Figure 1.4.: Influence of the antenna sitting position on the F-SAR antenna carrier.

The emergence of multifrequency SAR sensors also leads to the demand of compact and low-profile multiband metamaterial structures to deal with the external antenna interactions, and mitigate the influence of the antenna surroundings for multifrequency applications. Thereby, in the scope of this work, the design of a novel quad-band EBG unit-cell that provides surface-wave suppression at L-, S-, C- and X-band has been also investigated for its implementation in the antenna carrier of the F-SAR system.

1.2. Thesis Scope: DLR Projects Framework

This doctoral thesis has been performed as an industrial PhD, with part-time dedication working as a research scientist in the Microwaves and Radar Institute of the German Aerospace Center (DLR) in Oberpfaffenhofen, Germany.

The scientific output of this dissertation has been developed within the project frame-

works of DuoLIM, DBF-SAR and F-SAR, whose research scope will be next detailed:

- The project **DuoLIM** is a bistatic L-band airborne SAR system. As a bistatic sensor, the radar operation will be based on two aircrafts flying in different formations, one used for transmission and both for reception. Two electrical identical L-band antennas, whose design process is presented in this dissertation, will be mounted in the antenna carrier that is placed under each aircraft. Unlike other bistatic L-band airborne sensors such as BelSAR [41], that operates as a Frequency Modulated Continuous Radar (FMCW) radar, the DuoLIM project will become the first L-band pulsed bistatic airborne SAR sensor worldwide.

- **F-SAR** is the multifrequency polarimetric and interferometric airborne SAR system of the German Aerospace Center (DLR) that operates in the P-, L-, S-, C- and X-bands [18]. The system is mounted on the research aircraft Dornier Do-228. All the L-, S-, C-, and X-band antennas are mounted on the same antenna carrier, placed sideways on the airplane, as it is depicted in Figure 1.4. Due to its size, the P-band antenna is installed on its dedicated carrier that is attached under the aircraft. The novel L-band antenna, developed within the framework of the DuoLIM project, will be also implemented in the next-generation F-SAR system.

- **DBF-SAR** is a high-resolution airborne SAR sensor with digital beamforming capabilities operating in X-band [19]. On the system reception side, 12 Receive Antenna Modules (RAMs), operating as subarrays, can be combined in different configurations to fulfill the desired beam steering. In addition, the feeding network can be stacked up in order to achieve a higher degree of integration.

Methodology

The following methodology has been applied during the development of this PhD thesis.

1. All the proposed work presented in this dissertation has been validated by measurements of real prototypes. These hardware developments have been designed from the beginning, manufactured and assembled.

2. All the design stages, except the PCB production, have been developed on-site in the Microwaves and Radar Institute of the German Aerospace Center (DLR). This also includes the assembly of self-made cables for measurement purposes, the soldering of all connectors and resistors, as well as the hardware construction and assembly.

3. The mechanical parts of the antenna have been constructed by the Microwaves and Radar Institute's workshop.

4. The PCBs have been manufactured by Contag AG and Optiprint AG. While the first company is specialized in prototypes and express shipment, the second one produces high quality PCB products. At the same time, Optiprint offers protection layers against corrosion in their fabrication process, extremely important for airborne applications. In addition, the company offers the possibility of replacing discrete resistors by using thin-film resistor technology (Ticer film).

5. Most of the presented hardware designs are excited by means of 50 Ω SMP connectors [42]. This type of miniaturized connector presents the advantage that it can be easily connected/disconnected by pushing and pulling apart. In addition, it disposes of a given radial tolerance which makes it robust against misalignments and vibrations.

6. The electromagnetic analysis, based on full-wave simulations, and the optimization of the proposed electrical designs have been performed with HFSS. In order to generate the required gerber files for the PCB layout manufacturing, HFSS 3D Layout Design has been used. Both software tools belong to AEDT (Ansys Electromagnetic Desktop) 2017-2022.

7. After the electrical design has been completed, the generation of the mechanical CAD model, for its construction and assembly, has been performed in Autodesk Inventor Professional 2017-2022.

8. The results analysis has been supported by self-programmed scripts in IDL environment.

9. All the schematics, diagrams and image editing have been created with Inkscape vector graphics editor.

10. Most of the graphs and presentation results have been generated using ARCS software tool [43].

11. The measurements of the S-parameters have been performed using the Vector Network Analyzer (VNA) ZVA 24 from Rohde & Schwarz, with an operational bandwidth from 10 MHz to 24 GHz.

12. The spherical far-field measurements of the the antenna radiation pattern have been performed on-site at the DLR's Compact Test Range (CTR) [44], a dual reflector Compact Antenna Test Range (CATR) facility located in the Microwaves and Radar Institute of the German Aerospace Center in Oberpfaffenhofen, Germany. The post-processing measurement data has been done with ARCS.

1.3. Objectives and Thesis Outline

The development of this dissertation includes the achievement of the following objectives:

- ✔ Design of a compact and versatile feeding network in Substrate Integrated Waveguide (SIW) technology within the scope of the DBF-SAR project. This feeding configuration should excite the already available dual-polarized receive antenna modules (RAM), allowing different geometrical dispositions in stacked-up arrangements.
- ✔ In the framework of the DuoLIM project, a new L-band dual-polarized antenna for next-generation DLR airborne SAR sensors is required. This new design should exploit efficiently the limited antenna aperture size available on the research aircraft Do-228 (56.5 cm x 97.5 cm), in order to maximize the density of array elements. Thereby, the antenna beamforming capabilities can be enhanced to fulfill the demanding specifications of upcoming airborne SAR systems.
- ✔ Identify, in different practical scenarios, the impact on the antenna performance of the external interactions arisen between the antenna and its surroundings. Propose some methods to mitigate them, by means of low-profile techniques and approaches, in order to achieve the required antenna performance regardless its environment.
- ✔ Present a solution to mitigate the influence of the antenna sitting position on the F-SAR antenna carrier.

After this introduction chapter, the scope of this dissertation is structured as follows:

In **chapter 2** the fundamentals of SAR theory are presented. At the same time, the importance of the antenna performance in any SAR system is highlighted, as well as how the operation of next-generation SAR sensors impacts in the antenna electrical specifications. In addition, the versatility of airborne SAR systems as a powerful scope of research is explained.

The RAMs feeding network concept for the DBF-SAR project is presented in **chapter 3**. The proposed design, implemented in SIW technology and based on three geometrical variations of a balanced T-junction power divider operating in X-band, excite different RAM arrangements with the possibility of achieving vertical stacked-up dispositions, in order to further maximize the degree of integration. Furthermore, the proposed Coplanar Waveguide (CPW) excitation becomes a robust solution to deal with the increased structure sensitivity, regarding feeding tolerances, when extremely high permittivity substrates are used. In addition, a compact ultrawideband CPW-SIW V-slot transition in X-band with enhanced performance in the higher frequency band is also designed. A Thru-Reflect-Line

(TRL) calibration is developed and applied to different back-to-back transitions in order to perform a connector de-embeding process.

The first design stages of a novel L-band antenna for next-generation DLR airborne SAR sensors are presented in **chapter 4**. In the scope of this chapter, a dual-polarized aperture coupled stacked patch antenna enclosed in a cavity box assembly is designed, manufactured and measured. Next, a linear phased array of five elements with independent excitation is built, in order to assess the performance of the final antenna array in elevation. In addition, a novel sequential 90° rotation approach of the array elements is applied in order to improve the cross-polarization performance of the antenna within the main beam, whose approach is validated with measurements. This technique is compared with the standard equispaced alignment of array elements and with the alternative 180° rotation. To further extend the applicability of this novel cross-polarization suppression method, this sequential rotation approach is also extended to planar array applications.

In **chapter 5**, the following development process of the new L-band antenna is presented. First, a low-profile subarray antenna of 5x4 elements, with beam steering in elevation and asymmetric amplitude distribution in azimuth, is shown. In order to improve the element isolation, a truncated cavity assembly is used, and the proposed sequential 90° rotation approach is applied to enhance the cross-polarization suppression. Within this design stage, a multilayer feeding network that excites each of the array feeding rows in azimuth is developed. Later, the final planar phased array antenna of 5 x 8 elements, based on two mirrored electrical identical subarray antennas, is presented, manufactured and assembled. The measurements of the final constructed prototype, shown at the end of this chapter, successfully validate the proposed L-band antenna design.

Chapter 6 describes the influence of the antenna environment, considering practical scenarios such as the interaction of the radiated fields with the antenna housing structure or the antenna carrier. Several techniques to deal with these external interactions are analyzed, and low-profile solutions by means of EBGs are presented. In the scope of this chapter, additional work has been done about the design of a multiband unit-cell EBG that is briefly commented.

In the final **chapter 7** of this dissertation, the scientific outputs of this thesis are discussed, and summarized in the corresponding conclusions. Finally, some insights about the related future work are provided.

2. Principles of Synthetic Aperture Radar and Applications

In this chapter, the theory of Synthetic Aperture Radar (SAR) is presented. Since the scope of this work is not focused on advanced SAR concepts or novel signal processing techniques, only the basics of SAR are introduced. Thus, the application framework of this PhD thesis, and the impact of the antenna characteristics on the SAR system performance, can be properly highlighted.

Synthetic Aperture Radar has become nowadays, one of the most interesting and extremely versatile techniques of remote-sensing. SAR provides high-resolution imaging data, nearly weather independent, with the possibility of continuous day and night operation. Its wide range of capabilities has expanded its applicability in numerous fields: geoscience, environment monitoring, climate change, subsurface imaging, as well as military surveillance and reconnaissance, among other applications [45]. The unique capability of SAR to monitor dynamic processes on the Earth surface, has boosted the launch of many spaceborne SAR sensors in the last years [10–13]. Furthermore, the increasing concern in global warming will reinforce this trend in the future [46].

Since SAR arises as a technique to overcome the performance limitations of Side Looking Airborne Radars (SLARs), the operation principles of such systems are first introduced.

2.1. Side Looking Aperture Radar (SLAR)

Side Looking Aperture Radars, based on the principles of Real Aperture Radar (RAR), are typically installed on flying platforms that transmit electromagnetic pulses, and receive the backscattered signal produced by the reflection of the transmitted wave on the target. This process is repeated along the flight movement or azimuth direction, in order to provide a continuous illumination of the ground footprint or swath. The line-of-sight (LOS) distance given by the separation between the radar and the target, being perpendicular to the flight direction, is called slant range. The side-looking geometry scenario of the SLAR is depicted in Figure 2.1.

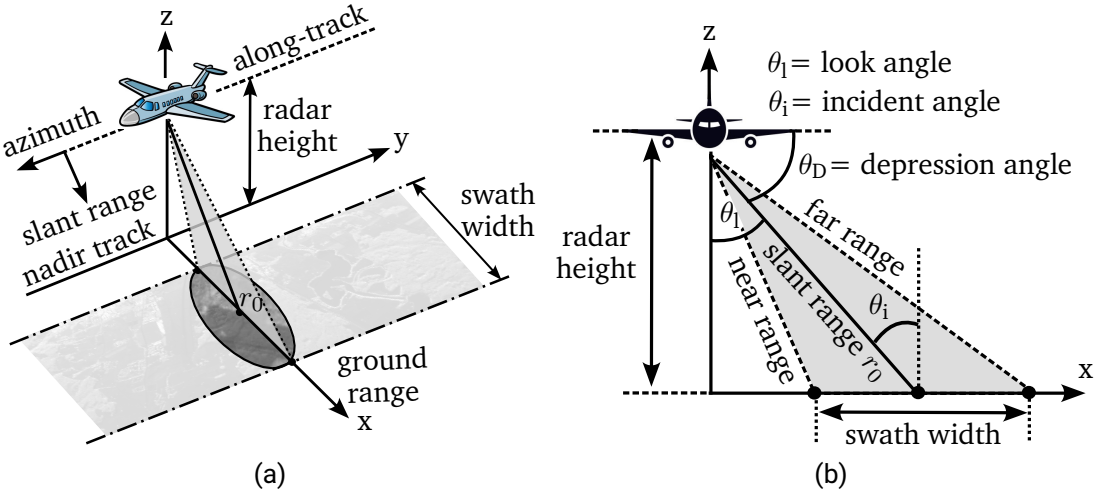

Figure 2.1.: Side Looking Radar (SLAR): (a) Acquisition geometry (b) Side view.

A fundamental parameter to evaluate the radar performance is its resolution, which is the capability of the radar to distinguish different targets. The resolution is given by the smallest spatial separation between two objects so they can be detected or imaged independently.

Range resolution

Considering the radar pulse duration of τ_p, c_0 the speed of light and r_0 the slant range distance between radar and target, the total time delay Δt of echo signal received by the radar is:

$$\Delta t = \frac{2\, r_0}{c_0} \tag{2.1}$$

Which establishes that, in order to detect two targets separately, the leading edge of the echo corresponding to the second target has to be received after the trailing edge of the echo received from the first object. Thus, this condition leads to the following slant range resolution:

$$\delta_\mathrm{r} = \frac{c_0\, \tau_\mathrm{p}}{2} \tag{2.2}$$

Alternatively, if a pulse compression technique is applied, the pulse duration τ_p can be related to the radar bandwidth by $B_\mathrm{r} = \frac{1}{\tau_\mathrm{p}}$, thus leading to:

$$\delta_{\mathrm{r}} = \frac{c_0}{2\,B_{\mathrm{r}}} \tag{2.3}$$

The sending and reception stage of the radar is repeated at a given time frame called Pulse Repetition Interval (PRI), which can be also expressed as the inverse of the Pulse Repetition Frequency (PRF), hence $PRI = \frac{1}{PRF}$. The timeframe where the radar listens, given by the time difference between the trailing edge of the transmitted pulse and the leading edge of the next pulse, is called receive window. The timing window of a radar system is depicted in Figure 2.2:

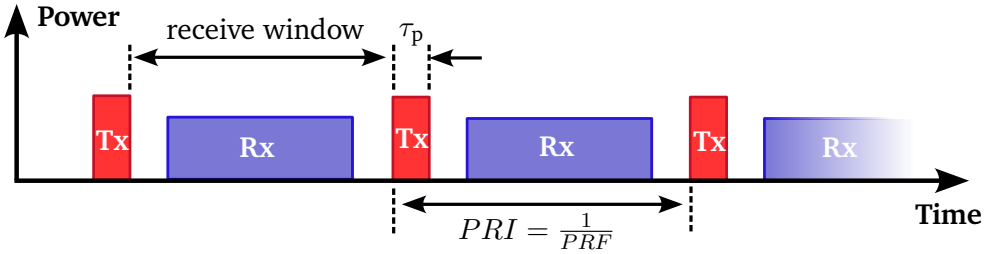

Figure 2.2.: Radar timing.

The slant range resolution can be also described in terms of ground range resolution δ_{rg}, that determines the maximal separation on the ground between two objects so they can be imaged independently, as it is shown in Figure 2.3.

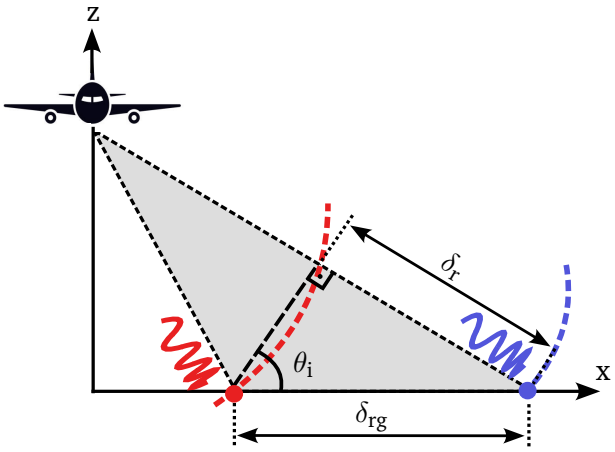

Figure 2.3.: The ground range resolution determines the distance between two objects on the ground in order to be detected independently.

$$\delta_{\mathrm{rg}} = \frac{\delta_{\mathrm{r}}}{\sin\theta_{\mathrm{i}}} = \frac{c_0\,\tau_{\mathrm{p}}}{2\,\sin\theta_{\mathrm{i}}} = \frac{c_0}{2\,B_{\mathrm{r}}\,\sin\theta_{\mathrm{i}}} \tag{2.4}$$

Note that this equation assumes no variation of the incidence angle θ_{i} along the swath, as well as flat surface Earth terrain $\theta_{\mathrm{l}} \approx \theta_{\mathrm{i}}$.

Swath width

The radar swath is the resulting footprint of the illuminated scene on the ground. Its width corresponds to the ground range separation between the closest and furthest slant range distance, known as near range (R_{near}) and far range (R_{far}) respectively, as it can be seen in Figure 2.4.

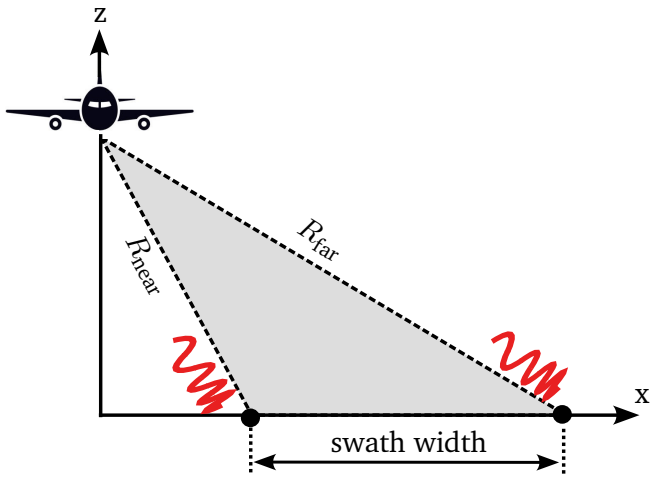

Figure 2.4.: Radar swath width.

Considering that the echo coming from the far range should be recorded within the radar receive window, as it is shown in Figure 2.2, the swath width can be expressed as a function of the PRF:

$$\frac{2\,R_{\mathrm{far}}}{c_0} \leq \frac{2\,R_{\mathrm{near}}}{c_0} + PRI \Rightarrow PRF \leq \frac{c_0}{2\,(R_{\mathrm{far}} - R_{\mathrm{near}})} \Rightarrow \text{swath width} \leq \frac{c_0}{2\,PRF\,\sin\theta_{\mathrm{i}}} \tag{2.5}$$

As it can be seen, the slant ground resolution or maximal swath width depends on the pulse duration or system bandwidth. Short pulse durations would increase the ground resolution, but at cost of limiting the transmitted power that will lead to low signal-to-noise ratio (SNR). This trade-off is overcome by using linear frequency modulated pulses

(chirp signals), thus achieving wider bandwidths with long pulses, i.e improving the range resolution and increasing the transmitted power.

Azimuth resolution

Considering that the antenna halfpower beamwidth in azimuth Θ_{a} can be approximated by $\Theta_{\mathrm{a}} \cong \frac{\lambda}{d_{\mathrm{a}}}$ [47], being λ the radar operation wavelength and d_{az} the effective antenna length in azimuth, as it is depicted in Figure 2.5, the azimuth resolution of the SLAR systems δ_{a} is given by:

$$\delta_{\mathrm{a}} \cong 2\, r_0\, \sin\left(\frac{\Theta_{\mathrm{a}}}{2}\right) \tag{2.6}$$

which determines that only one target can be detected within the antenna beamwidth. For small angles the previous equation can be approximated by means of $\sin\left(\frac{\Theta_{\mathrm{a}}}{2}\right) \approx \frac{\Theta_{\mathrm{a}}}{2}$, thus leading to:

$$\delta_{\mathrm{a}} \cong \frac{\lambda}{d_{\mathrm{az}}}\, r_0 \tag{2.7}$$

As it can be seen, the azimuth resolution depends on the range distance r_0, which means that the azimuth resolution capabilities of the SLAR system linearly deteriorate as the range distance increases. This drawback prevents the implementation of SLAR sensors for spaceborne applications, where high altitude platforms yield greater range distances and thus very low azimuth resolutions are achieved. In addition, compensating the loss of resolution by means of increasing the antenna length would lead to impractical antenna sizes.

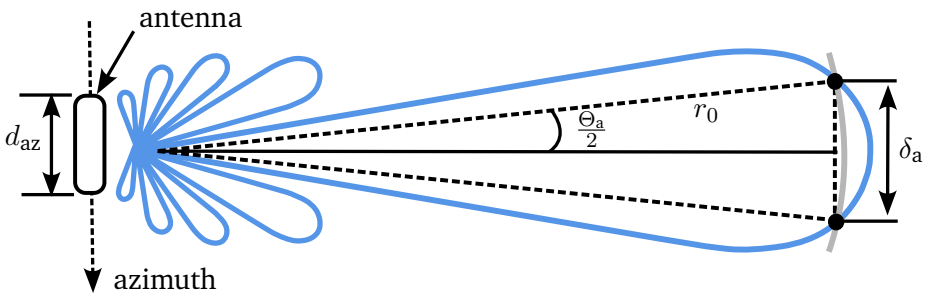

Figure 2.5.: Azimuth resolution of an SLAR system is dependent on the antenna radiation pattern.

2.2. Fundamentals of Synthetic Aperture Radar

Synthetic Aperture Radar (SAR) was developed in order to overcome the inherent limitations of the moderate to low azimuth resolution achieved in Real Aperture Radars. SAR makes use of the Doppler principle to achieve a finer spatial resolution, due to the radar platform motion. Since the scope of this chapter is focused on SAR principles and applications, for the sake of simplicity, some assumptions about the Doppler effect are taken for granted. However, for the interested reader, a theoretical background of the Doppler phenomenon can be found in Appendix A of this work.

SAR basic operation is based on the sequential transmission of radar pulses, and reception of the backscattered echoes while the radar platform is moving. The transmission and reception are performed in different along-track positions due to the radar movement, resulting in different frequency shifts of the transmitted signal or Doppler frequencies, arisen due to the distance variation between the radar and the target. Thus, two independent scatterers can be distinguished in the along-track or azimuth direction based on their different Doppler frequency shifts.

The SAR acquisition geometry and the formation of the "virtual" aperture are depicted, respectively, in Figures 2.6 and 2.7, and it is explained as follows. The radar platform moves at a velocity of v_{p} and stores, during a time period T_{obs}, all the received signals of the same target at different along-track positions from x_1 to x_2. Due to the movement of the radar platform, each of those received signals have a different Doppler frequency. Thus, the real physical antenna of shorter length d_{az} and beamwidth Θ_{a} sees any target on the ground for a longer period of time. This way, after the coherent combination of the received echoes through signal processing, a longer virtual antenna aperture of length $L_{\mathrm{sa}} \approx \Theta_{\mathrm{a}}\, r_0$ can be synthesized, yielding an enhanced azimuth resolution:

$$\delta_{\mathrm{sa}} = \Theta_{\mathrm{sa}}\, r_0 = \frac{\lambda}{L_{\mathrm{sa}}}\, r_0 = \frac{\lambda}{\Theta_{\mathrm{a}}\, r_0}\, r_0 \Rightarrow \delta_{\mathrm{sa}} = \frac{d_{\mathrm{az}}}{2} \tag{2.8}$$

whose theoretical derivation is detailed in Appendix A.

It can be noted that the azimuth resolution becomes independent on the range and the transmitted frequency (i.e geometrical resolution does not depend on the distance), which is the key feature of Synthetic Aperture Radar.

As Figure 2.6 shows, considering the distance r_0 as the closest approach between the radar and the target, the range variation of a point target for a given along-track coordinate or azimuth position can be expressed as:

$$r(x) = \sqrt{r_0^2 + x^2} \Rightarrow r(x) \approx r_0 + \frac{x^2}{2\, r_0} \tag{2.9}$$

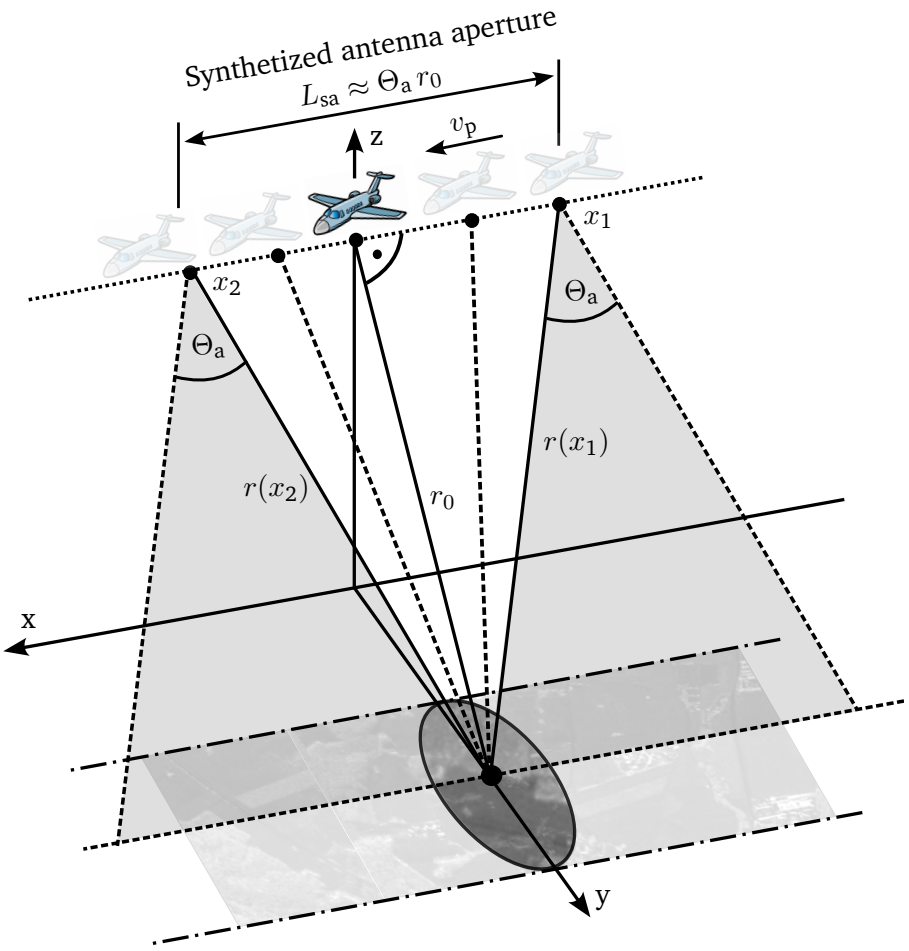

Figure 2.6.: SAR acquisition geometry.

which is an approximation considering that the displacement of the radar is negligible in comparison with the distance between the target and the radar ($\frac{v_p\, t}{r(x)} << 1$). In addition, the instantaneous range can be expressed considering the velocity of the radar v_p:

$$r(t) \approx r_0 + \frac{(v_p\, t)^2}{2\, r_0} \tag{2.10}$$

Then, the azimuth phase variation $\varphi_a(t)$ of the returned echo over time can be easily deduced, considering that the 4π factor comes from the two way range distance or round trip of the signal:

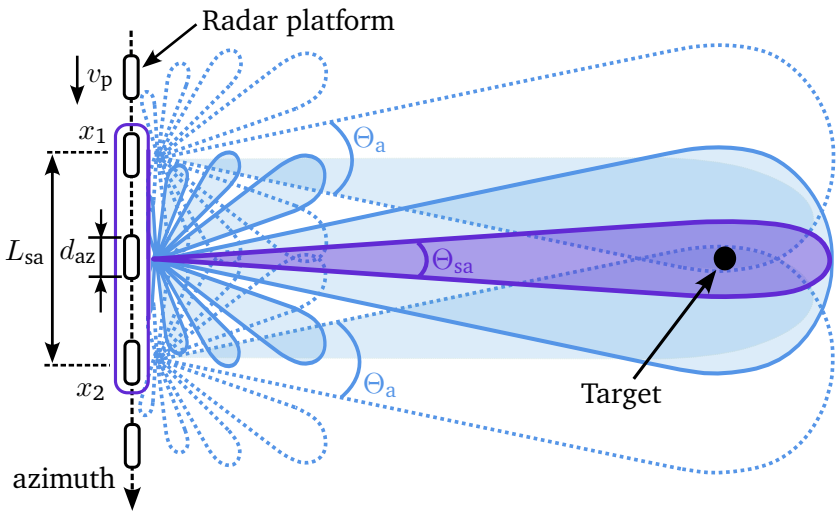

Figure 2.7.: Formation of the synthetic aperture.

$$\varphi_a(t) = -\frac{4\pi}{\lambda} r(t) \approx -\frac{4\pi}{\lambda}\left[r_0 + \frac{(v_p\, t)^2}{2\, r_0}\right] \tag{2.11}$$

Doppler frequency

The azimuth frequency or Doppler frequency f_D can be extracted by means of the partial derivative in time of the azimuth phase:

$$f_D(t) = \frac{1}{2\pi}\frac{\partial \varphi_a(t)}{\partial t} \approx -\frac{2v_p^2}{\lambda\, r_0}\, t = k_D\, t \tag{2.12}$$

The target on the ground is illuminated during a time T_{obs} given by:

$$T_{obs} = \frac{L_{sa}}{v_p} = \frac{\Theta_a\, r_0}{v_p} = \frac{\lambda\, r_0}{d_{az}\, v_p} \tag{2.13}$$

As a convention, $t = 0$ is the time of the closest approach between the radar and the target ($r(t = 0) = r_0$), which means that the target is illuminated from $t = \left[-\frac{T_{obs}}{2}, \frac{T_{obs}}{2}\right]$, so the Doppler bandwidth B_D can be computed as:

$$B_D = f_D\left(-\frac{T_{obs}}{2}\right) - f_D\left(\frac{T_{obs}}{2}\right) = \frac{2\, v_p}{d_{az}} \tag{2.14}$$

Precisely, considering that the highest Doppler frequency occurs at $t = -\frac{T_{\text{obs}}}{2}$, when the radar is furthest from the target:

$$f_{\text{D}}^{\text{max}} = f_{\text{D}}\left(\frac{T_{\text{obs}}}{2}\right) = \frac{v_{\text{p}}}{d_{\text{az}}} \tag{2.15}$$

which according to Nyquist's sample rate criterion yields to:

$$PRF \geq 2\, f_{\text{D}}^{\text{max}} \geq B_{\text{D}} \tag{2.16}$$

Furthermore, taking into account equation (2.5), then:

$$B_{\text{D}} \leq PRF \leq \frac{c_0}{2\,\text{swath width}\,\sin\theta_{\text{i}}} \tag{2.17}$$

From the previous analysis it follows, that the antenna length is dependent on the system parameters such as PRF, platform velocity, etc.

SAR imaging processing

To provide a rough overview of SAR data processing, the signal echoes acquired by the radar are amplified and demodulated, thus generating the so-called raw data. This data is a two-dimensional matrix (azimuth and range coordinates) of complex values, containing amplitude (given mainly by the backscattered coefficient σ_0) and phase information of the received signal. Only after raw data processing, the SAR image can be generated.

SAR signal processing is divided in two matched filtering operations along the range and azimuth dimensions, in order to maximize the signal-to-noise ratio. The first operation is called range compression, and it is applied in order to compress the chirp signal and to obtain a short pulse or point target response. The compressed signal is obtained by performing the convolution (in frequency domain to avoid computational complexity) of the received signal by the complex conjugated of the time-reverse transmitted chirp signal. Consequently, and following the same idea, an azimuth compression operation is also applied. The azimuth signal can be expressed as:

$$s_{\text{a}}(t) = A\,\sqrt{\sigma_0}\,e^{j\varphi_{\text{scatt}}}\,e^{-j\varphi_{\text{a}}(t)} = A\,\sqrt{\sigma_0}\,e^{j\varphi_{\text{scatt}}}\,e^{(-j\frac{4\pi}{\lambda}r(t))} \cong \overline{A_{\text{a}}}\,e^{(j\,2\pi\,k_{\text{D}}\,t^2)} \tag{2.18}$$

where $\overline{A_{\text{a}}}$ is a complex value weighted by a constant A, dependent on radar system parameters (transmitted power, system losses, antenna pattern), and the radar cross section given by the amplitude σ_0 and scattering phase φ_{scatt}.

Signal-to-noise ratio (SNR)

Another parameter that has a key impact on the quality of the SAR image is the signal to noise ratio (SNR), which determines the threshold of the received signal intensity that can be detected by the radar. The signal-to-noise ratio for SAR systems can be expressed as follows [48]:

$$SNR = \frac{\text{received signal power}}{\text{thermal noise power}} = \frac{P_{\text{avg}}\, G_{\text{tx}}}{4\pi\, r_{\text{tx}}^2}\; A_{\text{cell}}\, \sigma_0\; \frac{A_{\text{rx}}^{\text{eff}}}{4\pi\, r_{\text{rx}}^2 L_{\text{path}}}\; \frac{T_{\text{obs}}}{k\, T_{\text{s}}\, F} \tag{2.19}$$

where all the related parameters are listed in Table 2.1.

SNR contribution	Symbol	Definition
Transmission path $\Rightarrow \frac{P_{\text{avg}}\, G_{\text{tx}}}{4\,\pi r_{\text{tx}}^2}$	P_{avg}	Transmitted average peak power
	G_{tx}	Antenna transmission gain
	r_{tx}	Range distance in transmission
Target backscattering $\Rightarrow A_{\text{cell}}\, \sigma_0$	A_{cell}	Cell resolution (swath size)
	σ_0	Backscattering coefficient
Reception path $\Rightarrow \frac{A_{\text{rx}}^{\text{eff}}}{4\pi\, r_{\text{rx}}^2\, L_{\text{path}}}$	$A_{\text{rx}}^{\text{eff}}$	Effective antenna aperture in reception
	G_{rx}	Antenna reception gain
	r_{rx}	Range distance in reception
	L_{path}	Losses (atmosphere, receiver)
Receiver and processing $\Rightarrow \frac{T_{\text{obs}}}{k\, T_{\text{s}}\, F}$	T_{s}	Receiver noise temperature
	F	Noise figure
	k	Boltzmann constant
	T_{obs}	Target observation time

Table 2.1.: Signal-to-noise ratio parameters.

Considering a monostatic radar, where $r_{\text{tx}} = r_{\text{rx}} = r$, and using the same antenna for transmission and reception $G_{\text{tx}} = G_{\text{rx}} = G$, the signal-to-noise ratio is given by:

$$SNR = \frac{P_{\text{avg}}\, G^2\, \lambda^2\, c_0\, \sigma_0\, d_{\text{a}}\, T_{\text{obs}}}{(4\pi)^3\, r^4\, 4\, \sin\theta_{\text{i}}\, B_{\text{r}}\, L_{\text{path}}\, k\, T_{\text{s}}\, F} \Rightarrow SNR = \frac{P_{\text{avg}}\, G^2\, \lambda^3\, c_0\, \sigma_0}{(4\pi)^3\, r^3\, 4\, \sin\theta_{\text{i}}\, B_{\text{r}}\, L_{\text{path}}\, v_{\text{p}}\, k\, T_{\text{s}}\, F} \tag{2.20}$$

Noise Equivalent Sigma Zero (NESZ)

Related to the signal-to-noise ratio, the Noise Equivalent Sigma Zero (NESZ) can be derived, considering that the NESZ is the value of the backscattering coefficient σ_0 that

yields a $SNR = 1$. The NESZ describes when the received signal can not be differenciated from the inherent system noise and is described as follows [49]:

$$NESZ = \frac{2\,(4\pi)^3\,k\,T_{\mathrm{s}}\,F\,PRF\,N_{\mathrm{az}}\,\sin\theta_{\mathrm{i}}}{c_0\,\lambda^2\,P_{\mathrm{avg}}\,G_{\mathrm{tx}}\,G_{\mathrm{rx}}\,\delta_{\mathrm{a}}\,T_{\mathrm{obs}}}\,f(\theta,\varphi)\,r(\theta,\varphi) \tag{2.21}$$

Where $f(\theta, \varphi)$ is the two-way antenna radiation pattern, $r(\theta, \varphi)$ the range distance as a function of elevation and azimuth angles, and N_{az} the number of integrated pulses during azimuth compression.
As it can be seen, the NESZ measures the sensitivity of the SAR system, thus becoming a key parameter to assess the quality of the SAR imaging, since it determines the floor noise of the radar image.

Backscattering and penetration capability

The reflected backscattered signal measured by the radar can be quantified by means of the normalized Radar Cross Section (RCS) or backscattering coefficient σ_0:

$$\sigma_0 = \frac{\text{received energy by the sensor}}{\text{energy reflected in an isotropic way}} = \lim_{r\to\infty}\left[\frac{4\,\pi\,r^2}{A_{cell}}\,\frac{|E_{\mathrm{r}}|^2}{|E_{\mathrm{i}}|^2}\right] \tag{2.22}$$

where E_i and and E_r are the incident and reflected electric field, respectively.

The intensity of the backscattered signal σ_0 is typically driven by the surface roughness of the imaged object and its complex dielectric properties. While smooth surfaces generate specular reflection and thus produce a mirror-like signal reflection, rough surfaces provide diffuse scattering, when the energy is scattered in a broad range of directions. The surface roughness is dependent on the transmitted radar wavelength [50].

The scattering characteristics of the received signal are also influenced by the dielectric properties of the medium and conductivity, that determine how much energy is reflected or lost, due to absorption. In addition, the penetration capability of the radar is strongly dependent on the sensor frequency. Smaller wavelengths (X-band) can only backscatter on the vegetation canopy, while larger wavelengths (P-, and L-band) provide better vegetation penetration. Thus, for applications such as vegetation analysis and forest characterization (profile, height, biomass) lower radar frequencies are used. Furthermore, the density of the vegetation canopy also influences the penetration capability, which can prevent the use of wavelengths below L-band to penetrate in dense forests. Following the same reasons, the penetration depth into bare surfaces is even more dependent on the sensor wavelength, achieving only subsurface imaging by means of very low frequency operation.

2.3. SAR Applications

SAR capabilities can be further extended in order to enhance the retrieval of information, by means of different techniques such as polarimetry and interferometry. In this section, the basics of these techniques are introduced as well as their application possibilites.

SAR Polarimetry (PolSAR)

As an active radar system with its own illumination source, SAR allows to fully exploit the signal polarization for transmission and reception purposes. This key feature of SAR systems greatly enhances the retrieval of information, and thus, a wide range of scattering mechanisms and imaged objects can be classified.

SAR polarimetry can be characterized by a scattering matrix that describes the polarization response of the received signal when the same polarization is transmitted and received, given by $|S_{HH}|$ and $|S_{VV}|$ for the horizontal and vertical polarizations respectively, as well as $|S_{HV}|$ and $|S_{VH}|$ when the transmitted and received polarization differs. Since the transmitted signal interacts differently with the target depending on its polarization, thus affecting its scattering intensity, more information of the imaged area can be acquired, leading to a better object classification. This way, real physical parameters can be extracted from radar data.

For simplicity, SAR data are characterized considering three different types of scattering processes:

- **Rough surface scatterers**: like low vegetation fields, rough water, bare ground, roads or paved surfaces.
- **Dihedral or double-bounce scatterers**: for instance man-made structures (buildings, lighting poles), stemmy vegetation (tree trunks) or other vertical structures.
- **Volume scatterers**: such as vegetation, where the radar signal bounces as it goes through, or high-penetration dry soils. This nature of scattering typically changes the polarization state of the received wave.

The different scattering processes can be distinguised by the relative scattering strength received at each polarization channel. To highlight this polarization backscattering dependency, $|S_{HH}|$, $|S_{VV}|$, $|S_{HV}|$ data are often depicted in red, blue and green respectively, according to the classification model based on Pauli Decomposition [51].

Figure 2.8 shows an example of some polarimetric multifrequency SAR images with different resolutions acquired by the DLR airborne F-SAR system. It can be seen that the penetrating capabilities of L-band allow to distinguish volumetric scattering of forests,

Type of scattering	Scattering strength	Color
Rough surface	$\|S_{VV}\| \geq \|S_{HH}\| \geq \|S_{HV}\| \geq \|S_{VH}\|$	Blue
Double bounce	$\|S_{HH}\| \geq \|S_{VV}\| \geq \|S_{HV}\| \geq \|S_{VH}\|$	Red
Volume scattering	Mainly $\|S_{HV}\|$ and $\|S_{VH}\|$	Green

Table 2.2.: Relative scattering strength dependent on polarization.

depicted in green, while in X-band, rough surface scattering can be detected (blue areas). In between, S-band and C-band allow the characterization of crops and vegetation fields.

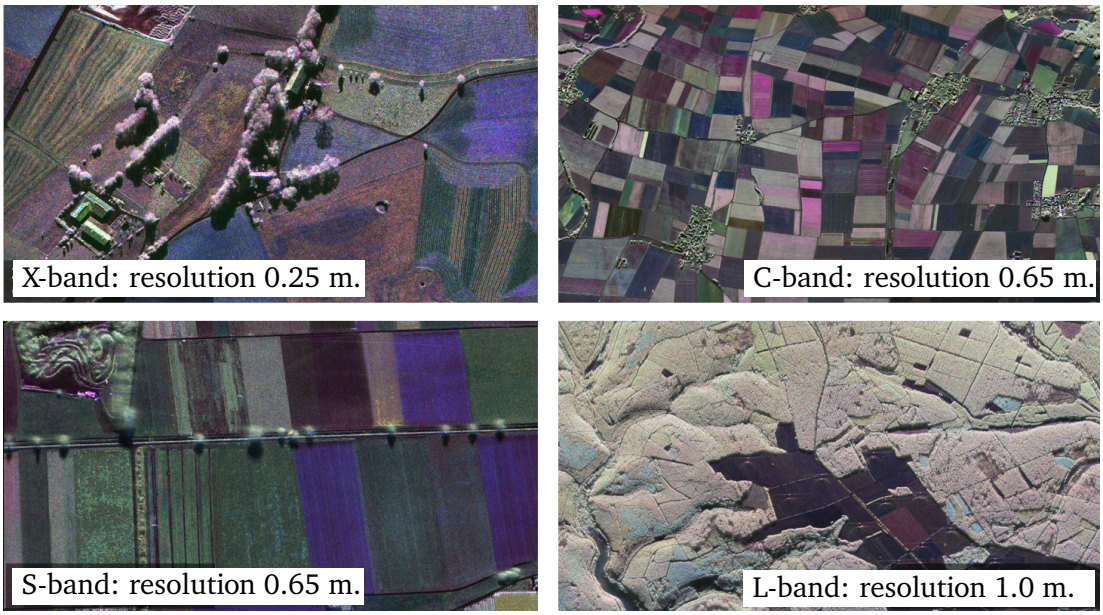

Figure 2.8.: Several multifrequency polarimetric images acquired by DLR's F-SAR system.

SAR Interferometry (InSAR)

Another powerful and extremely useful SAR technique is interferometry. Typical SAR processing only provides 2D imaging data, without generating information of the imaged scene height or elevation angle. InSAR exploits the phase variation between two different acquisitions or baselines to extract height information. They can be either at different positions (spatial baseline) or timespans (temporal baseline). The interferometric coherence measures the degree of correlation between the two SAR complex images by analysis of the phase difference. Due to the cyclical phase repetition, which yields a height ambiguity,

usually a phase unwrapping method has to be applied.

- **Across-track interferometry** makes use of an additional mapping of the SAR scene that is acquired by a second antenna, that is displaced from the first one geometrically (for instance, with different radar flights) or in the same radar, where the second antenna is displaced parallel or along cross-track direction, thus yielding different antenna heights. This way, the SAR scene can be mapped with different look angles. This technique allows to generate Digital Elevation Models (DEMs) for topography studies, with an accuracy in the range of the transmitted wavelength. Across-track interferometric data can be acquired using two antennas for reception (single pass), using the same transmission antenna or alternating between both antennas (ping-pong configuration). In addition, the SAR scene can be also mapped with the same antenna for transmission and reception (repeat-pass).

- **Along-track interferometry** exploits SAR data acquired in single-pass configuration with antennas placed at different along-track positions, in order to measure ocean currents, as well as to monitor and calculate the velocity of moving objects such as cars or ships. On the other side, Differential SAR interferometry (DInSAR) makes use of different SAR images acquired in repeat-pass configuration within time intervals from days to years, to detect dynamic processes such as Earth surface displacements due to subsidence, seismic events or glaciers. DInSAR makes use of an external DEM or topographic information that is subtracted from the interferometric data. Thus, the difference in the range distance (i.e displacement) can be detected.

SAR remote sensing capabilities can be even further enhanced when combining polarimetry and interferometry. This technique, also known as Pol-InSAR, allows to characterize the vertical structure of natural and artificial volume scatterers, being its main application the retrieval of forest information. In addition, Pol-InSAR allows to perform tomographic imaging with 3D resolution by means of synthesizing a larger aperture along the vertical direction, following the same SAR principle but in elevation [52].

Future SAR systems

Despite the outstanding remote-sensing capabilities of SAR, there is an inherent limitation regarding fine azimuth resolution along large swaths. As it can be extracted from equation (2.15), achieving better azimuth resolution involves a larger Doppler bandwidth, and thus increased sampling rate. However greater PRF limits the timespan when the radar transmits and listens, thus reducing the imaged swath width.

Thereby, the driving aspect to enhance the performance of next generation spaceborne SAR systems is to overcome this drawback. This limitation can be partly solved with ad-

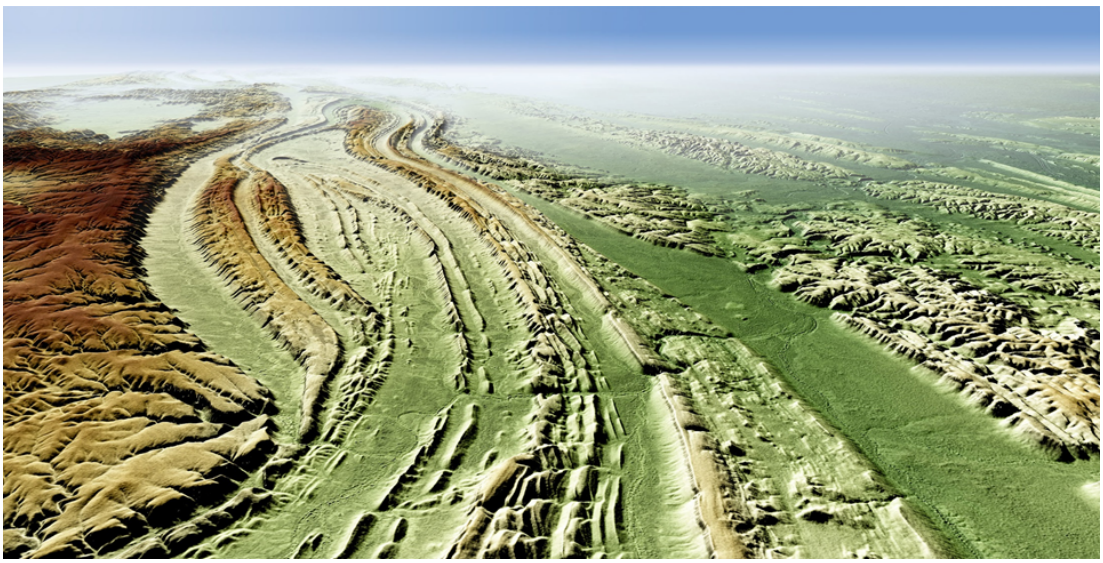

Figure 2.9.: Digital elevation model of Finke Gorge National Park (Australia). Data acquired from TerraSAR-X and TanDEM-X.

vanced SAR imaging modes such as ScanSAR [53] or Spotlight [54], where one parameter (swath width or azimuth resolution) can be improved at the expense of the other.

The trend of upcoming spaceborne SAR missions is to exploit multiple baselines with bistatic or multistatic constellations, that along with new imaging modes and digital beamforming methods, can significantly enhance the retrieval of information. These technological developments, together with short revisit times (i.e. improved temporal resolution), will allow, in the long term, to monitor globally and dynamically Earth surface processes in a weekly or even daily basis [55].

2.4. SAR Antenna

From the main principle of SAR, based on the synthesis of a virtual larger antenna aperture, it can be noted that the antenna plays a key role in the successful radar operation.

Considering the aforementioned fundamentals of SAR, the impact of the antenna radiation properties in the radar performance can be straightforward related by means of the following parameters:

- **Antenna bandwidth** limits the ground range resolution.

- **The antenna radiation pattern and gain** strongly influence the quality of the SAR imaging, since they determine the image floor noise given by the Noise Equivalent Sigma Zero (NESZ), and thus, the system sensitivity to assess the signal-to-noise ratio (SNR).
- **Antenna size in azimuth** determines the azimuth resolution.
- **Beam steering** of side-looking acquisition geometry of SAR systems typically lead to an electrically adjusted phased array antenna, that allows to control the angular direction of the antenna main beam.
- **Beam shaping capabilities** to fulfill a required side lobe level (SLL) suppression in elevation and azimuth plane, in order to deal with range and azimuth ambiguities that can lead to false targets. For airborne applications, and to avoid interferences from undesired areas, additional suppression in nadir direction and opposite swath are required, in order to mitigate the strong echoes coming from the perpendicular direction to the flight path and the scattering contribution received by the antenna backlobe, respectively.
- **Polarization purity and cross-polarization suppression** are inherent parameters of SAR polarimetric systems, that make use of the polarization diversity of scatterers to enhance the retrieval of information.

Figure 2.10 shows the direct dependency of different SAR performance parameters on the antenna characteristics.

Requirements for next generation SAR sensors

The increasing interest in SAR systems, and the trend to further expand its capabilities, will lead to more demanding sensor requirements, thus shaping the antenna specifications for future SAR sensors:

- Advanced SAR imaging modes require versatile phased array antennas with beam-forming capabilites (beam steering), in order to map the SAR scene with different look angles in elevation and azimuth for transmit or receive purposes [56].
- Since the ground range resolution is linked to the radar bandwidth, it is expected the use of greater system bandwidths in future SAR sensors, in order to enhance the resolution. Thus, broadband antennas will be required.
- Furthermore, the different remote-sensing capabilities of SAR systems, depending on the operational frequency, will also boost the appearance of multifrequency sensors with multiband antennas.

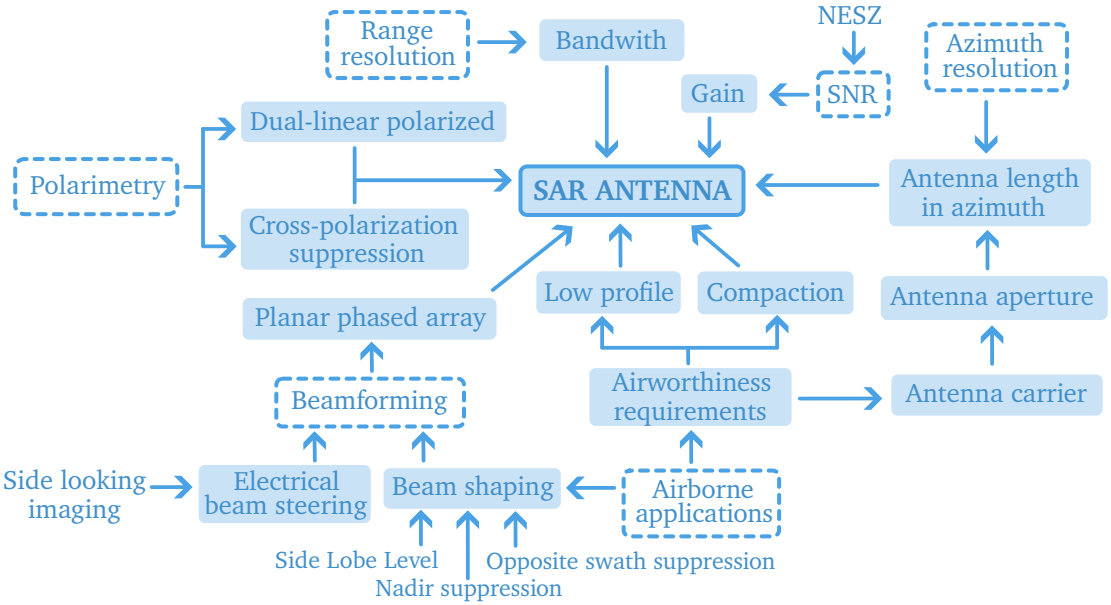

Figure 2.10.: Antenna requirements for SAR systems.

- The trend towards multistatic systems, in which one sensor transmits and several ones do receive, will also influence the specifications of next generation SAR sensors. In order to maximize the retrieval of information, several baselines are used, so different spatial and temporal acquisitions can be achieved. Since complex spaceborne constellations can considerably increase the cost of such systems, some multistatic SAR concepts using small satellites as receivers have been proposed [57]. Thus, a greatly effort in antenna compaction has to be achieved, so the radar front end can be installed in these small sensors. In addition, similar degree of miniaturization has to be fulfilled for airborne SAR applications, as well as for the nowadays increasingly demand of UAV and drone sensors [58].

2.5. Design Framework of Airborne SAR Sensors

Since airborne SAR systems are usually employed as a testing bench for spaceborne SAR missions, they have always been at the forefront of technological advancements. Their versatility provides an excellent scope of research to test novel radar concepts, new signal processing algorithms and state-of-the art hardware developments. Typical airborne SAR systems use PRF values of a few kHz, covering swath widths from a few to 20 Km.

Besides the aforementioned specifications involving antenna design for SAR systems, radar hardware design for airborne applications usually requires low-profile, highly integrated and light weight solutions, aimed to fulfill the airworthiness specifications, as shown in Figure 2.10.

Antenna carrier

Usually, airborne SAR antennas are installed on an attachment platform called antenna carrier, that is mounted sideways or below the aircraft. This holding structure has to be flight certified and aerodynamically adapted to the aircraft characteristics. The antenna aperture size is given by the limited area available on the carrier that cannot be exceed.

The multifrequency polarimetric and interferometric airborne SAR sensor of the German Aerospace, F-SAR [37], as well as its extension with digital beamforming capabilities, DBF-SAR [24], are installed on the research aircraft Dornier Do-228-212 D-CFFU, depicted in Figure 2.11. The new bistatic airborne SAR system DuoLIM will be additionally installed on the second research aircraft Do-228-101 D-CODE.

Figure 2.11.: DLR's research aircraft Do-228-212 D-CFFU. The antenna carrier is installed sideways on the aircraft.

For F-SAR and DBF-SAR sensors, the antenna carrier is placed laterally on the aircraft, as it can be seen in Figure 2.11. Since the F-SAR sensor is a multifrequency airborne SAR system, several antennas are installed on its carrier, as depicted in Figure 2.12. In addition, several X-band and S-band antennas are used for single-pass along-track and across-track interferometric purposes.

On the other side, the antenna carrier of the DuoLIM project is installed below the

aircraft, as shown in Figure 2.13. The reason for the different attachment position in comparison with the F-SAR system, is that the shorter length of the aircraft Do-228-101 D-CODE does not allow mechanically the attachment of the antenna carrier on its side. In addition, due to its circular shape, the antenna carrier is aerodynamically optimized which also allows to slightly rotate the antenna pointing direction.

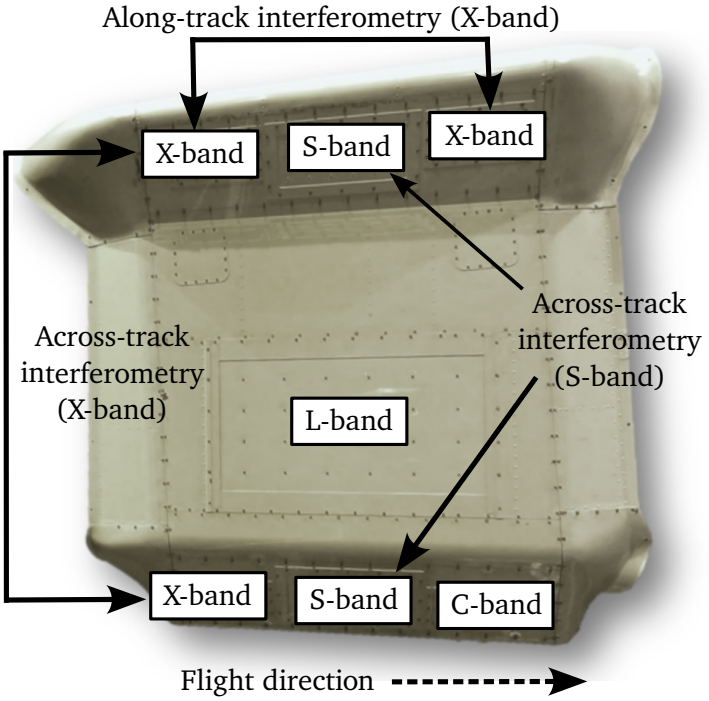

Figure 2.12.: F-SAR antenna carrier. Attachment on the aircraft side.

Despite the different attachment positions and holding structures, the next generation L-Band antenna for DuoLIM project will be adapted to maintain the available antenna aperture size of the F-SAR carrier. Thus, the same L-band antenna design will be implemented in both future airborne SAR sensors of the German Aerospace Center.

In summary, it can be noted that the antenna design for airborne SAR applications is strongly determined by two key aspects:

- **SAR-driven application:** that defines the electrical characteristics of the antenna that are required to fulfill the SAR system performance such as beam steering, gain, side lobe level, bandwidth, dual-linear polarization, etc.

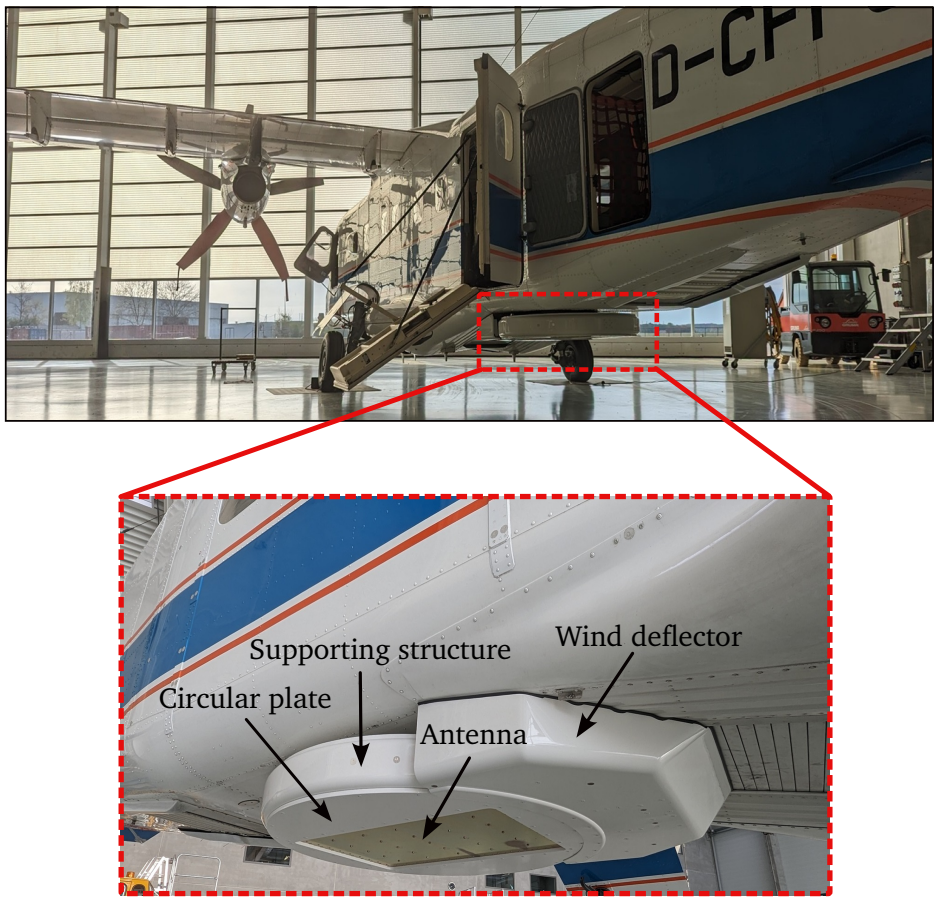

Figure 2.13.: DuoLIM antenna carrier. The attachment position is under the aircraft.

- **Airborne-driven application:** given by the fullfillment of the airworthiness requirements that determine the aerodynamic installation of the antenna on the aircraft and thus, its available aperture size, leading to highly integrated and light weight solutions. Furthermore, the antenna has to withstand corrosion and different atmospheric conditions of pressure, air condensation and electrostatic charge, as well as to endure aircraft vibrations.

3. DBF-SAR RAMs Feeding Network

In this chapter, the feeding network concept for the Receive Antenna Modules (RAMs) of the DLR's DBF-SAR airborne system is presented. This receving network topology, designed in Substrate Integrated Waveguide (SIW) technology, allows to combine the different RAMs alignments while achieving a high degree of integration. In addition, in the scope of this work, a compact ultrawideband V-slot transition between Grounded Coplanar Waveguide (GCPW) and SIW technologies with enhanced performance at higher frequencies is also designed.

3.1. DBF-SAR System Operation

The DLR's High-Resolution Digital-Beamforming Airborne SAR System, DBF-SAR [24], has been developed in order to demonstrate the potential of digital beamforming to overcome the limitations of SAR regarding large swaths and finer spatial resolution [15]. As a key technology to resolve this trade-off, SAR systems with digital beamforming capabilities have to be validated before its implementation in future spaceborne SAR missions [14].

Since a thoroughly operational description of the DBF-SAR sensor is beyond the scope of this PhD thesis, only the technical details regarding the receiving side of the system are explained. Thus, the main purpose of the application can be highlighted.

DBF-SAR receive system configuration

The DBF-SAR system uses one transmission antenna, while the receive path can be arranged to achieve different beam steering configurations in elevation and azimuth. This operational flexibility is accomplished with the combination of up to 12 receiver channels equipped with Receive Antenna Modules (RAMs). Each of these antenna modules consists of a subarray of 1×4 dual-polarized stacked microstrip patches operating at 9.6 GHz with a bandwidth of 1.8 GHz. Every RAM disposes of its own integrated feeding network that excites each subarray with constant amplitude and phase. A picture of an antenna receive module with its dimensions can be found in Figure 3.1.

The antenna housing of the DBF-SAR system allows a combination of a pair of RAMs in order to build up an array of 1×8 elements or 2×4, depending on the alignment direction,

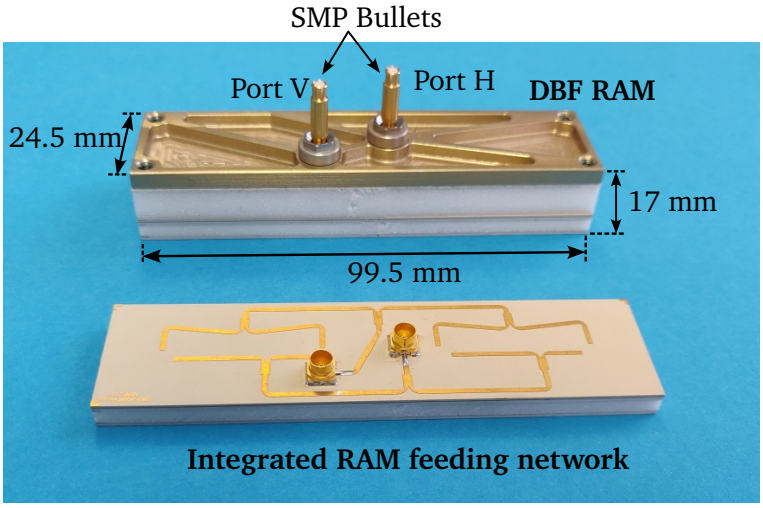

Figure 3.1.: Receive Antenna Module with integrated feeding network.

as it is depicted in Figure 3.2. As convention, the former will be named as configuration 1 or alignment in x-direction, while the latter will be known as configuration 2 or alignment in y-direction. Thereby, the receive array antenna is formed by combining different RAM configuration alignments in either along-track or across-track direction. The beam steering is performed digitally, so the received antenna beam can be electrically adjusted with different phase and amplitude weighting. Thus, a feeding network is required in order to combine the different RAMs configurations while providing a flexible topology.

3.2. DBF-SAR Feeding Network Requirements

The design of the DBF-SAR combiner network presents some challenges regarding electrical characteristics, versatility, and degree of integration that have to be overcome in order to achieve the desired performance. The most relevant system requirements that strongly determine the design framework of the feeding network are listed next:

- Operation in X-band, at the center frequency of 9.6 GHz with a bandwidth of 1.8 GHz. The feeding network has to excite each RAM with the same amplitude and phase.
- The feeding topology should be versatile to be adapted to excite both polarizations of the different RAM alignment configurations.
- The interconnection between the feeding network and the RAM should be performed

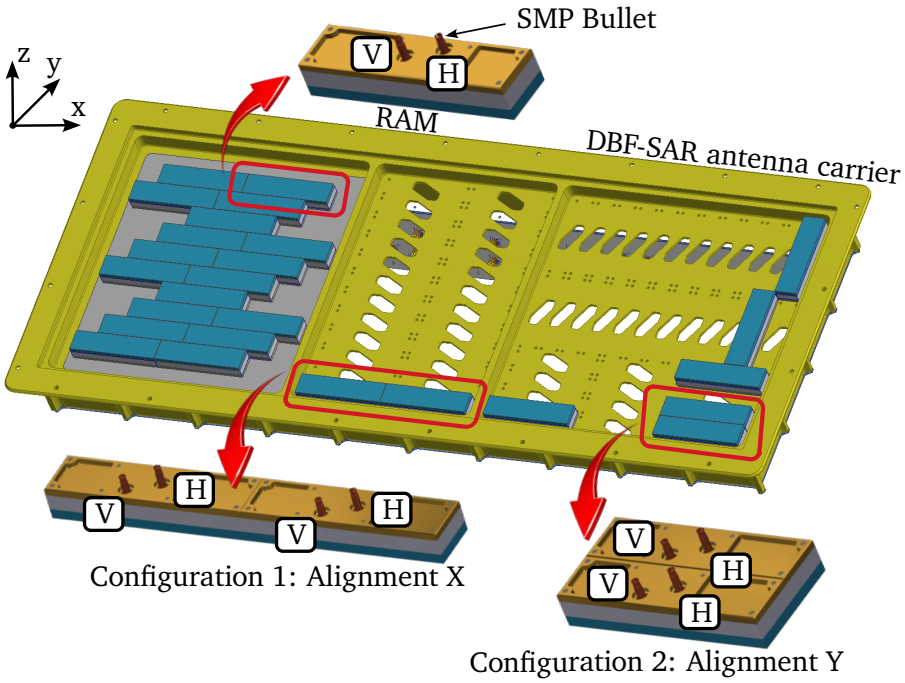

Figure 3.2.: DBF-SAR configuration: RAM alignments.

with SMP bullets [42], thus SMP connectors are needed. Thereby, a stacked assembly can be achieved with no need of cables, reaching a higher degree of integration.

- Due to the limited available space on the antenna carrier and the small electrical size of the RAMs, an extremely compact and electrically isolated solution has to be achieved.

A suitable technology to be used for the receiving network implementation is Substrate Integrated Waveguide (SIW). SIW presents the advantages of classic waveguides (high quality factor, good shielding, power handling and low loss), but at the same time it provides a large density of integration by using high dielectric permittivity substrates.

Substrate Integrated Waveguide (SIW)

Substrate Integrated Waveguide arises as a compact implementation of rectangular dielectric-filled waveguides, boosted by the miniaturization requirement of modern applications [59]. As a type of transmission line, the electromagnetic fields are confined within the structure and propagate along the waveguide length.

SIW structure is formed with a dielectric substrate inserted between two metallic layers that are electrically connected by means of periodic vias or plated holes, thus synthesizing the waveguide side walls. SIW behaves as a dielectric-filled waveguide with reduced height. Since the use of vias prevents the propagation of longitudinal currents along the side walls produced by Transversal Magnetic (TM) modes, only Transversal Electrical (TE) modes can be propagated through SIW structures, thus becoming TE_{10} the fundamental propagating mode.

A transmission line in SIW technology is depicted in Figure 3.3. A substrate with dielectric permittivity of ε_r and thickness h is used. The top and bottom conductive layers are electrically connected by means of periodically arranged metallic vias of diameter d_{via}. The spacing between vias is p, and the SIW line width a_{siw} is given by the distance between the vias rows.

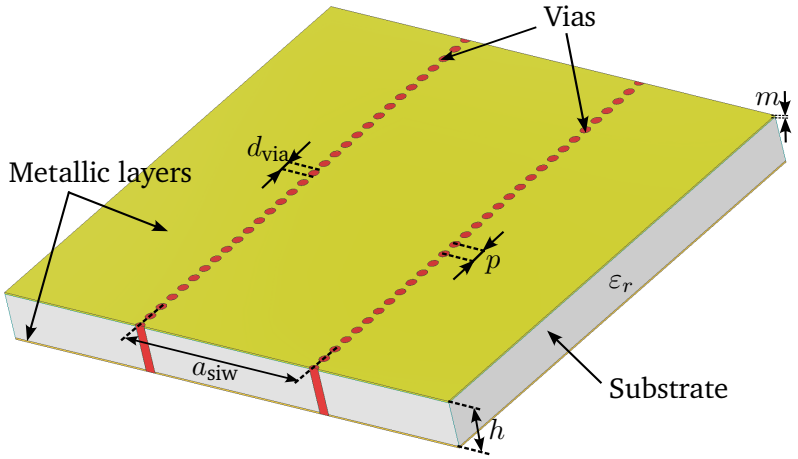

Figure 3.3.: Geometrical parameters of a SIW line.

Electrically, a SIW line behaves as a rectangular dielectric filled waveguide of an effective width of a_{eff} given by [60]:

$$a_{\text{eff}} = a_{\text{siw}} - \frac{d_{\text{via}}^2}{0.95\,p} \tag{3.1}$$

Thus, it is known from the waveguide theory that the cut-off frequency f_c of the fundamental mode TE_{10} can be expressed as:

$$f_c = \frac{c}{2\,a_{\text{eff}}} = \frac{c_0}{2\,\sqrt{\varepsilon_r}\,a_{\text{eff}}} \tag{3.2}$$

and the guided wavelength in the SIW structure at the center frequency of operation f_0 is given by:

$$\lambda_g = \frac{\lambda}{\sqrt{1 - \left(\frac{f_c}{f_0}\right)^2}} \tag{3.3}$$

being λ the operating wavelength in the substrate $\lambda = \frac{\lambda_0}{\sqrt{\varepsilon_r}}$.

In addition, since the electric walls of the SIW line are implemented by means of periodically equispaced vias, the following conditions have to be fulfilled in order to avoid leakage losses [61]:

$$\begin{aligned} p &\leq 2\, d_{\text{via}} \\ d_{\text{via}} &\leq \frac{\lambda_g}{5} \end{aligned} \tag{3.4}$$

The reasons why SIW technology becomes a suitable solution for the given application that fulfills all the aforementioned specifications, is summarized next in Table 3.1

DBF-SAR specifications	**SIW electrical advantages**
X-Band: center frequency of operation at 9.6 GHz and bandwidth 1 GHz.	SIW allows a low-profile waveguide implementation, thus providing a wide frequency range of operation.
Each RAM alignment has to be combined with **equal amplitude and phase**.	A 2-Way Balanced H-Plane T- Junction power divider can be implemented as a power combiner.
Versatile to combine different RAM configurations.	Geometry can be adapted to fulfill the separation of the RAM alignments.
Use of SMP connectors in order to achieve a stacked assembly.	The SIW structure is electrically closed, thus it can be directly connected with the RAM, leading to piled assemblies.
Compact implementation.	The use of a substrate with a high dielectric permittivity allows to reduce the overall structure size.

Table 3.1.: Favorable electrical properties of SIW to fulfill the system requirements.

Despite that the use of a dielectric substrate is inherent to SIW technology, recent breakthrough developments have shown SIW concepts and applications where no substrate

is required [62]. This technology, known as Empty Substrate Integrated Waveguide (ESIW), provides the miniaturized advantage of SIW but without the impact of the dielectric losses. However, since the scope of this application makes use of a high dielectric permittivity to achieve a higher degree of compaction, the standard SIW structure is considered.

3.3. 2-Way Balanced T-Junction SIW Power Divider

In order to combine the different RAM arrangements, a 2-Way Balanced T-Junction power splitter is used. This power divider, based on an H-Plane Waveguide T-Junction with inductive post [63], allows to combine each RAM with equal amplitude and phase.

As it is seen in Figure 3.4a, the power splitter is excited at the input port 1 and the fields are splitted equally at the output ports 2 and 3, yielding to an ideal (without losses) transmission factor $|S_{21}| = |S_{31}| \approx -3$ dB. Due to the symmetry of the structure, the path length between the input and each output is electrically equal, leading to identical output phase variation. The centered via serves as a matching element to improve the reflection $|S_{11}|$ at the input port. The electric field distribution of the propagating mode TE_{10} is shown in Figure 3.4b.

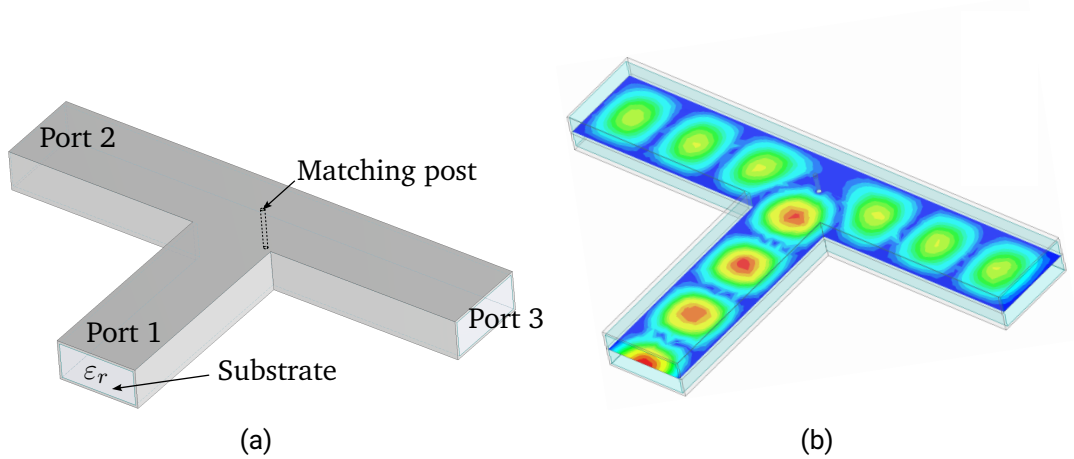

Figure 3.4.: Dielectric filled H-Plane waveguide T-Junction: (a) Structure geometry (b) Electric field distribution of fundamental mode TE_{10}.

In order to combine the different RAM configurations, as it is seen in Figure 3.5, three different geometrical variations of the same power divider have to be considered. Each of the proposed solutions is designed to have a distance between output ports given by the

spacing between RAMs for each configuration. Thus, the power dividers are named as H,V and HV depending on the excited polarization and alignment, as described in Table 3.2.

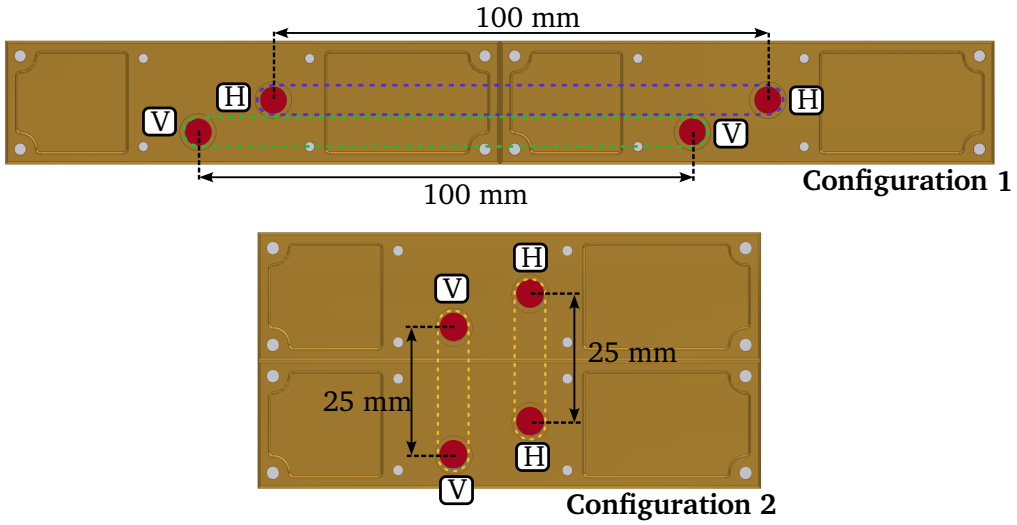

Figure 3.5.: Required geometrical adaptations of the power divider to combine all possible RAM alignments and polarizations.

Configuration 1		Configuration 2	
Power Divider H	Combines polarization H	Power Divider HV	Combines either polarization H or V
Power Divider V	Combines polarization V		

Table 3.2.: Nomenclature power dividers/combiners.

Figure 3.5 shows that in the configuration 1, two different power splitters are considered, unlike configuration 2, where the same identical electrical power divider is used. The reason for that is, since the available space is highly limited, both power dividers of the configuration 1 are combined forming a stacked assembly, as it is shown in the section 3.3.

It is important to point out that, for the given application, the presented 2-Way Balanced T-Junction works as a power combiner due to its reciprocity ($|S_{21}| = |S_{12}|$, $|S_{31}| = |S_{13}|$), since it is used on the receiver path of the system. Thus, despite that the terms power splitter or power divider are also used, it is meant to work as a power combiner. For the same reason, in the scope of this work, the concept feeding network excitation is indistinctly applied to transmission or reception purposes.

Equivalent dielectric filled rectangular waveguide (DFWG) model

To design the SIW structure of a 2-Way Balanced T-Junction power divider, first the equivalent model in dielectric filled rectangular waveguide (DFWG) is obtained. The standard waveguide size WR90 for X-band operation (8.2-12.5 GHz) has a waveguide width $a = 22.86\,\text{mm}$ and height $b = 10.16\,\text{mm}$, respectively [64].

The cut-off frequency of the different propagating modes in a rectangular waveguide can be calculated by:

$$f_{c_{mn}} = \frac{c_0}{2\sqrt{\varepsilon_r}} \sqrt{\left(\frac{m}{a}\right)^2 + \left(\frac{n}{b}\right)^2} \tag{3.5}$$

which, in the case of an air filled rectangular waveguide ($\varepsilon_r = 1$), the cut-off frequency of the fundamental mode TE_{10} is given by the previous expression evaluated at $m = 1$ and $n = 0$:

$$f_{c_{TE_{10}}} = \frac{c_0}{2\,a} = 6.56\,\text{GHz} \tag{3.6}$$

The cut-off frequency of the next propagating mode TE_{20} is calculated for $m = 2$, and $n = 0$ and yields $f_{c_{TE_{20}}} = 13.12$ GHz. Thus, the mono-mode operational bandwidth of the WR90 rectangular waveguide is given by the frequency band determined by the cutoff frequencies of the two first propagating modes, which yields a bandwidth of 6.56 GHz.

The waveguide width a_d and height b_d of the equivalent electrical DWFG model are given by $a_\text{d} = \frac{a}{\sqrt{\varepsilon_r}}$ and $b_\text{d} = \frac{b}{\sqrt{\varepsilon_r}}$ and depicted in Figure 3.6.

In order to achieve a higher degree of miniaturization that is mandatory for this application, a substrate Rogers TMM10 with a dielectric permittivity of $\varepsilon_r = 9.2$ and dielectric losses $\tan\delta = 0.002$ is used [65]. Thus, the equivalent width and height of the dielectric filled rectangular waveguide are $a_\text{d} = 7.53$ mm and $b_\text{d} = 3.35$ mm, respectively.

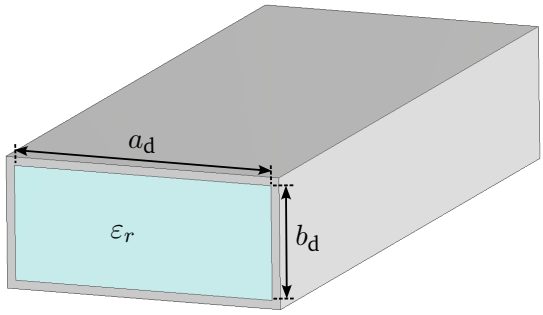

Figure 3.6.: Dielectric filled waveguide model.

SIW design

Considering a vias spacing $p = 0.65$ mm and vias diameter $d_{\text{via}} = 0.4$ mm, that fulfills the condition given in equation (3.4), the equivalent SIW width line a_{siw} can be calculated using equation (3.2), which for $a_{\text{eff}} = a_{\text{d}}$ leads to $a_{\text{siw}} = 7.83$ mm.

Since the substrate panels are only available in a given thickness provided by the manufacturer, a substrate thickness $h = 3.175$ mm is chosen, which becomes the closest value to the one (aforementioned) b_{d}. In addition, as it will be explained later, the SIW height has to be thick enough to allow the insertion of the feeding connector pin, that has a length of 2.5 mm, inside the substrate.

A comparison of the simulation results between the DFWG and the equivalent SIW model for the same waveguide length, in terms of return and insertion losses, is depicted in Figure 3.7. Both structures yield a return loss level better than 35 dB for the entire X-band. The insertion losses are also practically identical in both cases, which implies that no leakage losses are present in the SIW structure.

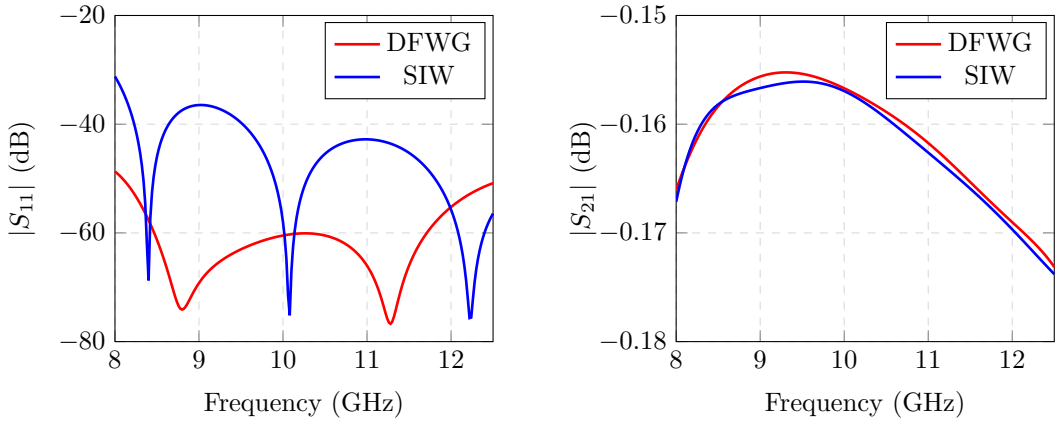

Figure 3.7.: Comparison DFWG and SIW models for $a_{\text{d}} = 7.53$ mm, $b_{\text{d}} = 3.35$ mm, $a_{\text{siw}} = 7.83$ mm, $h = 3.175$ mm, $p = 0.65$ mm, $d_{\text{vias}} = 0.4$ mm and $\varepsilon_r = 9.2$: (a) Reflection factor. (b) Transmission factor.

The guided wavelength λ_g at the center frequency of operation 9.6 GHz can be calculated applying equation (3.3). The theoretical value, as well as the one obtained in the simulation are shown in Table 3.3. As it can be noted, the calculated and simulated values are comparable.

Calculated λ_g	Simulated λ_g	
14.11 mm	DFWG	SIW
	14.1 mm	14.3 mm

Table 3.3.: Comparison guided wavelength values.

SIW T-Junction power divider design

An H-Plane waveguide T-Junction with inductive matching post in SIW technology has been implemented as a power divider. The structure is excited at port 1 and the power is equally distributed to both output ports 2 and 3. Due to the symmetry of the structure, both output signals have equal phase.

The centered via serves as a matching post to improve the reflection at the input port. This matching post behaves as an inductance that compensates the capacitance added by the waveguide splitting. The SIW T-junction is depicted in Figure 3.8.

The design of the structure has been performed using the full-wave electromagnetic simulation software HFSS. For the optimization process, first, the equivalent T-junction DFWG model is designed. Later, its implementation in SIW technology is performed considering the aforementioned SIW parameters, and optimizing the position d_{shift} and diameter of the centered via d_{center} in order to obtain a reflection factor $|S_{11}| \leq -20$ dB for the operational bandwidth. For the excitation of the structure, waveports are used so each port is adapted.

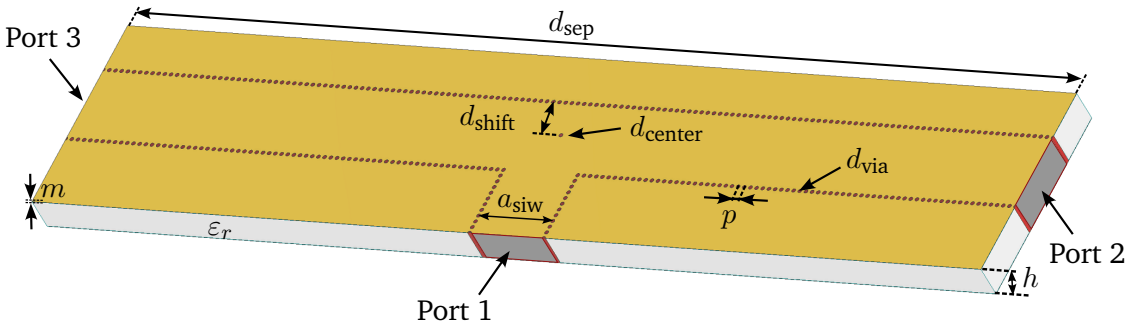

Figure 3.8.: SIW T-Junction model.

Considering a separation between output ports of $d_{\text{sep}} = 100$ mm, which is the distance between the H-ports of the RAM alignment given by the configuration 1 (see Figure 3.5), the simulated results of the equivalent SIW power divider are shown in Figure 3.9. The geometrical values of the SIW structure are listed in Table 3.4.

Description	Parameter	Value
Dielectric permittivity	ε_r	9.2
Substrate thickness	h	3.175 mm
SIW width	a_{siw}	7.83 mm
Distance between vias	p	0.6 mm
Vias diameter	d_{via}	0.4 mm
Position centered via	d_{shift}	3.6 mm
Diameter centered via	d_{center}	0.5 mm
Output ports separation	d_{sep}	100 mm
Thickness copper layer	m	0.35 mm

Table 3.4.: Electrical parameters SIW T-junction.

As simulation results show in Figure 3.9, the power divider is optimized for the center frequency of operation 9.6 GHz, where the return loss level is minimized. The transmission factors $|S_{21}|$ and $|S_{31}|$ are equally distributed due to the structure symmetry. However, the received power is slightly less than -3.5 dB. This power loss is entirely due to the substrate losses, since no conductor losses are considered and the leakage losses are negligible. The impact of the dielectric losses is also more visible due to the relatively long electrical size the SIW structure. The phase variation at the output ports $\Delta\varphi$, normalized at the center frequency of operation 9.6 GHz, is depicted in Figure 3.9c. It can be seen that the phase variation is linear and equal for both output ports, due to the same electrical path length.

Since the T-junction is reciprocal ($|S_{21}| = |S_{12}|$, $|S_{31}| = |S_{13}|$, $|S_{32}| = |S_{23}|$), and considering that a 3-port network can not be simultaneously reciprocal and perfectly matched [66], the reflection factor at the output ports ($|S_{22}|, |S_{33}|$) is inherently high, with values slightly lower than -6 dB, as depicted in Figure 3.9d. Precisely, these mismatch losses at the ports 2 and 3, where the received signal enters, present an electrical disadvantage for the use of the proposed T-junction as a combiner. However, this power loss is taken for granted since the framework conditions of the application (lack of space, integration, need of a stacked assembly) do not allow the implementation of other typical combiner solutions, such as a Wilkinson divider. Thus, the T-junction in SIW technology becomes a trade-off solution, due to its electrical and practical advantages such as miniaturization and adaptability.

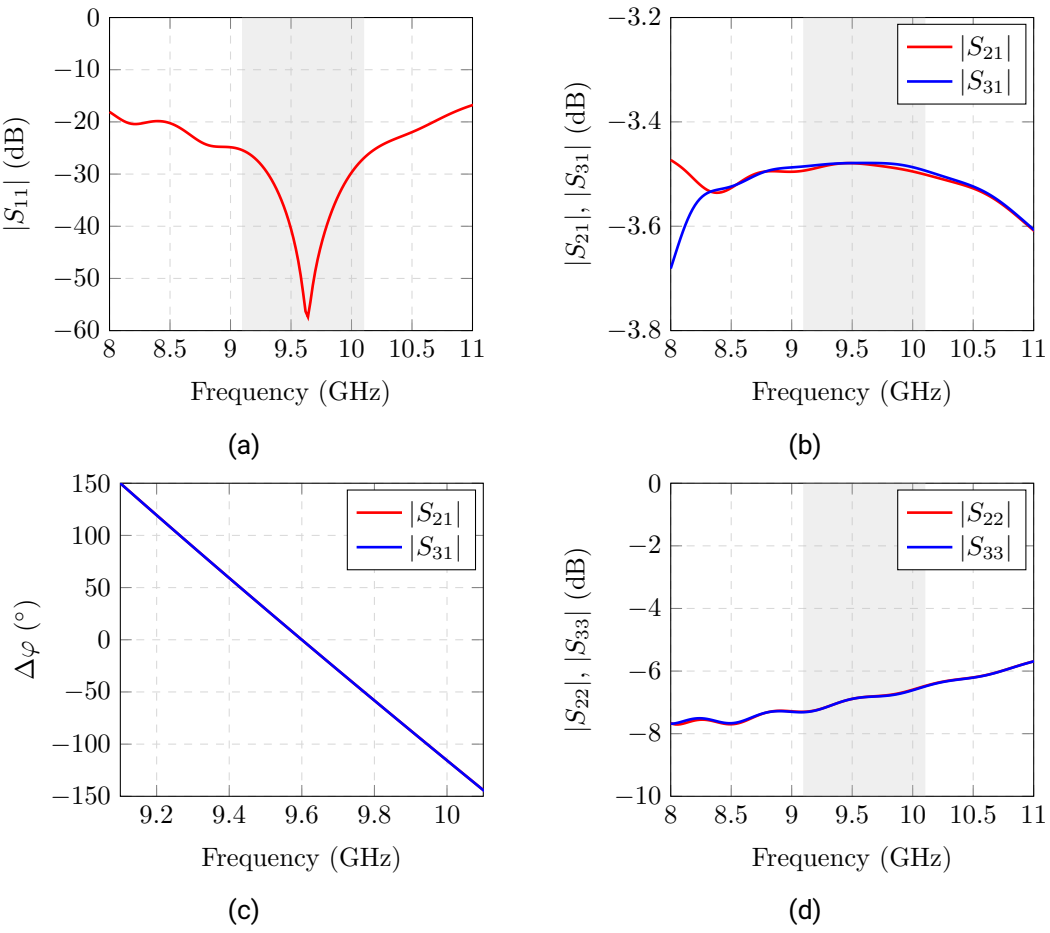

Figure 3.9.: Simulation results SIW T-junction power divider: (a) Reflection factor at the input port. (b) Transmission factor at the output ports. (c) Phase variation at the output ports. (d) Reflection factor at the output ports.

Structure excitation: SMP connector

The structure feeding is extremely important for the application, and it can strongly determine the final performance of the power dividers.

Since the interconnection between the feeding network and the RAM is done by means of SMP bullets, an SMP connector has to be used in order to excite each power divider. This way, a stacked assembly can be achieved, thus enhancing the degree of integration.

SMP connectors are a type of miniaturized plug-in SMA connector that allow the

electrical connection between different SMP components by inserting them [42], unlike the attachment of standard SMA connectors, that are screwed. Thus, piled structures can be achieved without the use of additional cables. In addition, SMP connectors are robust against vibrations and offer a given axial and radial tolerance in case of misalignment. All these reasons make SMP connectors extremely suitable for airborne applications.

Waveguides are typically excited by means of vertically-inserted coaxial pins. The connector probe is introduced in the center of the waveguide broad wall, exciting the fundamental mode TE_{10}. Since the feeding position is placed approximately $\lambda_g/4$ apart from the waveguide end, the wave that propagates towards the back-short is reflected and combined in-phase with the actual wave that propagates along the desired waveguide direction.

Thus, in order to excite the SIW power divider, an SMP inserted-pin connector is used. The feeding geometry of the structure, as well as the geometrical parameters of the connector, are depicted in Figure 3.10. It can be noted that the pin length is 2.5 mm, which irremediably leads to the use of a thicker substrate. For this reason, an electrically thick substrate of $h = 3.175$ mm is used.

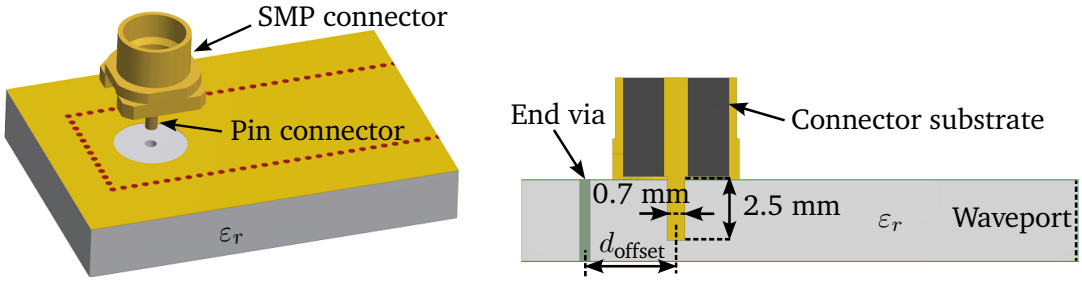

Figure 3.10.: SIW excitation geometry: (a) Connector position (b) Cross-section view.

The SIW feeding geometry is simulated in HFSS and, for this purpose, the real CAD model of the SMP connector is used. While on one side the structure is excited by means of the connector, on the other side, the SIW line is completely matched using a wave port excitation, as depicted in Figure 3.10b. Thus, the feeding matching of one connector can be electrically analyzed. Figure 3.11 shows the return loss and insertion loss level of the simulated structure for a connector position $d_{\text{offset}} = 3.6$ mm, which is approximately $\lambda_g/4$ given the waveguide wavelength value shown in Table 3.3. It can be seen that the operational bandwidth of the structure is considerably reduced, since the position of the connector is frequency dependent. Simulation results show that slightly increasing the SIW width a_{siw} improves the matching level at the center frequency, as well as it increases

the bandwidth where the return loss is better than 20 dB. Thus, for the final design, a SIW line width of $a_{\text{siw}} = 8.1$ mm is considered, that is optimized for the proposed feeding.

It can be noted from equation (3.5) that increasing the waveguide width leads to a decrease of the cut-off frequency of the fundamental model $f_{c_{TE_{10}}}$. In this case, slightly increasing the SIW width implies a value of $f_{c_{TE_{10}}} = 6.31$ GHz, which does not affect the performance of the proposed solution.

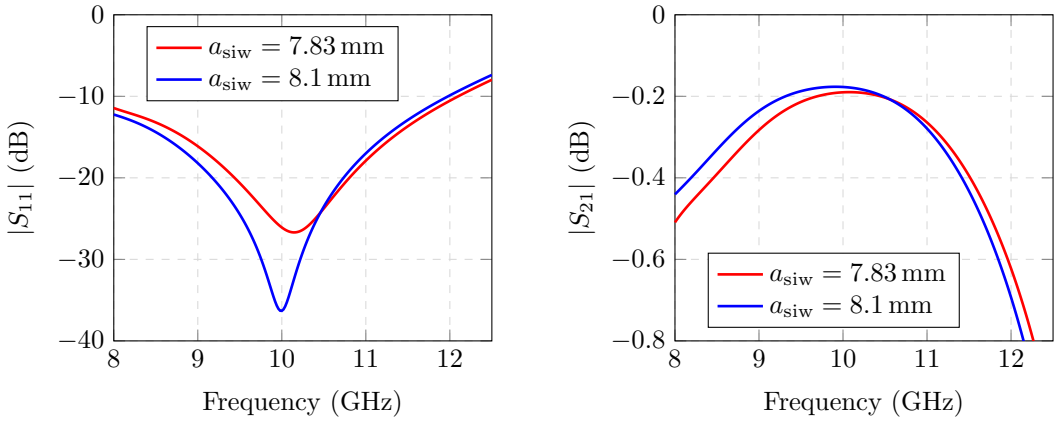

Figure 3.11.: SMP-fed SIW structure: (a) Reflection factor. (b) Transmission factor.

The proposed SIW power divider can be analyzed now with the SMP connector feeding. As it is shown in Table 3.2, three different geometrical variations of the same electrical power divider are required to feed both configurations, in order to combine all possible RAM alignments and polarizations.

Thus, the complete SIW structure with the connector is simulated, and the position of the matching post is slightly tuned in order to achieve a matching value at the input port better than 20 dB for the operational bandwidth, as well as a flat insertion loss response. For the optimization process, the structure is simulated with vias, conductor losses and real SMP connector models. Thus, the most possible realistic simulation scenario will be analyzed. To achieve a higher degree of accuracy, a fine mesh is used, as well as a reduced convergence tolerance in the simulated result is also considered. Finally, a discrete sweep is also performed to further validate the results. This optimization process and simulation conditions are applied to all the designs that are presented in this chapter.

RAMs Configuration 1

For the RAM alignment of the configuration 1, two independent power dividers are needed to combine both polarizations, namely power divider H and V. Each of the geometrical variations is depicted in Figure 3.12. The design parameters of each power divider are listed in Table 3.5.

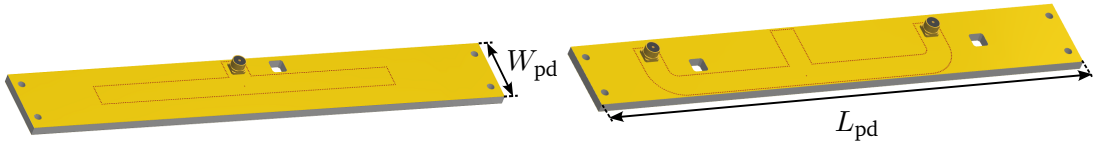

Figure 3.12.: (a) Power divider H. Top view. (b) Power Divider V. Bottom view.

Since a stacked assembly has to be achieved, the position of the input and output ports are placed on the top and bottom metallization layers of the structure, as it is seen in Figure 3.12a and Figure 3.12b respectively. Thus, a direct interconnection between the power divider and the RAM can be fulfilled. Furthermore, due to the electrical isolation of the SIW structure, both power dividers H and V can be also piled up in order to achieve a higher degree of integration, as depicted in Figure 3.13.

SIW parameter	**Configuration 1**		**Configuration 2**
	Power Divider H	**Power Divider V**	**Power Divider HV**
d_{shift}	3.8 mm	3.6 mm	3.4 mm
d_{sep}	100 mm		25 mm
$W_{pd} \times L_{pd}$	24.6 mm x 172 mm		49 mm x 100.7 mm
a_{siw}	8.1 mm		
p	0.65 mm		
d_{via}	0.4 mm		
d_{center}	0.5 mm		
m	0.35 mm		
h	3.175 mm		
ε_r	9.2		

Table 3.5.: Electrical parameters of the SIW power dividers.

The simulation results of each power divider are shown in Figure 3.14, and its geometrical parameters are listed in Table 3.5. As it is seen, the return loss values show a matching level better than 20 dB for the frequency band of operation 9.1-10.1 GHz, which

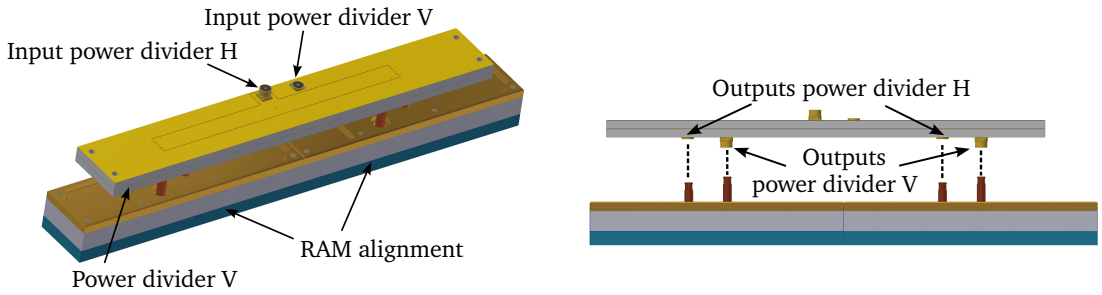

(a) (b)

Figure 3.13.: Feeding configuration 1: (a) Stacked assembly (b) Side view.

leads to a fractional bandwidth of 10.4%. The insertion losses of the power divider V are higher, due to the relatively longer electrical paths between the input and outputs, and hence, the impact of the dielectric losses is increased. In addition, the insertion losses of the connectors as well as the conductor losses are also considered in the simulation results, since copper is used as the conductor material.

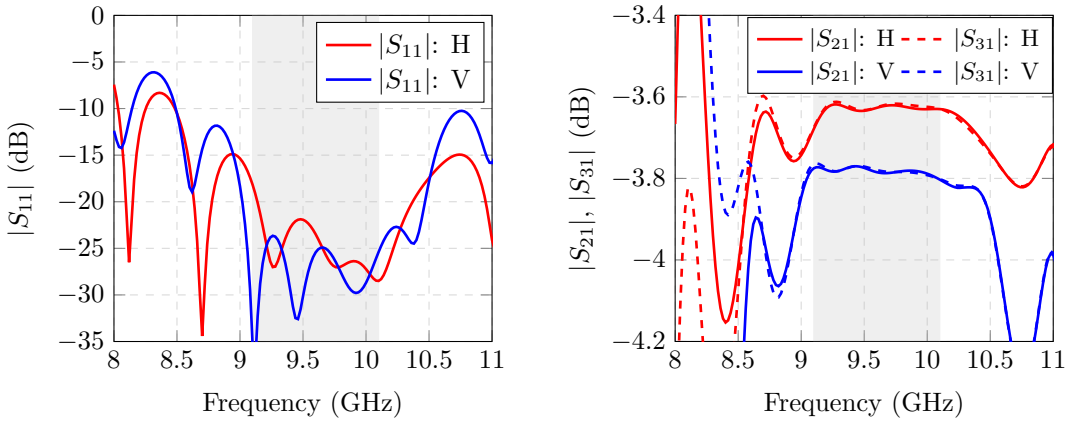

(a) (b)

Figure 3.14.: Simulation results power divider H and V: (a) Reflection factor. (b) Transmission factor.

The phase variation $\Delta\varphi$ at the outputs, normalized at 9.6 GHz, is depicted in Figure 3.15. As it can be seen, the slope of the phase variation is higher for the power divider V, since the electrical size of the structure is larger.

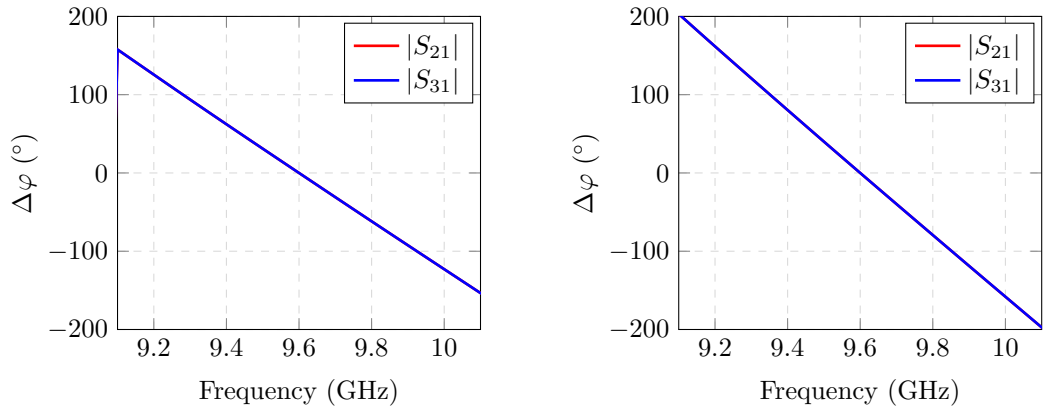

Figure 3.15.: Simulated phase variation $\Delta\varphi$: (a) Power divider H. (b) Power divider V.

RAMs Configuration 2

In the second RAM alignment, the polarization excitation of each RAM alignment can be done from opposite sides. Thereby, the feeding assembly is based on two identical mirrored electrical power dividers, as depicted in Figure 3.16.

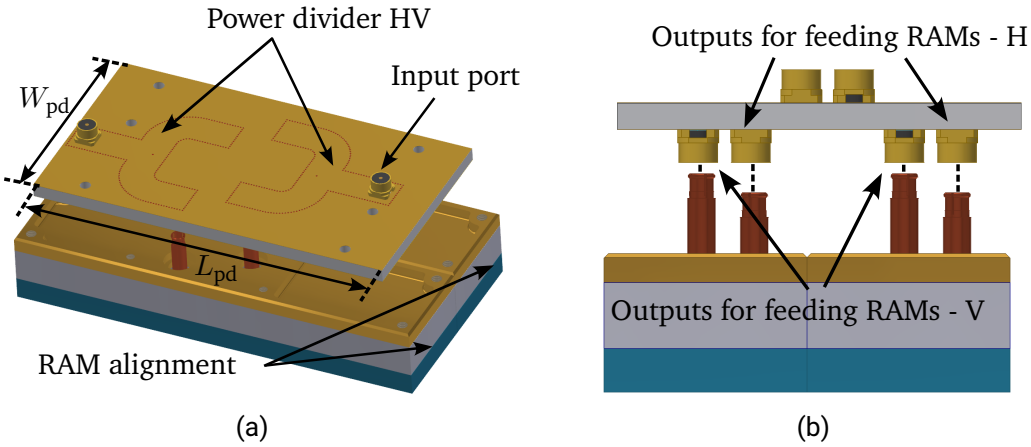

Figure 3.16.: Feeding configuration 2: (a) Stacked assembly (b) Side view.

The geometrical parameters of the power divider HV are listed in Table 3.2. The simulation results, depicted in Figure 3.17, show a return loss level better than 25 dB

for the center frequency of operation. It can be noted that the insertion losses are lower than the power dividers of the configuration 1, since the electrical path between the input and outputs is shorter. The phase variation at the output ports is the same, due to the symmetry of the structure.

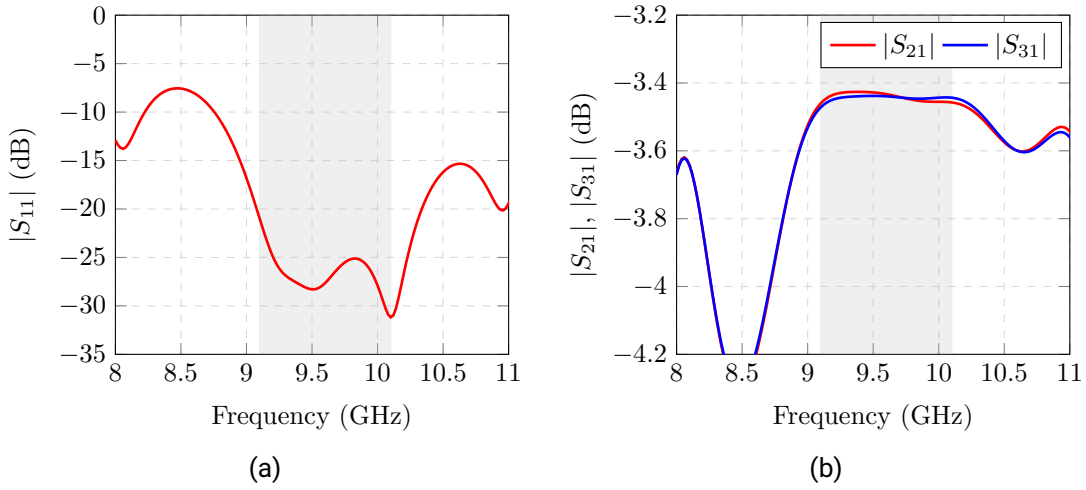

Figure 3.17.: Simulation results power divider HV: (a) Reflection factor. (b) Transmission factor.

Measurements of a manufactured prototype

All three power dividers were manufactured and measured. The SMP connectors were soldered using vapor phase techniques. The measurement of the S-parameters were performed using the network analyzer model ZVA 24 from Rohde&Schwarz.

Figure 3.18 shows a comparison analysis between measurement and simulation in terms of return and insertion losses. As it is seen, there is a clear disagreement between simulation and measurement.

This discrepancy is shown as a standing wave at the return loss that also leads to a ripple in the insertion losses. The measured $|S_{21}|$ and $|S_{31}|$ is, in all cases, lower than the simulated values, since the measurement also includes the insertion losses of the SMA-SMP adaptors, required for the measurement and not included in the calibration. Clearly, the appearance of the standing wave comes from a mismatch. This is produced by different impedance values of the connector and the SIW line. In order to assess the possible cause for the mismatch, a tolerance analysis regarding the connector geometry is performed.

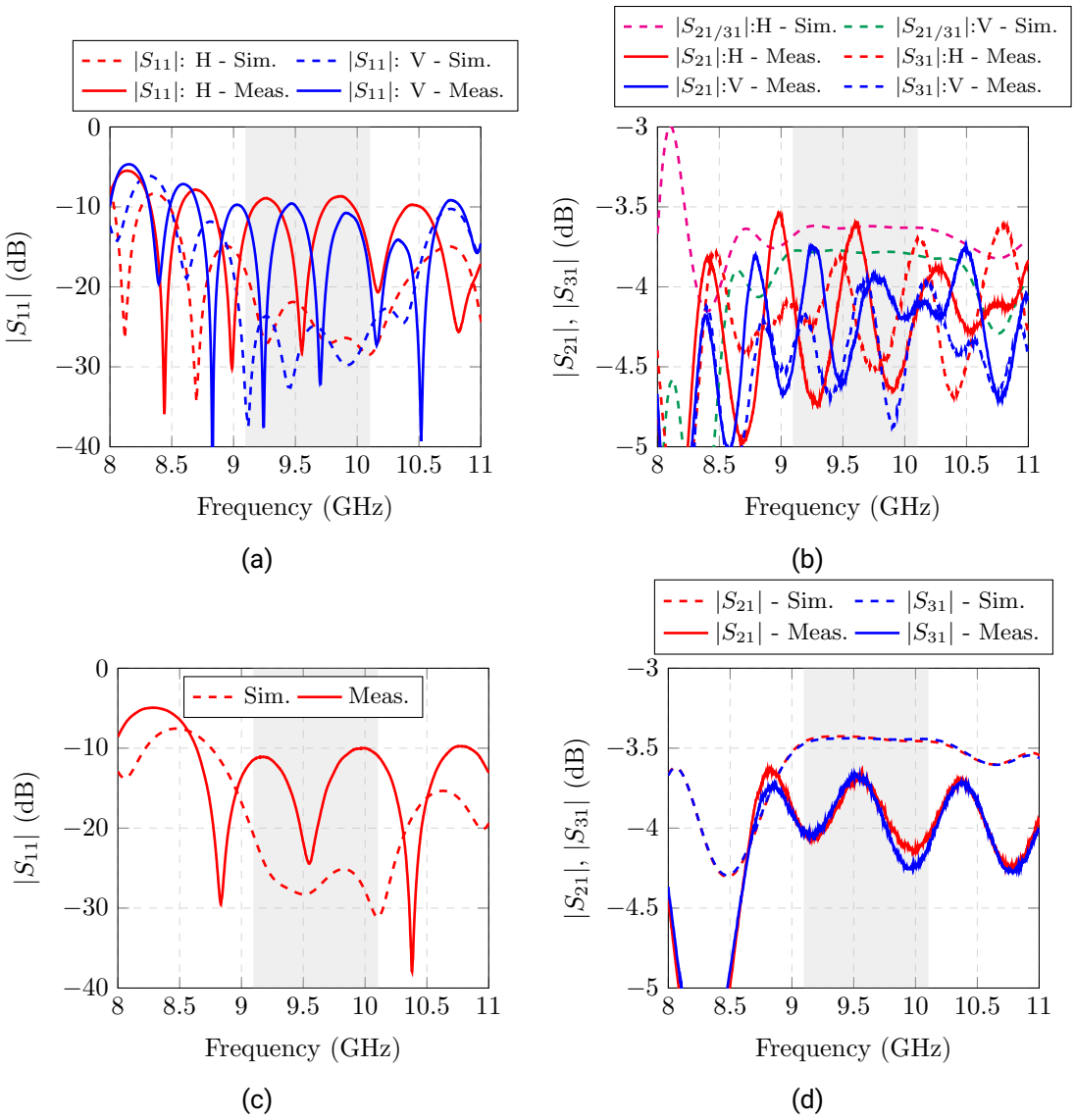

Figure 3.18.: Comparison simulation and measurement: (a) Reflection factor power divider H and V (b) Transmission factor power divider H and V (c) Reflection factor power divider HV (d) Transmission factor power divider HV.

Tolerance analysis

Before manufacturing, a tolerance analysis of the SIW structure regarding the position of the connector has been performed, being the structure robust against slight geometrical deviations. However, according to the connector data sheet, as it is shown in Figure 3.19, the only parameter sensitive to slight geometrical variations (due to fabrication tolerances) is the pin length, that has a nominal value of 2.5 mm.

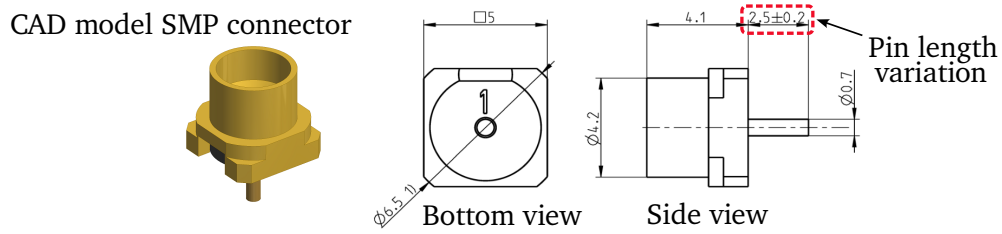

Figure 3.19.: Fabrication tolerances. Possible variation of the connector's pin length.

Figure 3.20 shows the simulation results of the SIW feeding structure depicted in Figure 3.10, considering a small variation of the connector pin length of ± 0.2 mm, which is the margin provided by the manufacturer.

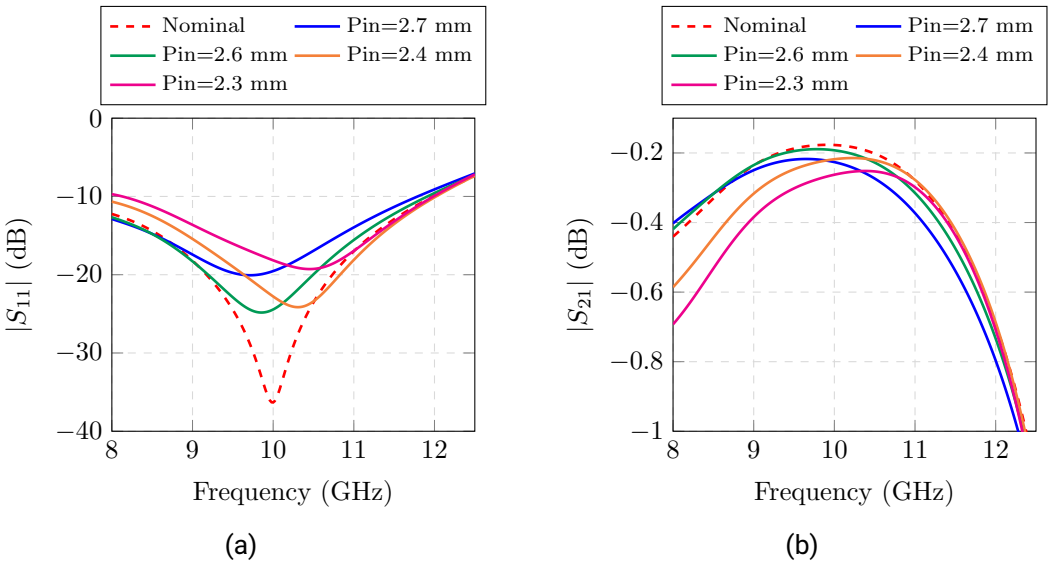

Figure 3.20.: Tolerance analysis connector pin length: (a) Reflection factor. (b) Transmission factor.

It can be seen that, despite that these deviations might seem negligible, the matching values change drastically, with variations up to 18 dB. If the pin length is lower than the nominal value, it results in a remaining air gap ($\varepsilon_r = 1$) between the pin and the substrate ($\varepsilon_r = 9.2$). Such difference of dielectric primitivities values between two mediums produces a higher wave reflection factor, and thus a feeding mismatch.

Considering the worst-case scenario in the power divider HV and reducing the pin length 0.2 mm, the simulation results are shown in Figure 3.21 and compared with the actual measurement. It can be noted the similarity between simulated and measured results. The simulated insertion loss level is slightly better, due to the additional insertion losses of the SMA-SMP adapters required for the measurement.

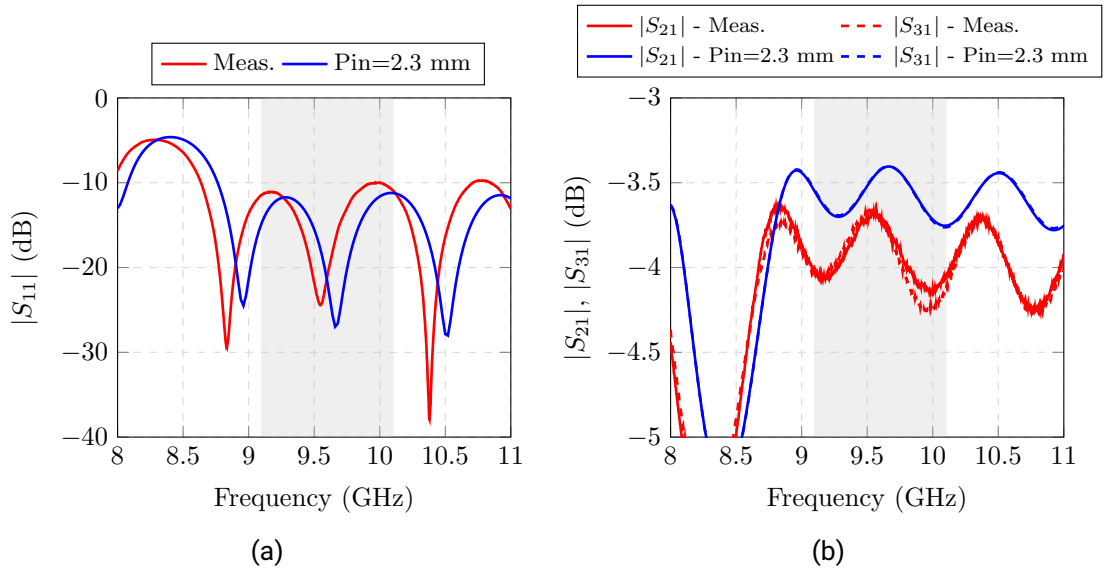

(a) (b)

Figure 3.21.: Tolerance analysis regarding connector pin length for power divider HV: (a) Reflection factor. (b) Transmission factor.

Even considering the nominal connector pin length, the drilling of the substrate can also lead to some inaccuracies regarding the depth, which will also lead to an air gap. In summary, the use of a high dielectric permittivity substrate makes the structure extremely sensitive to connector fabrication and installation tolerances. However, the use of lower permittivity substrates to deal with this sensitivity problem would increase the size of the feeding network, preventing to achieve the required miniaturized solution. Thus, a new type of structure excitation more robust against feeding tolerances is required.

3.4. CPW-SIW 2-Way Balanced T-Junction Power Divider

In order to avoid the aforementioned drawbacks regarding feeding tolerances, a redesign of the structure excitation is performed. Thus, the same electrical design of the power divider in SIW technology can be used.

In order to keep the advantages of the stacked assembly of the RAMs feeding, SMP connectors have to be used. Nevertheless, to prevent any feeding mismatch, a surface mounted SMP connector is used. Thereby, slightly variations in the pin length have a negligible impact in the structure excitation, since the feeding pin is not inserted in the substrate. Precisely, for this reason, no substrate drilling is required, thus minimizing possible causes of mismatch. By using a surface mounted connector, an additional feeding line is required onto which the connector pin is directly soldered.

In order to design the new feeding structure, two feasible transmission line implementations can be considered: microstrip and coplanar waveguide (CPW). Both solutions allow its interconnection with SIW structures by means of a transition that serves as an electrical interface between both technologies [67, 68]. A picture of a transmission line implemented in CPW and microstrip technologies is shown in Figure 3.22.

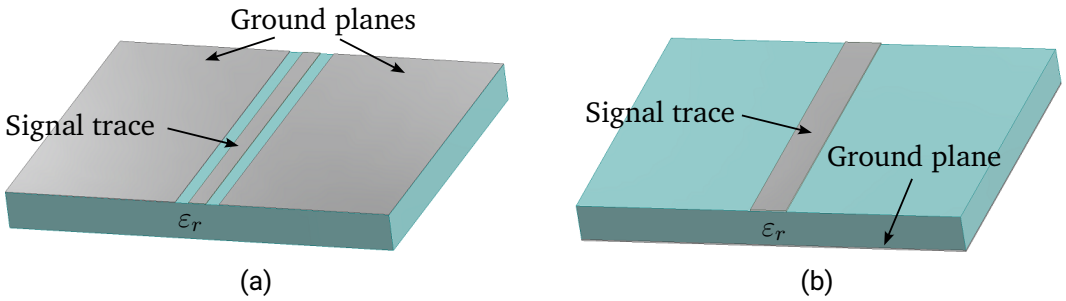

Figure 3.22.: (a) CPW line. (b) Microstrip line.

A microstrip line is based on a metallic strip that is vertically separated from the ground plane using a dielectric substrate material. On the other side, the CPW line and the ground plane are located on the same substrate surface, where the ground plane is placed on either side of the strip by a given separation.

However, there are some electrical advantages that support the use of CPW technology for the current application:

- Since the microstrip line excites a TEM mode, the fields propagate mainly within the substrate, being this technology more sensitive to substrate losses. On the opposite side, the CPW signal essentially travels along the air-metallic interface, and most of

the fields are not concentrated within the substrate

- In addition, due to the wave propagation nature in CPW, the field lines are more tightly confined than in microstrip, leading also to less radiation losses.
- Adding a secondary bottom metallic plate to the CPW line, the resulting structure called Grounded Coplanar Waveguide (GCPW) allows a smoothly interconnection to SIW. On the other side, the open nature of the microstrip line eases the field propagation within the substrate, thus preventing to be shielded using electric posts or vias.

For all these reasons, the new strucure excitation will be implemented in GCPW technology.

Grounded Coplanar Waveguide (GCPW) excitation

The new design will be implemented using the substrate Rogers TMM10i (ε_r=9.8, $\tan\delta = 0.002$) unlike the previous model TMM10. The reason for this new substrate is the minimal difference between the dielectric constant values of $\varepsilon_r = 9.8$ (process) and $\varepsilon_r = 9.9$ (design), according to the manufacturer data sheet [65]. These values contrast with the previous substrate TMM10, where the difference between both parameters, 9.2 and 9.8 respectively, leads to an increasing uncertainty of the real dielectric permittivity. Thus, tolerances regarding the electrical properties of the substrate can be minimized. In addition, the dielectric losses of the substrate TMM10i are slightly lower.

Since the surface mounted connector is soldered onto the feeding line, the pin insertion in the substrate can be avoided. Thus, no tolerances regarding the substrate drilling process are involved, as well as, a thinner dielectric can be used. In order to reduce the overall thickness, but without performing a full redesign of the SIW structure, a substrate thickness of $h = 1.905$ mm is used, which is a standard value given by the manufacturer. This new thickness represents a reduction of 40 % in comparison with the previous substrate.

Due to the 50 Ω impedance value of the connector, the GCPW feeding line should yield the same impedance, in order to avoid a mismatch. The impedance value Z_0 of a GCPW line is given by [69]:

$$Z_0 = \frac{30\pi}{\sqrt{\varepsilon_{\text{eff}}}} \frac{K(k')}{K(k)} \tag{3.7}$$

with the effective dielectrical permittivity ε_{eff} expressed by:

$$\varepsilon_{\text{eff}} = 1 + \frac{\varepsilon_r - 1}{2} \frac{K(k')K(k_1)}{K(k)K(k_1')} \tag{3.8}$$

and,

$$k = \frac{w}{w + 2s} \tag{3.9}$$

$$k_1 = \frac{\sinh\left(\frac{\pi w}{4h}\right)}{\sinh\left(\frac{(w+2s)\pi}{4h}\right)} \tag{3.10}$$

$$k' = \sqrt{1 - k^2} \tag{3.11}$$

In the aforementioned expression, K is the complete elliptic integral of the first kind. The parameters w, s and h correspond to the line width, gap and substrate thickness respectively, as depicted in Figure 3.23.

In addition, in order to provide a smooth CPW-SIW conversion and to avoid any leaky modes, a pair of vias row are placed along the GCPW line. Thus, in order to achieve a single mode operation in the GCPW line, the separation of the vias row v_{sep} has to fulfill the following condition [68]:

$$w + 2\,s + 2\,v_{\text{sep}} < \frac{c_0}{2 f_{\text{max}} \sqrt{\varepsilon_r}} \tag{3.12}$$

where f_{max} is the highest frequency of operation. The geometrical parameters of the GCPW line are depicted in Figure 3.23 and listed in Table 3.6.

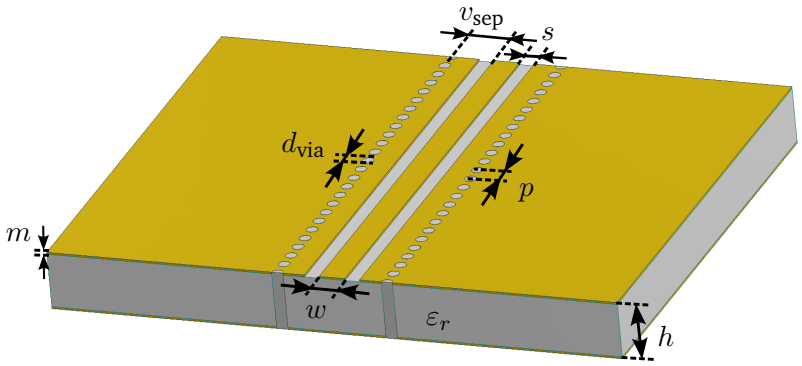

Figure 3.23.: GCPW line.

The simulation results of a GCPW line of length 16.25 mm are shown in Figure 3.24. The parameters w and s are set to yield a 50 Ω impedance line, as it is seen in Figure 3.24b. The vias diameter d_{via} and spacing p are equal to the SIW line. The separation of the vias row v_{sep} fulfills the condition given in (3.12) for the highest frequency in X-band.

w	s	v_{sep}	d_{via}	p	h	m	ε_r
0.9 mm	0.52 mm	0.95 mm	0.4 mm	0.65 mm	1.905 mm	35 μm	9.8

Table 3.6.: Electrical parameters GCPW line.

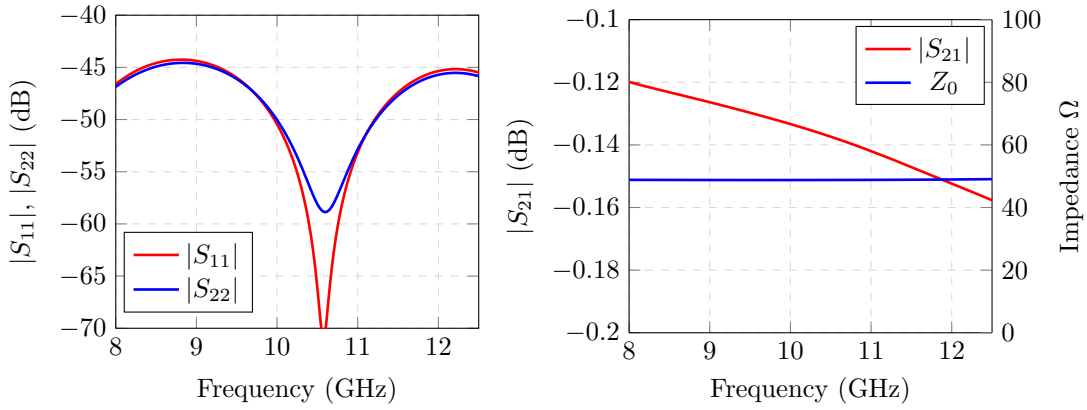

(a) (b)

Figure 3.24.: Simulated GCPW line. (a) Reflection factor. (b) Transmission factor and line impedance.

Since the GCPW feeding line is excited by means of a surface mounted SMP connector, a connector footprint is designed so its placement can be optimized for soldering purposes. Thus, possible mismatch losses can be reduced. The geometry of the feeding structure and the connector position is shown in Figure 3.25a

For simulation purposes, the optimization of the connector footprint is carried out considering only the SMP feeding on one side. Thus, the possible mismatch due to the SMP connector can be considered separately, since the other GCPW line end is properly matched due to the wave port excitation. As it can be seen, additional vias are placed around the connector footprint to ensure the electrical connection between the top and bottom ground plane. In addition, the beginning of the GCPW line is set so the connector pin can be properly soldered onto the line. The geometrical parameters ini_line, d_{f} and $line\_cpw$ are 0.87 mm, 3.8 mm and 7 mm respectively. The simulation results of the proposed feeding structure are shown in Figure 3.25b.

As it is shown, the return loss level is below 20 dB for the entire X-band frequency range, with values better than 25 dB at the center frequency of operation.

It can be noted that the operational bandwidth of this new feeding approach is much

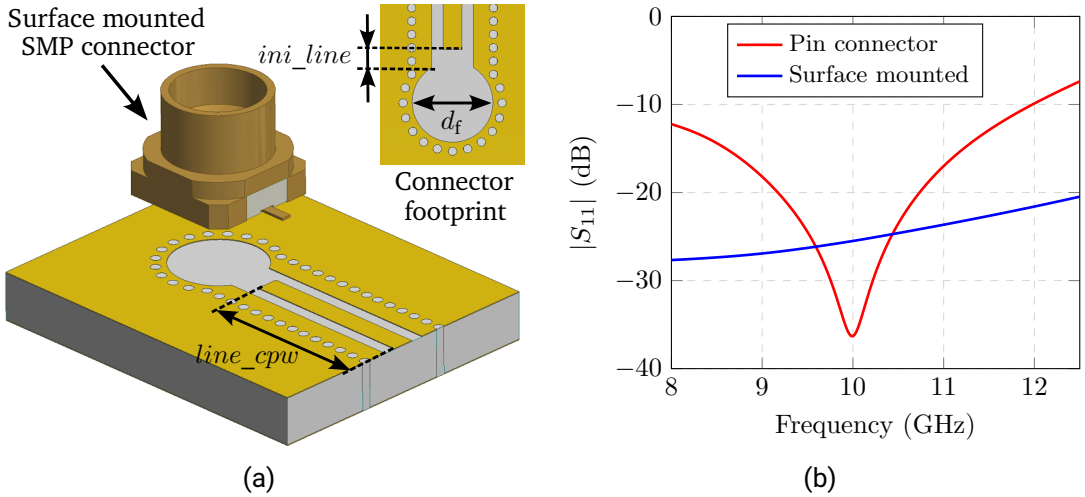

(a) (b)

Figure 3.25.: (a) Connector footprint. (b) Reflection factor.

broader than the previous one with an inserted pin SMP connector, since the connector position is not dependent on the frequency. With the new GCPW feeding, an operational bandwidth greater than 45% can be achieved, measured at a return loss level of 20 dB. On the contrary, with the pin connector a bandwidth of 15% is obtained.

With this new connector, no tolerances regarding the pin length are involved. In addition, no substrate drilling is required since the feeding pin is soldered on the GCPW line. This way, the proposed excitation topology becomes robust against feeding tolerances when high dielectric permittivity substrates are used.

GCPW-SIW transition

Considering that two different technologies are used, GPCW and SIW, a transition that serves as an electrical interface between both of them is required. Thus, the final electrical behaviour of the application is strongly dependent on the transition performance.

Some narrowband transition designs have been developed using, respectively, a current probe [70] and a 90° bent slot [71] based on H-field and E-field coupling. Some other proposals enhance its bandwidth by using a U-shaped slot antenna [72], combining the 90° bent slot with a stepped-impedance resonator [73] or modifying the stub angle [74]. An ultrawideband performance can be achieved by means of truncating the GCPW bottom conductor plane and its via-holed areas in different geometries [75], by adding an elevated CPW Section [76] or using a coupling slot with a triangular tapered aperture that serves as an improved impedance transformer [68]. This last solution is widely applied in a

broad range of applications.

Thus, for this application, the triangular tapered slot transition is used, due to its ultrawideband performance.

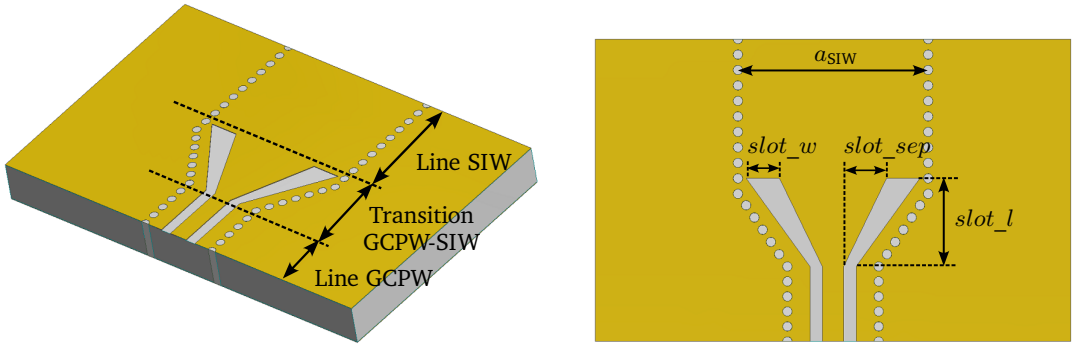

Figure 3.26.: Triangular tapered slot GCPW-SIW transition (a) Transition view. (b) Geometrical parameters.

The transition, depicted in Figure 3.26, works as an impedance transformer between the GCPW and SIW line, and it also acts as a coupling slot. The vias row along the GCPW line are tapered according to the transition aperture in order to match the SIW line width a_{SIW}. Typically, since the transition works as an impedance transformer, the slot has a length of approximately $\lambda_g/4$, being λ_g the guided wavelength in the SIW structure. For the optimization process, only one GCPW-SIW tapered slot transition is considered, since the opposite side of the SIW line is matched with a wave port.

The simulation results of the transition are shown in Figure 3.27, and the geometrical parameters are listed in Table 3.7.

$slot\_l$	$slot\_w$	$slot\_sep$	h	ε_r
3.7 mm	1.4 mm	1.8 mm	1.905 mm	9.8

Table 3.7.: Geometrical parameters of the GCPW-SIW transition.

As it can be seen, with the triangular tapered GCPW-SIW transition, a return loss level above 20 dB for the entire X-Band is achieved, with values better than 25 dB at the center frequency range. The proposed GCPW-SIW structure also provides a flat insertion losses of approximately 0.15 dB, which also includes the contribution of the GCPW and SIW

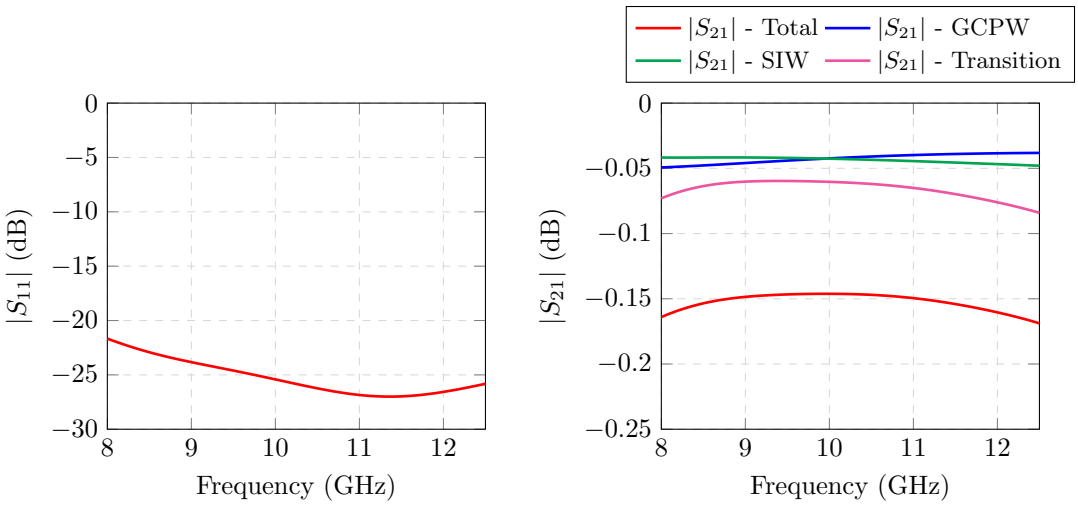

(a) (b)

Figure 3.27.: Simulation results transition GCPW-SIW (a) Reflection factor. (b) Transmission factor.

lines. In order to isolate the impact of the transition itself, the insertion losses of both lines are substracted from the total insertion losses, which leads to:

$$|S_{21}|_{\text{Transition}} = |S_{21}|_{\text{Total}} - |S_{21}|_{\text{GCPW}} - |S_{21}|_{\text{SIW}} \tag{3.13}$$

This analysis is performed in Figure 3.27b, and shows an insertion losses of the GCPW-SIW transition of approximately 0.06 dB for the center frequency range and slightly less for the lower and higher frequency band.

SIW T-Junction power divider excited by a GCPW line

Considering the aforementioned reasons, the dielectric permittivity of the substrate ε_r has been increased from 9.2 to 9.8, as well as the thickness h has been reduced. These new substrate parameters lead to a minimal redesign of the previous presented power dividers, where the line width a_{SIW} has been slightly reduced from 8.1 mm to 8 mm.

Once the electrical designs of the power divider and the transition have been optimized, the combination of the SIW power divider fed by the GCPW line can be analyzed. The new GCPW fed power divider HV is shown in Figure 3.28. It can be noted that the electrical length of each power divider has been increased, due to the additional GCPW feeding line. This is taken for granted, since the proposed solution serves as a proof of

concept. Subsequently, the electrical size of the overall structure can be reduced to fulfill the available space constraints of the RAM alignments.

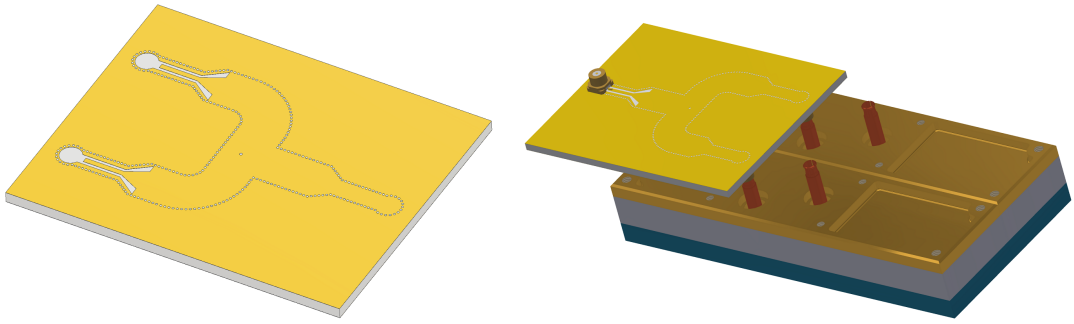

(a) (b)

Figure 3.28.: GCPW-SIW power divider HV: (a) Bottom view. (b) Feeding assembly RAMs configuration 2.

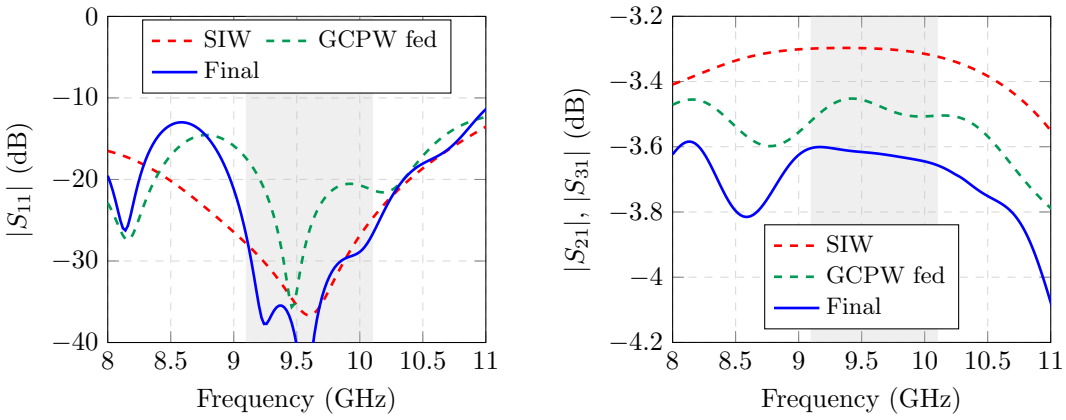

(a) (b)

Figure 3.29.: Simulation results GCPW-SIW power divider HV (a) Reflection factor. (b) Transmission factor.

A performance comparison of the new power divider HV considering only the SIW structure, excited by the GCPW line and the final design with the SMP connectors are shown in Figure 3.29. Simulation results of the final GCPW-SIW power divider HV show a matching level better than 30 dB for the operational frequency band. Despite its degree

of compaction, an insertion losses of 3.6 dB is achieved. It can be seen that the insertion losses of the SIW power divider HV is around 3.3 dB, which implies that the overall impact of the GCPW feeding lines, transitions and connectors is approximately 0.3 dB.

Measurement of the manufactured prototypes

The three power dividers H, V and HV are manufactured and measured. A picture of the fabricated prototypes is shown in Figure 3.30a.

The geometrical parameters of each power divider as well as of the GCPW feeding line are listed in Table 3.8 and 3.9. Figures 3.31 and 3.32 show a comparison between simulation and measurements of the power divider H and V, and HV respectively.

SIW parameter	**Configuration 1**		**Configuration 2**
	Power Divider H	**Power Divider V**	**Power Divider HV**
d_{shift}	3.55 mm		3.58 mm
d_{sep}	83 mm	94.6 mm	25 mm
$W_{\text{pd}} \times L_{\text{pd}}$	36.3 mm x 93 mm	36.5 mm x 108.6 mm	50 mm x 61.2 mm
a_{siw}	8 mm		
p	0.65 mm		
d_{via}	0.4 mm		
d_{center}	0.5 mm		
m	35 μm		
h	1.905 mm		
ε_r	9.8		

Table 3.8.: Electrical parameters of GCPW-SIW power dividers.

GCPW feeding line parameters					
w	s	v_{sep}	ini_line	d_{f}	$line\_cpw$
0.9 mm	0.52 mm	0.95 mm	0.87 mm	3.8 mm	7 mm

Table 3.9.: Electrical parameters of GCPW feeding line.

As it can be seen, the measurements agree rather well with the simulated data, except for the power divider V, where a mismatch is present at the output ports. In all cases there is a measured return loss level better than 20 dB for the center frequency of operation, and above 15 dB for the operational frequency band.

The measured insertion losses are 0.2-0.3 dB higher than the simulated values, since it includes the contribution of the SMA-SMP adapters that are not considered within the

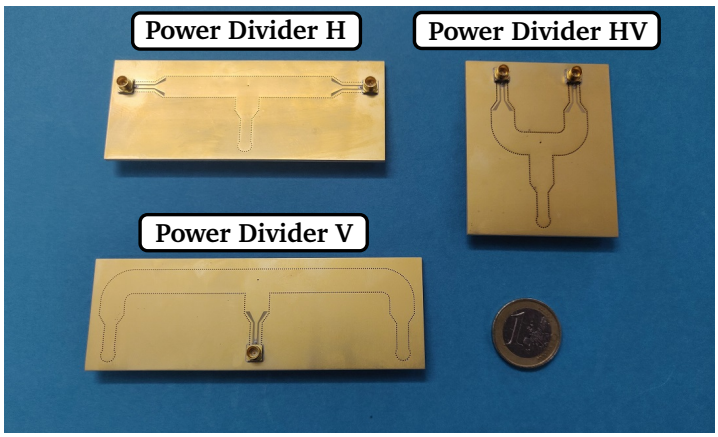

(a)

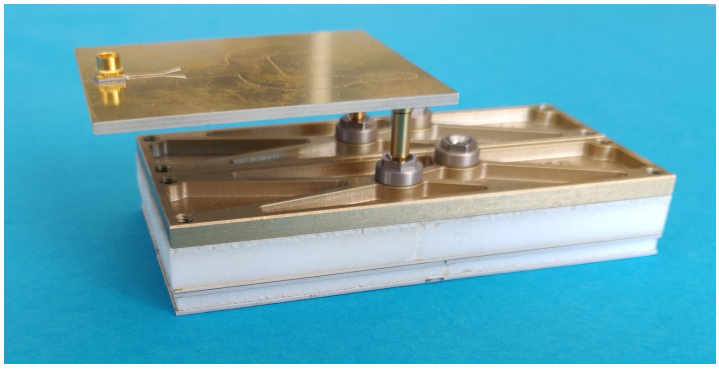

(b)

Figure 3.30.: (a) Manufactured protoypes. (b) Stacked assembly configuration 2.

calibration procedure of the network analyzer. The measured $|S_{21}|$ and $|S_{31}|$ parameters also show a slight standing wave due to a mismatch at the output ports. This effect can be also noted in the return loss level of both output ports $|S_{22}|$ and $|S_{33}|$, that are not equal, despite the symmetry of the structure. This deviation is more noticeable for the power divider V, whose performance disagreement can be certainly due to several reasons. First of all, the SIW power dividers had to be fabricated twice, since the first prototypes presented some manufacturing problems of the vias, that were found by means of a microscope inspection. Hence, the measured power divider V may still present some manufacturing problems. Secondly, since a high dielectric permittivity is used, the structure is sensitive to any slight geometrical variations such as innacuracies at the connector soldering or

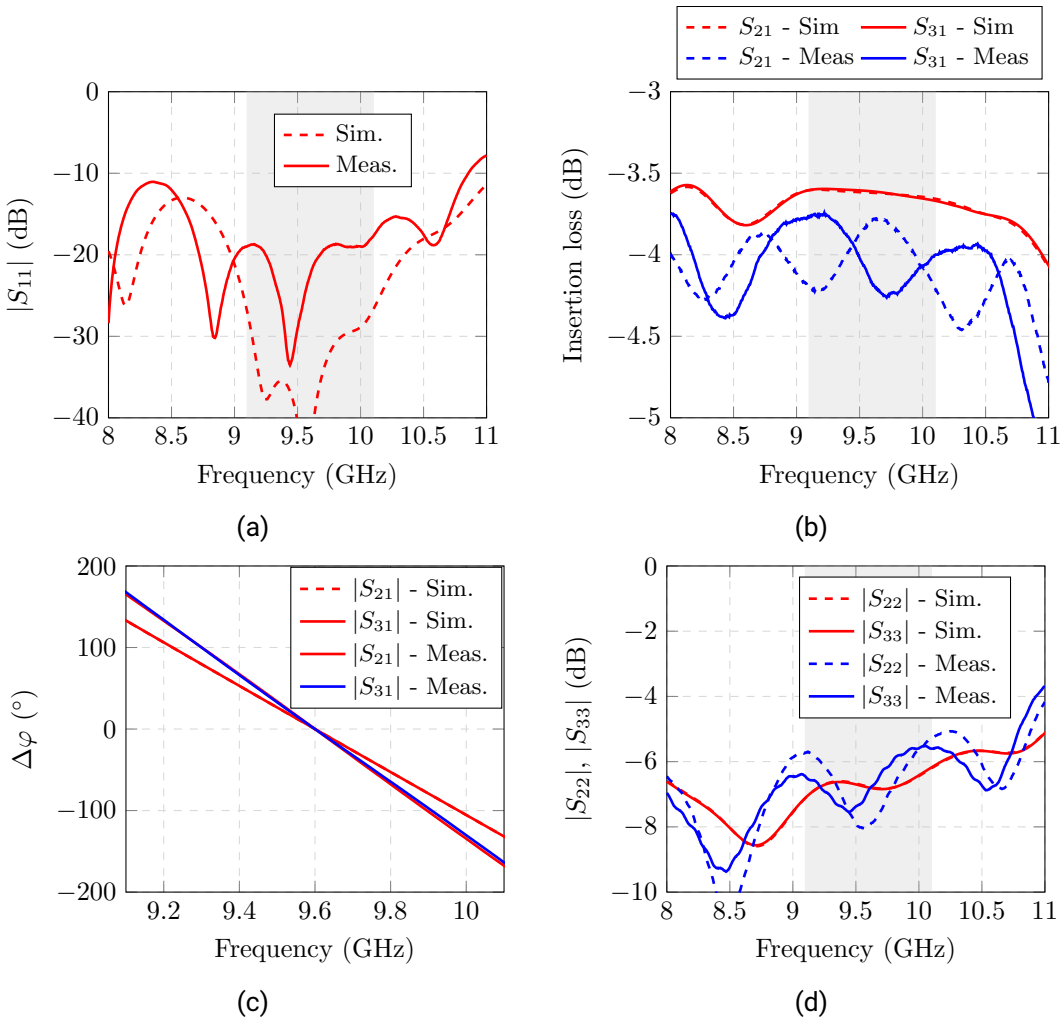

Figure 3.31.: Comparison simulation and measurement GCPW-SIW power divider HV: (a) Reflection factor input port. (b) Transmission factor. (c) Output phase. (d) Reflection factor output ports.

fabrication tolerances.

Nevertheless, the electrical performances of the power dividers H and HV are comparable to the predicted ones, and provides a robust excitation topology against feeding tolerances, which validates the proposed design solution.

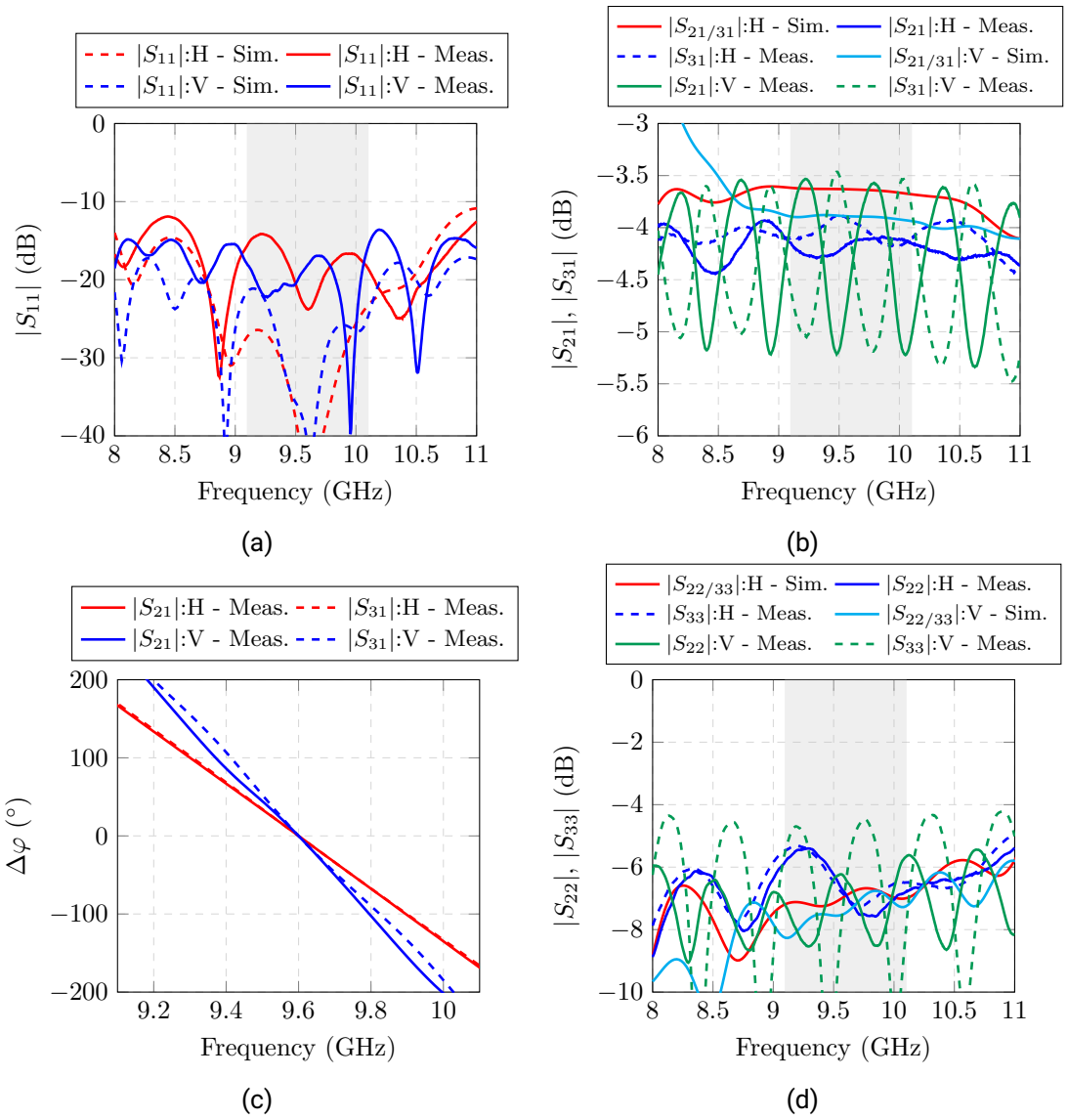

Figure 3.32.: Comparison simulation and measurement GCPW-SIW power dividers H and V: (a) Reflection factor input port. (b) Transmission factor. (c) Output phase. (d) Reflection factor output ports.

A comparison between the proposed solution and other works is shown in Table 3.10. As it can be noted, the presented design not only provides an overall good electrical performance but it is also implemented using the highest dielectric permittivity, leading to an extremely compact solution.

Reference	**Frequency**	**Feeding**	ε_r	**Return loss**	**Insertion loss**
[77]	5-11 GHz	CPW	3.38	11 dB	3.5 dB
[78]	58-63 GHz	CPW	2.2	15 dB	3.1 dB
[79]	2-3.5 GHz	Microstrip	6.15	14 dB	4.1 dB
[80]	11-15 GHz	Microstrip	2.2	15 dB	3.5 dB
[81]	8-12.5 GHz	Microstrip	2.2	15 dB	3.4 dB
This work	**8-11 GHz**	**CPW**	**9.8**	**15 dB**	**3.6 dB**

Table 3.10.: Comparison of the proposed GCPW-SIW power divider with previous works.

A possible disadvantage of the proposed solution for the given application is that due to the open nature of the GCPW fields, the new structure excitation is not electrically shielded. This prevents a stacked assembly of the power dividers H and V, as shown in Figure 3.13a, where if a conductor material is placed on the GCPW line, it would lead to a short-circuit. However, this disadvantage can be easily overcome if the GCPW line is left opened and filled with a layer of foam.

To sum up, the advantages of the proposed GCPW-SIW design are summarized next:

- ✔ The structure can be excited by means of an SMP connector, which allows a direct interconnection with the RAM alignments using SMP adaptors. Thanks to the different placement position of the input and output connectors, a stacked assembly can be achieved, as it is seen in Figure 3.28b, achieving a higher degree of integration.
- ✔ The proposed redesign only involves the structure excitation, and the same electrical design of the power dividers in SIW technology can be used.
- ✔ Since a surface mounted connector is used, it can be directly soldered onto the GCPW feeding line, and no pin connector inside the structure is required. Thus, no tolerance effects regarding the pin length are involved, that can highly degrade the feeding matching when high dielectric permittivities are used, as it has been previously shown. In addition, no substrate drilling is involved in the manufacturing process.
- ✔ Since the SIW structure is not excited with a vertical probe, the feeding position is not dependent on frequency, and thus, the operational bandwidth is enlarged.

3.5. Ultrawideband Tapered V-Slot GCPW-SIW Transition

In the scope of this work, a new GCPW-SIW transition has been developed with enhanced performance for higher frequencies.

The previously presented triangular GCPW-SIW transition usually disposes of a slot length of approximately $\lambda_g/4$, which is typically optimized for the center frequency of operation. The proposed transition modifies the slot aperture, providing a smoother tapering of the slot length. This geometrical variation leads to a vertex at the edge slot, resembling a V-shaped slot, as it can be seen in Figure 3.33. Thus, the new transition performance can be improved for the highest frequency band since the effective electrical length of the slot is reduced, while this geometrical modification is negligible for the lowest frequency range.

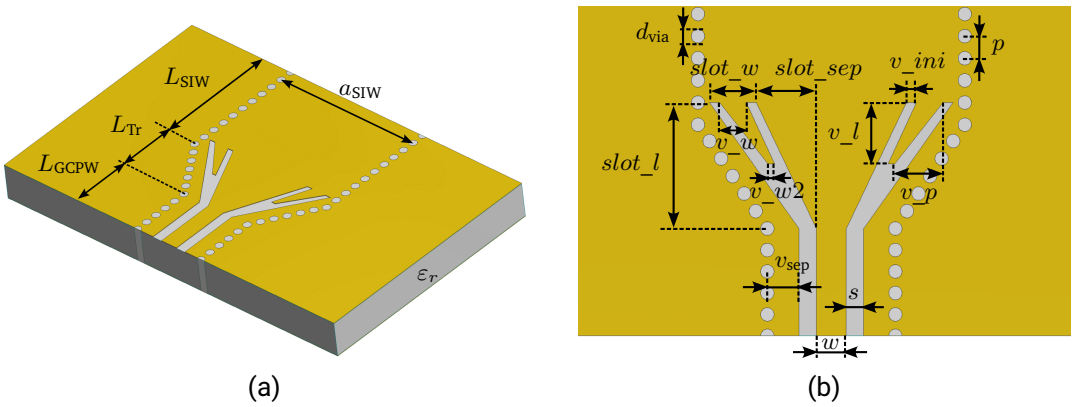

(a) (b)

Figure 3.33.: Proposed new GCPW-SIW V-Slot transition (a) Transition view. (b) Geometrical parameters.

GCPW values		Transition values				SIW values	
w	0.9 mm	$slot\_l$	3.7 mm	v_w	0.8 mm	a_{SIW}	8 mm
s	0.52 mm	$slot\_w$	1.4 mm	v_l	1.8 mm	d_{via}	0.4 mm
v_{sep}	0.95 mm	$slot\_sep$	1.8 mm	v_p	1.45 mm	p	0.65 mm
L_{GCPW}	3.5 mm	v_ini	0.3 mm	v_w2	0.2 mm	L_{SIW}	6.5 mm
		L_{tr}		3.05 mm			

Table 3.11.: Transition design parameters.

A performance comparison between the previous triangular slot and the new V-slot is shown in Figure 3.34. For this analysis, the same substrate Rogers TMM10i has been used. The geometrical parameters of the two transitions are listed in Table 3.11.

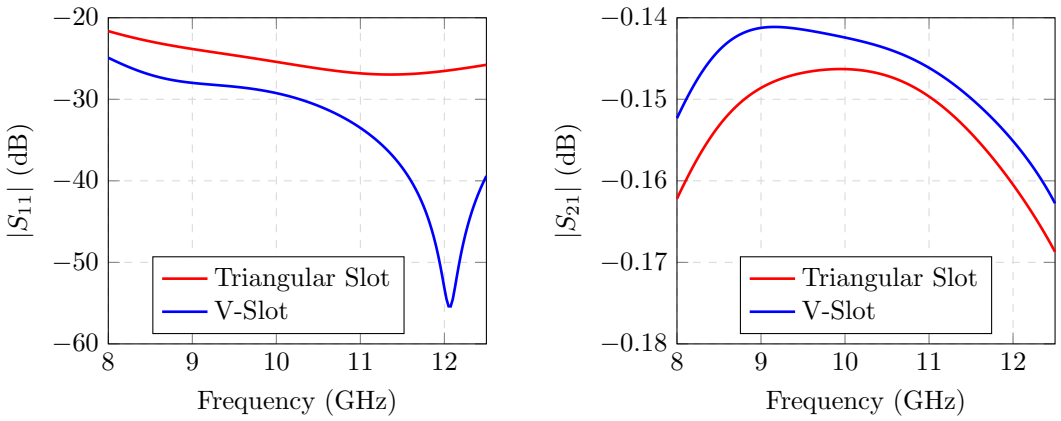

(a) (b)

Figure 3.34.: Comparison performance GCPW-SIW transitions: (a) Reflection factor. (b) Transmission factor.

It can be noted that both transitions share the same slot length $slot\_l$ and slot width $slot\_w$ values, being the inner slot tapering of the new transition the only geometrical variation. The length of the GCPW and SIW lines, L_{GCPW}, and L_{SIW} respectively, as well as the length of the transition section L_{tr}, are also the same ones.

As it can be seen, the proposed V-Slot transition provides an overall better matching level, specially at higher frequencies with significant improvements beyond 20 dB. Thus, the insertion loss level is also improved.

In order to further extend the analysis of the new transition, a comparison in terms of radiation losses between both designs has been performed.

Considering a lossless transmission line with no conductor, dielectric or radiation losses, the following condition has to be fulfilled:

$$|S_{11}|^2 + |S_{21}|^2 = 1 \tag{3.14}$$

which means that the total amount of power is the sum of the reflected and the transmitted power values.

Considering a perfect electric conductor and a lossless substrate, the contribution of the radiation losses can be described as:

$$\rho_{\text{rad}} = 1 - |S_{11}|^2 - |S_{21}|^2 \tag{3.15}$$

Thus, the radiation losses of the two transitions can be compared if both structures are simulated without conductor and substrate losses, leading to the analyisis depicted in Figure 3.35.

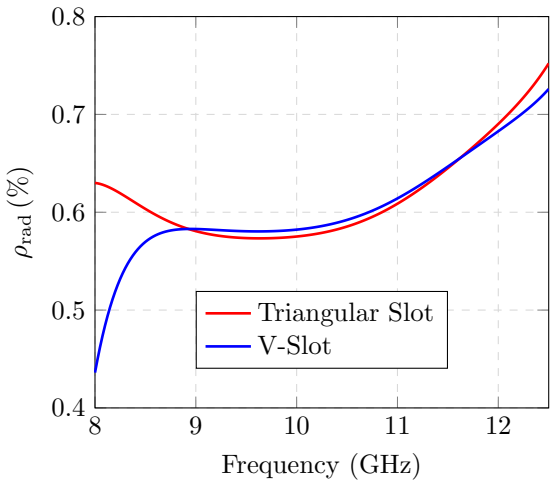

Figure 3.35.: Comparison radiation losses GCPW-SIW transitions.

The new transition provides almost the same radiation losses in the center frequency band, but better results at lower and higher frequencies.

Measurement of back-to-back transitions

In order to validate the proposed structure, two back-to-back transitions of both designs were manufactured and measured.

Each back-to-back transition is composed of an input and output transition that are connected by a SIW line of length L_1 and L_2, which corresponds to one and two guided wavelengths, 13.1 mm and 26.2 mm. The structure is excited with the same GCPW 50 Ω feeding line topology used for the GCPW-SIW power dividers. The manufactured back-to-back transitions can be seen in Figure 3.36. A performance comparison between simulation and measurement of the back-to-back transitions are shown in Figure 3.37.

As it can be seen, despite that the matching levels in all cases are mainly better than 15 dB, the return loss of both transitions presents a slight mismatch. The resulting standing wave is certainly caused by the installation of the connectors, since the structure is extremely sensitive to any minor variation in the excitation geometry due to the use

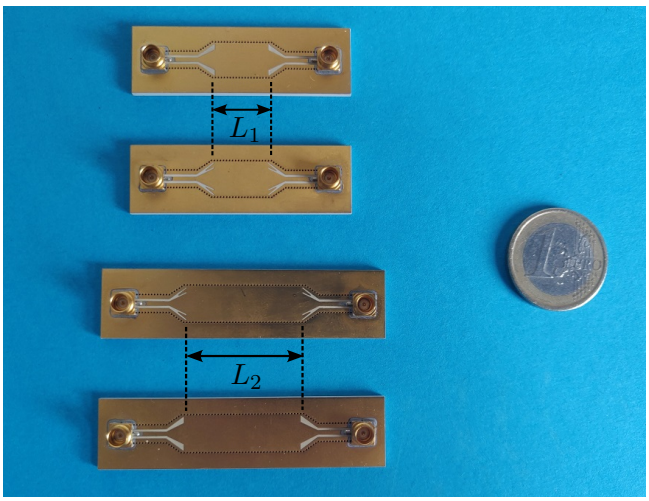

Figure 3.36.: Manufactured back-to-back transitions.

of a high permittivity substrate. The level of the standing wave varies according to the connector's position along the structure, depending on where the standing wave location is placed. In addition, since the return loss levels are, to a large extend, better than 20 dB, any small inaccuracy leads to a fluctuation of some dB.

The measured insertion loss level is also higher than the simulated data, due to the use of SMA-SMP adapters required for the measurement, that are not considered within the calibration. As it is expected, the longer electrical SIW line of length L_2 also leads to higher insertion losses.

In spite of the aforementioned effects, it can be also noted the good agreement between simulation and measured results. However, in order to perform a comparison analysis regardless the connectors, a deembeding procedure can be applied by means of a Thru-Reflect-Line (TRL) calibration [82].

Thru-Reflect-Line (TRL) calibration

The Thru-Reflect-Line (TRL) calibration performs a deembeding process, where the influence of all electrical contributions before a calibration plane can be removed from the measurement [83]. Thus, this calibration procedure allows to evaluate the performance of the back-to-back transitions without being masked by measurement deviations caused by the network analyzer, cables or feeding connectors. In order to apply a TRL calibration, a dedicated calibration kit is required.

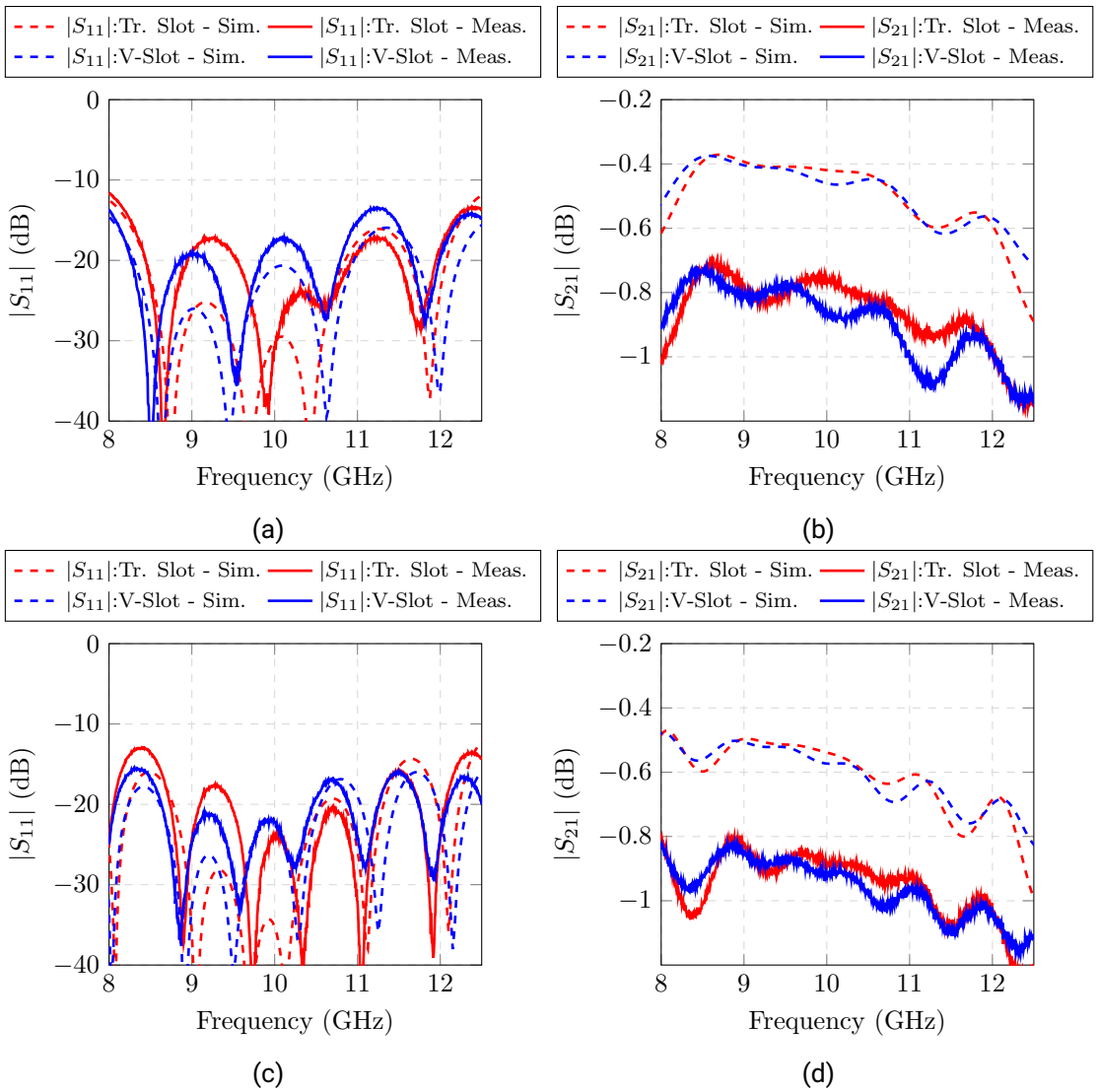

Figure 3.37.: Comparison simulation and measurement back-to-back transitions: (a) Input reflection factor length L_1. (b) Transmission factor length L_1. (c) Input reflection factor length L_2. (d) Transmission factor length L_2.

TRL calibration kit

In order to analyze exclusively the GCPW-SIW transition, the calibration plane is set 3.5 mm after the SMP connector. Thus, the effect of the SMP connectors, SMA-SMP

adapters and the cables can be subtracted from the measured data. In order to have the GCPW feeding excitation fully characterized, the calibration kit is composed of a Through (Thru), Reflect (open or short) and a GCPW transmission line.

- The Thru is composed of two GCPW feeding lines mirrored by the distance of the calibration plane.
- For the reflect, an open or short circuit that yields full reflection is considered. Thus, a GCPW feeding line with an open circuit at the calibration plane is used.
- The TRL line is an electrically longer implementation of the Thru. In order to maximize the calibration bandwidth, the electrically length of the line should yield a phase difference between 20° and 160° in comparison with the Thru.

The calibration kit is depicted in Figure 3.38.

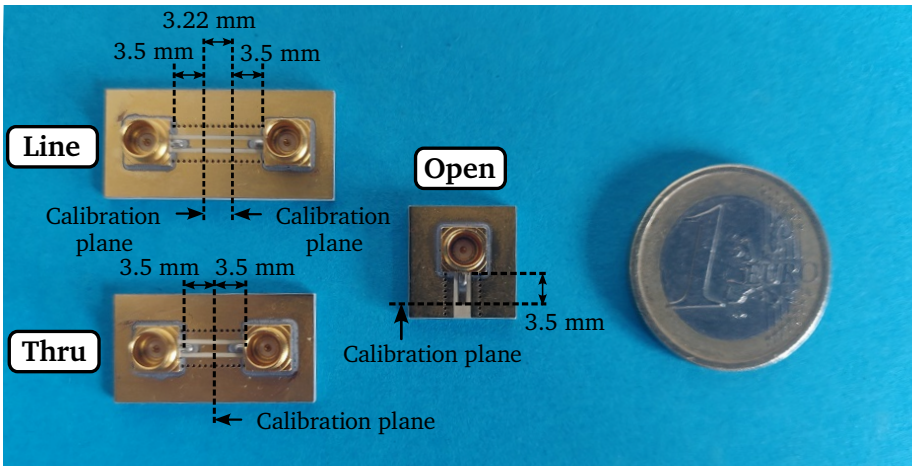

Figure 3.38.: TRL calibration kit.

Analysis of the back-to-back transitions after applying a TRL calibration

The measured results after performing a TRL calibration are shown in Figure 3.39. As it can be seen, no standing wave is present. In addition, since a section of the GCPW line as well as the impact of the connectors have been removed, the measured insertion loss levels are lower.

For both manufactured protoypes, the proposed V-Slot transition yields an overall matching level of up to 7 dB better than the triangular slot, as well as a flatter insertion

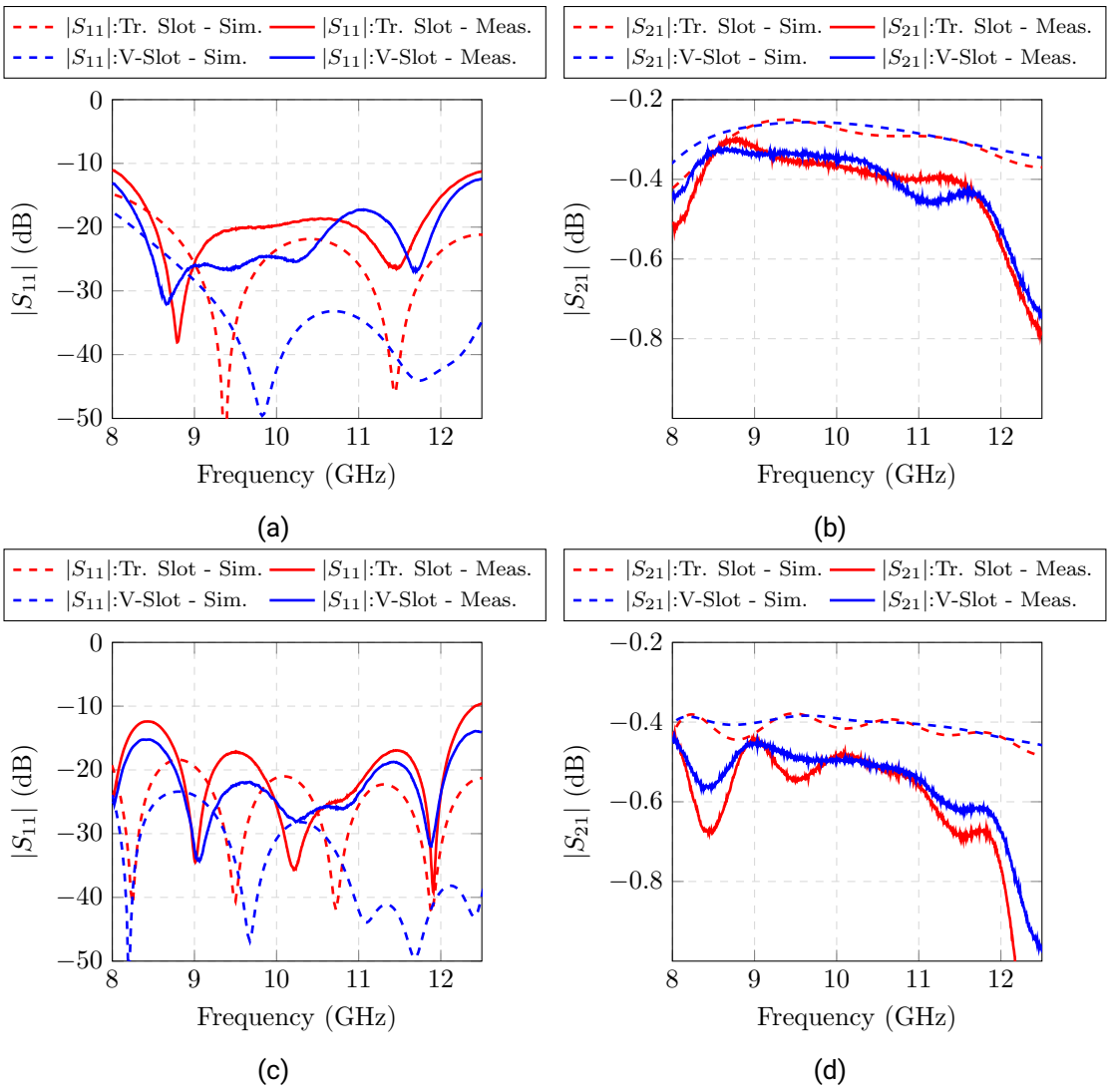

Figure 3.39.: Comparison simulation and measurement back-to-back transitions applying the TRL calibration: (a) Input reflection factor length L_1. (b) Transmission factor length L_1. (c) Input reflection factor length L_2. (d) Transmission factor length L_2.

losses response. However, the simulation results also show an improvement at the higher

frequency band that is not clearly visible in the calibrated measurements.

There are several reasons that can explain this disagreement between simulation and measurement. First of all, the connector placement and its soldering are not homogeneous, and this can lead to some inaccuracies in the calibration. This effect is also more noticeable for higher frequencies, since the sensitivity of the calibration increases. Furthermore, the use of a substrate of a high dielectric permittivity makes the structure extremely susceptible to fabrication tolerances, leading to further discrepancies. Last but not least, since the return loss levels are mainly below 20 dB, any slight inaccuracy (geometrical, calibration, soldering) can produce a variation of some decibels.

Nevertheless, the aforementioned disagreement is present for both types of transitions, since the same calibration procedure is used. Therefore, the enhanced performance of the proposed V-Slot transition leads to a more robust solution, providing a wider margin to deal with such effects.

Despite that the measurement of both transitions provide good matching levels, the performance improvement of the proposed V-Slot can be relevant in applications such as the DBF-SAR project. Since the whole system allows of up to 72 receive antenna modules, the proposed V-Slot transition can be used in the feeding network of each RAM alignment, thus cascading the transition improvement and enhancing the system performance.

Finally, the proposed new transition has not been implemented in the previously presented GCPW-SIW power dividers, so the feasibility of both solutions could be analyzed separately.

4. L-Band Linear Array Antenna for Next Generation DLR Airborne SAR Sensors

In the scope of this chapter, the first design stages of the new L-band antenna for next generation DLR airborne SAR sensors are introduced. In this section, the antenna electrical requirements within the F-SAR and DuoLIM projects framework are described, as well as the first single antenna element and linear array prototypes are designed, manufactured and measured. In addition, a novel cross-polarization suppression method based on the sequential 90° rotation of dual-polarized antenna elements in linear and planar array applications is also presented, and validated using the constructed prototypes.

Thereby, the presented work paves the way for the final phased array antenna design that will be presented in chapter 5.

4.1. Antenna System Requirements

In the framework of the DLR's DuoLIM project, an advanced L-band pulsed polarimetric bistatic airborne SAR sensor is under development, which is meant to support the scientific and technological development of the future spaceborne SAR mission Tandem-L. As its predecessor TanDEM-X, Tandem-L will enable the Earth environment monitoring making use of the penetrating capabilities of L-band signals.

Thus, a bistatic airborne SAR sensor enables the operation capabilities of such a satellite mission, where the transmitter and the receiver are installed on different aircrafts. The spatial separation between the transmitted and received antenna provides different looking acquisition geometries, by which the resolution capabilities and the target detection and classification are improved. In addition, using multiple aircrafts allows the flexibility to generate different baselines for across-track and along-track interferometric applications by means of several aircraft formations.

Thereby, for the operation of this novel bistatic L-band airborne SAR system, a new dedicated flight-certified phased array antenna with beam steering in elevation is required. The electrical sensor requirements are described next and summarized in Table 4.1.

- In order to take advantage of the penetrating capabilities at lower frequencies that are required for biomass studies, among other applications, the system operates in L-band at the center frequency $f_0 = 1.325$ GHz with a bandwidth of 150 MHz.
- The SAR side-looking acquisition geometry, depicted in Figure 4.1, is typically achieved by means of an electrically controlled phased array antenna. For the proposed application, a beam steering in elevation at 42° off-nadir in elevation direction is necessary. The half-power beamwidth in elevation and azimuth should be $\Theta_e = 35° \pm 2°$ and $\Theta_a = 15° \pm 3°$ respectively.
- Since it is a polarimetric SAR system, a dual-linear polarized antenna is required. Thus, two orthogonal linear polarizations, namely horizontal and vertical, are used to identify different scattering mechanisms and to enhance the retrieval of information. In addition, a cross-polarization suppression better than 25 dB should be fulfilled to assure polarization purity.
- In order to attenuate radar ambiguities in azimuth and range direction, a side lobe level better than 18 dB has to be achieved.
- Additionally, in airborne SAR applications a higher suppression in nadir and opposite swath direction should be fulfilled, in order to mitigate the strong echoes coming from the perpendicular direction to the aircraft flight path, and to attenuate the contribution of the opposite imaged scene, respectively.

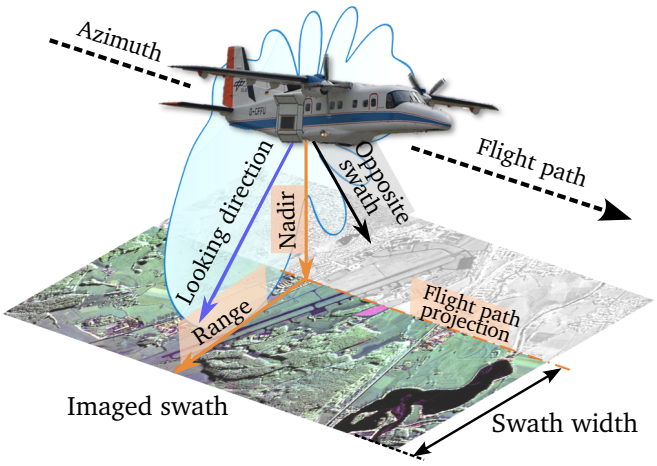

Figure 4.1.: Airborne SAR side-looking acquisition geometry.

Finally, the antenna aperture size is 53 cm $\times$ 85.5 cm (El.$\times$ Az.), and is given by the limited space on the F-SAR carrier that is available for the antenna. This way, the new antenna will be also used in the next generation multifrequency DLR's airborne SAR sensor.

In addition, in order to enhance the degree of freedom to shape the radiation capabilities, the new antenna should efficiently exploit the available aperture size by maximizing the density of array elements. Thus, the resulting planar array size has to dispose of a larger number of array elements than the current L-band antenna of the F-SAR system, based on a planar phased array of 4$\times$6 antenna elements as depicted in Figure 4.2.

Airborne SAR system requirements.	
Frequency of operation	1.325 GHz
Bandwidth	150 MHz
Side-looking SAR acquisition	Beam steering in elevation at 42°
Half-Power Beamwidth	35° $\pm$ 2° (Elevation) / 15° $\pm$ 3° (Azimuth)
Polarimetric SAR	Dual-linear polarization
Side Lobe Level (SLL)	$\geq$ 18 dB
Cross-polarization suppression	$\geq$ 25 dB
Antenna aperture size	53.3 cm $\times$ 85.5 cm

Table 4.1.: SAR system requirements.

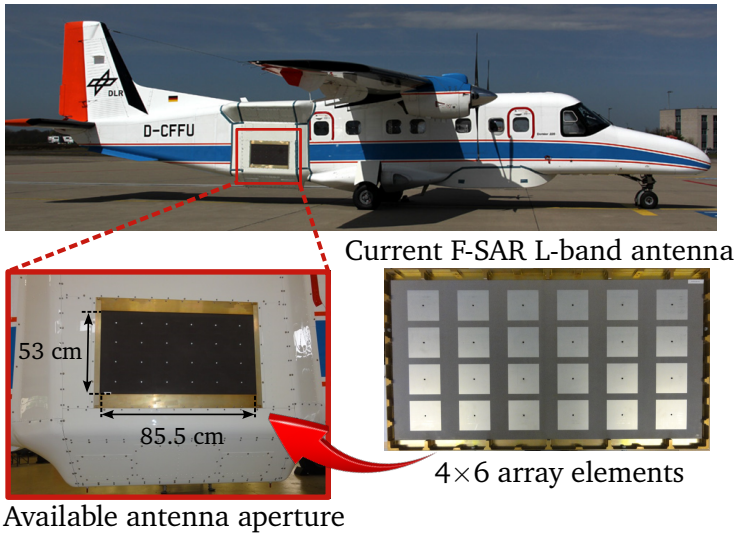

Figure 4.2.: Available antenna aperture on the F-SAR carrier and current L-band antenna.

4.2. Design of the antenna single element

Due to the side-looking operation of airborne SAR sensors, phased array antennas with beam steering capabilities are usually employed.

Airborne radar antennas are typically implemented in planar or waveguide technology. While planar antennas enable a higher degree of integration due to their miniaturization capabilities, waveguide implementations such as slotted waveguide or horn antennas would lead to a bulkier and heavier solutions due to the L-band operation frequency. In addition, planar designs allow a more advantageous implementation of the dual polarization characteristic in the same antenna element, while providing a low-profile and cost-effective solution. On the contrary, in order to fulfill the dual-linear polarization operation with slotted waveguide antennas, usually two different antennas will be required with the slots either placed on the narrow or on the broad wall of the waveguide, which would reduce the effective antenna aperture area. Furthermore, planar antennas are more versatile for electrically controlled beamforming applications with a high density of array elements. In addition, they are also easier and more simple to manufacture using printed circuit photolithographic techniques. For these reasons, the antenna design is implemented in planar technology using a microstrip patch as a single radiating element.

4.2.1. Microstrip patch antenna

A microstrip patch antenna is based on a rectangular, very thin conductive strip, printed on top of a dielectric substrate that is covered on the bottom side by another metal layer or ground plane, resembling a truncated microstrip line, as depicted in Figure 4.3.

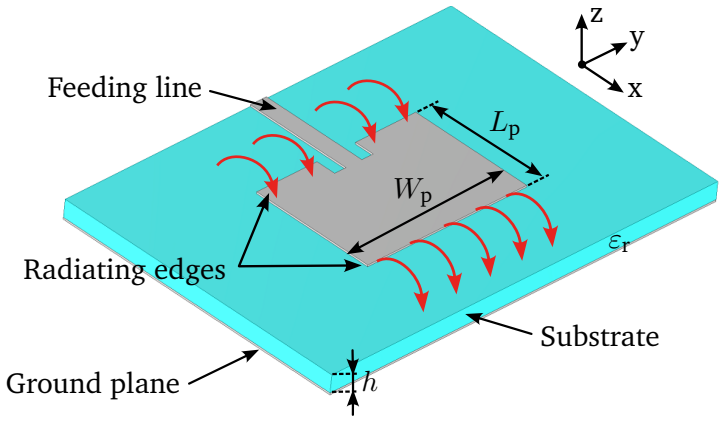

Figure 4.3.: Microstrip patch antenna.

Electrically, mictrostrip patch antennas behave as a planar resonant dielectric loaded cavity with leaking edges that can be considered as radiating slots.

When properly excited, the radiation mechanism of the microstrip patch comes from the fringing fields at the edges. Since the patch antenna can be considered as an open transmission line, the voltage at the end of the patch is maximum, while on the other side is of opposite sign, due to the approximately half wavelength distance between edges that determines the patch length L_p. This way, a sinusoidal electric field distribution, as shown in Figure 4.4, is created below the patch that leads to the generation of fringing fields on the edges by which radiation occurs. Thus, a microstrip patch can be modeled as an antenna array of two apertures or slots that are separated by the patch length, whereby broadside radiation is achieved. For linear polarized microstrip patch antennas, the polarization is given by the orientation of the induced electric and fringing fields that are determined by the alignment direction of the patch edges, as shown in Figure 4.4.

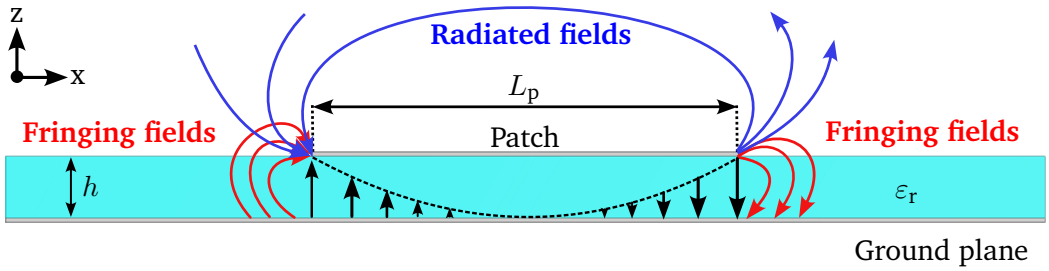

Figure 4.4.: Electric field lines below the patch and resulting fringing and radiated fields.

The distance between radiating edges given by the patch length L_p, which is usually around half of the wavelength, defines the resonant length of the patch, and thus the frequency of operation f_0. On the other side, the patch width W_p controls the impedance bandwidth. Due to its resonant nature as a cavity, a microstrip patch antenna provides only a given performance over a limited relative bandwidth around 3-5%.

Precisely, the antenna bandwidth is strongly dependent on the dielectric substrate properties, both dielectric constant ε_r and thickness h. Thicker substrates with low dielectric permittivity provide wider bandwidths and higher efficiencies at the expense of a larger patch size. On the contrary, thinner substrates with higher dielectric constants reduce the antenna bandwidth but leads to more compact patch sizes.

The length L_p and width W_p of a single polarized microstrip patch antenna can be calculated using the following expressions [47]:

$$
\begin{aligned}
L_{\mathrm{p}} &= \frac{c_0}{2\, f_0 \sqrt{\varepsilon_{\mathrm{eff}}}} - 0.824\, h\, \frac{(\varepsilon_{\mathrm{eff}} + 0.3)\left(\frac{W_{\mathrm{p}}}{h} + 0.264\right)}{(\varepsilon_{\mathrm{eff}} - 0.258)\left(\frac{W_{\mathrm{p}}}{h} + 0.8\right)} \\
W_{\mathrm{p}} &= \frac{c_0}{2\, f_0 \sqrt{\left(\frac{\varepsilon_{\mathrm{r}}+1}{2}\right)}}
\end{aligned}
\tag{4.1}
$$

where the term $\varepsilon_{\mathrm{eff}}$ stands for the effective dielectric permittivity, considering that the wave propagates only in an homogeneous substrate with dielectric permittivity $\varepsilon_{\mathrm{eff}}$, since some of the fields are concentrated within the substrate and others, such as the fringing fields, also propagate partially in air, as shown in Figure 4.4.

$$
\varepsilon_{\mathrm{eff}} = \frac{\varepsilon_{\mathrm{r}} + 1}{2} + \frac{\varepsilon_{\mathrm{r}} - 1}{2} \left[\frac{1}{\sqrt{1 + 12\left(\frac{h}{W_{\mathrm{p}}}\right)}} \right]
\tag{4.2}
$$

According to [84], for a microstrip patch located on the XY plane, where the normal radiation is in Z direction, the spherical components of the radiated fields of a microstrip patch antenna can be expressed as:

$$
\begin{aligned}
E_\theta &= \frac{\sin\left(\frac{k\, W_{\mathrm{p}} \sin\theta \sin\varphi}{2}\right)}{\frac{k\, W_{\mathrm{p}} \sin\theta \sin\varphi}{2}} \cos\left(\frac{k L_{\mathrm{p}}}{2} \sin\theta \cos\varphi\right) \cos\varphi \\
E_\varphi &= -\frac{\sin\left(\frac{k\, W_{\mathrm{p}} \sin\theta \sin\varphi}{2}\right)}{\frac{k\, W_{\mathrm{p}} \sin\theta \sin\varphi}{2}} \cos\left(\frac{k L_{\mathrm{p}}}{2} \sin\theta \cos\varphi\right) \cos\theta \sin\varphi
\end{aligned}
\tag{4.3}
$$

which yields a quasi omnidirectional radiation pattern in broadside direction (perpendicular to the antenna plane) with a radiation null on a infinite ground plane. Typical directivity values of a square microstrip patch antenna on an electrically thin substrate ($h/\lambda_0 < 0.05$) are in the range of approximately 5-7 dBi [66].

4.2.2. Feeding method

An aperture-coupled feeding method is used for the antenna excitation. The antenna is fed by means of an aperture or slot on the ground plane that is coupled by a microstrip line placed below. This configuration allows an independent design of the radiation and

feeding part of the antenna, as well as it also enhances the antenna bandwidth. The geometrical arrangement of the aperture-coupling feeding method for a single polarized microstrip patch antenna is depicted in Figure 4.5.

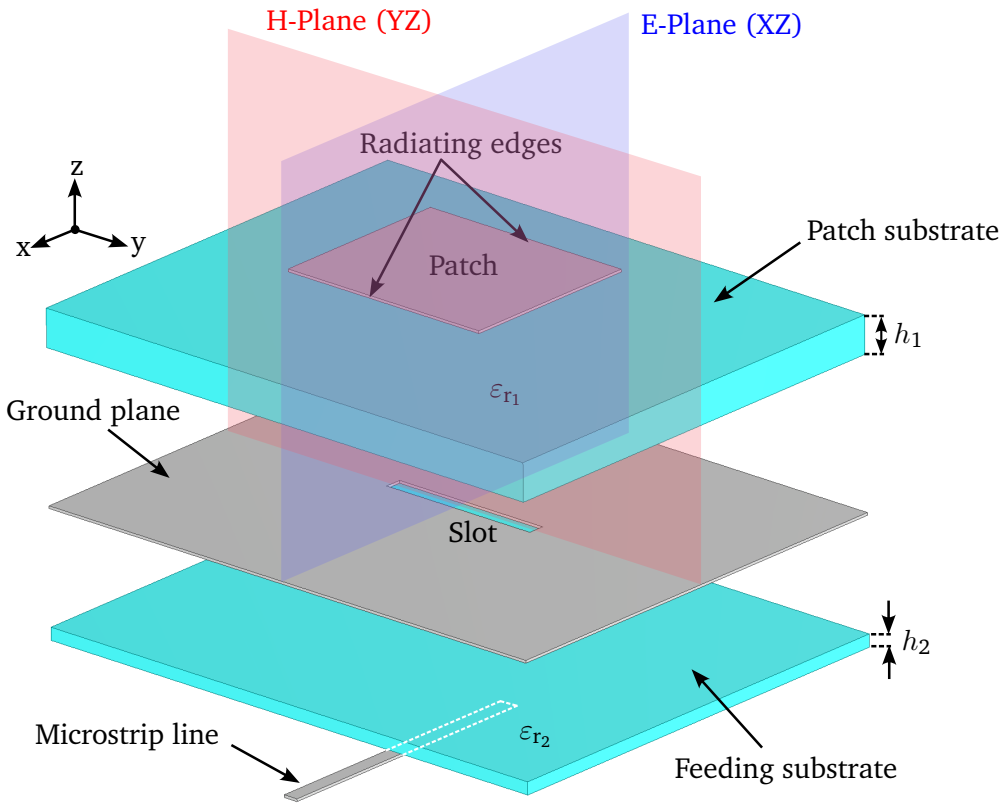

Figure 4.5.: Aperture-coupling feeding method.

- The coupling level is specially determined by the slot length, and to a lesser extent, by the slot width. A typical slot width to length ratio is around 1/10.
- The coupling is maximized when the slot is centered regarding the patch, and decreases if the slot position is shifted along the E-plane. Moving the slot in the direction of the H-plane has a negligible effect.
- The end of the microstrip length (measured from the center of the slot) works as a tuning stub to adjust the reactance excess of the antenna. Usually this length is slightly less than $\lambda_g/4$.

In order to shape the antenna radiation pattern to fulfill the system requirements, a planar array has to be considered, that leads to a two-dimensional geometrical arrangement of single antenna elements. Thus, the radiation characteristics of the antenna can be enhanced due to the contribution of each array element, that otherwise can not be achieved with a single radiator. The theoretical analysis of the antenna group can be found in Appendix B.

4.2.3. Number of antenna elements

In the proposed work, the number of antenna elements is directly determined by the restricted antenna aperture on the aircraft. A key aspect of the new design is to exploit efficiently this limited antenna aperture in order to maximize the number of array elements, and thus, to enhance the radiation properties of the antenna.

As it is seen in Figure 4.2 the maximum aperture size available is 53 cm $\times$ 85.5 cm. In addition, the new L-band antenna has to dispose of a larger number of array elements than the current L-band antenna of the F-SAR system, composed of 4$\times$6 antenna elements.

The extension of the array in each direction (azimuth or elevation) is dependent on the chosen interelement spacing d_{a} as well as the patch size, that is mostly determined by the substrate dielectric permittivity.

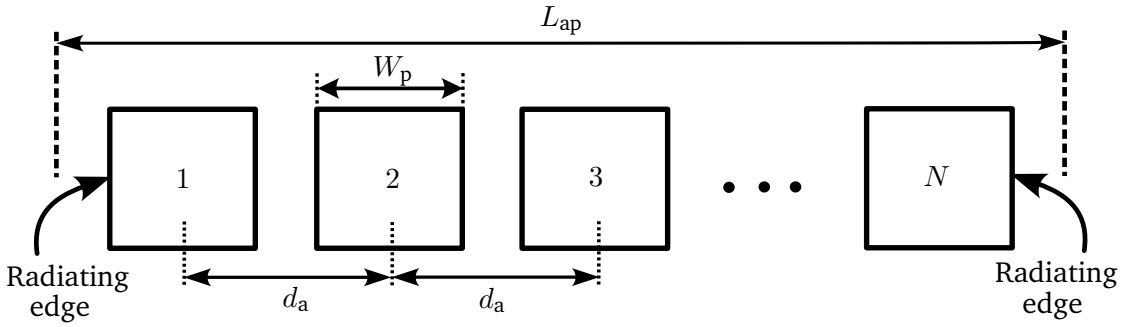

Figure 4.6.: Number of array elements in elevation.

Since the available aperture length in elevation is less than in azimuth, the possible number of array elements in elevation is first estimated.

As depicted in Figure 4.6 and considering an effective aperture length in elevation $L_{\mathrm{ap}} = 50$ cm, that is slightly less than 53 cm to account for the radiating slots of the patches placed at the array edges, the number of antenna elements N can be easily calculated by:

$$N = \frac{L_{\text{ap}} - W_{\text{p}} + d_{\text{a}}}{d_{\text{a}}} \tag{4.4}$$

The dual-polarization leads to square patches, by which the pair of radiating edges for each polarization is orthogonal to the other one. Thus, it can be assumed $L_{\text{p}} \approx W_{\text{p}}$.

The size of the rectangular patch can be estimated using equation (4.1) which leads to $L_{\text{p}} < W_{\text{p}}$. Thus, as a worst case scenario, the patch width is considered for the patch size. This way, for a given interelement spacing d_{a}, the number of array elements that fit in the available area can be calculated for different dielectric permittivities using equation (4.4).

Table 4.2 shows an analysis in terms of number of elements, patch size and dielectric permittivities for an interelement spacing $d_{\text{a}} = 0.45\lambda_0$. This separation is used as a starting value because it is the greatest interelement spacing that assures 5 array elements considering a substrate with the lowest dielectric permittivity ($\varepsilon_{\text{r}} = 2.2$).

ε_{r}	W_{p}	N
2.2	89.49 mm	5.03
4.4	68.9 mm	5.23
6.15	59.87 mm	5.32

Table 4.2.: Number of array elements for $L_{\text{ap}} = 50\,\text{cm}$, $d_{\text{a}} = 0.45\lambda_0$.

It can be seen that regardless the substrate used, 5 array elements can be arranged in elevation (N>5), which already exceeds the 4 elements of the previous L-band antenna. However, such a tight interelement spacing would lead to a strong coupling among array elements, especially for lower dielectric permittivities, where the radiating etches of the patches would be really close to each other.

Considering a larger interelement spacing, such as $d_{\text{a}} = 0.5\lambda_0$, would mitigate, to some extend, the coupling between elements, as well as to avoid the appearance of grating lobes. However, it would also prevent to achieve 5 array elements, as seen in Table 4.3.

ε_{r}	W_{p}	N
2.2	89.49 mm	4.62
4.4	68.9 mm	4.8
6.15	59.87 mm	4.88

Table 4.3.: Number of array elements for $L_{\text{ap}} = 50\,\text{cm}$, $d_{\text{a}} = 0.5\lambda_0$.

Thus, for an intermediate spacing value of $d_{\text{a}} = 0.48\lambda_0$, an extremely tight disposal of radiating elements can be avoided using a higher dielectric permittivity ($\varepsilon_r = 6.15$), as

well as the requirement of 5 array elements can be fulfilled, as shown in Table 4.4.

ε_r	W_p	N
2.2	89.49 mm	4.77
4.4	68.9 mm	4.96
6.15	59.87 mm	5.05

Table 4.4.: Number of array elements for $L_\mathsf{ap} = 50\,\mathrm{cm}$, $d_\mathsf{a} = 0.48\lambda_0$.

Note that all the previous calculations are based on a substrate thickness h=1 mm, that slightly influences the patch length L_p but has no impact on the patch width. Thus, further analysis can be performed using different thicknesses leading to the same outcome.

The previous investigation is an approximation that considers an antenna model with only one substrate. As it will be explained later, additional foam layers of low dielectric permittivity ($\varepsilon_\mathrm{r} \approx 1$) will be used to increase the bandwidth. The resulting multilayer antenna structure will lead to a reduction of the overall effective dielectric constant, and thus an increase of the patch size. In order to compensate this trade-off, a substrate with a high dielectric permittivity ($\varepsilon_\mathrm{r} \uparrow$) has to be considered. Thus, in order to assure 5 array elements in elevation, a substrate with $\varepsilon_\mathrm{r} = 6.15$ is used.

Obviously, the use of this dielectric permittivity value also determines the number of antenna elements that can be arranged along azimuth direction. This way, using an interelement spacing $d_\mathsf{a} = 0.48\lambda_0$ and a substrate with a dielectric permittivity $\varepsilon_\mathrm{r} = 6.15$, a planar phased array of 5×8 can be built. Thus, the new design will provide 16 more elements than the current F-SAR L-band antenna, leading to an increase of 66% that will allow to shape more accurately the radiation pattern for beamforming purposes.

4.2.4. Bandwidth enhancement

Figure 4.7 shows the simulation results of a single-polarized aperture coupled patch antenna using a patch substrate Rogers RT/Duroid 6006 ($\varepsilon_{\mathrm{r}_1} = 6.15$, $\tan\delta = 0.0019$) with different substrate thickness values h_1. The feeding substrate is implemented on a FR4 epoxy ($\varepsilon_{\mathrm{r}_2} = 4.4$, $\tan\delta = 0.02$) with thickness $h_2 = 1.22\,\mathrm{mm}$, and the width of the microstrip line is optimized to yield an impedance of 50 Ω.

As it can be seen, the antenna bandwidth, measured at a return loss level of 10 dB, increases when thicker patch substrates are used. On the other side, larger bandwidths also lead to lower gains, since the fields propagating within electrically thicker substrates are more affected by its losses. It can be also noted that, due to the resonant nature of the microstrip patch, a relatively high electric thick substrate of 7 mm only provides a

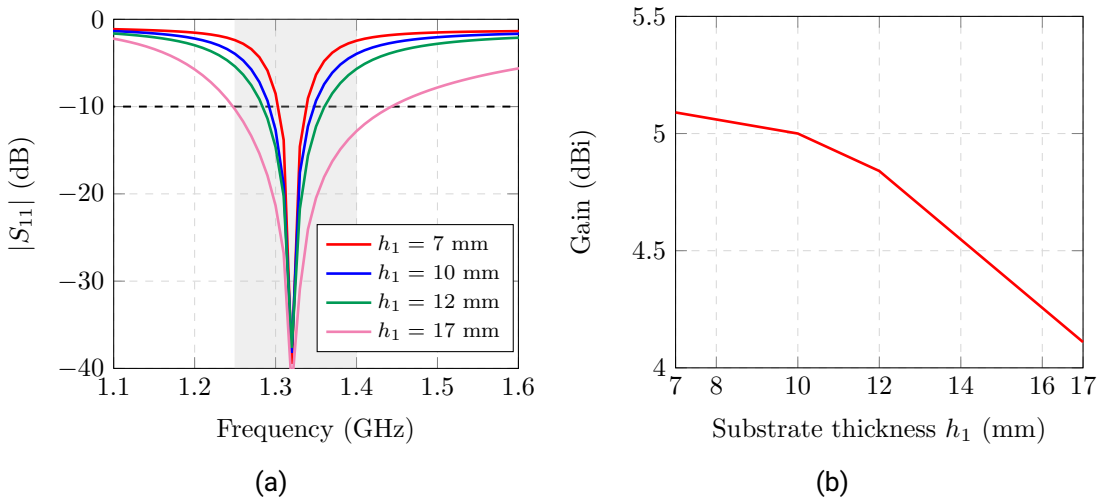

(a) (b)

Figure 4.7.: Performance of aperture coupled antenna with dielectric permittivity of the patch substrate $\varepsilon_{r_1} = 6.15$ (a) Bandwidth (b) Gain @ $f_0 = 1.325$ GHz.

bandwidth of 40 MHz (3%), that does not fulfill the required operational bandwidth of 150 MHz (15%), as listed in Table 4.1. In addition, substrate panels are usually available with thickness values way below 7 mm, which prevents the use of such electrically thick substrates. Thus, a stacked patch configuration is applied to enhance the antenna bandwidth.

Stacked patch configuration

A dual patch structure is used to improve the antenna bandwidth. This broadband technique uses two microstrip patches spaced by low dielectric permittivity foam layers [85, 86]. The bandwidth enlargement comes from the effect of three resonant structures: the coupling slot, the bottom and the top patches that have distinct sizes to resonate at slightly different frequencies. In addition, the use of thick foam layers below the substrate patches allows to reduce the effective dielectric permittivity and increases the bandwidth. The use of high dielectric permittivity substrates for the patches enables to reduce the patch size. The multilayer antenna assembly can be seen in Figures 4.8 and 4.9, and the electrical and geometrical properties of each layer are listed in Table 4.5.

The dual-polarization characteristic of the antenna leads to square patches. The top patch is placed below the substrate, that serves as a superstrate or radome layer to protect it from atmospheric and aircraft conditions.

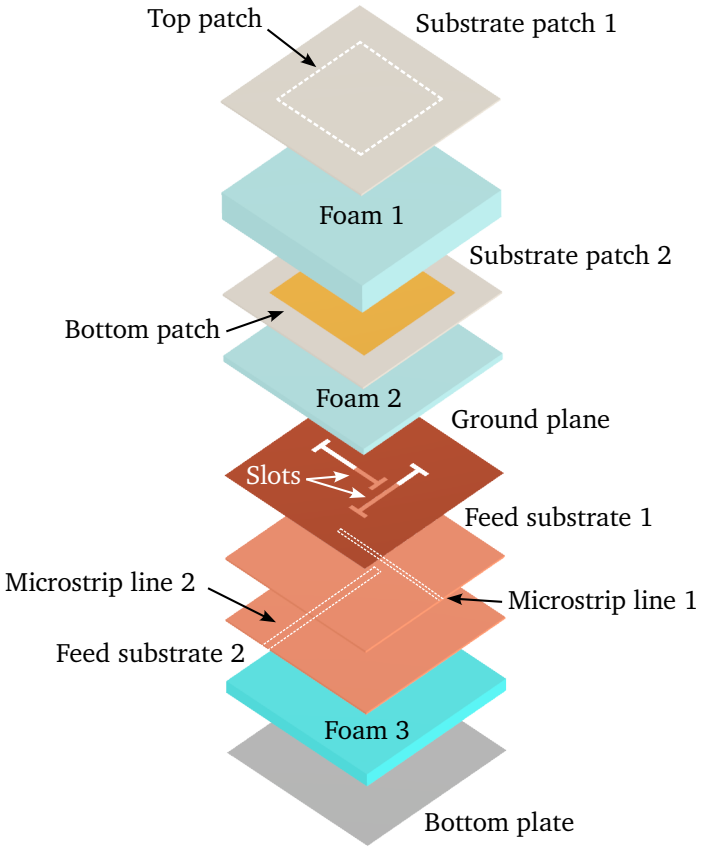

Figure 4.8.: Antenna multilayer structure.

Aperture coupling feeding

Each polarization is excited by means of an aperture slot that is etched on the ground plane and coupled by a microstrip line. In order to improve the isolation between them, the feeding lines are placed on different substrate heights, as depicted in Figure 4.9. This line position variation (different substrate thickness) leads to distinct line widths, that are designed to provide a 50 Ω impedance value. More information about the calculation of the microstrip lines and their characterization in HFSS can be found in Appendix C.

To provide a mechanical stability to the whole antenna structure, an additional foam layer and metallic plate are added at the bottom. This separation h_{foam3} is set to avoid interference of the bottom plate with the electric field propagation of the quasi-TEM mode

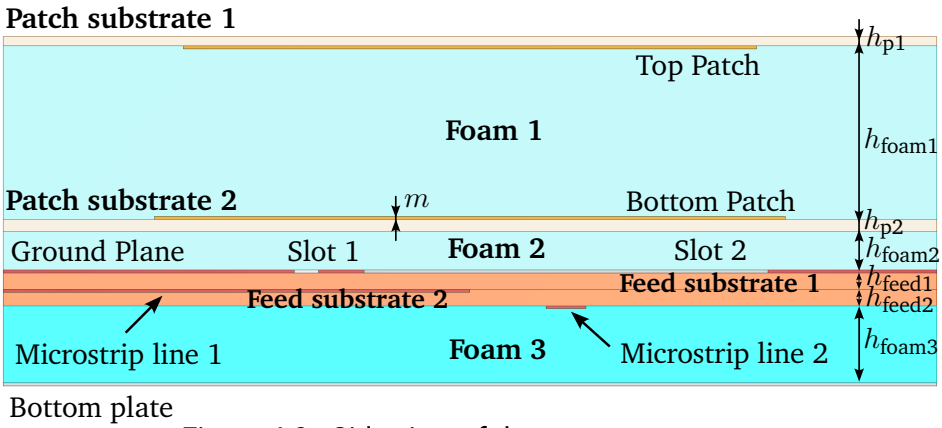

Figure 4.9.: Side view of the antenna structure.

Layer	Material	ε_r	Thickness	
			Name	Value
Substrate patch 1	Rogers RT/Duroid 6006	6.15	h_{p1}	1.27 mm
Foam 1	Rohacell HF 51	1.06	h_{foam1}	14 mm
Substrate patch 2	Rogers RT/Duroid 6006	6.15	h_{p2}	1.27 mm
Foam 2	Rohacell HF 51	1.06	h_{foam2}	4 mm
Feed substrate 1	FR4 Epoxy	4.4	h_{feed1}	1.27 mm
Feed substrate 2	FR4 Epoxy	4.4	h_{feed2}	1.27 mm
Foam 3	Rohacell HF 51	1.06	h_{foam3}	5 mm
Metallization (patches, ground plane and lines)	Copper	-	m	35 μm

Table 4.5.: Electrical properties of each antenna layer.

created by the microstrip line 2.

Each slot excites one polarization, being orthogonal to each other just like the radiating pair of patch edges whose distance determines the resonant length and, thus the polarization direction. As convention, the slots 1 and 2, placed parallel to the y- and x-axis, excites the horizontal and vertical polarization respectively.

The H-shaped slot improves the coupling between the slot and the bottom patch [87], and it also reduces its electrical length making it convenient to optimize the available space. The slot position is given by its offset, by which the isolation between both polarizations can be enhanced with values above 30 dB. The different geometrical parameters of the slots, feeding lines and patches are shown in Figure 4.10 and listed in Table 4.6.

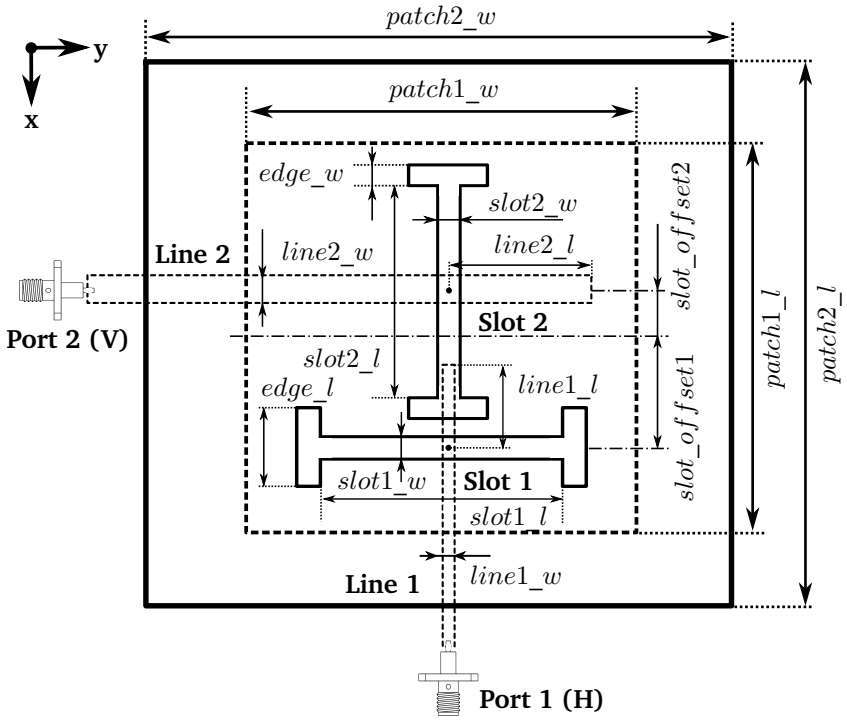

Figure 4.10.: Geometrical parameters of the aperture coupling feeding and patches.

Optimization process

The antenna is simulated in HFSS, and the following design goals are established to determine the required performance. The antenna is designed to minimize the return loss level at the center frequency of operation 1.325 GHz, in order to enhance the gain ($|S_{11}|, |S_{22}| \leq$ -20 dB), as well as to achieve a matching level better than 10 dB within the operational bandwidth 1.25 GHz$\sim$1.4 GHz. In addition, the reduction of cross-polarization levels is desired, thus aiming for high polarization isolation values ($|S_{21}| \leq$ -20 dB). Furthermore, a similar electrical performance of both polarizations is expected, with comparable radiation characteristics such as gain and orthogonality of radiation patterns.

The optimization process is performed considering the electrical influence of each geometrical parameter:

- The patches lengths $patch1\_l$, $patch2\_l$ and widths $patch1\_w$, $patch2\_w$ determine the resonant frequency for the horizontal and vertical polarization, respectively. A square patch is considered in order to achieve a similar radiation performance

for both polarizations, thus leading to comparable patch length and width values that correspond to the resonant length for the horizontal and vertical polarization, respectively. The top and bottom patches have distinct sizes in order to resonate at slightly different frequencies to increase the bandwidth. To reduce complexity, the size of the top and bottom patches are related by means of a small length and width variation given by Δl, Δw so they can be expressed as $patch2\_l = patch1\_l + \Delta l$ and $patch2\_w = patch1\_w + \Delta w$.

- The slot lengths $slot1\_l$ and $slot2\_l$ are determined to maximize the coupling and minimize the backward radiation of the slot, which improves the return loss level. The slot length to width ratio is slightly less than 1/10. The slot positions are given by the offsets $slot\_offset1$ and $slot\_offset2$ that maximize the isolation between both polarizations $|S_{21}|$ with values better than 30 dB. The slot lengths also determine the value of the offsets, that prevents the intersection between slots. The slot edges allow to reduce the effective length of the slot and improves its coupling.

- The end of the microstrip line lengths $line1\_l$ and $line2\_l$, measured from the slot center, compensates the antenna reactance, thus improving the matching level.

- A standard substrate thickness $h_{\mathrm{p1}} = h_{\mathrm{p2}} = 1.27$ mm is used for the patch implementation, along with a high dielectric permittivity substrate ($\varepsilon_{\mathrm{r}} = 6.15$) that allows to reduce the patch size. A bottom foam layer is added to reduce the effective dielectric permittivity and thus increasing the bandwidth of the bottom patch, since the use of a thin substrate of high dielectric permittivity leads to an extremely narrow band antenna. The upper foam layer also improves the antenna bandwidth, however thick layers can also reduce the coupling between patches, thus also decreasing the antenna gain.

The geometrical parameters of the antenna, namely the patch sizes, feeding lines and coupling slots are shown in Table 4.6.

Patch size		**Aperture coupling feeding geometry**					
$patch1\_l$	67.2	$slot1\_l$	37	$slot1\_w$	2.5	$slot2\_l$	37
$patch1\_w$	65.3	$slot2\_w$	2.5	$slot\_offset1$	17	$slot\_offset2$	10
$patch2\_l$	73.7	$line1\_l$	40	$line2\_l$	45.5	$line1\_w$	1.85
$patch2\_w$	68.3	$line2\_w$	4.15	$edge\_l$	11	$edge\_w$	2.5

Table 4.6.: Patch size and feeding parameters (in mm).

Simulation results

The antenna simulation scenario in HFSS is shown in Figure 4.11. Each microstrip line is excited with a 50 Ω lumped ports, as they are internal feeding ports. The antenna is placed in an airbox, where a radiation boundary is applied in order to simulate the far-field propagation, by which the radiated fields are absorbed and no reflected waves come back to the radiating source. The ground plane size is determined by the distance between the antenna radiating edges and the airbox walls that is $\lambda_0/4$, thus avoiding surface wave diffraction. Even though the smallest required distance for radiation boundaries is $\lambda_0/4$, the airbox height in z direction is set to be $\lambda_0/2$.

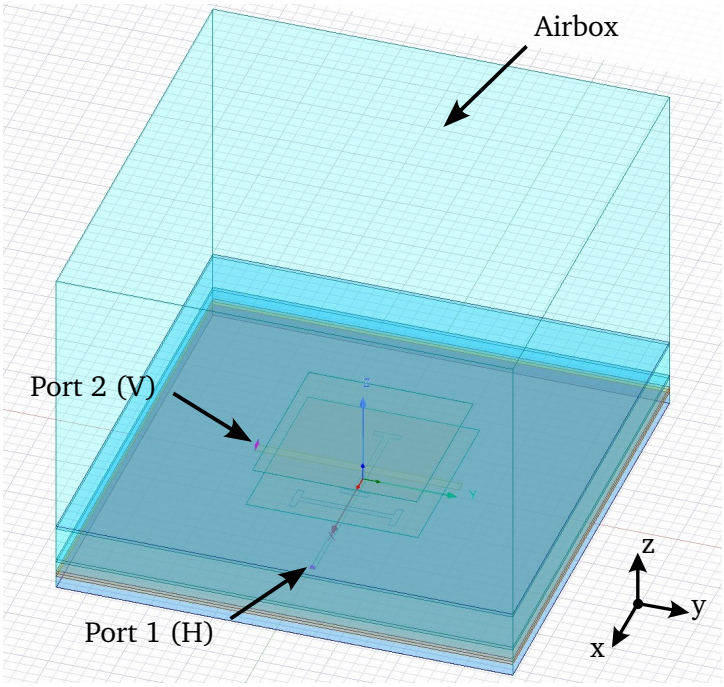

Figure 4.11.: Simulation scenario of the aperture coupled stacked patch model in HFSS.

The simulation results of the stacked patch configuration are shown in Figures 4.12 and 4.13, where the antenna matching levels and radiation pattern are plotted, respectively. As seen in Figure 4.12a, the return loss levels for both polarizations $|S_{11}|$, $|S_{22}|$ are better than 30 dB at the center frequency of operation, and below 10 dB for the operational bandwidth. The polarization isolation values $|S_{21}|$ remain better than 30 dB, with values around 40 dB at the center frequency band. An alternative representation of the antenna

adaptation is depicted with the Smith Chart in Figure 4.12b. It can be seen that the input impedance at the center frequency of operation is at the center of the chart, i.e a purely resistive input impedance of 50 Ω is achieved with no reactance or imaginary value, thus leading to the best matching case. As expected, the adaptation is slighty lower for the frequency range out of the center band, with the highest mismatch level at the lower frequencies below the operational bandwidth.

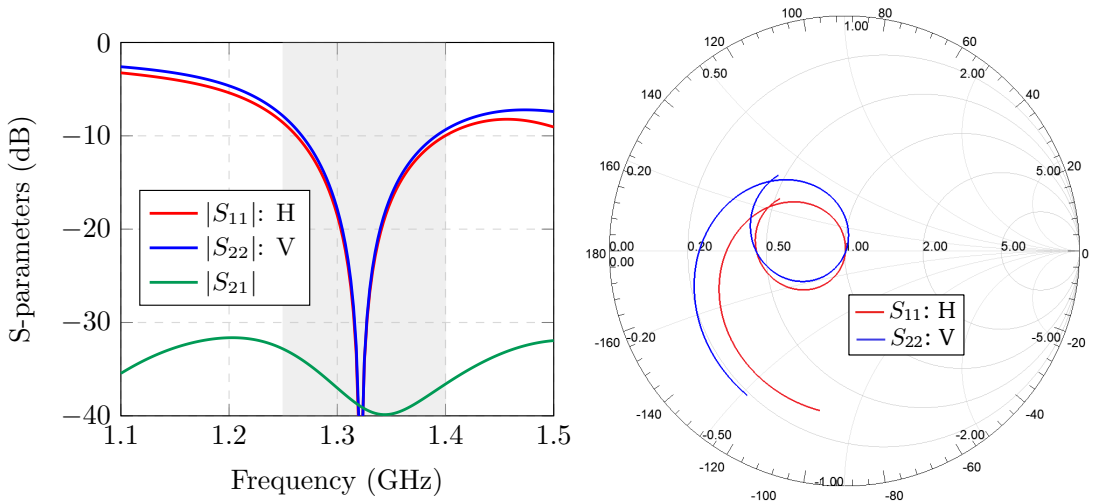

(a) (b)

Figure 4.12.: Simulated antenna matching: (a) Reflection factor and polarization isolation levels. (b) Smith chart representation.

The antenna gain is, respectively, 7.84 dBi and 7.9 dBi for the horizontal and vertical polarization, respectively. The directivity for both polarizations is 8.19 dBi, which yields an efficiency of around 93%. The main cuts of the antenna radiation pattern are plotted in Figure 4.13. Due to the polarization orthogonality the cut in the E-plane for the horizontal polarization (plane XZ, $\varphi = 0°$) coincides with the E-plane of the vertical polarization (plane YZ, $\varphi = 90°$). The same observation can be done for the the H-plane.

Shifting the slot 1 along the x-axis (E-plane direction for the horizontal polarization), slightly decreases the coupling level, which also leads to a light pattern asymmetry in such plane [88]. On the other side, moving the slot in the H-plane, as for the vertical polarization, has little effect.

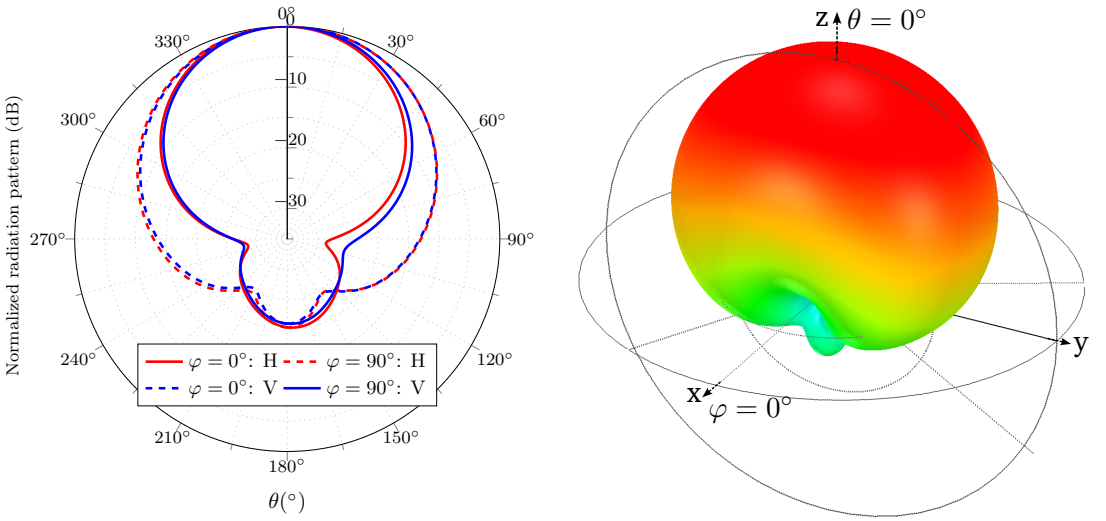

(a) (b)

Figure 4.13.: Simulated radiation pattern: (a) Pattern cuts. (b) 3D radiation pattern. Horizontal polarization.

4.3. Linear array formation

Once the antenna single element is designed, a linear array of 5 elements is built. The electrical performance of this array plays a key role in the operation of the antenna system, since it determines the shaping capabilites of the radiation pattern in elevation by means of beamforming and amplitude tapering. Thus, this design stage not only allows to study the feasibility of the proposed solution, but it also paves the way for the implementation of the final planar array of 5×8 elements.

Figure 4.14 shows the HFSS model of the linear array along y-axis considering an interelement spacing of $d_a = 0.48\lambda_0$, as proposed in section 4.2. The overall patch to patch length d_e, measured from the edge bottom patches is d_e=50.27 cm, which does not exceed the available aperture length in elevation L_{ap}. Each antenna element is excited with a pair of ports H_i, V_i that controls, respectively, the horizontal and vertical polarization excitation.

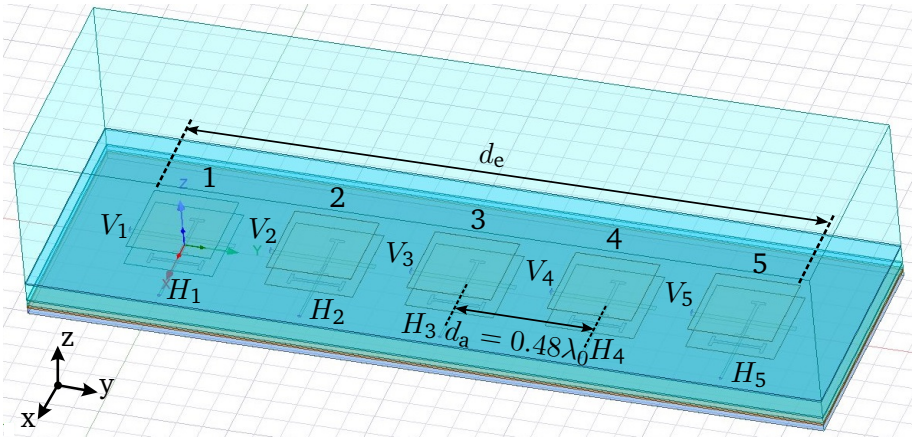

Figure 4.14.: Linear array of 5 stacked patches along y-axis. HFSS model.

4.3.1. Beam steering and amplitude tapering

The side-looking operation of the DuoLIM airborne SAR system demands beam steering in elevation. Thus, the proposed linear phased array determines the performance of the complete antenna in elevation. According to the airborne SAR system specifications listed in Table 4.1, a beam steering at 42° off-nadir is required.

From the array theory presented in Appendix B, the required progressive phase difference α between array elements, to fulfill the desired angular direction of maximum radiation θ=42°, is given by:

$$\alpha = k d_a \sin\theta \tag{4.5}$$

where $k = \frac{2\pi}{\lambda_0}$ and d_a=0.48λ_0 that leads to $\alpha \approx$120°. Be noted that due to the positive progressive phase difference ($\alpha > 0$), the main beam will point toward θ=318°=-42° in the depiction of the radiation pattern. When the antenna is mounted on the aircraft, this angular direction corresponds to the right side looking according to the flight path, as shown in Figure 4.1.

Furthermore, a triangular amplitude tapering is applied to reduce the side lobe level, that is required to mitigate radar ambiguities.

The proposed weighting coefficients are shown in Figure 4.15, and they are optimized considering the following criteria:

- Due to the symmetry and the odd number of array elements, the centered antenna element is excited with the maximum amplitude.

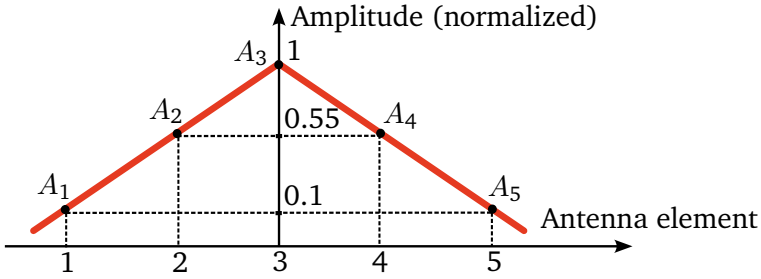

Figure 4.15.: Triangular amplitude distribution.

- Since the number of antenna elements is restricted to 5, other amplitude distributions such as cosine over pedestal becomes difficult to implement, due to the limited degree of freedom. On the other side, a triangular amplitude weighting is feasible to perform with 5 array elements.
- The proposed amplitude tapering, along with the beam steering, allows to achieve a side lobe level better than 20 dB, as well as nadir suppression higher than 25 dB, thus fulfilling the system requirements listed in Table 4.1.

Thus, the array factor can be described by:

$$AF(\psi) = \sum_{n=1}^{5} A_{\mathrm{n}} e^{j(n-1)(kd_{\mathrm{a}} \sin\theta \sin\varphi + \alpha)} = \sum_{n=1}^{5} A_{\mathrm{n}} e^{j(n-1)\psi} \tag{4.6}$$

Simulation results

The linear array is simulated in HFSS. The amplitude A_i and phase coefficients φ_i for each feeding port are listed in Table 4.7.

The simulated pattern in elevation (YZ plane, $\varphi = 90°$) for both polarizations is shown in Figure 4.16. The gain values for the horizontal and vertical polarization are 11.62 dBi and 11.24 dBi respectively.

It can be noted that the radiation pattern for both polarizations is not identical, despite that the single antenna performance for the horizontal and vertical polarization is comparable. One of the reasons is that the linear array is built along the y-axis, where the YZ plane corresponds to the E-plane of the vertical polarization and the H-plane of the horizontal one. Thus, the geometrical asymmetry of the structure affects differently each field polarization. For this reason, the field interaction with the array edges leads to slightly distinct main beams and backlobe radiation. On the other side, the radiation

Horizontal polarization			Vertical polarization		
H_1	A_1	φ_1	V_1	A_1	φ_1
	0.1 W	0°		0.1 W	0°
H_2	A_2	φ_2	V_2	A_2	φ_2
	0.55 W	120°		0.55 W	120°
H_3	A_3	φ_3	V_3	H_3	φ_3
	1 W	240°		1 W	240°
H_4	A_4	φ_4	V_4	A_4	φ_4
	0.55 W	0°		0.55 W	0°
H_5	A_5	φ_5	V_5	A_5	φ_5
	0.1 W	120°		0.1 W	120°

Table 4.7.: Amplitude and phase coefficients.

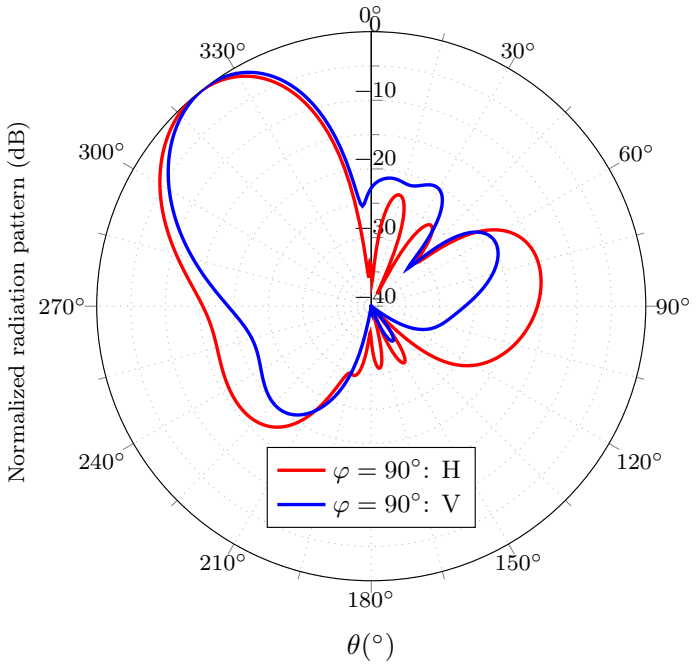

Figure 4.16.: Normalized radiation pattern in elevation for both polarizations.

pattern of the horizontal polarization is more accurately shaped with a side lobe level better than 25 dB, as well as an strengthen suppression in nadir range ($\theta \pm 5°$) with

values above 30 dB. This is especially relevant in remote-sensing imaging in order to avoid radar ambiguities, as well as to mitigate the strong echoes coming from the direction perpendicular to aircraft flight path, respectively.

The second cause for the discrepancy between the radiation shaping capabilities of both polarizations comes from the coupling between array elements. Due to the proximity of the antenna elements, the coupling among them is increased, so each antenna can not be excited independently and is electrical influenced by all neighbours elements.

Since for the vertical polarization an E-plane coupling takes place, the patch radiating edges are aligned to the array axis, which leads to a more intense electric fields between the patches, and thus it increases the coupling. For the horizontal polarization an H-plane coupling occurs, which is lower. For this reason, the higher coupling between antenna elements in the vertical polarization prevents a more accurate pattern beamforming.

Figure 4.17a depicts the electric field magnitude of the vertical polarization between two antenna elements. Figure 4.17b shows the coupling levels $|S(H_2, H_1)|$, $|S(V_2, V_1)|$. It can be noted the intensity of the electric field between both antennas (red areas) when one single element is excited. The coupling at the center frequency of operation is -12 dB and -17 dB for the vertical and horizontal polarization, respectively.

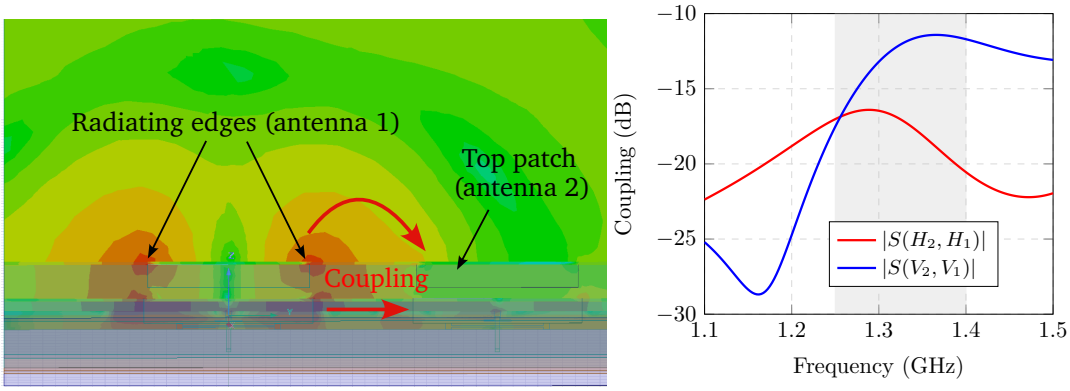

(a) (b)

Figure 4.17.: Simulation results coupling between two antenna elements: (a) Electric field magnitude (vertical polarization). (b) Isolation values between antennas.

The very same analysis can be performed considering the linear array built in x-axis, as shown in Figure 4.18. Due to the orthogonality of both polarizations and similar antenna performance regardless the polarization, the complementary situation occurs, being the horizontal polarization more affected by the coupling, thus preventing a more

accurate radiation pattern shaping. It can be noted that the radiation patterns shown in Figure 4.18a are almost identical to the ones in Figure 4.16 but swapping polarizations.

This analysis proves that the electrical performance of the single antenna allows to achieve the desired radiation pattern characteristics for both polarizations, providing that the isolation between array elements is sufficient. Thus, reducing the antenna coupling in E-plane would lead to a finer shaping capabilites and more alikeness between both patterns, thus achieving a similar radiation performance regardless the polarization.

One simple way to reduce the coupling between array elements is increasing the interelement spacing d_{a}. However, for the given application, the separation between elements is strictly set and can not be increased due to the limited antenna aperture.

Some other well-known planar approaches use electromagnetic bandgaps (EBGs) to reduce the coupling. However, the multilayer nature of the antenna, as well as the use of foam layers and the lack of space between array elements, prevent its application. Other solutions like defected ground structure (DGS) are not suitable in aperture coupling feeding antennas, due to the inherent modification of the ground plane, where the feeding slots are placed. A cost-effective approach is to place the antenna element within a closed casing structure such as a cavity box [89]. This antenna assembly improves the interelement coupling along E-Plane, leading to a compact and low-profile antenna solution.

4.4. Cavity-box aperture coupled stacked patch antenna

The aperture coupled stacked pach antenna is enclosed within four conductive solid walls that resemble a closed cavity, as depicted in Figure 4.19. Thus, when considering an array formation, the antenna elements are separated by means of electric walls that reduce the coupling and the propagation of surface waves. This way, the isolation in E-plane is enhanced. Due to the close proximity between array elements, the coupling contribution as a result of the actual radiation can not be avoided.

The proximity of the patches with the electric walls also leads to a shift of the antenna operation to lower frequencies, as well as a bandwidth reduction, due to the resonant nature of the closed cavity structure. Thus, the thickness of the top foam layer is increased in order to improve the bandwidth, that also leads to a gain decrease.

Unlike the previous stacked patch antenna design, the electric walls allow to use a wave port to excite each microstrip feeding line, as seen in Figure 4.19a, since internal waveports require to be placed on conductive surfaces. It can be also noted that the microstrip line that couples the slot 2, and thus excites the vertical polarization, is also bended. Thus, the antenna feeding ports can be placed on opposite directions for mechanical purposes, easing the antenna element feeding when a prototype of the linear array is manufactured.

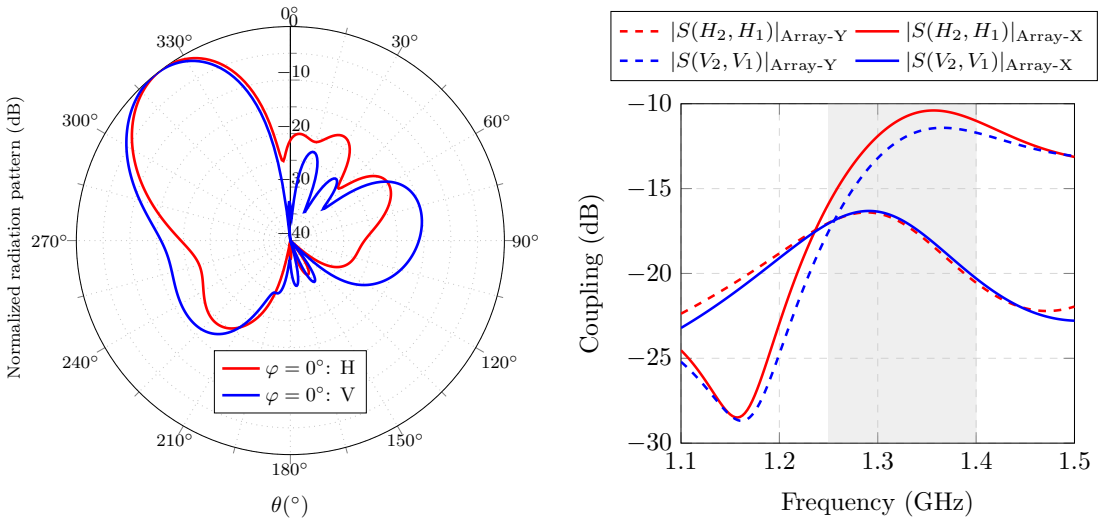

(a) (b)

Figure 4.18.: Simulation results considering a linear array along x-axis: (a) Normalized radiation pattern in elevation for both polarizations. (b) Polarization isolation.

The optimization process is performed following the design steps presented in the previous section. The electrical properties of each antenna layer, as well as the geometrical parameters, are listed in Tables 4.8 and 4.9.

Layer	**Material**	ε_r	**Thickness**	
			Name	**Value**
Substrate patch 1	Rogers RT/Duroid 6006	6.15	h_{p1}	1.27 mm
Foam 1	Rohacell HF 51	1.06	h_{foam1}	18 mm
Substrate patch 2	Rogers RT/Duroid 6006	6.15	h_{p2}	1.27 mm
Foam 2	Rohacell HF 51	1.06	h_{foam2}	4 mm
Feed substrate 1	FR4 Epoxy	4.4	h_{feed1}	1.27 mm
Feed substrate 2	FR4 Epoxy	4.4	h_{feed2}	1.27 mm
Foam 3	Rohacell HF 51	1.06	h_{foam3}	5 mm

Table 4.8.: Electrical properties of each antenna layer.

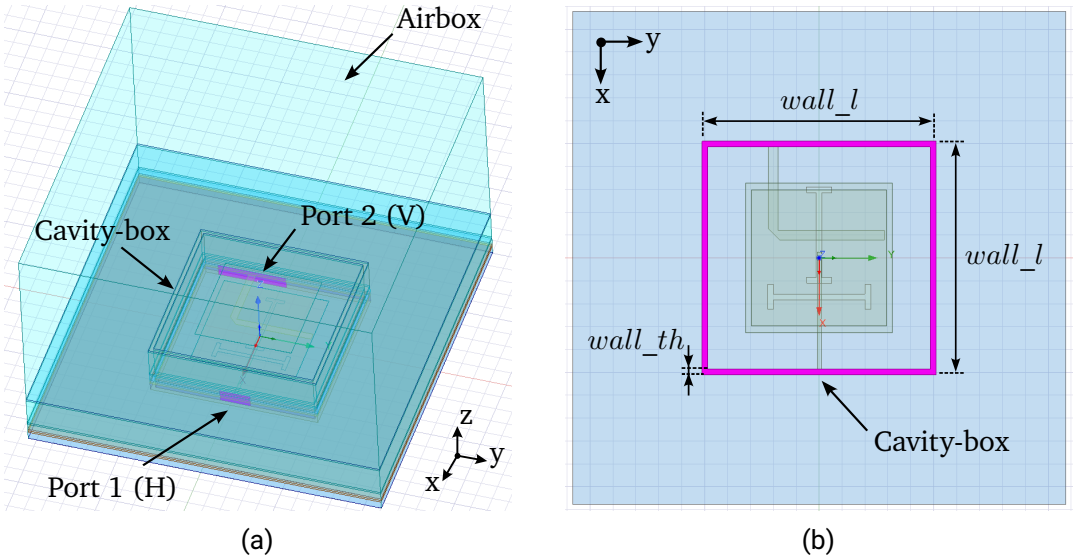

Figure 4.19.: (a) HFSS model of the cavity-box stacked patch antenna. (b) Top view.

$patch1\_l$	59.6	$slot1\_l$	40	$slot1\_w$	2.5	$slot2\_l$	37
$patch1\_w$	58.8	$slot2\_w$	2.5	$slot\_offset1$	17	$slot\_offset2$	10
$patch2\_l$	65.6	$line1\_l$	18.5	$line2\_l$	28.5	$line1\_w$	1.85
$patch2\_w$	63.8	$line2\_w$	4.15	$edge\_l$	11	$edge\_w$	2.5
$wall\_l$		102.1		$wall\_th$		2.5	

Table 4.9.: Antenna geometrical parameters (in mm).

4.4.1. Simulation results

The antenna single element, as well as the linear array, are simulated in HFSS and the results are presented as follows.

Antenna single element

The simulated return loss level and the radiation pattern of each polarization for a single cavity-box aperture coupled stacked patch antenna are shown in Figure 4.20 and 4.21, respectively. Simulation results show an optimized return loss better than 20 dB at the center frequency of operation, as well as a matching level higher than 10 dB within the operational bandwidth. The polarization isolation values are better than 30 dB for the

center frequency range. From the Smith Chart depicted in Figure 4.20b, it can be seen that the best matching is achieved for the center frequency of operation that corresponds to the center of the chart.

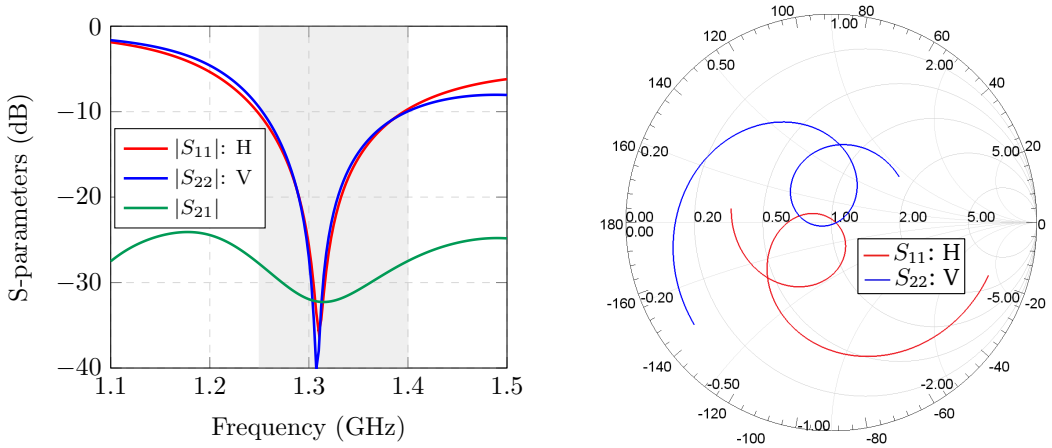

(a) (b)

Figure 4.20.: Simulated matching for the cavity-box aperture coupled stacked patch. (a) Reflection factor and polarization isolation levels. (b) Smith chart.

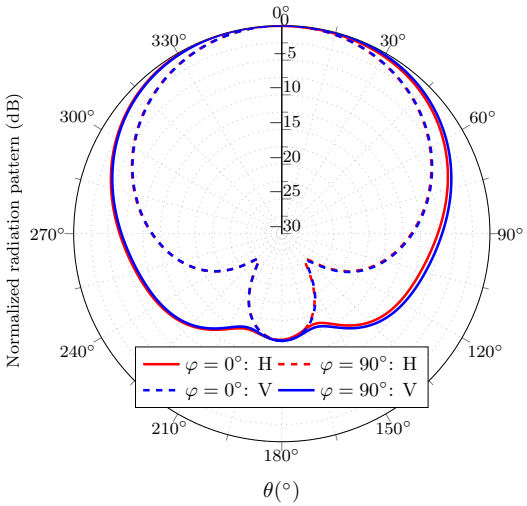

Figure 4.21.: Radiation pattern of the cavity-box aperture coupled stacked patch antenna.

The antenna gain is 5.44 dBi and 5.29 dBi for the horizontal and vertical polarization, respectively. The antenna efficiency is approximately 93% for both polarizations. From Figure 4.21 can be noted that the radiation pattern of both polarizations is complementary due to its orthogonality, with similar E-plane and H-plane patterns excepting a slight asymmetry in the E-plane of the horizontal polarization due to the slot offset.

Linear array

The isolation between two dual-polarized cavity-box aperture coupled stacked patch antennas spaced $d_a = 0.48\lambda_0$ is shown in Figure 4.22. It can be seen that the coupling for the vertical polarization is reduced 5 dB, achieving values of approximately -17 dB for the center frequency of operation. On the other side, the isolation between the horizontal polarizations is reduced, even though still acceptable isolation values better than 14 dB are obtained. This is explained due to the induced surface currents on the cavity walls structure. As it is depicted in Figure 4.23, for the horizontal polarization the currents are induced along the array axis, thus propagating with higher intensity to the other element. For the vertical polarization the magnitude of the induced current is concentrated on the orthogonal direction, perpendicular to the array axis.

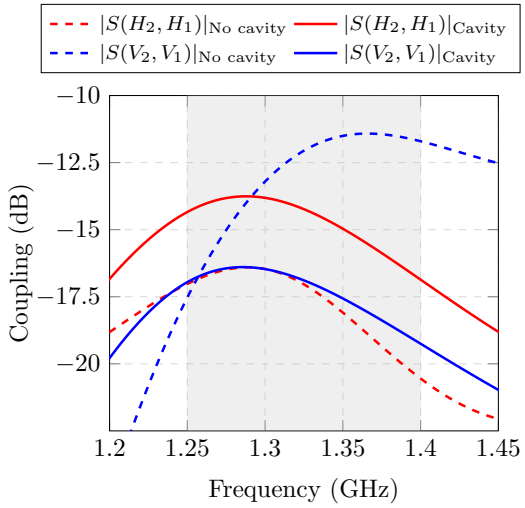

Figure 4.22.: Comparison between coupling w/o cavity structure.

A linear array of 5 elements along y-axis is simulated and the same amplitude and phase tapering given by Table 4.7 is applied. The spacing between array elements (i.e

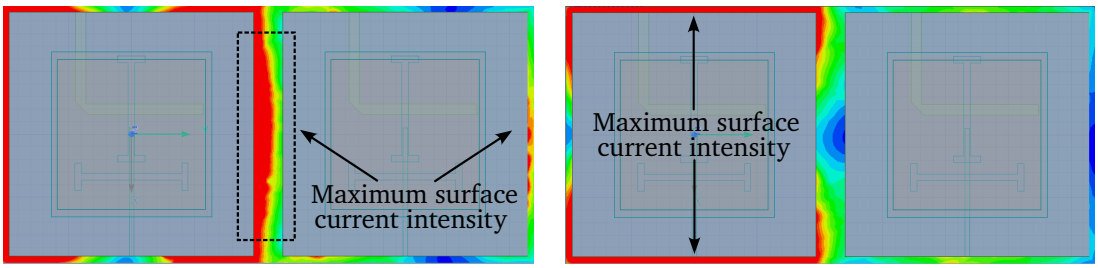

(a) (b)

Figure 4.23.: Magnitude of the induced currents on the surface walls along a two elements linear array. (a) Horizontal polarization. (b) Vertical polarization.

antenna walls) is filled with an intermediate aluminum plate that will be used to attach the different manufactured antenna elements in the constructed prototype. The simulated HFSS model is shown in Figure 4.24. The total antenna aperture length is $L_{\text{ap}} \approx 54$ cm.

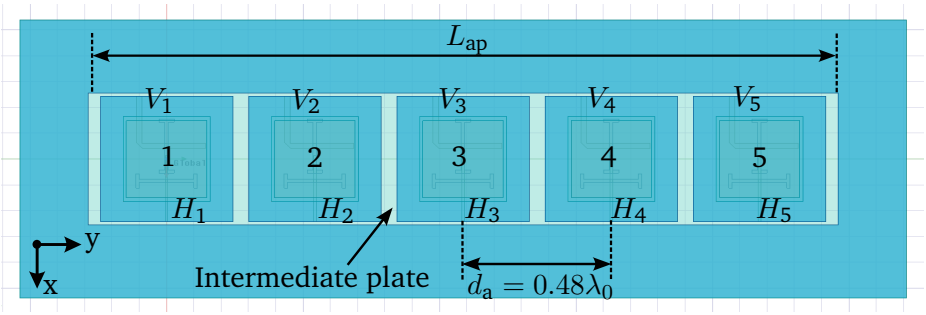

Figure 4.24.: Linear array of 5 cavity-box stacked patches along y-axis. HFSS model.

The simulated radiation patterns at YZ plane ($\varphi = 90°$) compared with the case without cavity, are shown in Figure 4.25.

The gain for the horizontal and vertical polarization is 10.5 dBi and 10.69 dBi, respectively. It can be noted that the pattern for the horizontal polarization remains similar to the previous case without cavity, despite that the coupling is slightly increased. The direction of maximum radiation coincides for both polarizations. On the other side, the side lobe level of the vertical polarization is slightly improved, as well as the radiation nulls are more defined. In addition, the beamwidth of the vertical polarization is wider than the horizontal case, as well as it yields a higher backlobe radiation. This is explained due to the asymmetric array geometry (YZ plane corresponds to the E-plane for the vertical

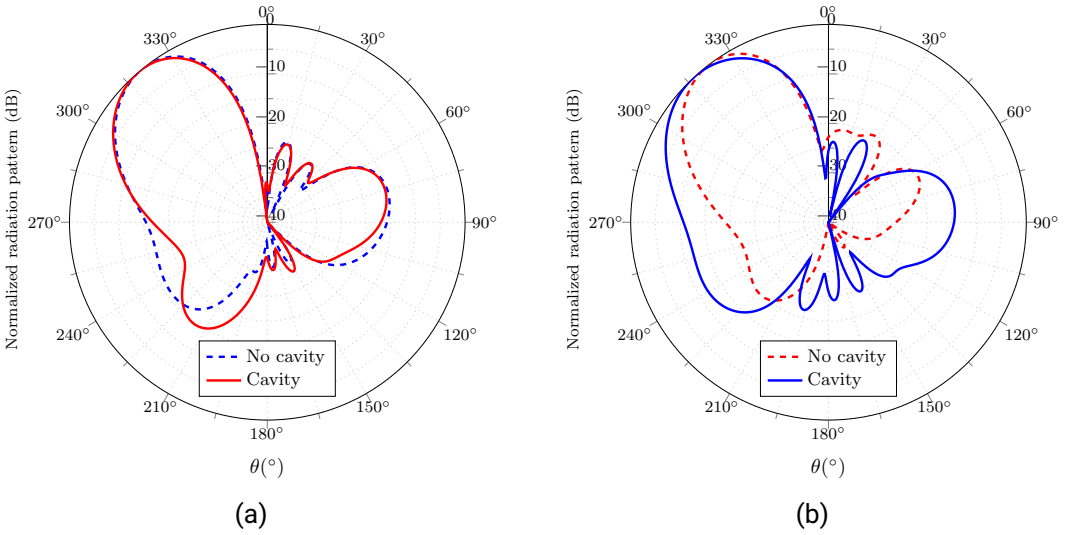

Figure 4.25.: Comparison radiation pattern in elevation w/o cavity structure. (a) Horizontal polarization. (b) Vertical polarization.

polarization and H-plane for the horizontal one), which also leads to a different interaction of the polarized fields with the antenna casing. Due the polarization orthogonality, building the array in the x-direction yields the same results but exchanging polarizations.

In practical scenarios, the array will be embedded in a housing structure or surrounded by a metallic surface, such as the antenna carrier or the aircraft. Thus, the interaction between the radiated fields and the cavity edges can be mitigated, since no electrical discontinuity is presented on the radiation plane. In addition, the metallic plate surrounding the antenna will also serve as an attachment structure on the CTR positioner for measurement purposes.

Figure 4.26 depicts the HFSS model of the linear array with an additional metallic plate of approximately λ_0 along x and y directions. The array is simulated considering the plate edges and using PML (Perfect Matched Layers) boundaries, that improve the absorption for far-field simulations in comparison to the standard radiation boundary at the expense of higher computational workload.

The simulation results are shown in Figure 4.27. The simulated gain for the horizontal polarization is slightly reduced to 10.1 dBi, while it is increased to 11 dBi for the vertical polarization. It can be noted the similarity between both patterns, not only regarding the main beam, but also concerning the side lobe levels that are higher than 20 dB, and the nadir suppression with values beyond 30 dB. Thus, it can be seen the excellent radiation

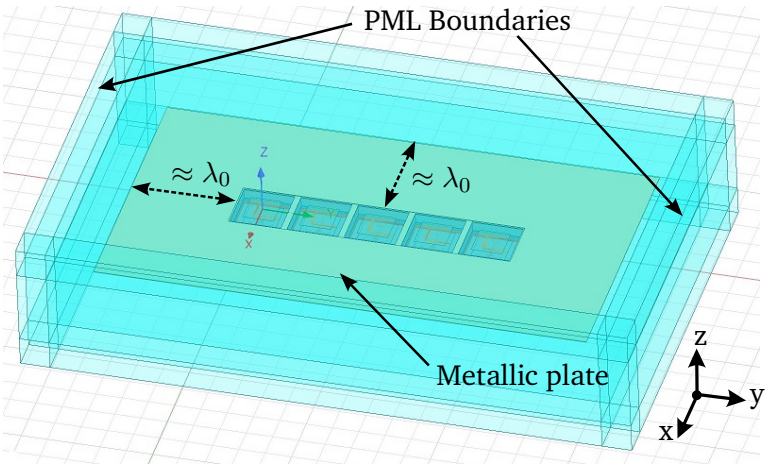

Figure 4.26.: HFSS model of the linear array with the metallic plate.

performance for both polarizations that fulfills the system specifications.

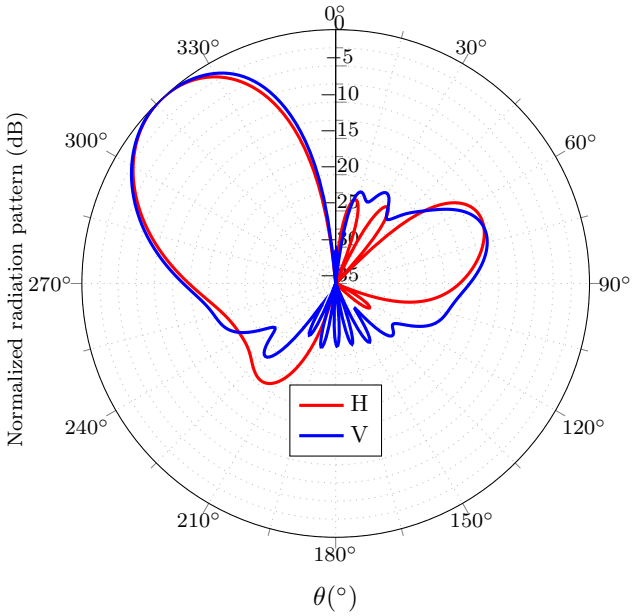

Figure 4.27.: Final radiation pattern in elevation for both polarizations.

4.4.2. Measurements of a manufactured prototype

The cavity-box aperture coupled stacked patch antenna is manufactured and measured. Since the sharp edges at the corners are demanding to manufacture, the cavity structure is constructed attaching four individual aluminum plates by means of holding blocks, as seen in Figure 4.28. In additon, these blocks allow the interconnection of different antenna elements using intermediate plates, so the linear array can be assembled.

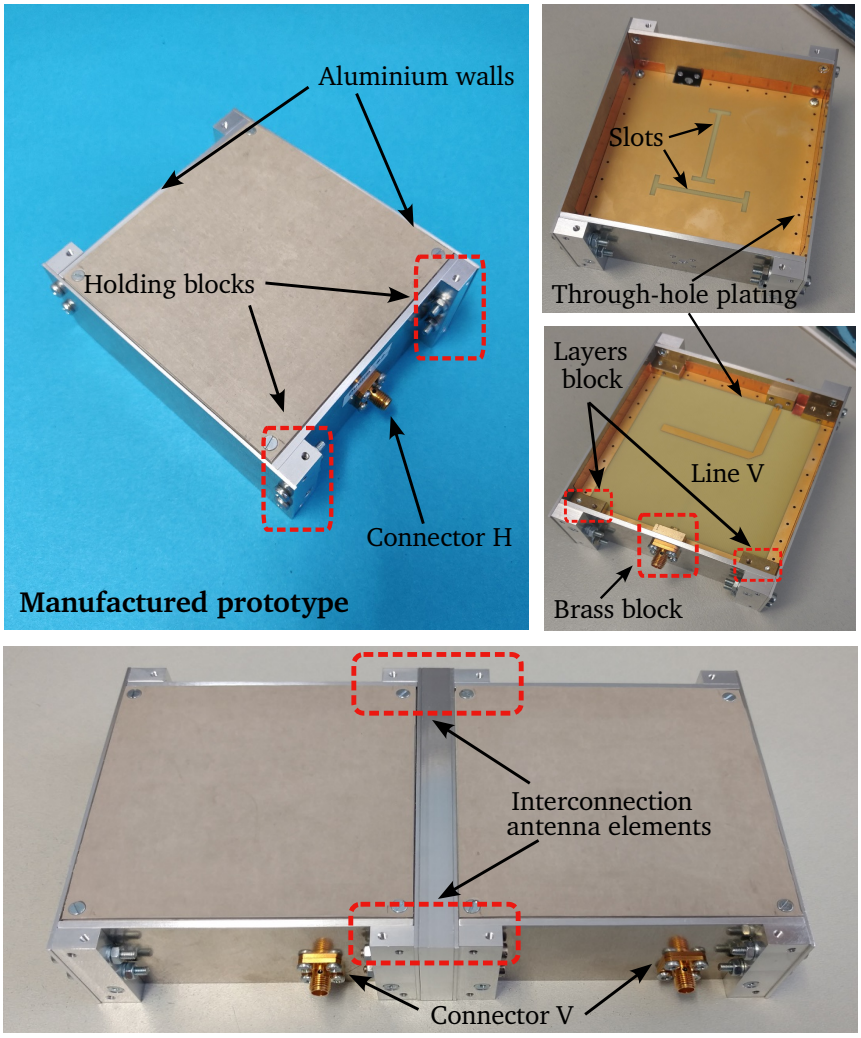

Figure 4.28.: Manufactured cavity-box aperture coupled stacked patch prototype.

The antenna feeding substrate layers are electrically connected to the ground plane by means of a copper frame using through-hole plating. The brass blocks serve as an attachment structure for the SMA connectors, and unlike aluminium, it can be soldered to the copper frame to assure proper ground connection. On the other side, the blocks placed on each corner allow to fix the different antenna layers by means of countersunk screws.

One of the most critical aspects of the antenna construction is to assure the electrical conductivity between the copper ground plane and the antenna aluminum walls. Due to construction and assembly tolerances, the presence of unavoidable air gaps or discontinuities prevent its electrical continuity. This issue had to be overcome adding copper tape soldered between both conductive surfaces, as shown in Figures 4.29a and Figures 4.29b.

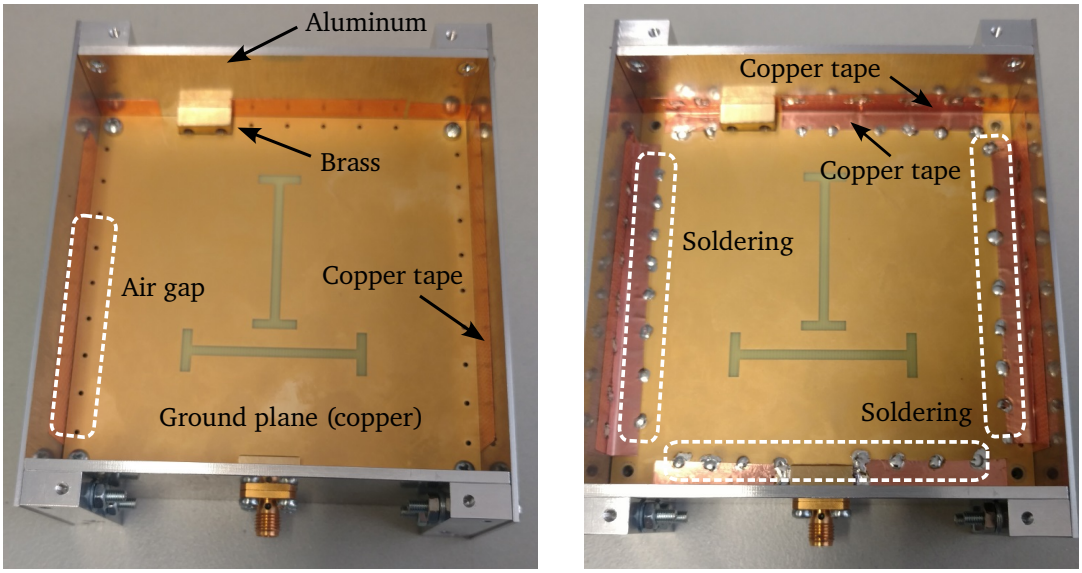

(a) (b)

Figure 4.29.: (a) Prototype construction process. (b) Additional soldering to assure electrical continuity.

The real antenna prototype is modeled and simulated in HFSS, as shown in Figure 4.30a. A comparison between the simulated and measured S-parameters of a single antenna element is depicted in Figure 4.30b. Despite that there is a slight shift to lower frequencies of the operational bandwidth, certainly due to fabrication and mechanical tolerances, it can be stated that the measurements meet very well the simulated results.

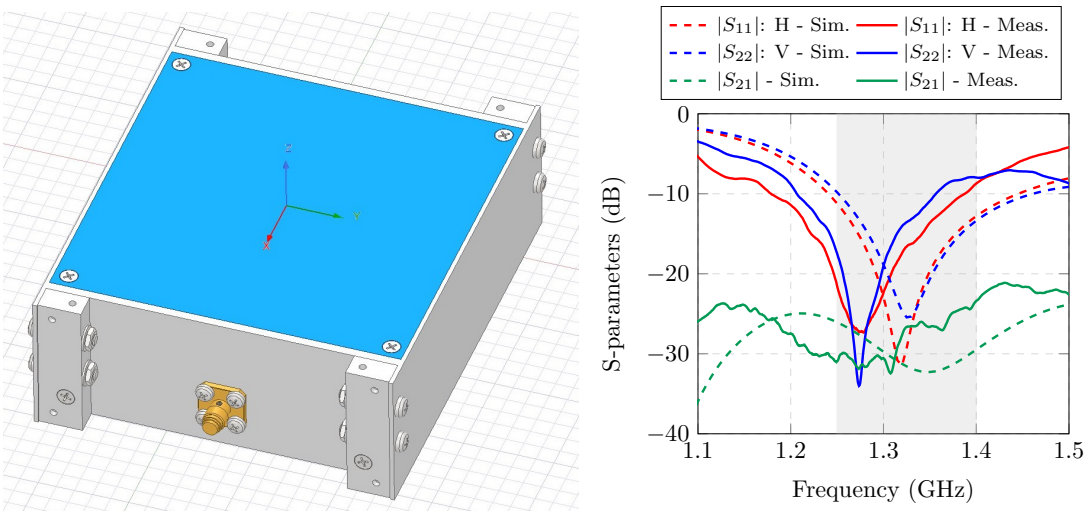

(a) (b)

Figure 4.30.: (a) HFSS model of the manufactured antenna prototype. (b) Comparison between simulated and measured S-parameters.

The radiation pattern of the prototype is also measured in the DLR's Compact Test Range. A metallic plate is used to ease the antenna attachment required for the measurement, as seen in Figure 4.31. The holding structure is 400 $\times$ 400 mm, and it is given by the position of the attachment points that allows its fixation to the CTR positioner. The measured radiation pattern for both polarizations, as well as a comparison with the simulated data, are shown in Figures 4.32a and 4.32b. As it can be seen, the measured patterns agree very well with the simulated data. The E-plane pattern for both polarizations is widened due to the use of the metallic plate. The measured gains are 6.1 dBi and 6 dBi for the horizontal and vertical polarization respectively, which differs approximately 0.3 dB from the simulated value.

Consequently, a linear array is built attaching five antenna elements by means of intermediate plates to assure the element spacing of $d_\mathrm{a} = 0.48\lambda_0$. As previously explained and for practical reasons, the array is surrounded by a metallic plate that also allows its mounting for measurement purposes.

Since each antenna element disposes of its own connector feeding for each polarization, the array feeding network is implemented as follows:

- The beam steering is applied using custom made cables with the proper electrical length, in order to fulfill the required phase difference at each antenna port.

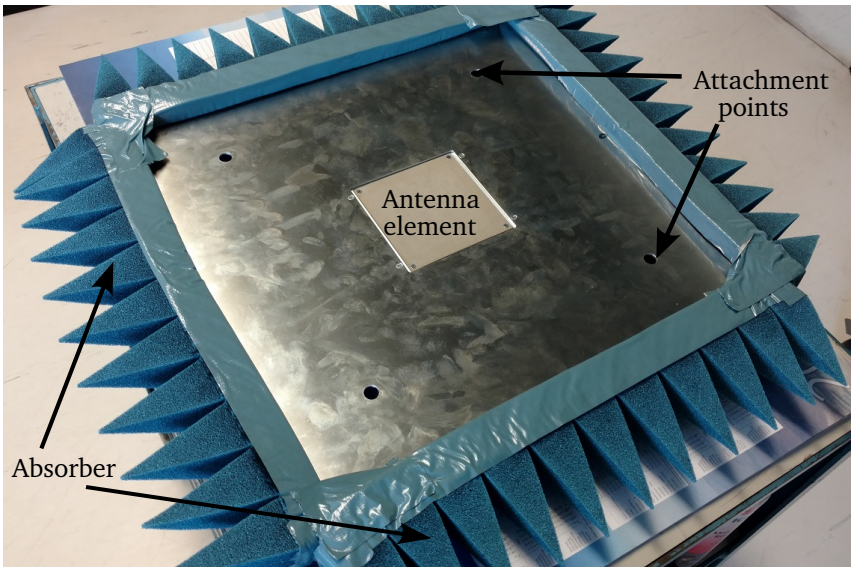

Figure 4.31.: Antenna prototype with metallic plate for measurement.

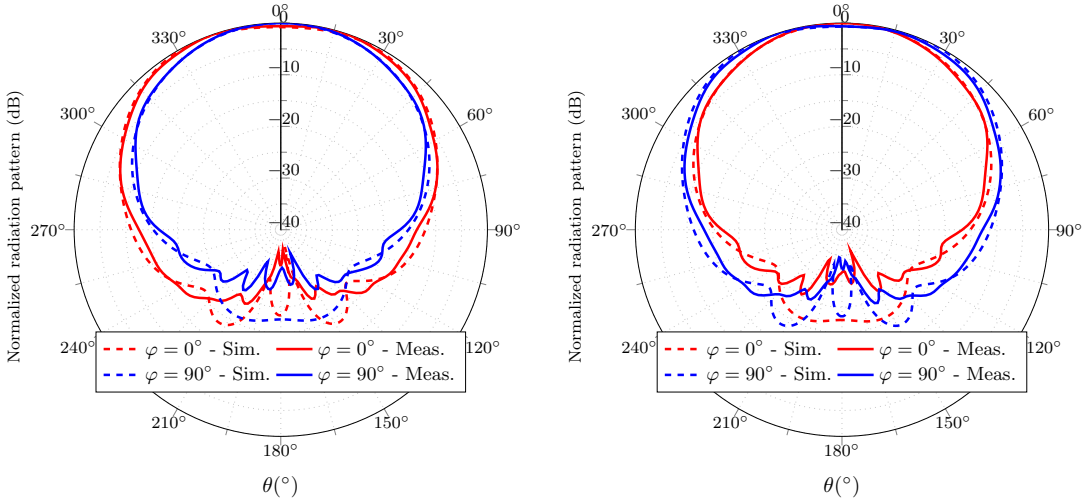

(a) (b)

Figure 4.32.: Measured radiation pattern of the antenna prototype and comparison with simulation. (a) Horizontal polarization. (b) Vertical polarization.

- The amplitude tapering is performed as follows: each polarization port is excited with a 1:6 power divider by which one of the five output ports is connected to each antenna element. Thus, each antenna is excited with approximately 1/6 of the input power. At the same time, the amplitude weighting is implemented providing intentional losses using 10 dB and 3 dB attenuators, that are directly connected to the corresponding antenna port. The block diagram of the feeding network and the real measurement setup are shown in Figures 4.33 and 4.34, respectively. The actual excitation power to each antenna element is listed in Table 4.10.

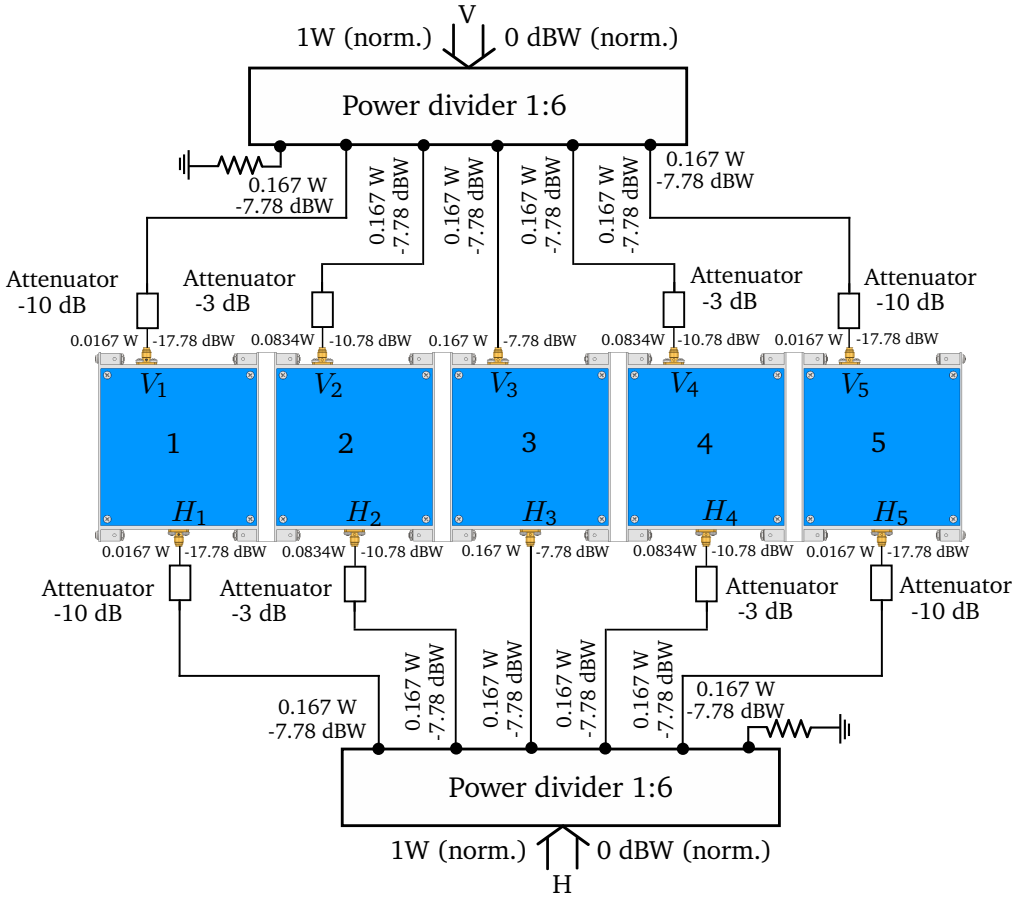

Figure 4.33.: Block diagram of the elevation feeding network.

Figure 4.35 shows the measured patterns along with the simulation results at the center frequency of operation 1.325 GHz. As it can be seen, the measurements agree well

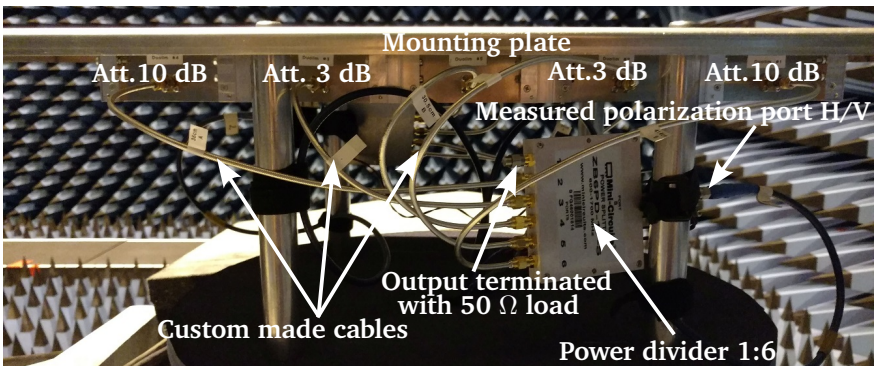

Figure 4.34.: Feeding network of the linear array.

Horizontal polarization			Vertical polarization		
H_1	Linear	Log	V_1	Linear	Log
	0.0167 W	-17.77 dBW		0.0167 W	-17.77 dBW
H_2	Linear	Log	V_2	Linear	Log
	0.0834 W	-10.78 dBW		0.0834 W	-10.78 dBW
H_3	Linear	Log	V_3	Linear	Log
	0.167 W	-7.77 dBW		0.167 W	-7.77 dBW
H_4	Linear	Log	V_4	Linear	Log
	0.0834 W	-10.78 dBW		0.0834 W	-10.78 dBW
H_5	Linear	Log	V_5	Linear	Log
	0.0167 W	-17.77 dBW		0.0167 W	-17.77 dBW

Table 4.10.: Normalized amplitude tapering.

with the simulated data. Due to the passive feeding network that forces the intentional losses to implement the amplitude tapering, the measured gain values are lower than the simulation. Thus, the antenna directivity becomes a more meaningful parameter to assess the radiation performance. The measured directivity is 12 dBi for both polarizations, which is slightly higher than the simulated values of 10.82 dBi and 11.71 dBi for the horizontal and vertical polarizations, respectively. This variation, especially in the case of the horizontal one, can be explained due to the slight frequency shift of the antenna performance as depicted in Figure 4.30, the unavoidable differences in each element construction, as well as some small innacuracies in the measurement setup. The measured pattern at the center and limit frequencies is depicted in Figure 4.36. It can be noted the good frequency stability of the radiation pattern within the operational bandwidth.

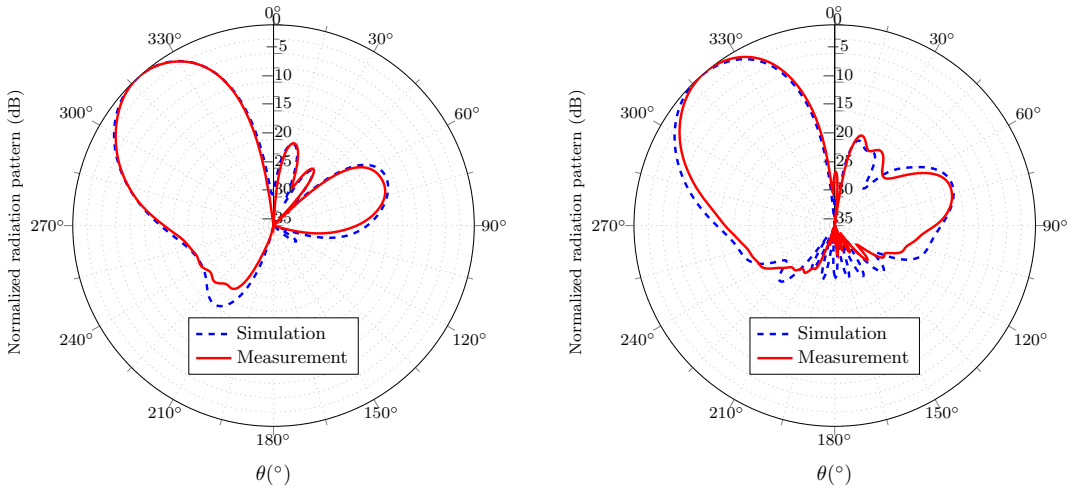

Figure 4.35.: Measured radiation pattern of the linear array and comparison with simulation. (a) Horizontal polarization. (b) Vertical polarization.

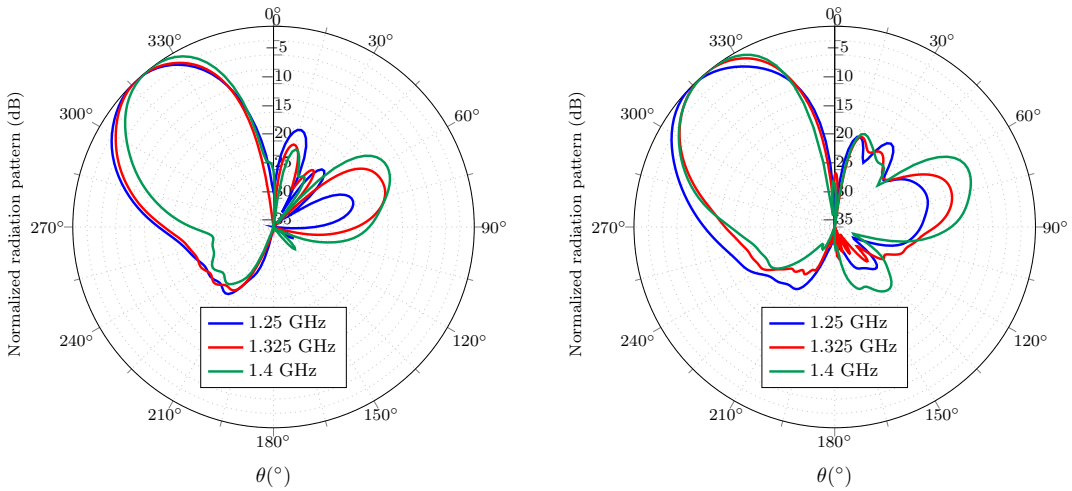

Figure 4.36.: Comparison measured radiation pattern at 1.25 GHz, 1.325 GHz and 1.4 GHz. (a) Horizontal polarization. (b) Vertical polarization.

4.5. Cross-polarization suppression improvement by means of sequential 90° rotation of dual-polarized antenna elements

As mentioned in Appendix B, electromagnetic waves can not be generated purely polarized. Besides the main polarization or co-polarization to be intended to radiate or receive, there is always an additional undesired contribution of the orthogonal polarization, also known as cross-polarization.

Since SAR polarimetry applications make use of the polarization diversity in order to exploit the information of the scattered signals, the cross-polarization suppression of the antenna determines an important parameter of the system performance, and its reduction becomes a relevant design aspect.

Some previous research has been made, and different techniques have been proposed in order to reduce the cross-polarization level. An extended approach is splitting a planar array into subarrays of 2×2 elements according to a rotation pattern based on the image theory arrangement, which also minimizes the side lobe level [34]. This method has been widely used in a broad range of applications [35, 36, 90]. A further analysis extends this approach by considering the inter-element coupling [91]. Some other techniques improve the cross-polarization level by rotating the antenna elements in reflectarray applications [92], or combining the 180° rotation of the antenna structure along with a 180° alternate feeding based on the overlapping of different multipolar moments [93]. Further rotation topologies, such as the sequential rotation, is typically used for arrays of circular polarized antennas, as it leads to an improvement of the axial ratio bandwidth or the polarization purity [94–98]. Generally, the majority of cross-polarization suppression techniques start from the decomposition of planar arrays into subarrays, and a very few applications consider linear arrays. In [99], a 90° sequential rotation technique is implemented in a circularly polarized linear array of circular patches. Later, this analysis is extended by considering the scanning properties of linear phased arrays [100]. However, this approach is simplified as the radiation effect of higher order modes is neglected, and no real geometrical 90° sequential rotation is applied.

In this section, a novel approach to reduce the cross-polarization level in linear phased array applications, based on the sequential 90° rotation of dual-polarized antenna elements, is presented.

4.5.1. Analysis considerations

The proposed cross-polarization suppression rotation technique is demonstrated using the manufactured cavity-box aperture coupling stacked patch antennas. The enhanced

array element isolation allows to properly adjust the amplitude and phase of each antenna element, that becomes an essential requirement for the analysis.

Thus, three different linear array configurations of five elements are built and measured. Each geometrical arrangement corresponds to a different rotation topology of the antenna elements: non-rotation or normal, sequential rotation of 180° and 90°. An accurate analysis of the cross-polarization performance of the array leads to consider scenarios with antenna beam steering. Therefore, the validation of the proposed cross-polarization suppression method covers two scenarios for each configuration: broadside radiation with equal amplitude and phase distribution (uniform) and beam steering with amplitude tapering.

In addition, the following design aspects are considered:

- The spacing between the antenna elements is set to be $0.6\lambda_0$, unlike the previous section. This is chosen for mechanical reasons, since the geometrical 90° rotation of the antenna elements limits the access to the connectors.
- The linear array is built along the y-axis, as in previous examples.
- The antenna feeding ports ($H_1 - H_5$, $V_1 - V_5$) correspond to the antenna element numeration (1-5), starting from the left, as shown in Figure 4.37.
- In the beamforming case and for simplicity, the same amplitude and phase distribution is applied as shown in Table 4.7. However, given that a larger interelement spacing is used, the resulting radiation pattern is not optimized for a determined application. This is taken for granted, since the proposed analysis serves as a proof-of-concept.
- The phase control of each antenna element is adjusted with custom manufactured cables of the corresponding electrical length. All the cables dispose of comparable lengths, in order to assure a similar phase variation within the desired frequency range.
- The amplitude distribution for each polarization is implemented by means of 1:6 power dividers along with 3 dB and 10 dB attenuators, as depicted in Figure 4.33.
- All the measurements are carried out with a rectangular aluminum plate (50.1 $\times$ 104.2 cm) that is attached to the linear array. As in previous measurements, this allows the fixation of the structure under test on top of the CTR positioner tower.
- The simulated and measured results are presented for the center frequency of operation 1.325 GHz. Since the interest is on the cross-polarization suppression

values (relative to the absolute gain or directivity in maximum direction of radiation), the normalized radiation patterns are shown. In addition, only the patterns on the array axis (plane YZ, $\varphi = 90°$) is represented. Due to the low cross-polarization levels and to ease the interpretation of the results, a rectangular cartesian plot is used, instead of a polar representation.

4.5.2. Non-rotation array

The non-rotation array corresponds to the standard case of the linear array arrangement with all the antenna elements identically aligned, as shown in Figure 4.37. Each antenna is interconnected by means of aluminum blocks, in order to provide an interelement spacing of $0.6\lambda_0$. The connectors that feed each polarization (H_i,V_i) are placed along the same side of the array.

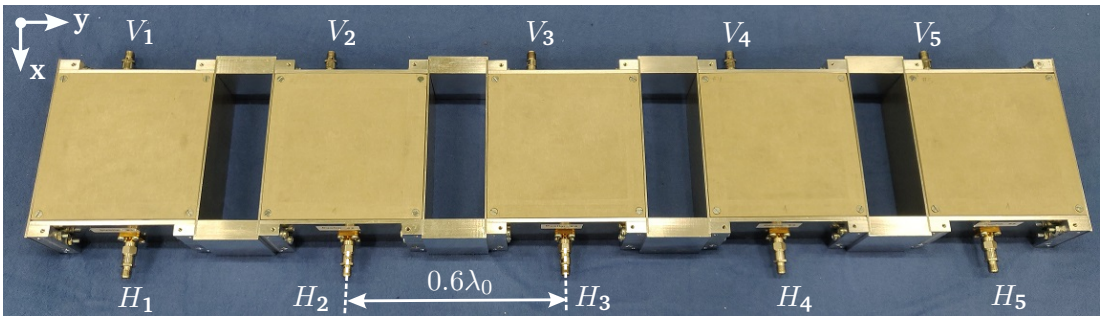

Figure 4.37.: Normal array arrangement.

This standard configuration, that has been used in the previous section, is identified as a normal array, and it is considered as a reference case for later comparisons.

Uniform amplitude and phase distribution

For the uniform case, the same amplitude and phase is applied to each antenna element. The measured co-polar and cross-polar patterns, and a comparison with the simulation results are shown in Figure 4.38. The measured cross-polarization suppression values, 23 dB and 28 dB for the horizontal and vertical polarization, respectively, are lower than the simulated data. This difference can be certainly due to different reasons, especially the accuracy of the measurement, since the low cross-polarization level values lead to a extremely sensitive measurement, by which any small variation is shown as a difference of several dBs. Other aspects such as the fabrication and manufacturing tolerances should

also be considered. On the other hand, it can be also seen a slight asymmetry in the measured co-polar patterns regarding the side lobe levels, especially in the case of the vertical polarization, unlike the simulated data. This can be explained due to some small inaccuracy in the amplitude tapering, caused by the implementation of the feeding network, along with the inevitable difference among the construction of each antenna elements. Nevertheless, it can be seen that the measured patterns meet the expected results very well.

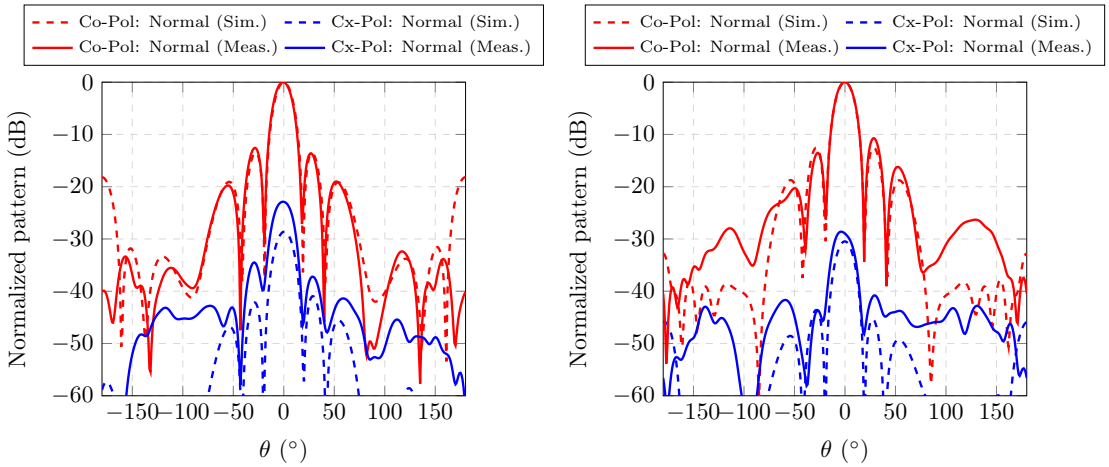

Figure 4.38.: Comparison simulation and measurement of the standard array arrangement. Uniform amplitude and phase distribution. (a) Horizontal polarization. (b) Vertical polarization.

Beam steering

In this case, the same amplitude and phase distribution as in previous examples, and shown in Table 4.7, is applied. The measured patterns are shown in Figure 4.39. As already mentioned, the radiation pattern is not optimized to fulfill any requirement, but it serves as a proof-of-concept for the given analysis. The measured cross-polarization level is also slightly higher than the predicted values. The measured cross-polar suppression at the antenna main beam for the horizontal and vertical polarization is 23 dB and 26 dB, respectively.

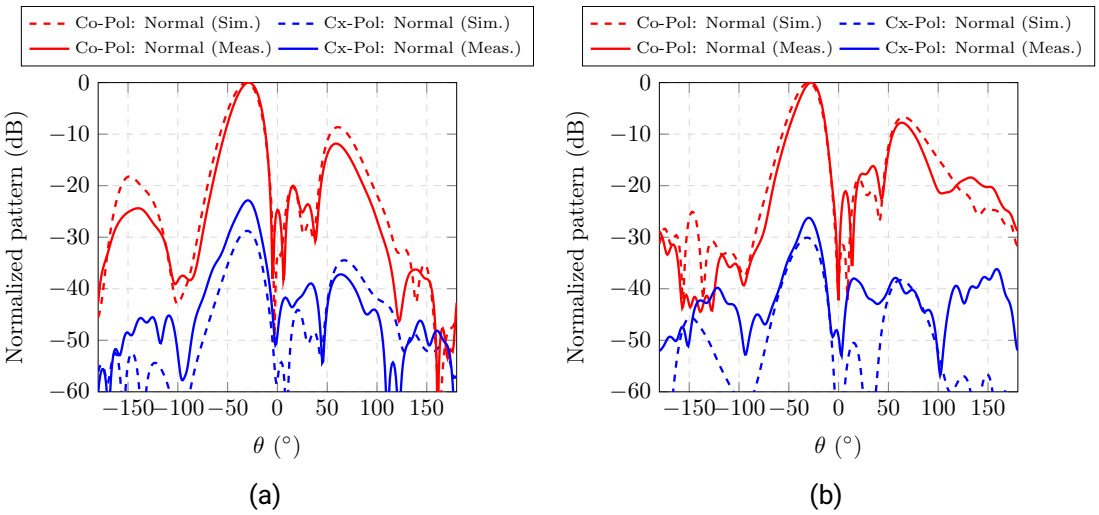

Figure 4.39.: Comparison simulation and measurement of the standard array arrangement. Beam steering (a) Horizontal polarization. (b) Vertical polarization.

4.5.3. Sequential 180° rotation of the antenna elements

In this configuration, a 180° sequential rotation of the array elements that involves the rotation of antennas 2 and 4 is performed, as it can be seen in Figure 4.40a. This approach requires the 180° out-of-phase feeding of the rotated elements. This feeding arrangement can lead to a suppression of the cross-polarized fields due to the phase inversion, while maintaining the same co-polarization pattern [36]. It can be noted in Figure 4.40b, that despite the 180° rotation of the array elements 2 and 4, the same geometrical slots as the previous configuration are involved in order to excite each polarization.

Uniform amplitude and phase distribution

Thus, considering the out-of-phase excitation of antennas 2 and 4, the amplitude and phase coefficients for each array element of the uniform case are listed in Table 4.11. In order to provide the inversion feeding to the rotated antennas, these elements are fed by means of cables with a longer extension of half the corresponding guided wavelength.

A comparison of this configuration with the normal array in terms of co-polar and cross-polar patterns is shown in Figure 4.41. The measured co-polar patterns of the array with the 180° rotation are really similar to the measured patterns of the normal array. The measured cross-polarization, especially for the horizontal polarization, is higher than

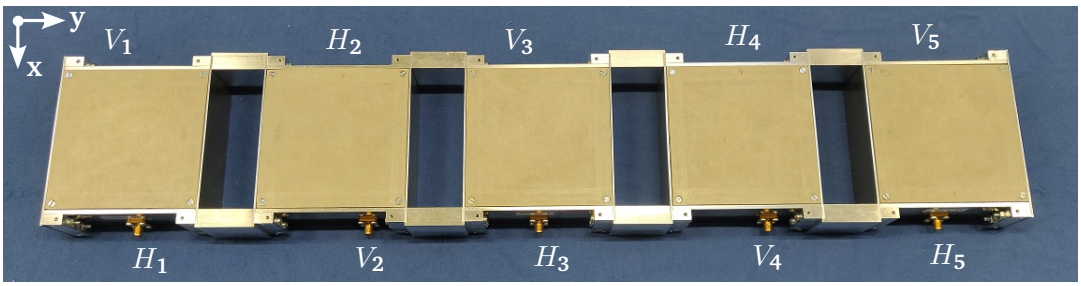

(a)

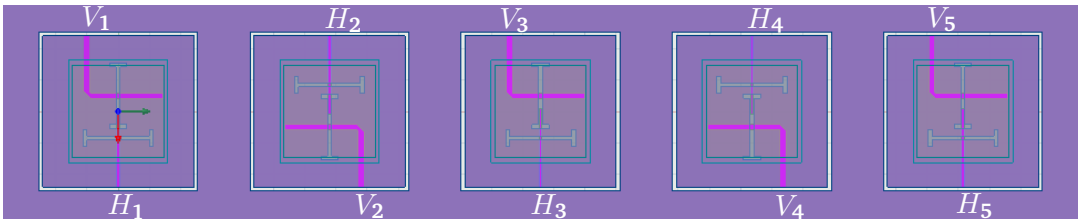

(b)

Figure 4.40.: (a) Geometrical arrangement of the linear array with sequential 180° rotation of the antenna elements. (b) HFSS model.

Horizontal polarization			**Vertical polarization**		
H_1	A_1	φ_1	V_1	A_1	φ_1
	0 dBW	0°		0 dBW	0°
H_2	A_2	φ_2	V_2	A_2	φ_2
	0 dBW	180°		0 dBW	180°
H_3	A_3	φ_3	V_3	H_3	φ_3
	0 dBW	0°		0 dBW	0°
H_4	A_4	φ_4	V_4	A_4	φ_4
	0 dBW	180°		0 dBW	180°
H_5	A_5	φ_5	V_5	A_5	φ_5
	0 dBW	0°		0 dBW	0°

Table 4.11.: Sequential 180° rotation of antenna elements. Amplitude and phase coefficients. Uniform amplitude und phase distribution.

the simulated value. The overall cross-polarization performance of this configuration is comparable to the normal array, but it presents a higher sidelobe level. The cross-polarization suppression for both configurations is similar.

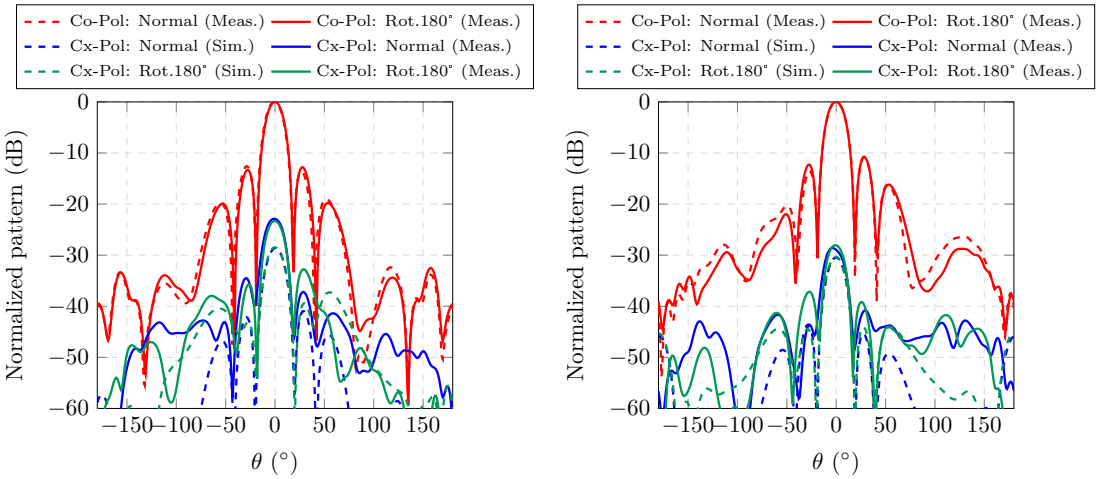

Figure 4.41.: Comparison simulation and measurement of the 180° rotation array. Uniform amplitude and phase distribution. (a) Horizontal polarization.(b) Vertical polarization.

Beam steering

The same amplitude and phase tapering as in the previous configuration is applied, but considering the inversion phase feeding of elements 2 and 4, as in the case of the uniform amplitude und phase distribution. The measured results compared with the configuration of the standard array arrangement are shown in Figure 4.42. The measurements of the co-polar patterns for both polarizations agree very well with the simulation results. The measured cross-polarization values are again comparable for both configurations, with a slight deterioration besides the main beam when the elements are rotated 180°, leading to an increase of the sidelobe level. As occured in the case of the normal array, the measured cross-polarization levels are higher than the simulated values. This difference is again more visible for the horizontal polarization.

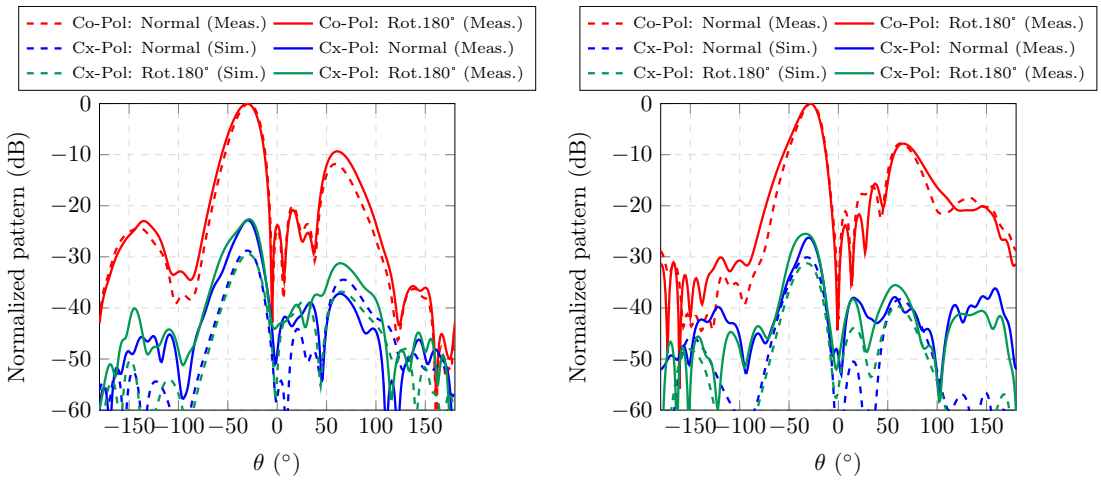

Figure 4.42.: Comparison simulation and measurement of the 180° rotation array. Beam steering. (a) Horizontal polarization. (b) Vertical polarization.

4.5.4. Sequential 90° rotation of the antenna elements

In this third configuration, a sequential 90° rotation approach of the array elements is performed. This leads to an element rotation topology where the antenna elements 2, 3 and 4 are respectively 90°, 180° and 270° rotated, while the elements 1 and 5 remain in the same position. The geometrical arrangement of the array is depicted in Figure 4.43a.

The geometrical 90° rotation involves an exchange of the polarization excitation of the antenna elements 2 and 4, since it leads to a slot rotation. This polarization swapping causes that each polarization is excited by array elements with different slot arrangements. Since each slot is fed by a microstrip line placed on a different substrate height, the electrical length of each feeding line is unequal, and thus each polarization is excited with a different phase. This electrical length unbalancement can be compensated by adding an additional phase shift.

The length of the microstrip line that feeds each slot (measured from the wave port to the slot center) is l_{H}=31.55 mm and l_{V}=60.72 mm for the horizontal and vertical polarization, respectively, as depicted in Figure 4.43b. It can be noted that for the vertical polarization the length is greater due to the bending line. It should be noticed that the guided wavelength of each feeding line, $\lambda_{\mathrm{g}}^{\mathrm{H}}$ $\lambda_{\mathrm{g}}^{\mathrm{V}}$, is different due to the position of the microstrip line on the feeding substrate, as already depicted in Figure 4.9. The computed

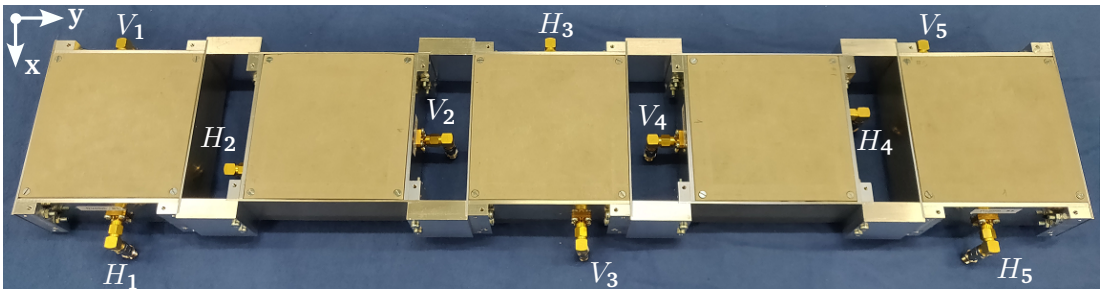

(a)

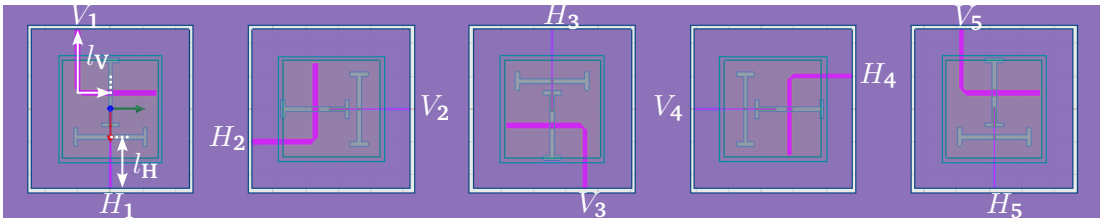

(b)

Figure 4.43.: (a) Geometrical arrangement of the linear array with sequential 90° rotation of the antenna elements. (b) HFSS model.

wavelength values in HFSS are λ_g^H=113 mm and λ_g^V=128 mm. Thus, each polarization is excited with a distinct electrical length that yields a feeding phase of:

$$\begin{aligned} \varphi_H &= \left(\frac{l_H}{\lambda_g^H}\right) 360^\circ = 100.5^\circ \\ \varphi_V &= \left(\frac{l_V}{\lambda_g^V}\right) 360^\circ = 170.77^\circ \end{aligned} \tag{4.7}$$

by which a feeding phase variation of $\Delta\varphi$ has to be applied:

$$\Delta\varphi = \varphi_V - \varphi_H \approx 70^\circ \tag{4.8}$$

Thus, this unbalancement between the electrical lengths of the two microstrip lines can be compensated by considering a phase variation in the feeding, so all the antenna elements are excited in phase regardless the position of the microstrip line used.

Uniform amplitude and phase distribution

Thus, the phase distribution applied to each antenna element for the uniform case is listed in Table 4.12. It can be noted that the feeding phase also depends on the orientation of the microstrip lines, by which the out-of-phase lines have to be compensated adding 180°.

Horizontal polarization			**Vertical polarization**		
H_1	A_1	φ_1	V_1	A_1	φ_1
	0 dBW	0°		0 dBW	0°
H_2	A_2	φ_2	V_2	A_2	φ_2
	0 dBW	70°		0 dBW	110°
H_3	A_3	φ_3	V_3	H_3	φ_3
	0 dBW	180°		0 dBW	180°
H_4	A_4	φ_4	V_4	A_4	φ_4
	0 dBW	250°		0 dBW	-70°
H_5	A_5	φ_5	V_5	A_5	φ_5
	0 dBW	0°		0 dBW	0°

Table 4.12.: 90° rotation. Amplitude and phase coefficients. Uniform.

The normal array and the array with the sequential 90° rotation of the antenna elements, when applying uniform amplitude and phase, are compared in Figure 4.44.

It can be noted that both configurations provide the same co-polar pattern with broadside radiation, with slight differences regarding the side lobe level of the vertical polarization. The measured cross-polarization is again higher than the simulation, as it is experienced in the previous measurements. However, it can be seen that the cross-polarization performance of the array with the sequential 90° rotation is considerably enhanced within the main beam, with the penalty of increasing it in the ranges $\theta \pm 50°$ but far beyond the antenna main beam. The measured improvement at $\theta = 0°$ is almost 10 dB and 8 dB for the horizontal and vertical polarization, respectively, thus achieving a measured cross-polarization suppression values of 32 dB and 36 dB, which still remain below the previous simulated values. This slight difference can be expected, since the measured range of the cross-polarization values are relatively low in the logarithmic scale, leading to an extremely sensitive measurement. It has to be also considered that the antenna elements are not exactly identically constructed, due to fabrication tolerances and manufacturing processes. It can be also seen that the measured cross-polarization patterns agree with the predicted simulation data.

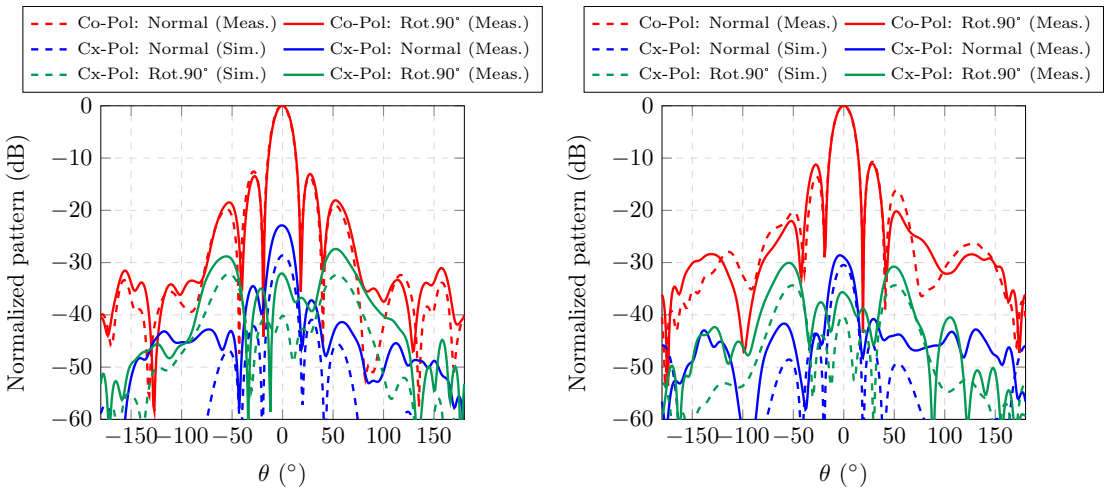

Figure 4.44.: Comparison simulation and measurement of the 90° rotation array. Uniform amplitude and phase distribution (a) Horizontal polarization. (b) Vertical polarization.

A comparison in terms of cross-polarization suppression values of the normal array and the sequential 90° rotation of the antenna elements is shown in Table 4.13. An additional polar representation of the cross-polarization suppression values as a function of θ and φ for the horizontal polarization is depicted in Figure 4.45. It can be seen that with the sequential 90° rotation, a great improvement of the cross-polar suppression within the antenna main beam is achieved.

Horizontal polarization			**Vertical polarization**		
Normal Array	Sim.	Meas.	**Normal Array**	Sim.	Meas.
	28.6 dB	22.87 dB		30.46 dB	28.1 dB
Rotation 90°	Sim.	Meas.	**Rotation 90°**	Sim.	Meas.
	40.17 dB	32.15 dB		40.28 dB	35.72 dB

Table 4.13.: Comparison of cross-polarization suppression values between normal array and sequential 90° rotation of antenna elements. Uniform amplitude und phase distribution.

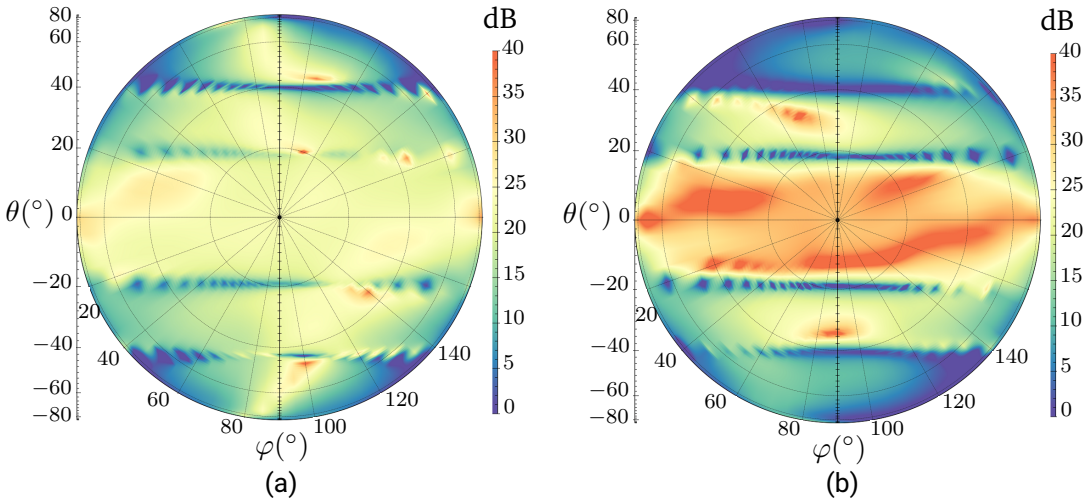

Figure 4.45.: Measured cross-polar suppression values. Horizontal polarization. (a) Normal array. (b) Rotation 90°.

Beam steering

The applied amplitude and phase distribution, considering the sequential 90° rotation of the antenna elements and for the beamforming case, is shown in Table 4.14.

Horizontal polarization			**Vertical polarization**		
H_1	A_1	φ_1	V_1	A_1	φ_1
	-10 dBW	0°		-10 dBW	0°
H_2	A_2	φ_2	V_2	A_2	φ_2
	-3 dBW	70°+120°		-3 dBW	110°+120°
H_3	A_3	φ_3	V_3	H_3	φ_3
	0 dBW	180°+240°		0 dBW	180°+240°
H_4	A_4	φ_4	V_4	A_4	φ_4
	-3 dBW	250°		-3 dBW	-70°
H_5	A_5	φ_5	V_5	A_5	φ_5
	-10 dBW	0°+120°		-10 dBW	0°+120°

Table 4.14.: 90° rotation. Normalized amplitude and phase coefficients. Beam steering.

The performance of this configuration is compared with the normal array in Figure 4.46

when beamforming is applied. Both array configurations provide a similar co-polar patterns, as expected. Despite the fact that the measured cross-polar levels for the horizontal polarization at the antenna main beam direction $\theta = 30°$ is higher than the simulated value, it remains 10 dB below the measured value for the normal array. The measurement of the vertical polarization shows an improvement of almost 14 dB in comparison with the normal array, achieving a cross-polarization suppression of 40 dB. The sequential 90° rotation of the antenna elements also provides a shift of the cross-polarization maximum beyond the antenna main beam. The overall measured cross-polar patterns meet the simulated data, which demonstrates the improvement of the cross-polarization performance by means of the presented 90° rotation approach.

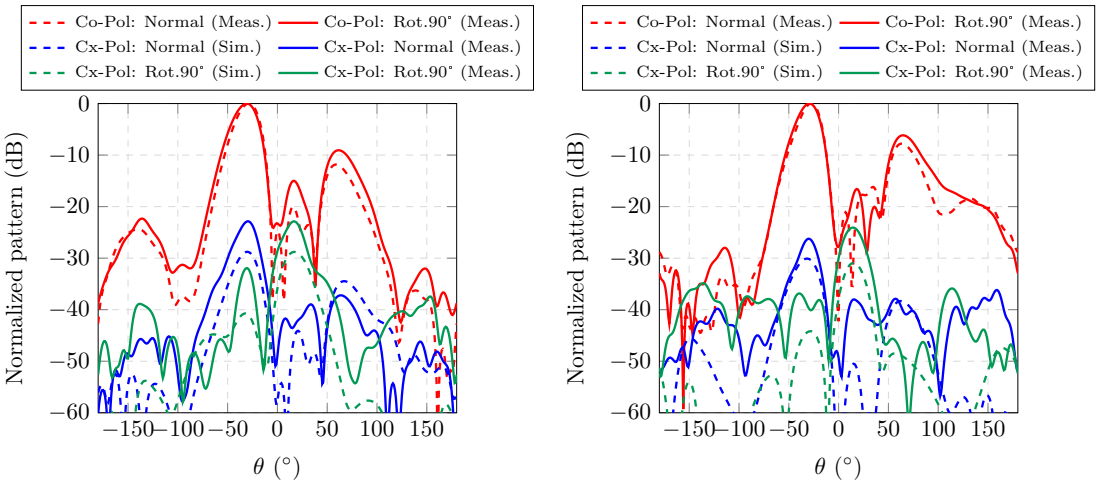

Figure 4.46.: Comparison simulation and measurement of the 90° rotation array. Beam steering. (a) Horizontal polarization. (b) Vertical polarization.

An overview in terms of the cross-polarization suppression values of this configuration and the normal array, when applying beamforming, is shown in Table 4.15 and Figure 4.47. The polar plot provides an additional angular representation, where the improvement achieved in the antenna main beam direction is clearly seen, especially over the direction $\varphi = 90°$. A more symmetric cross-polarization pattern is also achieved in the angular range $\theta < 0°$, with a deterioration for values $\theta > 0°$, far beyond the direction of the main radiation.

Horizontal polarization			Vertical polarization		
Normal Array	Sim.	Meas.	**Normal Array**	Sim.	Meas.
	28.75 dB	22.82 dB		30.14 dB	26.03 dB
Rotation 90°	Sim.	Meas.	**Rotation 90°**	Sim.	Meas.
	40.85 dB	31.95 dB		44.23 dB	39.71 dB

Table 4.15.: Comparison cross-polarization suppression values between normal array and sequential 90° rotation of antenna elements. Beam steering.

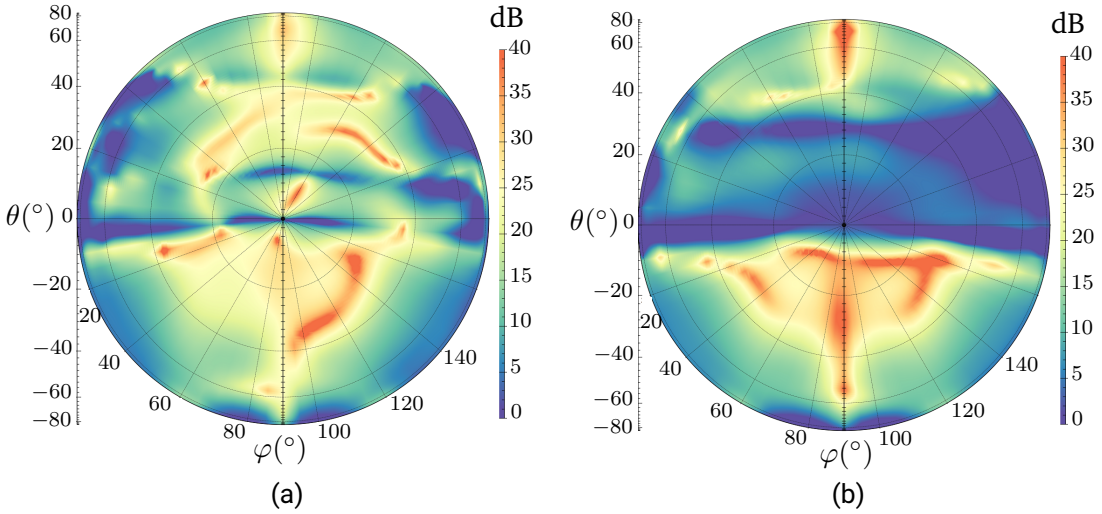

Figure 4.47.: Measured cross-polar suppression values. Vertical polarization. (a) Normal array. (b) Rotation 90°.

4.5.5. Sequential 90° rotation of the antenna elements in planar arrays applications

In this section, the sequential 90° rotation approach is extended and applied along both axis of a planar array of 5 × 5 antenna elements. The same analysis is performed in HFSS, comparing the standard array arrangemement and the sequential 90° rotation using the cavity-box aperture coupled stacked patch antennas. In this case, all the array elements are excited with the same amplitude and phase (uniform amplitude and phase distribution). The simulated HFSS model is shown in Figure 4.48.

The simulated results for both polarizations, and a comparison between both geometrical

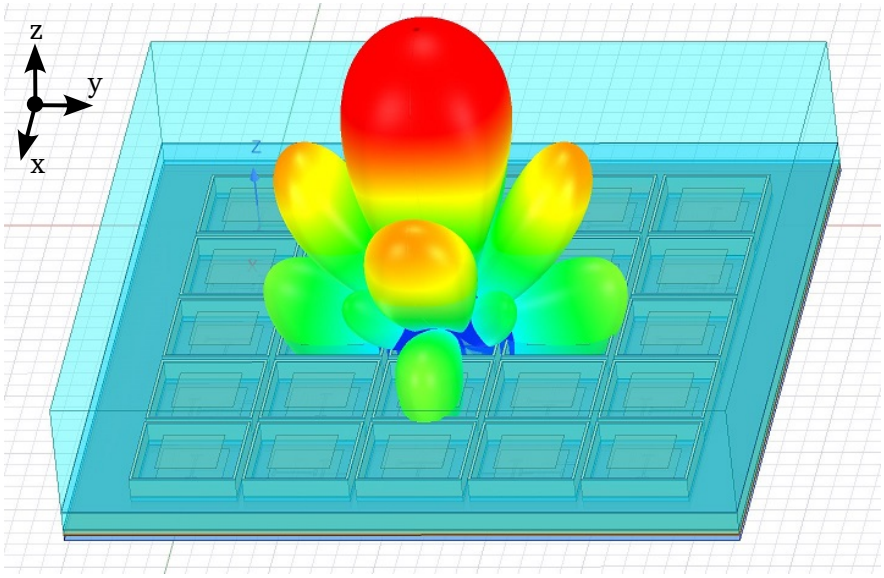

Figure 4.48.: HFSS model of the planar array 5×5 with sequential 90° rotated antenna elements along x- and y-axis. 3D radiation pattern with uniform amplitude and phase.

array arrangements in the planes XZ ($\varphi = 0°$) and YZ ($\varphi = 90°$), are shown in Figures 4.49 and 4.50. The co-polar patterns of both configurations coincide very well, unlike the cross-polarization levels of the the array with the rotated elements, that are considerably lower. It can be seen that for the horizontal polarization, cross-polarization suppression values beyond 50 dB are achieved, which yield an improvement of up to 24 dB in comparison with the standard array arrangement. For the vertical polarization, cross-polarization suppression enhancements of approximately 20 dB are obtained. Thus, the proposed cross-polarization suppression method is proved to be a very effective method to reduce the antenna cross-polarization levels in planar arrays applications.

Table 4.16 shows a comparison of the proposed cross-polarization suppresion method with other previously cited works. It can be noted the low cross-polarization values obtained with the proposed sequential 90° rotation. The presented method is also extended to 5×5 elements in order to have a fairer comparison with other planar arrays.

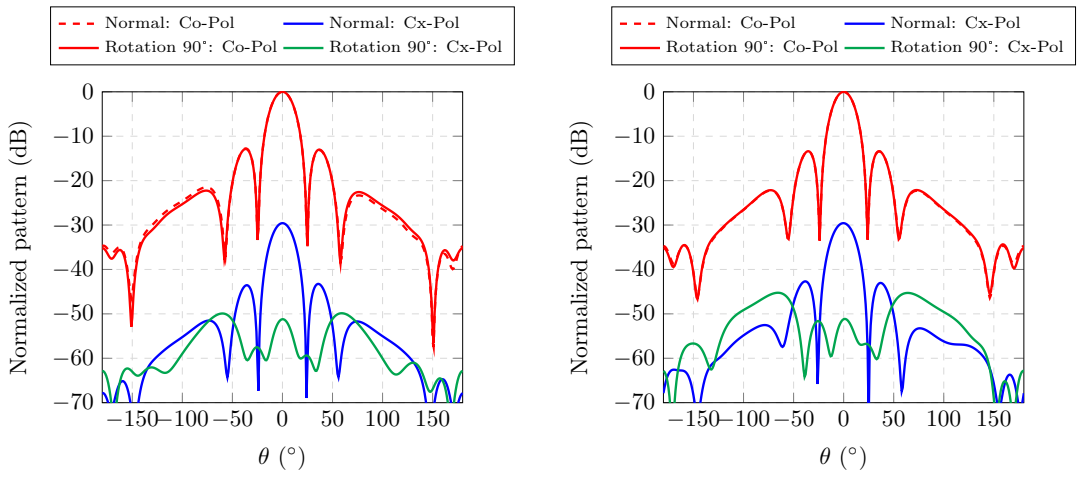

Figure 4.49.: Comparison co-polar and cross-polar patterns of normal and sequential 90° rotated array elements. Horizontal polarization. (a) XZ plane ($\varphi = 0°$). (b) YZ plane ($\varphi = 90°$).

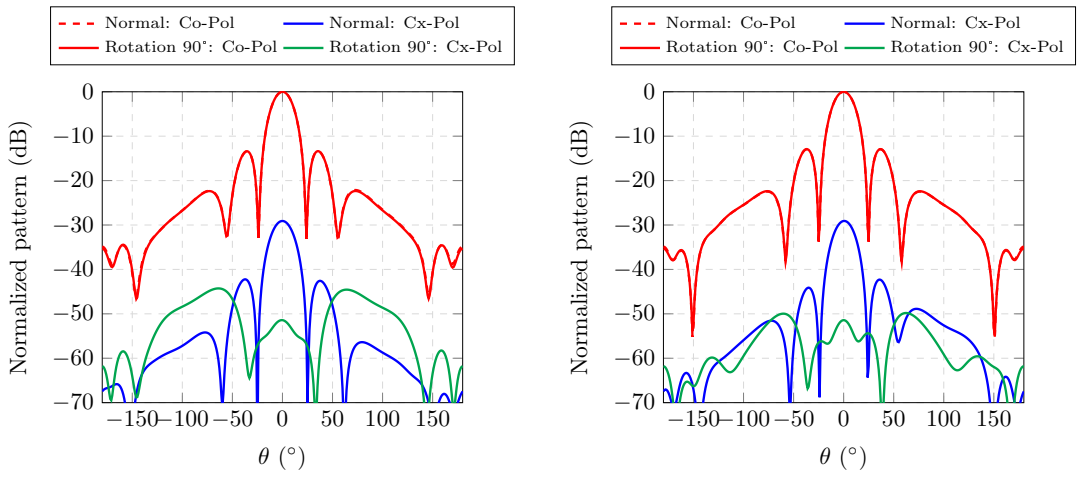

Figure 4.50.: Comparison co-polar and cross-polar patterns of normal and sequential 90° rotated array elements. Vertical polarization. (a) XZ plane ($\varphi = 0°$). (b) YZ plane ($\varphi = 90°$).

Reference	Frequency band	Array size	Antenna element	Cross-Polar Suppression
[34]	L-band	8×2	Probe-fed patch	38 dB
[35]	L-band	8×2	Probe-fed stacked patch	39 dB
[36]	S-band	6×6	Hybrid-fed patch	36 dB
[90]	L-band	12×12	Aperture coupled stacked patch	30 dB
[92]	X-band	20×20	Orthogonal set of dipoles	40 dB (simulated)
[93]	X-band	8×8	Single-polarized probe-fed U-Slot	Improvement 20 dB
Sequential rotation 90°	L-band	5×1	Cavity-box aperture coupled stacked patch	39.7 dB
Sequential rotation 90°	L-band	5×5	Cavity-box aperture coupled stacked patch	51.4 dB (simulated)

Table 4.16.: Comparison in terms of cross-polarization performance between proposed solution and some of the given references.

5. L-Band Planar Phased Array Antenna for Next Generation DLR Airborne SAR Sensors

In this chapter, the final development steps of the new L-band antenna are presented. First, the design of the planar subarray of 5×4 elements, as well as its integrated azimuth feeding network are introduced, manufactured and measured. Consequently, the final planar phased array of 5×8 elements is designed, by means of two mirrored subarrays that are excited by the required elevation feeding network. Furthermore, the antenna assembly process that allows its mechanical attachment on the aircraft is also highlighted. Finally, the proposed solution is validated by means of measurements of a final constructed antenna prototype.

5.1. Planar array design approach: subarray mirroring

Once the performance in elevation of the antenna design has been succesfully assesed with the linear array, the proposed antenna solution is extended to build the complete planar array. As already highlighted in the previous chapter, the restricted available antenna aperture on the aircraft allows a deployment of a planar array of up to 5×8 elements.

In order to simplify the increasing complexity that involves the design of the final planar phased array, the antenna development is divided in two stages. First, a planar subarray of 5×4 elements is designed, and consequently the final planar phased array antenna of 5×8 elements based on the mirroring of two subarrays is presented.

5.1.1. Subarray 5×4: half antenna design

Since the final planar phased array 5×8 consists of two mirrored electrical identical planar arrays 5×4, each of them is considered as a subarray that corresponds to half of the final antenna. Thus, the design of the next planar array becomes an essential development stage to predict the performance of the final phased array. In addition, the scope of this

work also allows to test novel antenna concepts (such as the previous cross-polarization suppression enhancement technique), as well as highly integrated antenna assemblies and new fabrication technologies.

The feeding configuration of the subarray 5×4 can be seen in Figure 5.1. In this stage, the azimuth feeding network is also designed and integrated. Unlike the linear array scenario, the elevation direction is set along x-axis and azimuth (flight direction) along y-axis. Due to the later subarray mirroring, the amplitude tapering along azimuth is now asymmetric. In order to reduce complexity in this design stage, the elevation feeding network is implemented in the same way as done for the linear array.

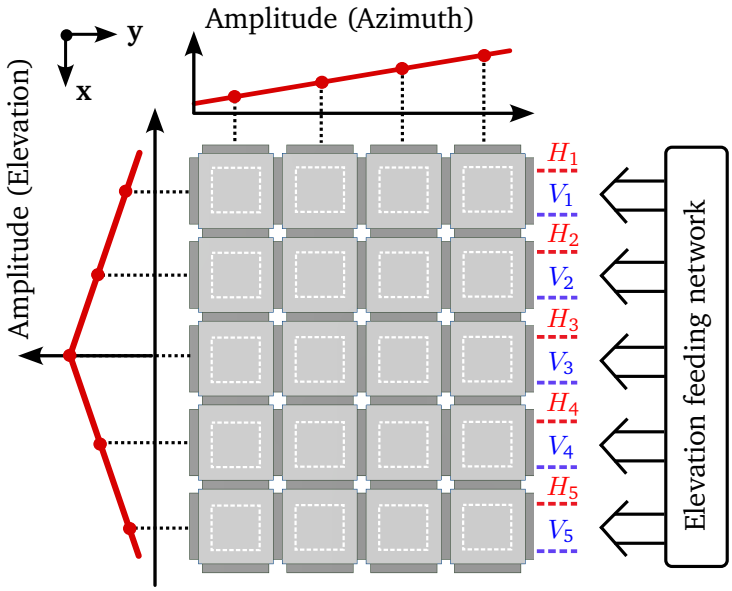

Figure 5.1.: Subarray 5×4 feeding configuration.

5.1.2. Final planar array 5×8

The final planar phased array 5×8 is built by means of two mirrored electrical identical subarrays 5×4. No additional electrical redesign has to be performed, and only the elevation feeding network is designed in order to provide the required phase and amplitude distribution. The antenna is assembled in a flight-certified housing that enables its mechanical installment onto the antenna carrier, that is mounted under the aircraft.

The feeding arrangement of the planar array is depicted in Figure 5.2. The amplitude distribution in azimuth becomes symmetric, due to the mirroring of the second

subarray 5×4. The elevation feeding network provides the required beamforming for both polarizations and subarrays, and it is directly connected to each azimuth subarray feeding network.

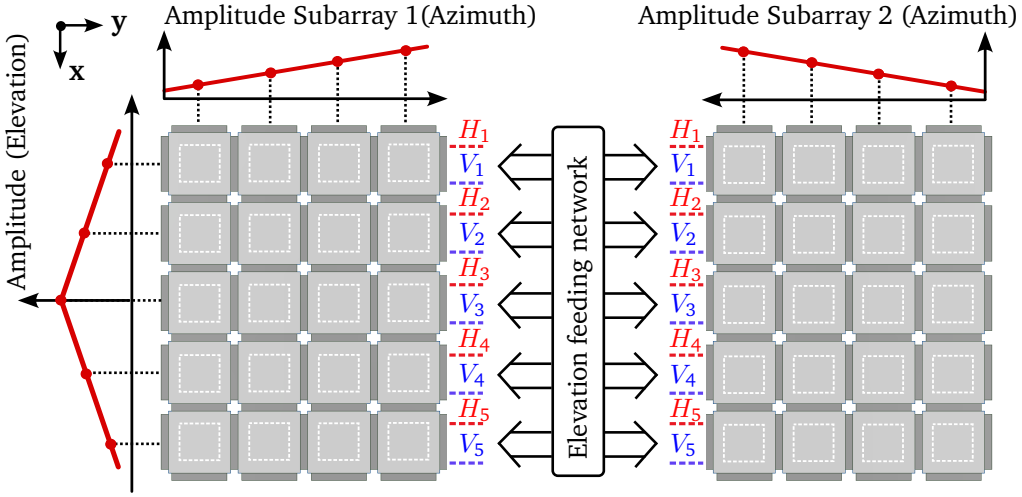

Figure 5.2.: Array 5×8 feeding configuration. Mirroring of two subarrays 5×4.

As convention, and from this chapter on, the electric field of the vertical linear polarization is aligned with the x-axis, being the XZ its E-plane. Hence, the electric field of the horizontal linear polarization is aligned with the y-axis, corresponding to the azimuth or flight direction, thus being parallel to the horizon, becoming the YZ its E-plane.

5.2. Design of the planar subarray 5×4

The presented concept of the aperture coupled stacked patch antenna in chapter 4 is extended in order to implement a planar array of 5×4 elements. Thus, the electrical performance of half of the final antenna can be assessed.

Nevertheless, some mechanical disadvantages of the previous prototype arise, that irremediably prevent the use of the closed cavity-box as an isolation enhancement method for planar array applications.

First of all, the mechanical realization of the cavity walls corners is extremely demanding, and it could only be achieved using additional attachment blocks in the last manufactured prototype, as already shown in Figure 4.28. This solution works for linear array arrangements but it is hardly feasible along two directions such as planar arrays, by which the complexity is considerably increased, especially for a high density of antenna elements.

In addition, assuring the electrical conductivity between the ground plane and the cavity becomes an additional challenge, as occurred with the single antenna prototype. A possible solution would be to replace the electric walls of the cavity using vias, as depicted in Figure 5.3a. The vias diameter corresponds to the wall thickness $d\_via = 2.5$ mm, and the spacing between vias $p = 3.83$ mm is set to be much less than the wavelength for the center frequency of operation ($p << \lambda_0/10$). The resulting S-parameters of the antenna and a comparison with the solid cavity walls, is shown in Figure 5.3b.

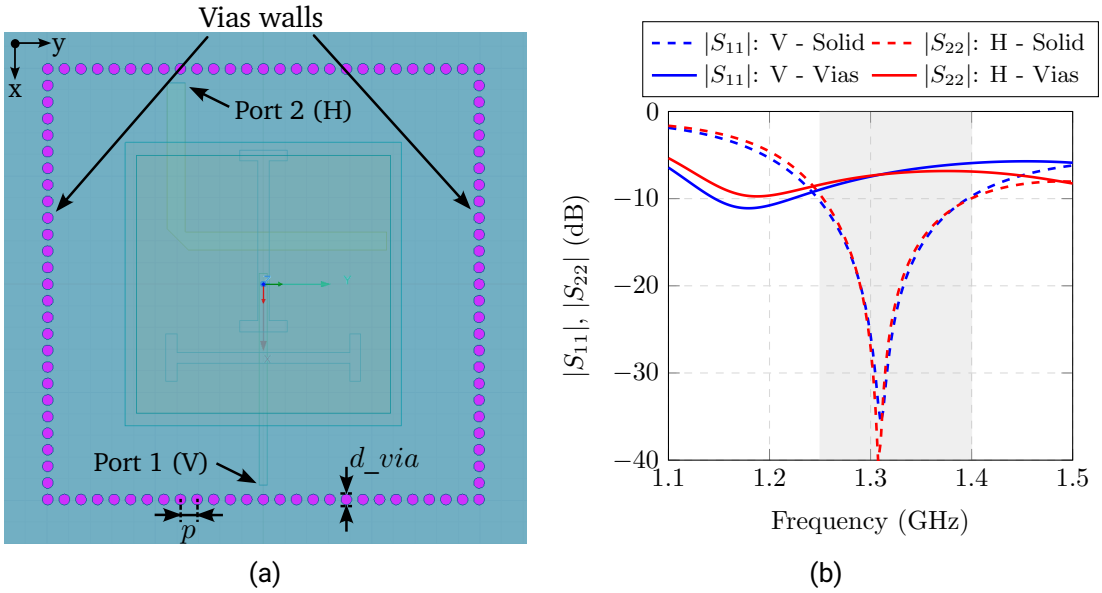

(a) (b)

Figure 5.3.: Cavity walls replacement by means of vias. (a) HFSS model. (b) Comparison of the reflection factor with the closed cavity-box.

It can be noted from the simulated reflection factor, that the electrical performance of the antenna is considerably affected. This is explained since the use of vias interrupts the currents that are induced on the cavity walls. Figure 5.4a and 5.4b show the surface current distribution induced on the walls along x-axis (Y constant) and y-axis (X constant) for the solid cavity-box antenna when the vertical polarization (port 1) is excited.

It can be seen that, for the pair of walls along x-axis, the surface current lines given by the vector orientation are colinear to the wall length. On the other side, the current lines are mainly transversal to the walls along y-axis. That means that, when the vertical polarization is excited, the pair of walls along y-axis are less susceptible to be replaced by vias, since the current lines are mostly colinear to the vias orientation, unlike the

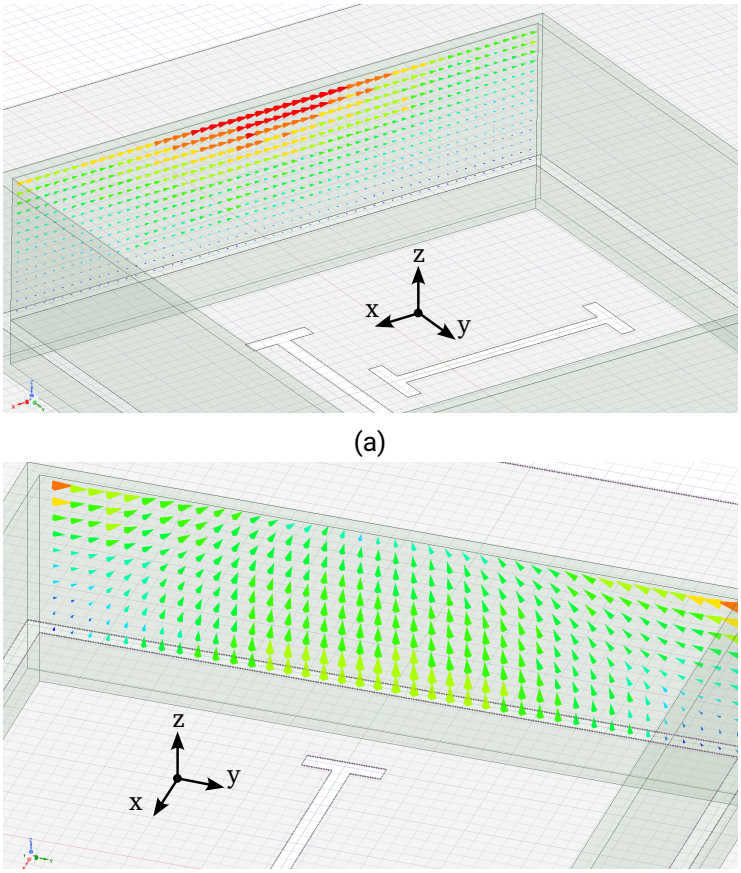

Figure 5.4.: Induced currents on the cavity walls. Vertical polarization. (a) Wall along x-axis. (b) Wall along y-axis.

case of the walls along x-axis, where the current lines are perpendicular to them. This is demonstrated in Figure 5.5, where only the pair of walls along y-axis are replaced with vias.

From 5.5b it can be seen that the walls replacement with vias along y-axis especially affects the horizontal polarization, while the return loss of the vertical polarization still remains comparable to the closed cavity, with a slight frequency shift.

Due to the orthogonality of polarizations, the same occurs for the horizontal polarization if the walls along x-axis are replaced with vias.

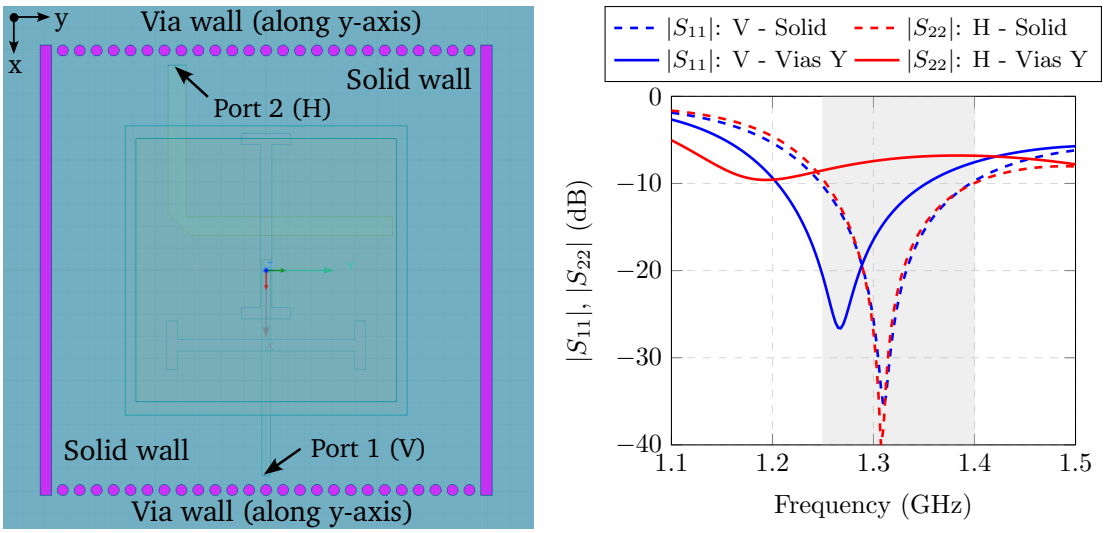

(a) (b)

Figure 5.5.: Replacement of cavity walls along y-axis by means of vias (a) HFSS model. (b) Comparison of the reflection factor with the closed cavity-box.

In addition, the multilayer antenna structure with soft foam layers also prevent the realization of through-hole plating, by which vias are manufactured. Thus, an alternative implementation of the cavity-box antenna isolation assembly, that leads to a feasible mechanical realization for planar arrays applications, is required.

5.2.1. Truncated cavity assembly

The aforementioned limitations can be overcome using a truncated cavity assembly, composed of four open walls that can be attached to the antenna ground plane, as depicted in Figure 5.6. This way, and since no corners are involved in the casing structure, its mechanical construction for planar arrays is considerably simplified.

The feeding network is placed below the antenna element. Since the ground plane of the antenna and the feeding network are splitted due to construction purposes, the electrical conductivity between both planes has to be assured. This is achieved by means of screws that tightly fix the feeding network below the antenna ground plane. This construction assembly demands an accurate alignment of both layers, since the coupling slots are placed on both ground planes. For this reason, the slots on the antenna ground plane are slightly larger in order to deal with possible misalignments between both layers

during the antenna construction process.

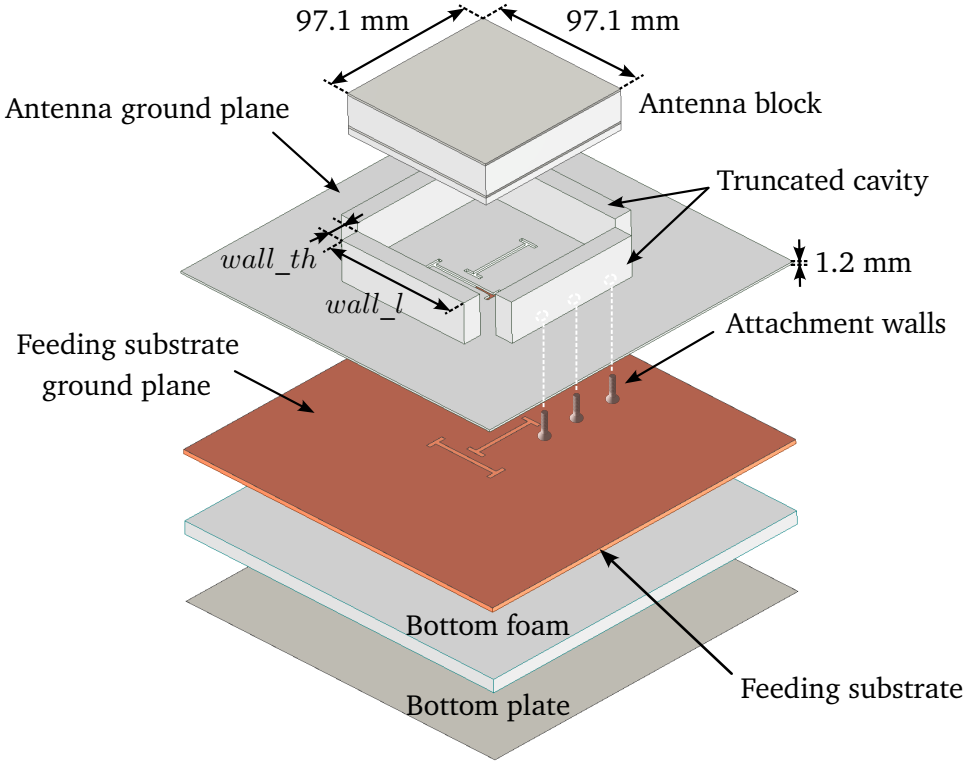

Figure 5.6.: Truncated assembly.

Measurement of a manufactured single prototype with truncated cavity assembly

Figure 5.7 shows the measured S-parameters of a manufactured prototype with the truncated assembly and a comparison with the simulation. The single antenna element of size 97.1 mm $\times$ 97.1 mm is electrically identical to the closed cavity with the same multilayer structure. The truncated cavity assembly is made of four aluminum solid walls of length $wall\_l = 86.1$ mm and thickness $wall\_th = 2.5$ mm. The wall length $wall\_l$ has been slightly reduced, in comparison with the closed cavity antenna, in order to achieve a similar electrical performance but without performing a full redesign. The antenna ground plane is also made of aluminum with a thickness of 1.2 mm, that allows the insertion of the counterstunk screws from below to attach the walls, as already shown in Figure 5.6.

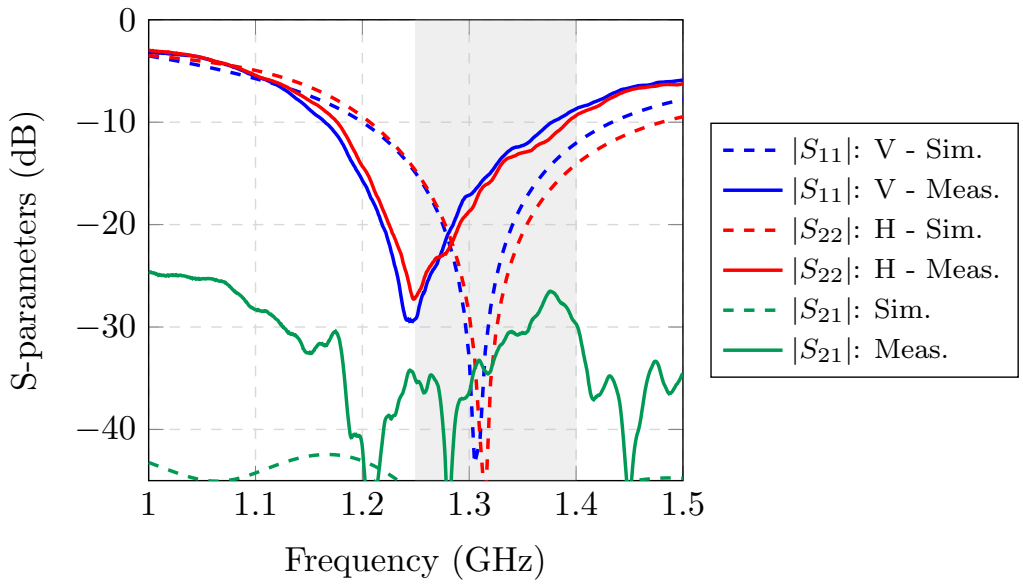

Figure 5.7.: Comparison simulated and measured S-parameters of a single antenna prototype with truncated assembly.

The measured prototype achieves a comparable return loss for both polarizations with an operational bandwidth higher than 200 MHz, that leads to a relative bandwidth of approximately 18%, measured at 10 dB matching level. The operational frequency range is increased in comparison with the cavity-box configuration, since the open structure mitigates the bandwidth reduction due to the resonant nature of closed cavities. Despite that the antenna performance is slightly shifted towards lower frequencies, as compared to the previous prototype, certainly due to fabrication and construction tolerances, the return loss level at the center frequency remains better than 15 dB. It can be also noted the extremely good isolation between both polarizations.

Coupling analysis

Figure 5.8 depicts a comparison, in terms of coupling, between two single polarized aperture coupled stacked patch antennas separated $0.48\lambda_0$ without the cavity assembly, with the closed and the truncated cases. It can be seen that with the truncated assembly, unlike the closed cavity, symmetric isolation values of approximately 17 dB at the center frequency of operation 1.325 GHz, and for both E- and H-planes can be achieved. This

improved isolation in H-plane is explained since, due to the truncation of the walls, the conductive surface on top of the walls, where surface currents are induced, is reduced.

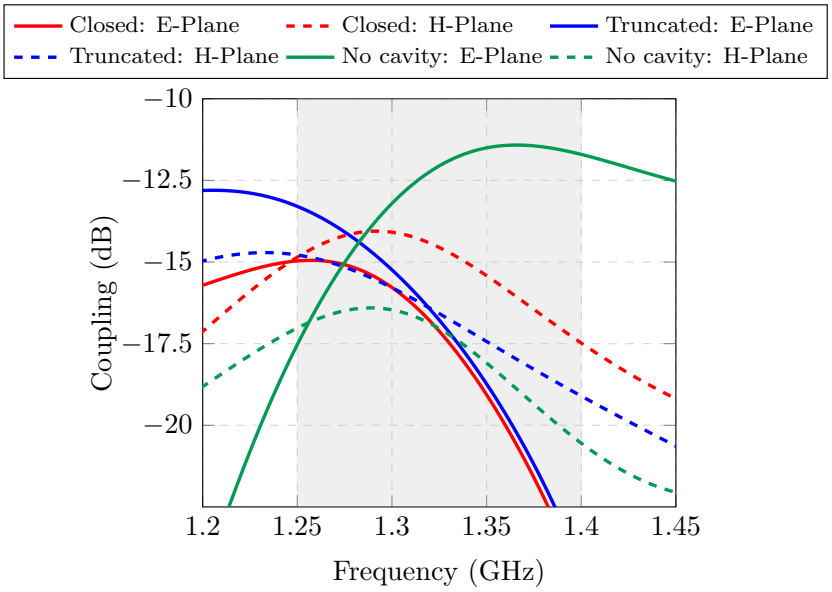

Figure 5.8.: Comparison of coupling w/o cavity, with the closed and the truncated cases between two single-polarized aperture coupled stacked patch antennas.

5.2.2. Design of dual-polarized truncated cavity array elements for sequential 90° rotation

For the design of the planar subarray 5×4, a redesign of the antenna feeding substrate is performed. Unlike previous designs, by which the antenna feeding network has been implemented using a FR4 epoxy substrate, from now on a Rogers RT/Duroid 6006 dielectric substrate is used. The reasons that support this design change are summarized as follows:

- The FR4 epoxy is a lossy substrate with a dielectric loss value $\tan\delta = 0.02$. This electrical parameter is not relevant in the previously manufactured antenna prototypes, since each single element disposes of its own feeding network. However, the implementation of the feeding network for the subarray leads to a relatively large electric design in microstrip technology of several wavelengths in extension, by which the dielectric losses can significantly impact the array efficiency. Thus, reducing the substrate losses becomes an important design aspect to consider.

- Increasing the dielectric permittivity of the substrate allows to reduce the electrical size of the feeding network. This is especially relevant, since a multilayer feeding network has to be designed in order to excite each polarization. In addition, the limited available area on the aircraft also demands for a compact implementation.

For these reasons, the substrate Rogers RT/Duroid 6006 ($\varepsilon_{\mathrm{r}} = 6.15, \tan\delta = 0.0019$) becomes as a good compromise between FR4 ($\varepsilon_{\mathrm{r}} = 4.4, \tan\delta = 0.02$) and other substrates with higher dielectric permittivies (but at the expense of higher dielectric losses, being also more sensitive to manufacturing tolerances).

Design of the truncated cavity single element

The geometrical parameters of the single antenna element with the new feeding substrate, as well as the different antenna layers, are listed in Tables 5.1 and 5.2. In comparison with the closed cavity antenna, a minimal redesign of the electrical parameters has been performed, in order to achieve a comparable performance with the new feeding substrate and the truncated assembly. As it can be noted, the width of the microstrip lines for both polarizations have been reduced to yield 50 Ω impedance, since the dielectric permittivity of the feeding substrate has been increased.

Layer	**Material**	ε_{r}	**Thickness**	
			Name	**Value**
Substrate patch 1	Rogers RT/Duroid 6006	6.15	h_{p1}	1.27 mm
Foam 1	Rohacell HF 51	1.06	h_{foam1}	18 mm
Substrate patch 2	Rogers RT/Duroid 6006	6.15	h_{p2}	1.27 mm
Foam 2	Rohacell HF 51	1.06	h_{foam2}	4 mm
Feed substrate 1	Rogers RT/Duroid 6006	6.15	h_{feed1}	1.27 mm
Feed substrate 2	Rogers RT/Duroid 6006	6.15	h_{feed2}	1.27 mm
Foam 3	Rohacell HF 51	1.06	h_{foam3}	6 mm

Table 5.1.: Electrical properties of each antenna layer.

The input feeding line lengths $line1\_in$, $line2\_in$ are set to achieve the same electrical length for both polarization lines. Being β_{V} and β_{H} the propagation constants, as well as $\lambda_{\mathrm{g}}^{\mathrm{V}}$=9.54 cm and $\lambda_{\mathrm{g}}^{\mathrm{H}}$=10.93 cm the guided wavelengths calculated in HFSS at the center frequency of operation for the vertical and horizontal polarization respectively, then:

$$\beta_{\mathrm{V}}\, line1\_in \approx \beta_{\mathrm{H}}\, line2\_in \Rightarrow \left(\frac{2\pi}{\lambda_{\mathrm{g}}^{\mathrm{V}}}\right) line1\_in \approx \left(\frac{2\pi}{\lambda_{\mathrm{g}}^{\mathrm{H}}}\right) line2\_in \tag{5.1}$$

$patch1\_l$	56	$slot1\_l$	38	$slot1\_w$	2.5	$slot2\_l$	37
$patch1\_w$	57.2	$slot2\_w$	2.5	$slot\_offset1$	17	$slot\_offset2$	8
$patch2\_l$	61	$line1\_l$	12.2	$line2\_l$	19.7	$line1\_w$	1.37
$patch2\_w$	63.2	$line2\_w$	3.55	$line1\_in$	40	$line2\_in$	45
$edge\_l$	11	$edge\_w$	2.5	$wall\_l$	86.1	$wall\_th$	2.5

Table 5.2.: Patch size and feeding parameters (in mm).

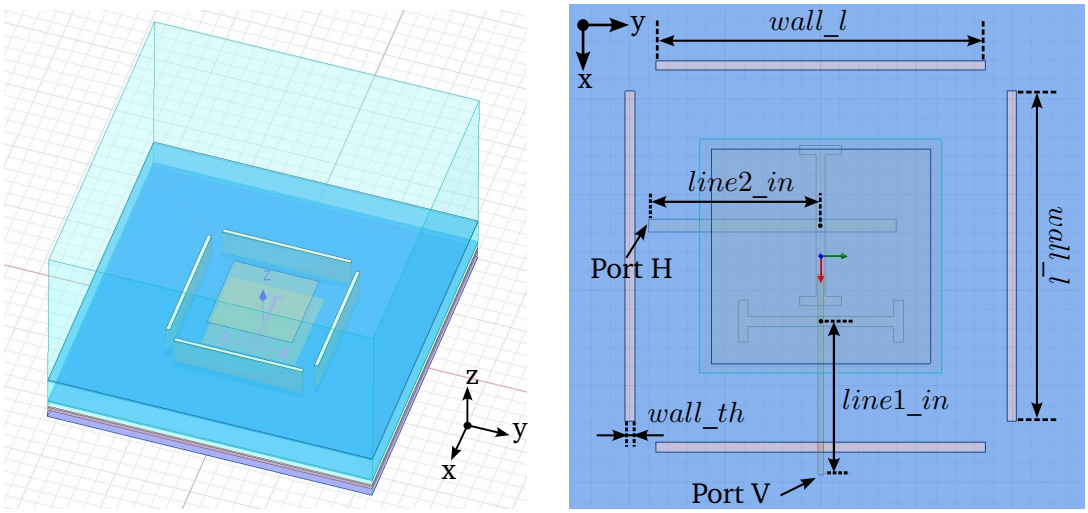

(a) (b)

Figure 5.9.: (a) HFSS model of the simulated aperture coupled stacked patch antenna with truncated walls. (b) Top view.

Be noted that, in the closed cavity design, each antenna element disposes of its own independent feeding within the antenna casing. However, in the proposed truncated cavity design, the feeding substrate is open, since all the array elements are excited using a single feeding network. Figure 5.9 depicts the HFSS model. The S-parameters, in logarithmic scala and in the Smith Chart, are shown in Figure 5.10. It can be seen that, considering a comparable electric design as for the closed cavity antenna with the same multilayer structure, the use of a truncated cavity yields a larger bandwidth, providing matching levels better than 10 dB for a bandwidth slightly below 300 MHz. The improved matching is also seen in Figure 5.10b, where the antenna adaptation within the operational bandwidth are focused in the center of the Smith Chart. The slight difference between the reflection factor of both polarizations is due to the shifting position of slot 1.

The simulated radiation patterns for both polarizations are plotted in Figure 5.11. The antenna gain is 5.1 dBi and 5.2 dBi for the vertical and horizontal polarization respectively. It can be noted that the pattern cut for the vertical one, that corresponds to the E-plane ($\varphi = 0°$), is not entirely symmetric, unlike the E-plane for the horizontal polarization ($\varphi = 90°$). This asymmetry comes from the slot 1 offset that yields an unequal electrical path between the slot position and the patch radiating edges. Shifting the slot along E-plane reduces the coupling, leading to a pattern tilt in that plane [88]. Moving the slot in H-plane has a slight impact, by which the radiation pattern of the horizontal polarization is unaffected.

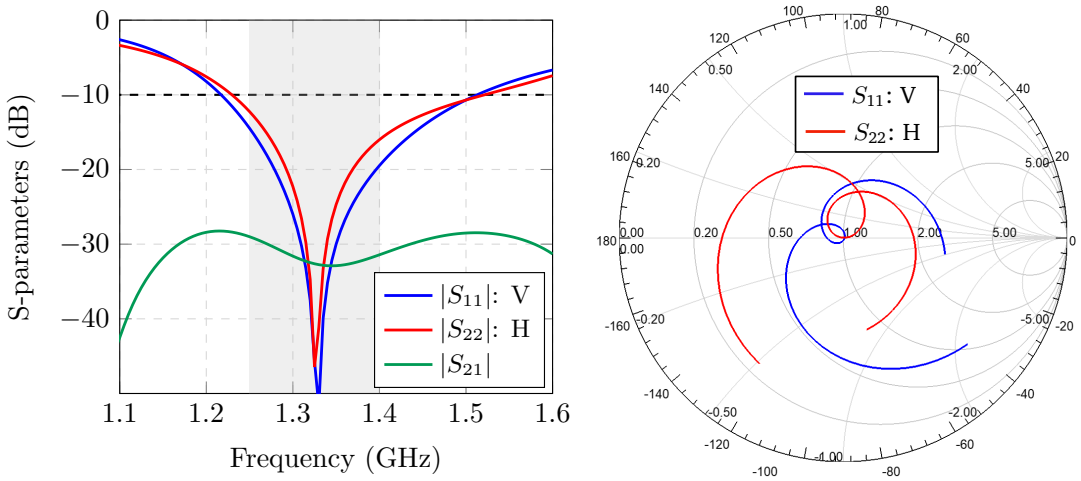

(a) (b)

Figure 5.10.: Matching levels of the aperture coupled stacked patch antenna with truncated walls. (a) Reflection factor and polarization isolation. (b) Smith Chart.

Application of the sequential 90° rotation of the antenna elements

In order to improve the cross-polarization suppression of the antenna array, a sequential 90° rotation of the array elements is applied, as presented and demonstrated in chapter 4.

The proposed technique leads to a geometrical disposition of the antenna elements, by which each polarization is excited by the combination of different geometric arrangements of the slots, as depicted in Figure 5.12.

As it can be seen, as the slot orientation changes, so does the position of the feeding line. Thus, the resulting polarization excitation (given by the same slot direction) is excited by

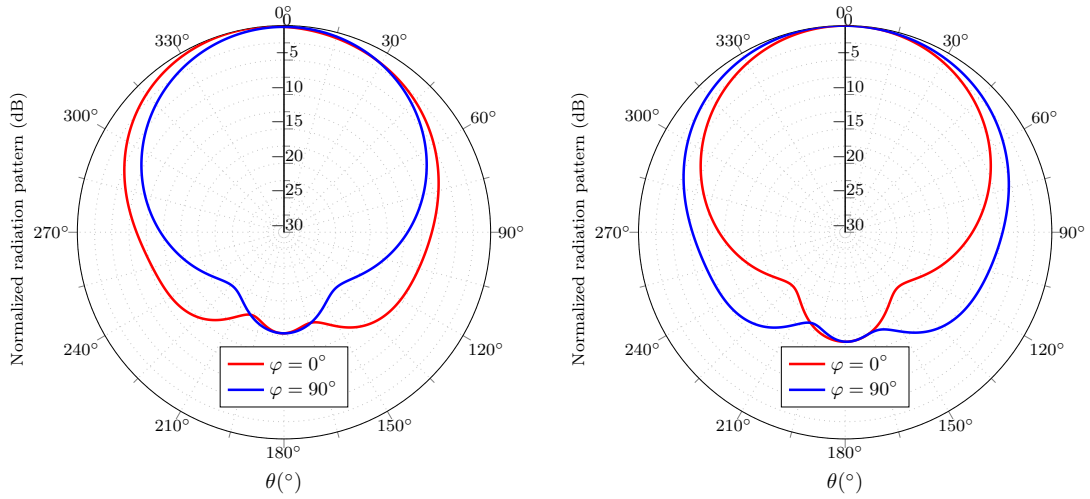

Figure 5.11.: Simulated main cuts of the radiation pattern. (a) Vertical polarization. (b) Horizontal polarization.

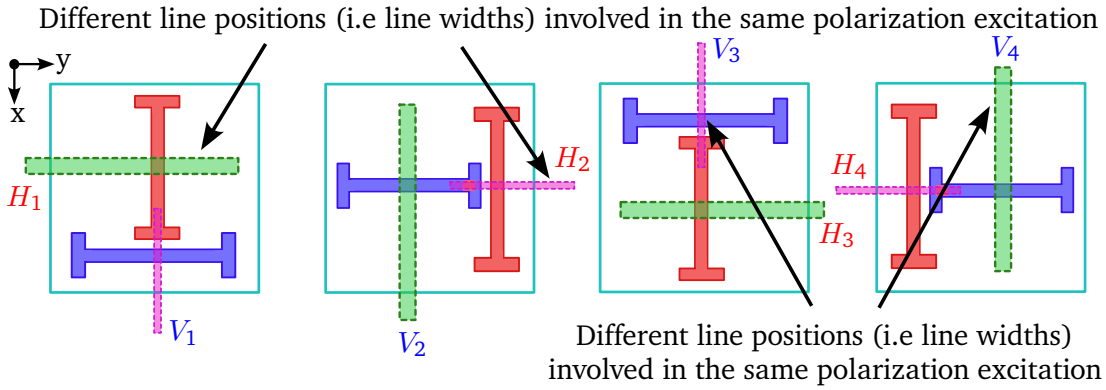

Figure 5.12.: Sequential rotation of same antenna elements. Distinct line widths (given by different substrate positions) involved in the same polarization excitation.

microstrip lines that are placed on different substrate heights. This design aspect was not relevant with the previous closed cavity prototypes since each constructed single element disposes of its own feeding, thus allowing to excite each antenna independently. However, the implementation of a single feeding network to excite each array polarization using

feeding lines on different substrate positions would become extremely complex. This design drawback can be overcome by replacing the rotated element by an equivalent antenna but swapping the position of the polarization feeding lines, as it is shown in Figure 5.13. From now on, the previous truncated cavity antenna element is known as antenna A. The electrical equivalent one, exchanging the position of the feeding lines, that leads to different line widths for each polarization excitation, is referred as antenna B.

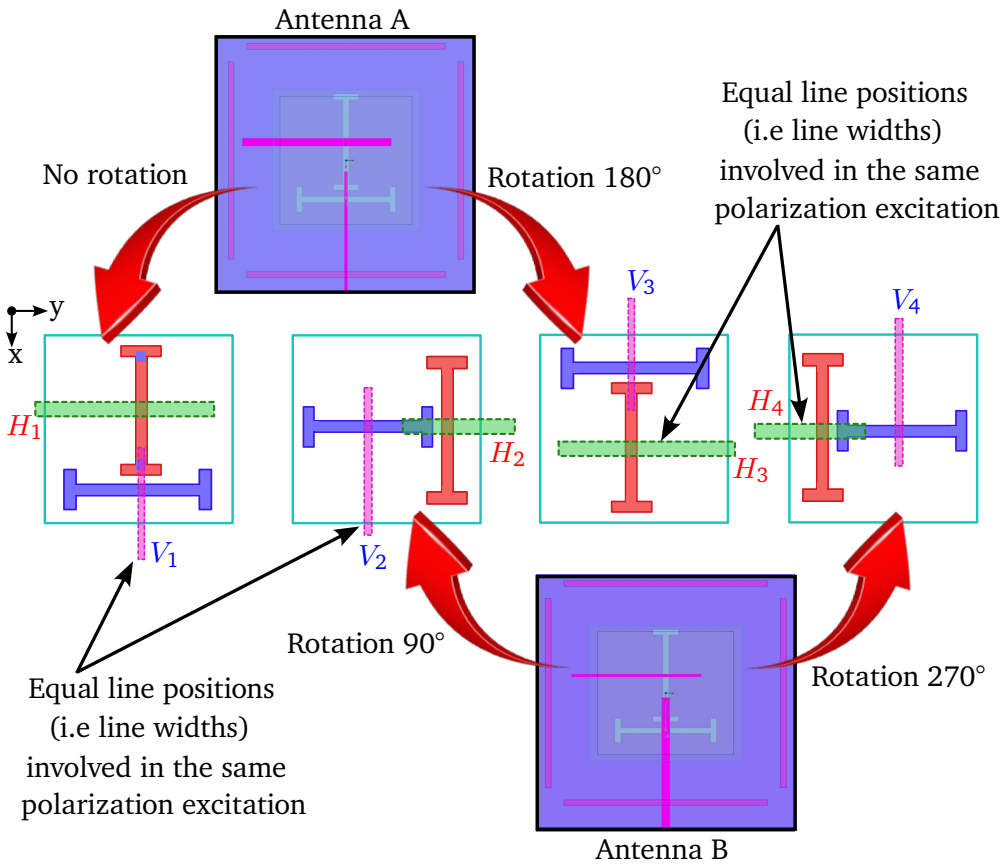

Figure 5.13.: Sequential rotation of antenna elements exchanging position lines. Each polarization is excited with lines placed on the same substrate position.

The truncated cavity antenna element B is the electrical equivalent of the antenna element A but switching the position of the microstrip line by which each slot is excited. Therefore, the geometrical parameters of the antenna B are practically identical as the antenna A, except a slight variation of the patch width, as it can be seen in Table 5.3.

Figures 5.14 and 5.15 show the simulation results of the antenna B compared with the antenna A. It can be noted that both antennas provide an almost identical electrical performance.

$patch1\_l$	56	$slot1\_l$	38	$slot1\_w$	2.5	$slot2\_l$	37
$patch1\_w$	57.4	$slot2\_w$	2.5	$slot\_offset1$	17	$slot\_offset2$	8
$patch2\_l$	61	$line1\_l$	15	$line2\_l$	15.1	$line1\_w$	3.55
$patch2\_w$	64.4	$line2\_w$	1.37	$line1\_in$	45	$line2\_in$	40
$edge\_l$	11	$edge\_w$	2.5	$wall\_l$	86.1	$wall\_th$	2.5

Table 5.3.: Patch size and feeding parameters (in mm).

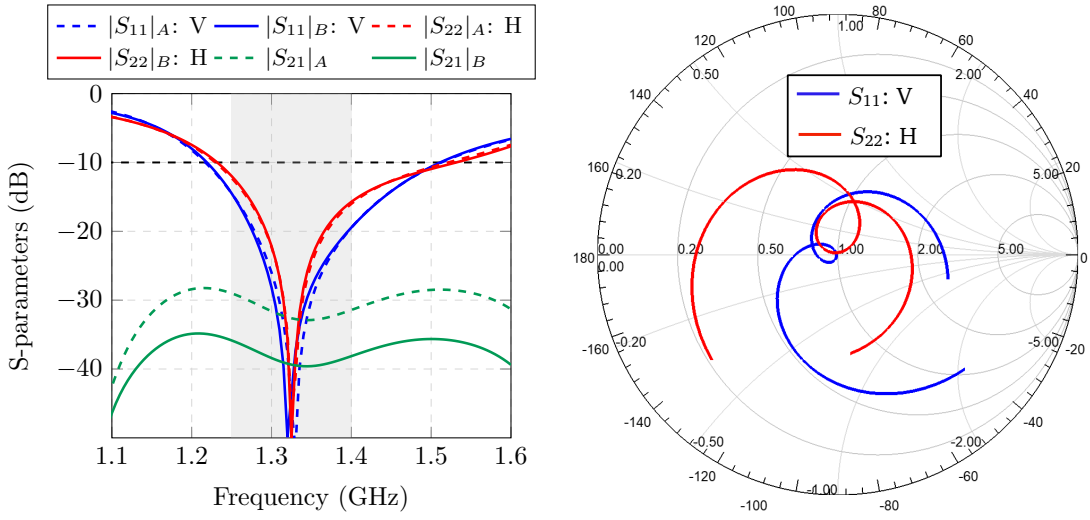

(a) (b)

Figure 5.14.: Simulated S-parameters antenna B. (a) Reflection factor and polarization isolation level. Comparison with the antenna A. (b) Smith Chart.

The antenna gain is 5.05 dBi and 5.2 dBi for the vertical and horizontal polarization, respectively. The asymmetry of the radiation pattern along the E-plane for the vertical polarization due to the slot offset can be also seen in Figure 5.15a.

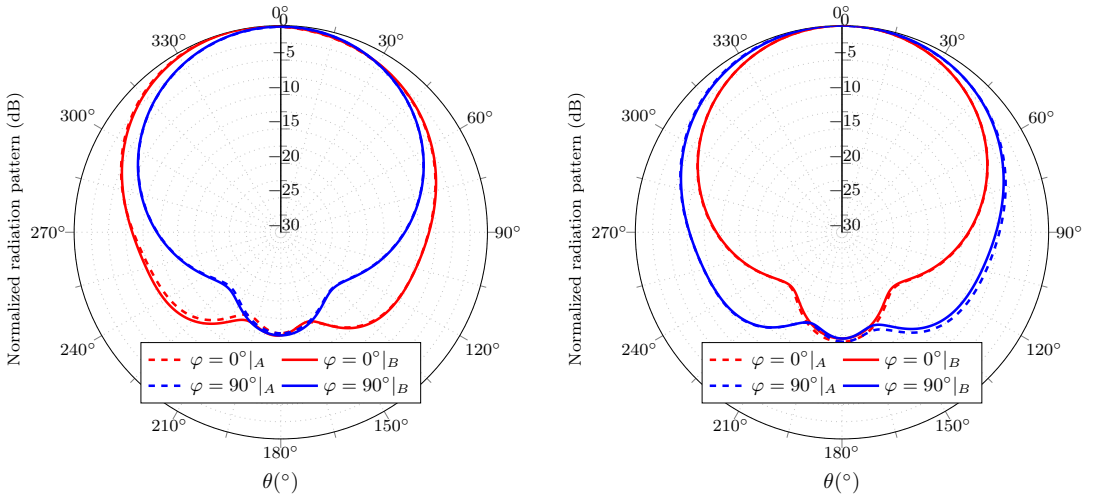

Figure 5.15.: Simulated radiation pattern of the antenna B and comparison with the antenna A. (a) Vertical polarization. (b) Horizontal polarization.

Analysis of a linear array formation

As in the previous chapter, first the performance of a linear array is examined and then the analysis is extended to a planar array formation.

Figure 5.16 depicts the electric field magnitude on the top patches for the vertical polarization of a linear array 1×4 along y-axis, applying the same amplitude and phase to each element. Figure 5.16a considers a linear array of 4 identical antenna elements (antenna A) while Figure 5.16b shows the case with the sequential 90° rotation of array elements combining antennas A and B, as previously explained. In this later case, the elements 2 and 3 of the horizontal polarization and the elements 3 and 4 of the vertical one, are excited with 180° phase difference, since due to the rotation, the feeding lines are placed along the opposite direction, and thus, these elements are excited out of phase, as occured in the sequential rotation of the array elements in chapter 4.

It is clearly noted from Figure 5.16b, where the sequential 90° rotation is applied, that not all the patches resonate uniformly, unlike Figure 5.16a. This means, that the sinusoidal electric field variation of the electric field on all the patches is not identical due to a phase variation, by which the maximum field intensity is not achieved simultaneously for all the radiating elements. It can be seen that the antenna elements A resonate equally, but being different as the antenna elements B, that also resonate uniformly among them. This

design aspect is equivalent as if the antenna elements are excited with a different feeding phase, thus becoming relevant to provide the required field interference between the array elements to shape the radiation pattern as desired. This phase imbalance can be compensated adding the proper phase difference among the antenna elements.

This aspect can not be explained due to the unequal electric length of the microstrip feeding lines that yield a different feeding phase, as already explained in chapter 4 with the closed clavity elements. This design aspect has already been taken into account, since $(\beta_{\mathrm{V}}\, line1\_in) \approx (\beta_{\mathrm{H}}\, line2\_in)$, as mentioned in (5.1).

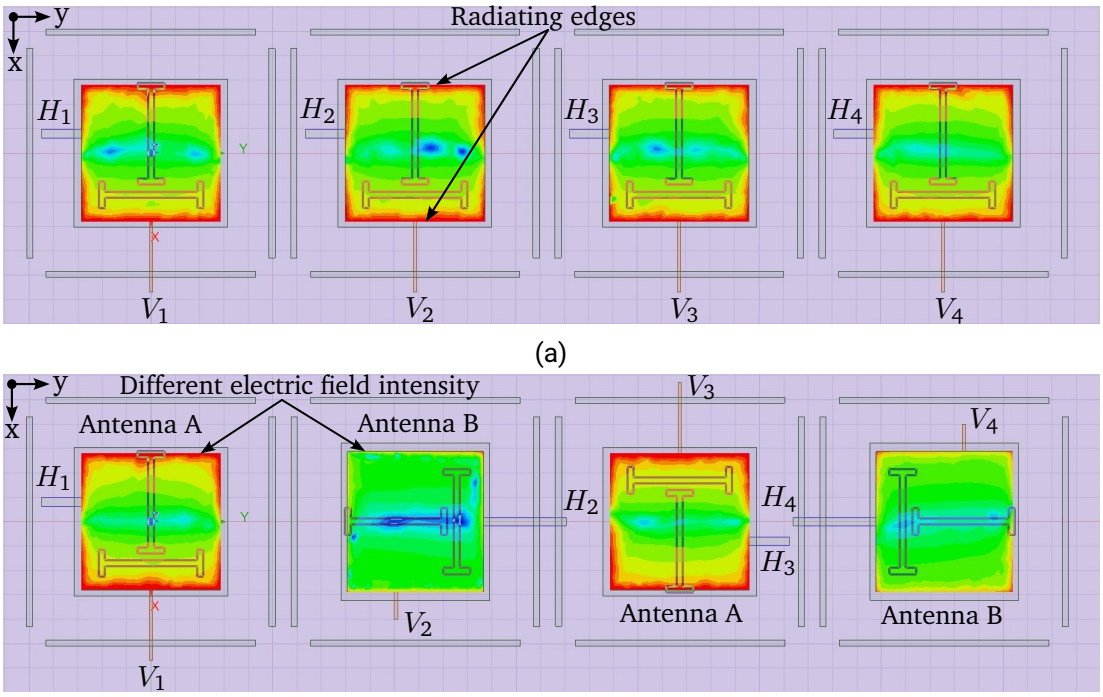

Figure 5.16.: Magnitude of the electric field on the top patches with equal amplitude and phase. Vertical pol. (a) Standard array arrangement with antenna element A. (b) Sequential 90° rotation of array elements combining antennas A and B.

The aforementioned phase difference among the antenna elements is mainly related to the change position of the slot offsets that are involved in the same polarization excitation, along with the use of a relative electric thick antenna ground plane. It is well known that shifting the slot along E-Plane produces a pattern tilt or asymmetry in that plane that

influences the phase of the radiated electric fields, that can be seen in Figures 5.11a and 5.15a. Thus, to yield a constructive interference of the radiated electric fields coming from array elements that are excited with different slots arrangements (centered and shifted slot positions), this aspect has to be considered. In addition, this effect is enhanced due to the large slot depths, given by the unusual electrically large antenna ground plane of thickness 1.2 mm, that is required for the truncated cavity assembly.

Analysis of the phase compensation

This phase imbalance can be compensated applying the proper phase difference among antenna elements. In order to obtain the required feeding phase value to be applied, the radiated phase of the electric fields in HFSS can be analyzed. The calculated phase of the radiated electric field is independent on the radiated distance (far-field region) by which the absolute phase value is not relevant but it does become important to estimate the phase difference.

Figure 5.17 shows the radiated phase along θ direction in the E-Plane ($\varphi = 0°$) for the vertical polarization of the antenna A considering different values of the feeding line length $line1\_in$.

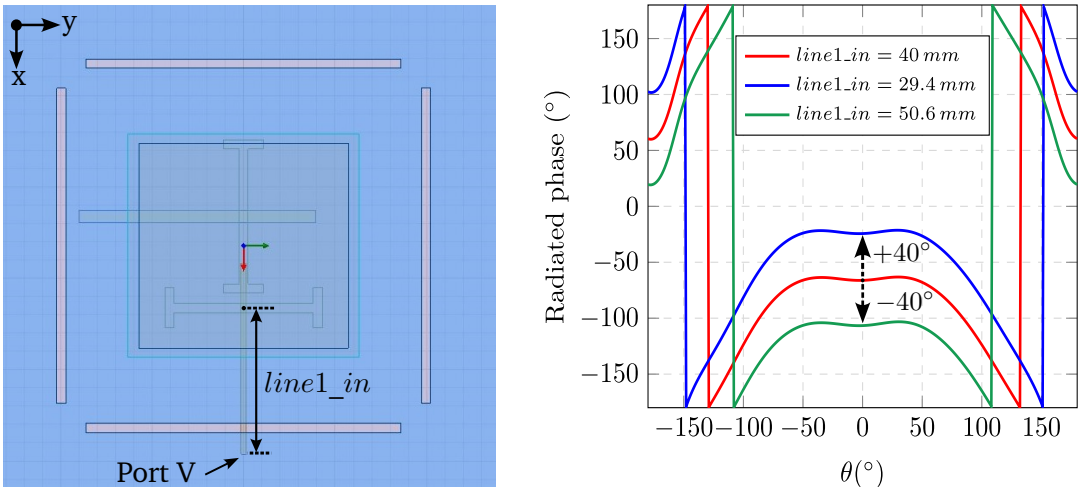

(a) (b)

Figure 5.17.: Phase of the radiated electric fields. Antenna A. Vertical polarization. (a) HFSS model. (b) Radiated phase values for different feeding line lengths.

Figure 5.17b plots the phase of the radiated electric fields for distinct feeding length

values, yielding different excitation phase values. The leap in the phase occurs when the values are above 180° or below -180°, since due to the cyclic phase repetition only values between ±180° are plotted. It can be seen that, for the default length $line1\_in = 40\,\text{mm}$ the value of the radiated phase at the broadside radiation ($\theta = 0°$) is -66°.

Changing the electrical length of the feeding lines yields a proportional variation of the radiated field phase. As an example, increasing or decreasing the feeding length by 10.6 mm produces a variation in the radiation phase of ±40°, leading to radiated phase values of -66°-40°=-106° and -66°+40°=26° respectively, as depicted in Figure 5.17. This can be easily related by:

$$\left(\frac{\pm 40°}{360°}\right)\lambda_g^V = \left(\frac{\pm 40°}{360°}\right) 95.4\,\text{mm} = \pm 10.6\,\text{mm} \tag{5.2}$$

The same analysis can be performed rotating 90° the antenna B in order to have the same polarization reference (slot direction and feeding line orientation) as the antenna A for a direct comparison.

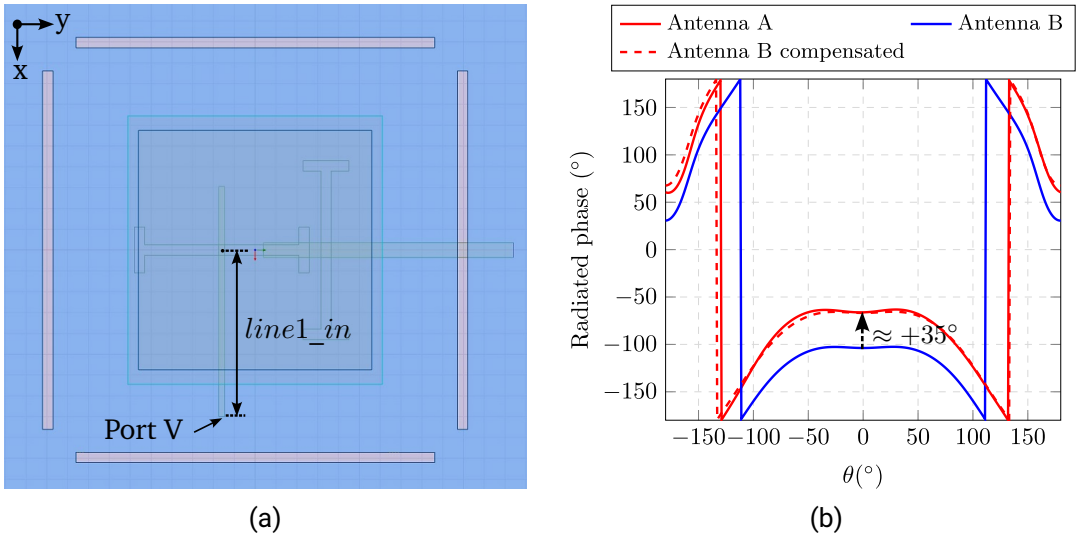

(a) (b)

Figure 5.18.: Phase of the radiated electric fields. Antenna B. Vertical polarization. (a) HFSS model (b) Radiated phase values compared with antenna A for the same feeding line length $line1\_in = 40\,\text{mm}$.

It can be seen that, for the same feeding line length $line1\_in = 40$ mm the phase of the radiated fields for the antenna B does not match with the antenna A, as shown in

Figure 5.18b. It can be also noted that the phase variation is flatter unlike the antenna A, since in the antenna B there is no slot offset in the E-Plane for the vertical polarization involved, but in H-Plane. This phase variation can be thus compensated applying a feeding phase of +35° in the antenna B regarding the antenna A, as it seen in Figure 5.18b.

The same analysis can be performed considering the horizontal polarization, but since the position of the slots are exchanged, a phase imbalance of -35° is present.

This phase variation can be considered as a phase offset whose value remains approximately constant in the antenna operational bandwidth 1.25 GHz∼1.4 GHz.

Thus, applying the amplitude and phase values that are listed in Table 5.4, all the patches can be excited in phase, as depicted in Figure 5.19 and like Figure 5.16a.

Vertical polarization			**Horizontal polarization**		
V_1	A_1	φ_1	H_1	A_1	φ_1
	1 W	0°		1 W	0°
V_2	A_2	φ_2	H_2	A_2	φ_2
	1 W	35°		1 W	-35°+180°
V_3	A_3	φ_3	H_3	A_3	φ_3
	1 W	180°		1 W	180°
V_4	A_4	φ_4	H_4	A_4	φ_4
	1 W	35°+180°		1 W	-35°

Table 5.4.: Required amplitude and phase variation for the linear array 1×4 perfoming the sequential rotation of array elements and combining antenna A and B.

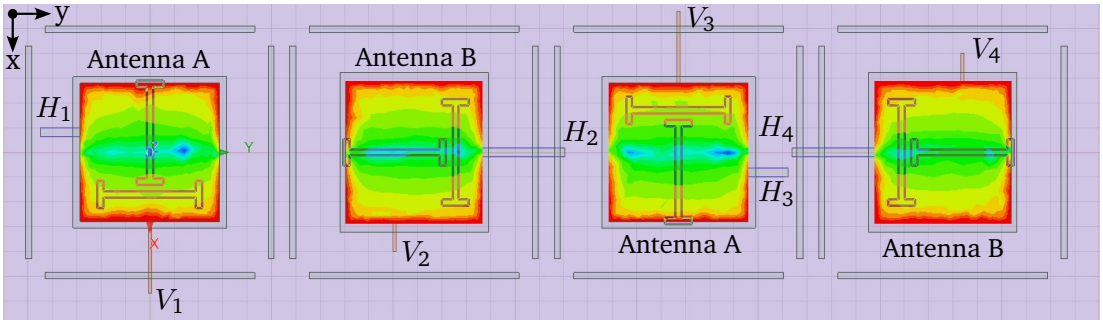

Figure 5.19.: Electric field magnitude of the top patches with the same amplitude and phase, and rotating antenna elements A and B. Vertical polarization.

Figure 5.20 plots a comparison of the simulated results between the standard linear

array arrangement of Figure 5.16a and the sequential rotation of array elements combining antennas A and B, as shown in Figure 5.19.

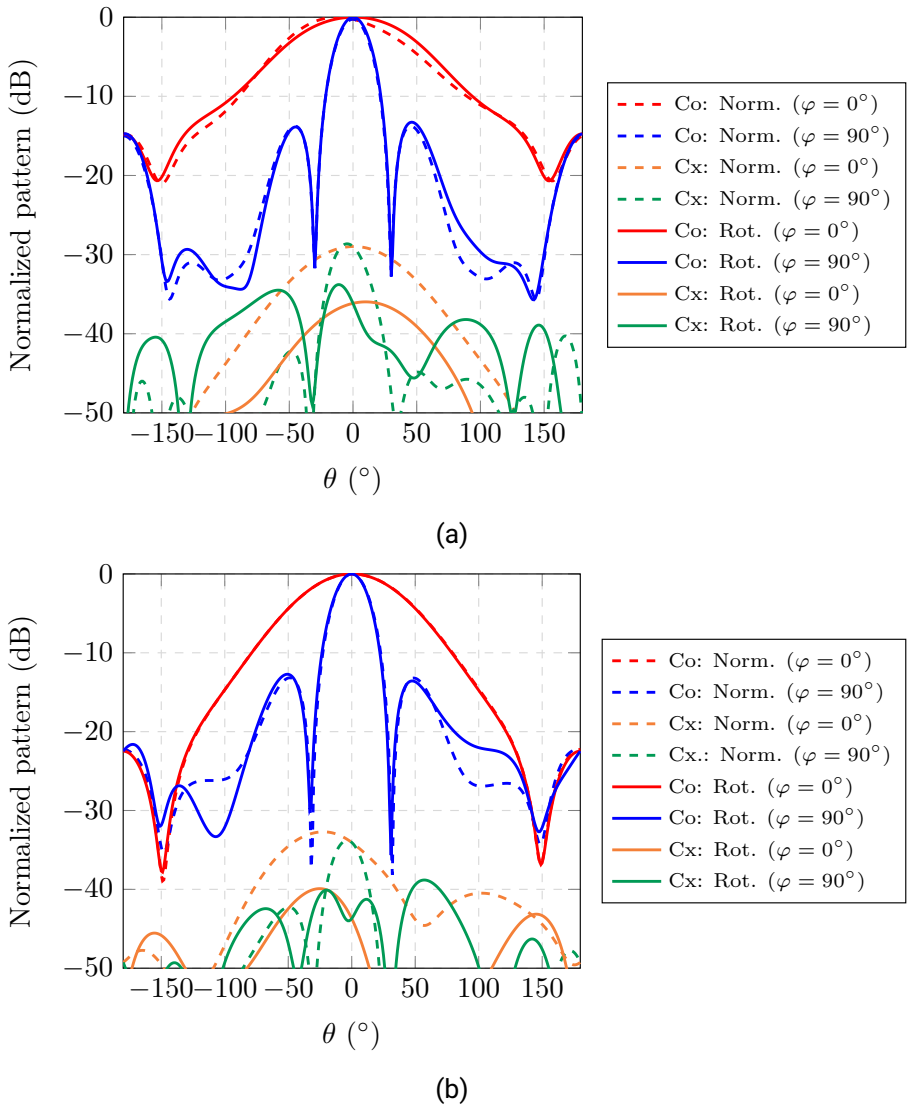

Figure 5.20.: Simulated radiation pattern. Comparison between normal linear array and sequential rotation. (a) Vertical polarization. (b) Horizontal polarization.

It can be seen that the co-polar patterns of both linear arrays for the two polarizations

are comparable, as well as the gain values. It can be also noted that the array with the rotated elements provide a slighter asymmetry in the YZ plane ($\varphi = 90°$). This effect is more visible in the horizontal polarization of the array with the rotated elements, since this configuration leads to antenna elements with slots shifted along E-Plane, which corresponds to the YZ plane of this polarization. Nevertheless, this asymetry is mainly visible in values considerably below -20 dB. On the other side, the linear array with the rotated elements provide the following advantages:

- Thanks to the rotation, the pattern tilt in the E-Plane for the vertical polarization due to the slot offset (plane XZ, $\varphi = 0°$) is clearly compensated, leading to a more symmetric pattern, as seen in Figure 5.20a.
- The cross-polarization suppression levels for both polarizations are improved and they will be enhanced for a planar array application.
- The sequential rotation of array elements, along with the combination of antennas A and B, enable the design simplification of the feeding network to excite each polarization at different substrate levels.

Variation of the phase compensation depending on the antenna geometrical parameters

Previously, it has been presented the impact that produces the slot shift in the phase of the radiated fields and how it can be compensated straight-forward. In order to further understand the electrical influence of the antenna geometrical parameters in the radiated phase independently, a parametrical analysis is performed, where the phase variation is examined considering the variation of one electrical parameter of the antenna. For this investigation, the following approach is applied:

- To simplify the analysis, one polarization is considered. The findings for the other polarization can be easily implemented due to to its reciprocity.
- As a standard case, a single truncated cavity antenna without slot offset is considered, as depicted in 5.21. Thus, any geometrical or electrical variation, is always compared to this reference case. Precisely, to provide a comparison with an electrical equivalent performance, all the different cases under study provide the same return loss level.
- Only one geometrical parameter of the antenna is gradually modified at the same time, namely the slot offset in E- and H-plane, the slot length and the ground plane thickness.

- For all the geometrical variations under study the feeding line has the same electrical length ($line1\_in = 40\,\text{mm} = \text{constant}$).

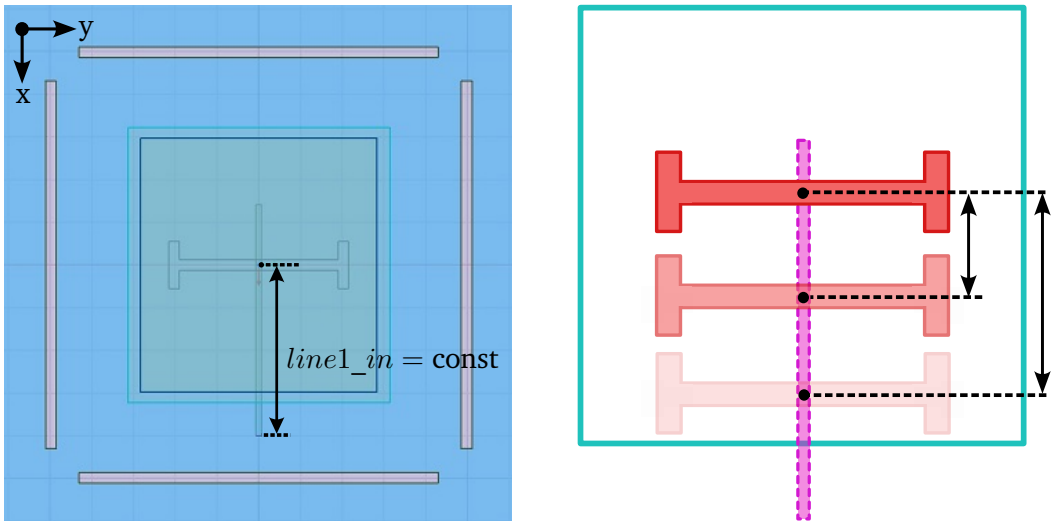

Figure 5.21.: Analysis radiated phase for one polarization (vertical). (a) HFSS model (b) Variation of the slot offset along x-axis.

1. Variation of the slot offset along x-axis

Figure 5.22 plots the absolute variation of the radiation phase when the slot is shifted along x-axis (E-plane direction) considering different values of the ground plane thickness. Moving the slot reduces its coupling level and it shifts the operational frequency band to lower frequencies. For small offset values this effect can be negligible, however it is more visible the thicker the ground plane is, which is directly related to the slot depth. The frequency shift can be easily compensated with a slight variation of the patch resonant length. Shifting the slot also produces a pattern tilt or asymmetry that is increased for slot positions closer to the radiating edges of the patch.

As it can be seen in Figure 5.23a, a comparable return loss level for each slot offset variation is considered. The pattern tilt produced in the E-plane (Plane XZ, $\varphi = 0°$), when shifting the slot position, is depicted in Figure 5.23b.

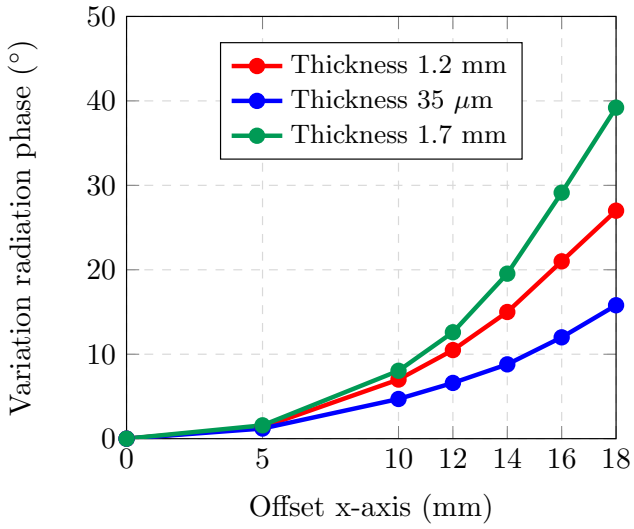

Figure 5.22.: Variation of the radiated phase for different slots positions and values of the ground plane thickness.

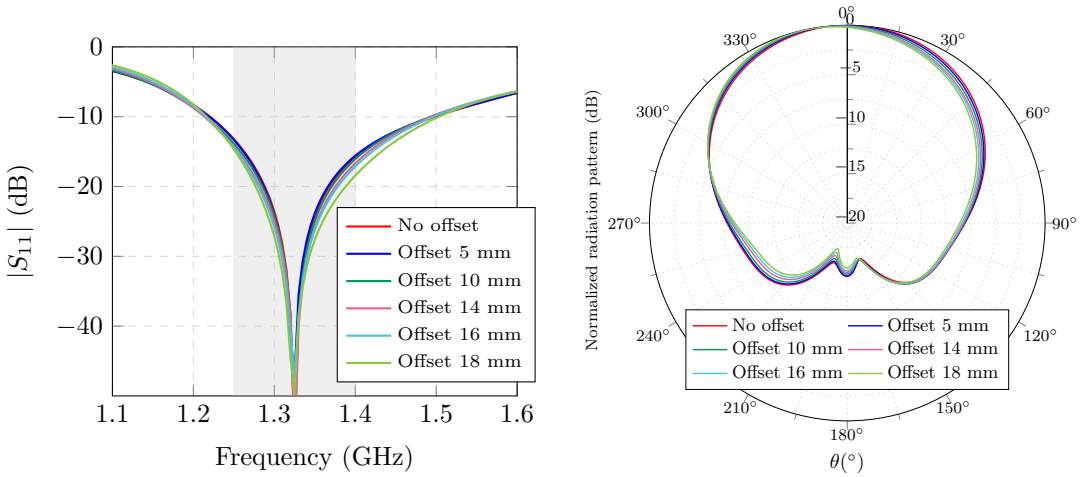

(a) (b)

Figure 5.23.: Variation of the slot offset for a thickness of 1.2 mm (a) Reflection factor. (b) Radiation pattern in E-plane ($\varphi = 0°$).

It can be seen that shifting the slot offset more than 10 mm, along with the use of electrical thick ground planes, can lead to phase variations higher than 20°, considering an equivalent antenna performance regardless the slot position.

This can also explain why in the case of the closed cavity antenna, by which the thickness of the ground plane was 35 µm, the phase variation was mainly due to the unequal electrical length of the microstrip lines, and not due to the relative position between slots.

2. Variation of the slot offset along y-axis

The same analysis is performed but shifting the slot along y-axis. In this case, no pattern tilt is produced since the slot is moved along the H-plane, by which the slot coupling levels remain comparable. Figure 5.24a plots the variation of the radiated phase considering two different cases: without a slot offset in the E-plane and with an additional slot displacement of 17 mm in x-axis. It can be seen that shifting the slot in the H-plane barely impacts the radiated phase, only a few degrees, but this effect is slightly enhanced if an additional offset in E-plane is also considered, since the antenna is more sensitive to any geometrical variation.

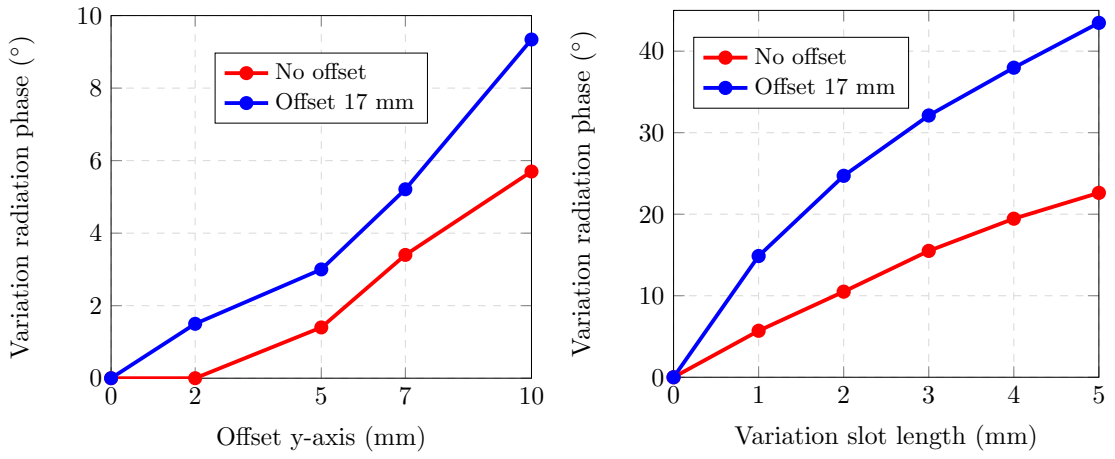

Figure 5.24.: Analysis variation of the radiated phase (a) Slot offset along y-axis. (b) Increment of the slot length.

3. Variation of the slot length

A similar study is depicted in Figure 5.24b but considering only a variation of the slot length. In this case a slot length of 4.2 mm is set and incremented gradually in steps of 1 mm. It can be seen that the variation of the slot length has an impact in the radiated phase, especially when an offset in x-axis is also involved, by which the antenna performance becomes extremely sensitive to anly variation of its electrical parameters.

The aforementioned parametric analysis enlightens the phase variation that has to be applied between antenna elements in the case of the sequential rotation of array elements. Thus, the phase difference can be explained as the total contribution of the following effects:

- The relative difference position between slots impacts in the radiated phase. This effect is more noticeable when greater offsets in E-plane direction are involved and it is enhanced with an electrical thick antenna ground plane.
- Shifting the slot in H-plane usually leads to a variation of a few degrees. The impact of small offset values can be negligible.
- Slight slot lengths differences can lead to considerable radiated phase variations, especially when a slot offset in E-plane is involved, by which the antenna electrical performance is sensitive to any modification of its geometrical parameters.

5.2.3. Feeding configuration of the subarray 5×4. Analysis of the amplitude tapering in azimuth and beam steering in elevation.

The subarray 5×4 is analyzed with the corresponding excitation in azimuth and elevation, as depicted in Figure 5.25. In this development stage, and in order to exploit the degree of freedom to achieve the proper feeding coefficients, each array element i disposes of its own independent feeding port for each polarization $H_{\mathrm{i}}, V_{\mathrm{i}}$.

The subarray is built applying the sequential 90° rotation along both axis and combining the antenna elements A and B. Thus, the phase difference that has to be applied among array elements is considered in order to excite all the antenna elements in phase.

Unlike in previous cases the elevation direction is set to be in x-axis, thus being y-axis the azimuth direction. The beam steering is only applied in elevation and it is given, respectively, by the amplitude $E_{\mathrm{i}}^{\mathrm{H}}, E_{\mathrm{i}}^{\mathrm{V}}$ and phase coefficients $\alpha_{\mathrm{i}}^{\mathrm{H}}, \alpha_{\mathrm{i}}^{\mathrm{V}}$ for the horizontal and vertical polarizations. The amplitude coefficients for each antenna element i in azimuth are defined by $A_{\mathrm{i}}^{\mathrm{H}}$ and $A_{\mathrm{i}}^{\mathrm{V}}$ for the horizontal and vertical polarization, respectively.

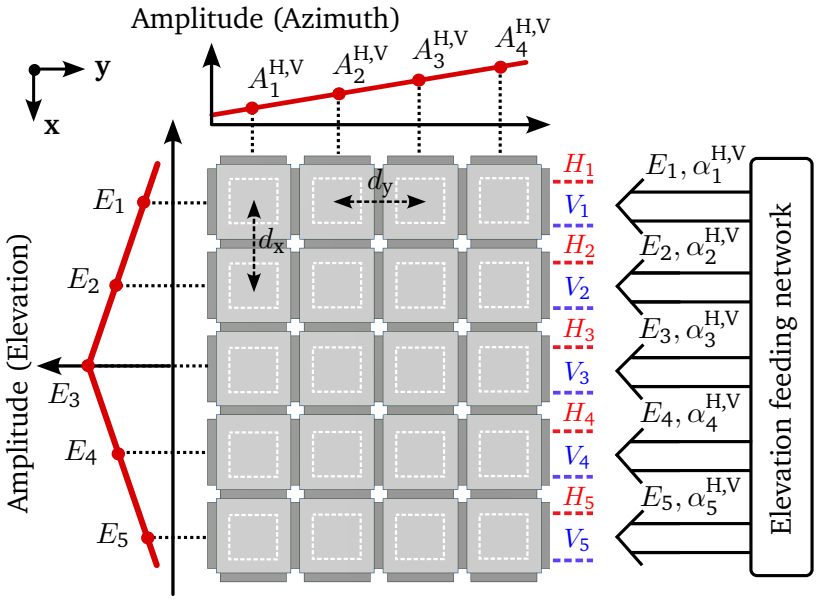

Figure 5.25.: Subarray 5×4 feeding configuration in azimuth and elevation.

Considering an interelement spacing between array elements of $d_x = d_y = 0.48\lambda_0$, then the array factor can be expressed by:

$$AF(\psi)^{H,V} = AF(\psi_x)^{H,V}\, AF(\psi_y)^{H,V} = \\ = \sum_{m=1}^{5} E_m e^{j(m-1)(kd_x \sin\theta\cos\varphi + \alpha_i^{H,V})} \sum_{n=1}^{4} A_n^{H,V} e^{j(n-1)(kd_y \sin\theta \sin\varphi)} \tag{5.3}$$

Figure 5.26 depicts the subarray 5×4 model in HFSS, that is simulated to analyze the different amplitude and phase tapering values. The determination of the proper feeding coefficients is performed according to the following design goals:

- The triangular amplitude tapering has been already proved to be successful to reduce the side lobe level, when it has been applied in the prototype of the linear array 1×5. Thus, a triangular amplitude distribution is also used to excite the array elements in azimuth given by $A_i^{H,V}$, in order to achieve a side lobe level better than 18 dB, as specified in the system requirements listed in Table 4.1.
- Besides the side lobe level attenuation, the suppression in nadir direction has to be

maximized in order to mitigate the strong echoes coming from the perpendicular direction to the aircraft flight path.

- The same beam steering in elevation at $\theta = 42°$ is required. Thus, the analysis of the subarray leads to a slight redesign of the phase tapering that has to be applied ($\alpha_i^{H,V}$), in comparison with the simple case of a linear array 1×5. The triangular amplitude tapering in elevation $E_i^{H,V}$ remains the same.
- A reasonable low forward-to-backward ratio has to be fulfilled (FBW$\geq$15 dB) to attenuate the contributon of the opposite imaged area, known as opposite swath.

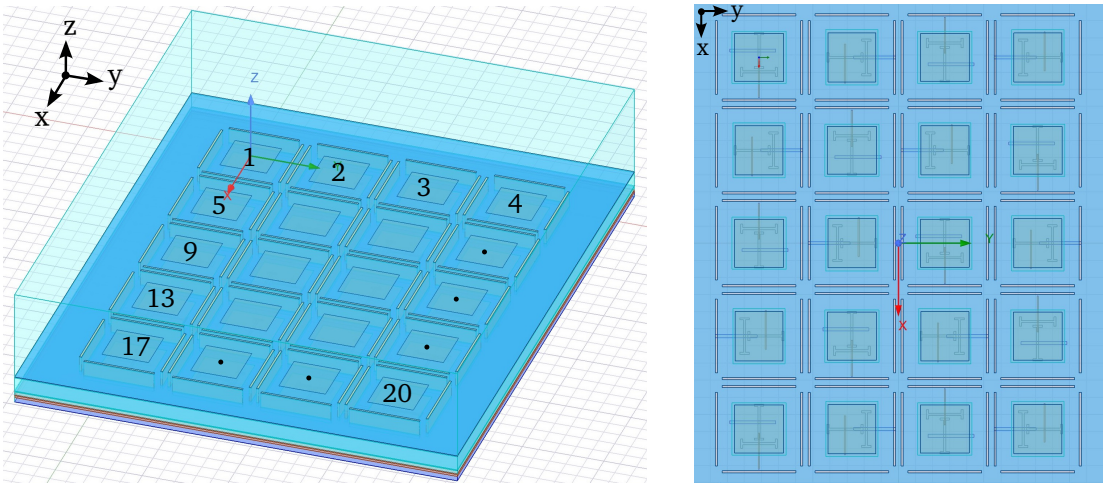

(a) (b)

Figure 5.26.: (a) Simulated HFSS model of the subarray 5×4 with element numeration. (b) Top view with the slots arrangement.

Amplitude tapering along azimuth direction

Since the final array 5×8 is based on two mirrored subarrays 5×4, the amplitude tapering in azimuth has to be asymmetric, as shown in Figure 5.2. After the optimization process to fulfill the aforementioned design goals, the normalized amplitude coefficients for each antenna element and polarization are listed in Table 5.5.

As it can be seen, the amplitude distribution for both polarizations is comparable to the tapering in elevation but slightly different. This is explained, as it will be shown later,

Vertical polarization			Horizontal polarization		
A_1^{V}	Linear	Log	A_1^{H}	Linear	Log
	0.185 W	-7.33 dBW		0.1 W	-10 dBW
A_2^{V}	Linear	Log	A_2^{H}	Linear	Log
	0.315 W	-5.01 dBW		0.3 W	-5.22 dBW
A_3^{V}	Linear	Log	A_3^{H}	Linear	Log
	0.5 W	-3.01 dBW		0.6 W	-2.22 dBW
A_4^{V}	Linear	Log	A_4^{H}	Linear	Log
	1 W	0 dBW		1 W	0 dBW

Table 5.5.: Normalized amplitude tapering along azimuth.

since the position of the feeding network for each polarization on the feeding substrate determines the electrical size of the microstrip lines and passive components, such as power dividers, couplers, etc. Thus, in order to exploit efficiently the lack of available space, and to enhance the isolation between the feeding networks, different power balancements have to be considered for each polarization. The design of passive components in microstrip technology can be found in Appendix C.

Amplitude tapering along elevation direction

The amplitude and phase tapering applied among the array elements in elevation are listed in Table 5.6. The same triangular amplitude distribution, as in previous examples, is considered. The phase coefficients have been slightly adapted to fulfill the required beam steering, along with the side lobe level reduction and nadir suppression.

The amplitude value applied to each array element can be calculated multiplying its azimuth coefficient $A_{\mathrm{i}}^{\mathrm{H,V}}$, given by the antenna element position within a subarray row, by the amplitude in elevation coefficient $E_{\mathrm{i}}^{\mathrm{H,V}}$, that corresponds to its subarray row. The resulting normalized amplitude for each array element is listed, respectively, in Tables 5.7 and 5.8 for the vertical and horizontal polarization.

Simulation results

The simulated S-parameters and radiation pattern in elevation of the subarray 5×4 are shown in Figures 5.27 and 5.28, respectively. The return loss level for a given array element i for the horizontal and vertical polarization $|S(H_{\mathrm{i}}, H_{\mathrm{i}})|$, $|S(V_{\mathrm{i}}, V_{\mathrm{i}})|$, corresponding to the element numeration of Figure 5.26a, are depicted in Figure 5.27a. It can be seen

Vertical polarization			Horizontal polarization		
V_1	E_1	α_1^{V}	H_1	E_1	α_1^{H}
	0.1 W	0°		0.1 W	0°
V_2	E_2	α_2^{V}	H_2	E_2	α_2^{H}
	0.5 W	135°		0.5 W	120°
V_3	E_3	α_3^{V}	H_3	E_3	α_3^{H}
	1 W	260°		1 W	235°
V_4	E_4	α_4^{V}	$H4$	E_4	α_4^{H}
	0.5 W	20°		0.5 W	0°
V_5	E_5	α_5^{V}	H_5	E_5	α_5^{H}
	0.1 W	145°		0.1 W	120°

Table 5.6.: Normalized amplitude and phase coefficients for each polarization.

Azimuth element / Elevation element	1	2	3	4
1	0.0185 W	0.0315 W	0.05 W	0.1 W
2	0.0925 W	0.1575 W	0.25 W	0.5 W
3	0.185 W	0.315 W	0.5 W	1 W
4	0.0925 W	0.1575 W	0.25 W	0.5 W
5	0.0185 W	0.0315 W	0.05 W	0.1 W

Table 5.7.: Normalized amplitude for each subarray element. Vertical polarization.

that, for most antenna elements, and due to the coupling among array elements, the return loss level is affected, usually shifting the center frequency of operation to higher frequencies. Several coupling levels between adjacent array elements for each polarization $|S(H_{\mathrm{i}+1}, H_{\mathrm{i}})|$, $|S(V_{\mathrm{i}+1}, V_{\mathrm{i}})|$ are plotted in Figure 5.27b. The isolation levels for the center frequency of operation are quite comparable for both polarizations, regardless if an E-plane or H-plane coupling occurs, as already shown in Figure 5.8.

The simulated normalized radiation pattern of the subarray 5×4 in elevation ($\varphi = 0°$) for both polarizations are depicted in Figures 5.28a and 5.28b. The antenna gain is 13.47 dBi and 15.09 dBi for the vertical and horizontal polarization, respectively. It can be noted that for both polarizations, a side lobe level better than 19 dB is achieved, as well as a nadir suppression higher than 30 dB. In addition, a forward to backward ratio better than

Azimuth element / Elevation element	1	2	3	4
1	0.01 W	0.03 W	0.06 W	0.1 W
2	0.05 W	0.15 W	0.3 W	0.5 W
3	0.1 W	0.3 W	0.6 W	1 W
4	0.05 W	0.15 W	0.3 W	0.5 W
5	0.01 W	0.03 W	0.06 W	0.1 W

Table 5.8.: Normalized amplitude for each subarray element. Horizontal polarization.

15 dB is also fulfilled. Despite that the cross-polarization suppression levels are satisfactory, achieving maximal values in the main beam around 29 dB, they will be improved for the final antenna 5×8, when a symmetric amplitude tapering in azimuth is applied. Despite the proximity between array elements, enhanced beamforming capabilities are achieved, that allow to shape the radiation pattern accurately.

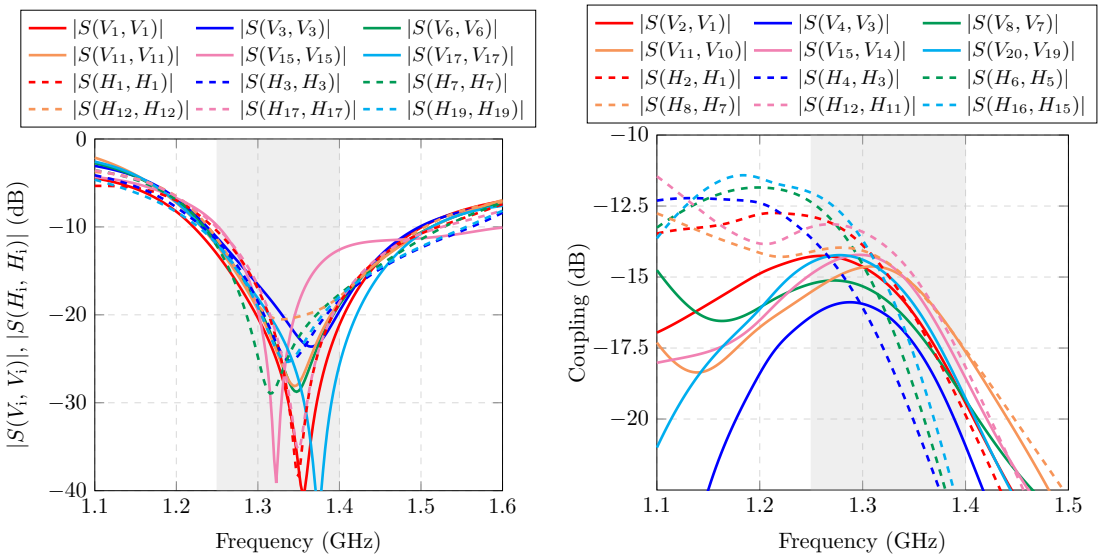

Figure 5.27.: Simulated S-parameters of the subarray 5×4. (a) Reflection factors. (b) Coupling between array elements.

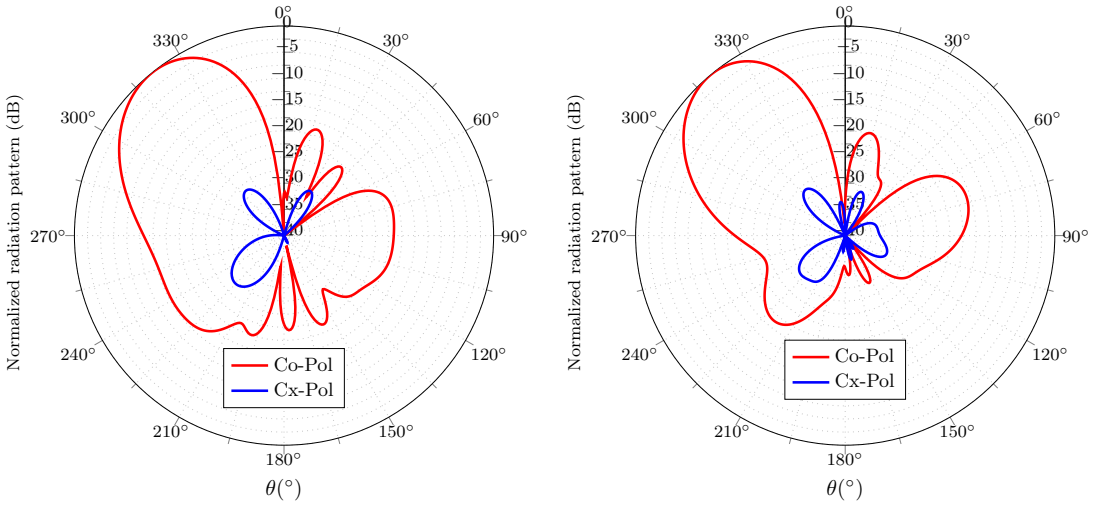

Figure 5.28.: Simulated normalized co-polar and cross-polar patterns in elevation ($\varphi = 0°$). (a) Vertical polarization. (b) Horizontal polarization.

5.2.4. Design of the azimuth feeding network

After determining the required amplitude distribution in azimuth, the next design step is to implement it by means of an integrated feeding network.

The azimuth feeding network excites the polarization of each subarray row i given by the feeding ports $H_\mathrm{i}, V_\mathrm{i}$, as depicted in Figure 5.25. Thus, each azimuth feeding row excites the four antenna elements in phase, and provides the asymmetric amplitude distribution according to the values shown in Table 5.5.

Design approach

The design of the feeding network in azimuth is divided in pairs of feeding rows, one for each polarization, that excite the four antenna elements of each subarray row. The following design steps have been performed in order to design the azimuth feeding network:

- The amplitude tapering is realized combining balanced and unbalanced Wilkinson power dividers along with 10-dB coupler lines. The layout for each polarization

network differs, leading to slightly distinct power balancements, since the electrical size of the feeding network for the horizontal polarization demands more space. Further information about the design of power dividers and other passive components in microstrip technology, that are used in this work, are presented in Appendix C.

- As a passive feeding network, each array element is excited with a phase given by the electrical path between its coupling slot and the input of the feeding network. In order to excite all the antenna elements in phase, the phase difference that has to be applied due to the different slot arrangements is considered and compensated in the electrical path.
- Since the slope of the phase variation is given by the electrical length of the feeding line, a comparable electrical path in terms of wavelengths, between the feeding input and the slots, is required. A detailed explanation can be found in Appendix C.
- In order to enhance the isolation between both polarization networks, each layout is optimized to exploit efficiently the available space on the substrate, thus preventing the intersection between different polarization feeding lines. This design aspect determines the feeding orientation of the microstrip lines (±x, ±y) depending on the position of the power dividers by which, in some cases, an out of phase difference has to be compensated, increasing the electrical length of the line by 180°.

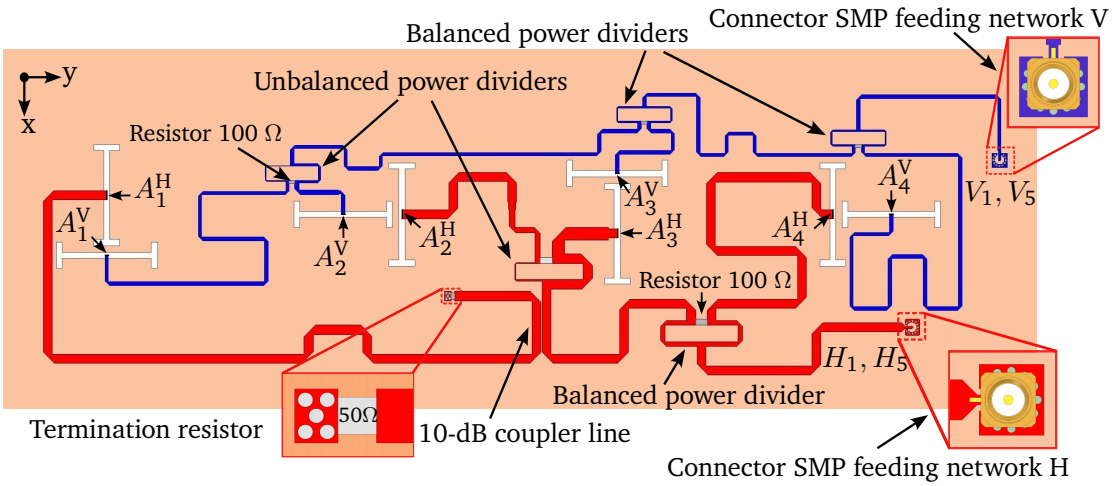

Figure 5.29.: Design approach of the azimuth network. Slots are non-model objects.

Figure 5.29 depicts an example of the design of the first and fifth row of the azimuth feeding network. Due to the sequential rotation, the slot geometry of both subarray rows

coincides, thus the same network layout can be used to excite both rows. Each polarization feeding network is excited with an SMP connector at the input H_1, H_5 and V_1, V_5, and the power is distributed until each output $A_{\mathrm{i}}^{H,V}$ where a lumped port is placed. The position of each output corresponds to the center of the slot by which non-model slot objects are used as a reference. The Wilkinson and termination resistances are implemented by means of resistive thin films [101]. This technology has been succesfully tested on purpose, and related information is presented in Appendix C.

Table 5.9 shows the amplitude and phase values applied to each output. The power ratio agrees with the normalized amplitude distribution listed in Table 5.5, considering that the array element 4 ($A_4^{H,V}$) is excited with almost half of the available power. The feeding phase coefficients coincide with the values obtained in Table 5.4, except for the elements 2 and 4 of the vertical polarization and element 3 of the horizontal, since the orientation of the microstrip lines have been changed and, thus, a phase inversion has to be applied (+180°). This is explained since the network layout is optimized to exploit the limited available space, as well as to enhance the isolation between both polarization feeding networks, which leads to a given geometrical arrangement of the power dividers that determines the orientation of the feeding lines.

Vertical polarization			**Horizontal polarization**		
Element 1	A_1^{V}	φ_1	Element 1	A_1^{H}	φ_1
	-10.9 dB	0°		-14.9 dB	0°
Element 2	A_2^{V}	φ_2	Element 2	A_2^{H}	φ_2
	-8.7 dB	35°+180°		-9.5 dB	-35°+180°
Element 3	A_3^{V}	φ_3	Element 3	A_3^{H}	φ_3
	-6.6 dB	180°		-5.7 dB	0°
Element 4	A_4^{V}	φ_4	Element 4	A_4^{H}	φ_4
	-3.6 dB	35°		-3.8 dB	-35°

Table 5.9.: Amplitude and phase at each output port of the feeding network.

The simulated S-parameters of the feeding network are shown in Figure 5.30. It can be noted that the reflection factor $|S(H_{\mathrm{i}}, H_{\mathrm{i}})|, |S(V_{\mathrm{i}}, V_{\mathrm{i}})|$ for both polarizations is lower than -20 dB for the operational bandwidth, and better than -30 dB for the center frequency of operation. The isolation between both feeding networks $S(H_{\mathrm{i}}, V_{\mathrm{i}})$ is really high, with values mainly better than 40 dB for the frequency range of operation.

The same methodology is applied for the remaining azimuth feeding networks designed to excite both polarizations of each subarray row. The final layout is shown in Figure 5.31.

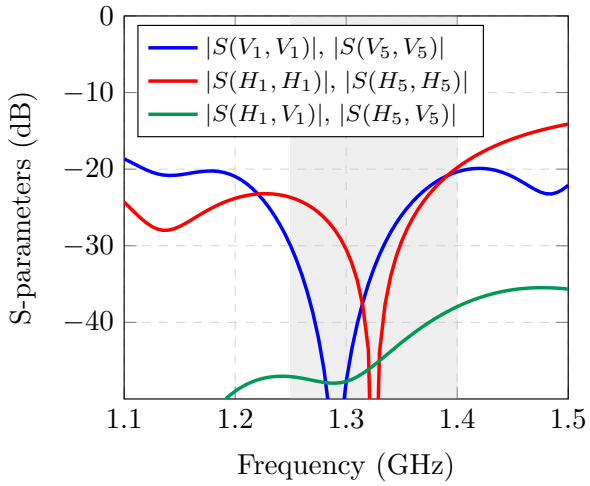

Figure 5.30.: Return loss and isolation between polarization feeding networks.

Due to manufacturing limitations, the size of the feeding network has been reduced to meet the maximal standard substrate panel size that is available (610 mm $\times$ 460 mm).

Simulation results of the subarray 5$\times$4 with the integrated azimuth feeding network

Figure 5.32a shows the simulated subarray in HFSS with the azimuth feeding network.

In order to prepare the electrical design for construction purposes, some screw holes have been added to allow the attachment of the azimuth feeding network to the ground plane, as well as the covering top plate. The slots on the aluminum ground plane are slightly larger than the ones etched on the copper ground layer of the feeding network, in order to deal with a possible misalignment due to manufacturing or construction tolerances. For simplicity, the spacing between truncated walls has been considered as one solid aluminum wall. Since the patch sizes for the antenna elements A and B are slightly different, and in order to simplify the manufacturing, the top and bottom patch sizes are unified, having the length and width values listed in Table 5.10.

$patch1\_l$	58	$patch1\_w$	59.4	$patch2\_l$	63	$patch2\_w$	66

Table 5.10.: Final patch sizes (in mm).

In addition, the simulated HFSS model also includes a holding structure, placed below the antenna, that enables its mechanical attachment on the CTR positioner.

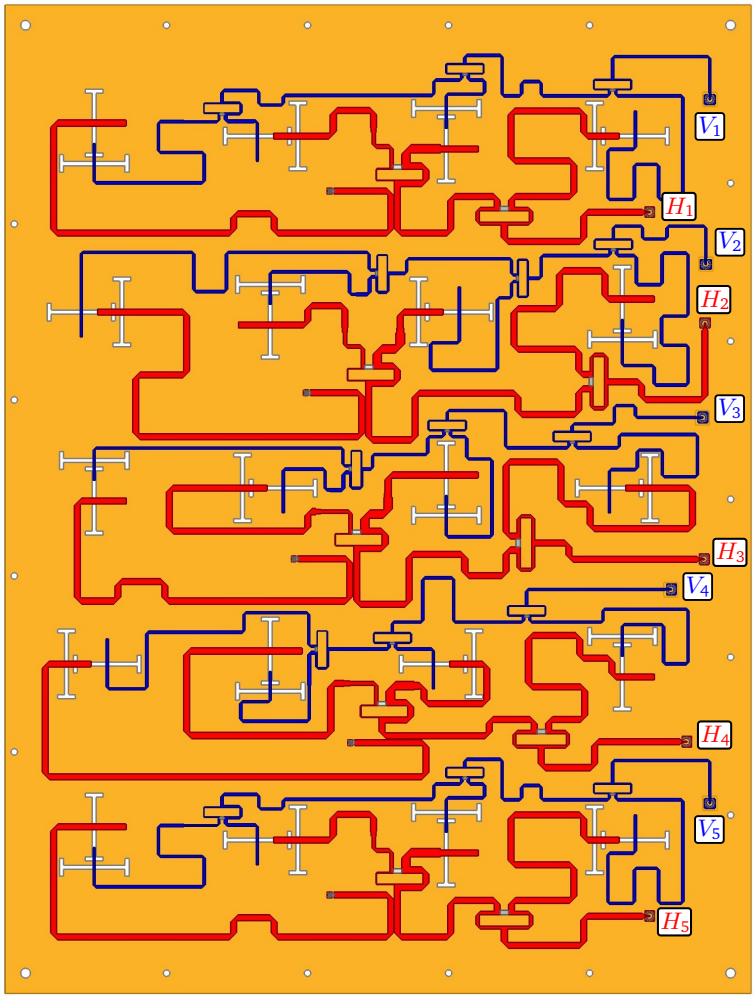

Figure 5.31.: Layout of the azimuth feeding network (top view). The overall size of the feeding network has been reduced to meet the maximal standard substrate panel size available by the manufacturer. The layout of the first and fifth rows coincide with the one depicted in Figure 5.29.

The radiation pattern in elevation of the subarray 5×4 with the integrated azimuh feeding network, and compared with the results of the subarray with independent array element excitation, are shown in Figure 5.33.

The performance of the azimuth feeding network can be assessed by examining the

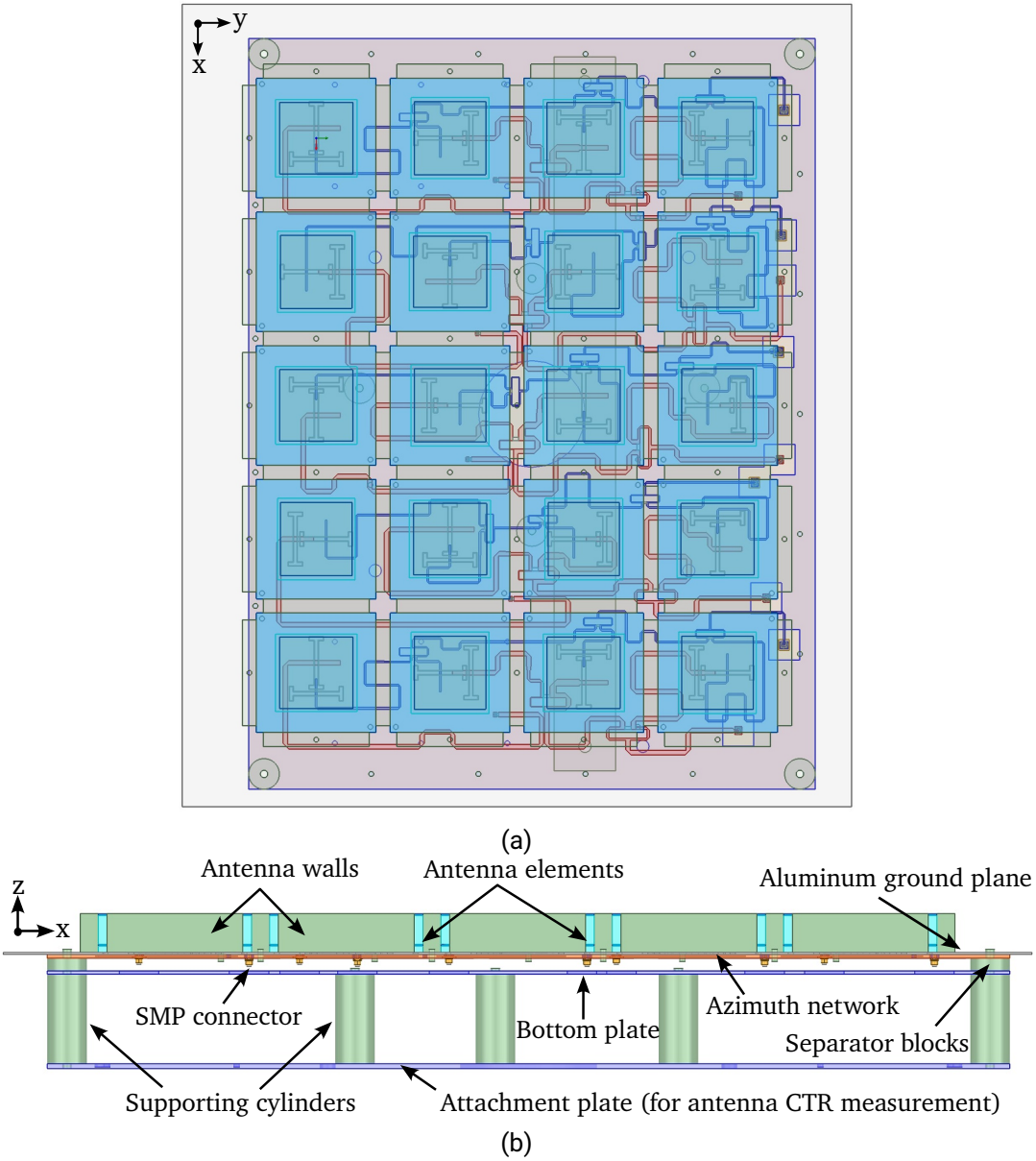

Figure 5.32.: Simulated HFSS model of the subarray 5×4 with integrated azimuth network and CTR attachment suporting structure. (a) Top view. (b) Side view.

radiation pattern in the azimuth direction (plane YZ), that will be shown later. Nevertheless, the radiation pattern in elevation is a good indicator of the subarray performance. It can be noted the excellent agreement of the radiation patterns in elevation, with and without the azimuth feeding network. These results clearly confirm the antenna beamforming capabilities, not only due to the good isolation between array elements but also among each polarization feeding row.

The phase coefficients in elevation for the horizontal polarization have been slightly adapted, in order to achieve a comparable elevation pattern, as shown in Figure 5.33b. The phase values are listed in Table 5.11. The beam steering values for the vertical polarization remain unaltered.

The simulated gain with the integrated azimuth network is 13.31 dBi and 14.47 dBi for the vertical and horizontal polarization, respectively. The values are slightly lower than the case without feeding network, due to the additional substrate losses.

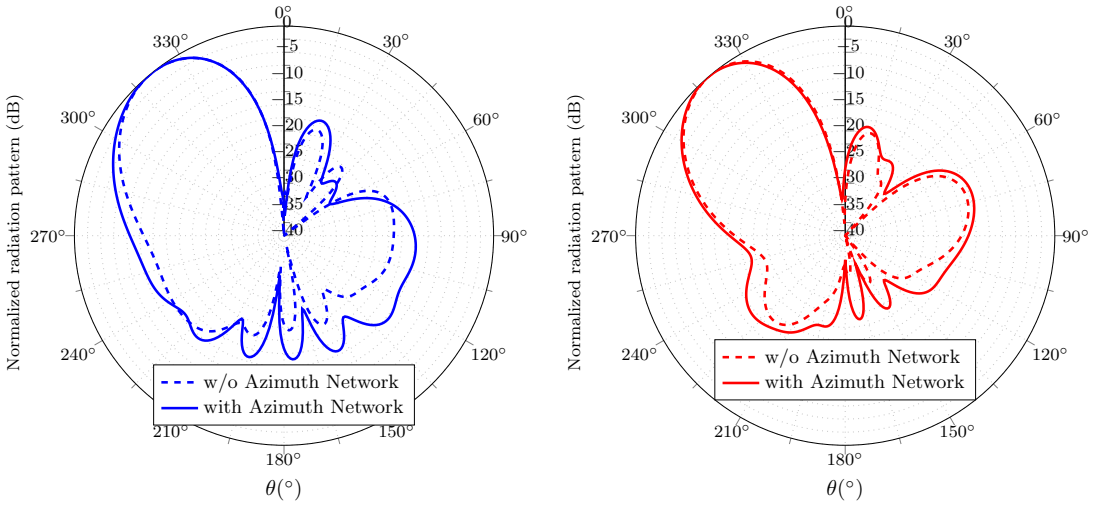

Figure 5.33.: Comparison simulated subarray pattern in elevation with and w/o azimuth feeding network. (a) Vertical polarization. (b) Horizontal polarization.

α_1^H	0°	α_2^H	115°	α_3^H	230°	α_4^H	5°	α_5^H	125°

Table 5.11.: Final phase coefficients in elevation. Horizontal polarization.

5.2.5. Measurements of a manufactured subarray 5×4 prototype

The subarray 5×4, depicted in Figure 5.32, has been manufactured, constructed and measured. Figures 5.34a and 5.34b show the aluminum structure with the antenna ground plane along with the walls, and the manufactured azimuth feeding network, respectively.

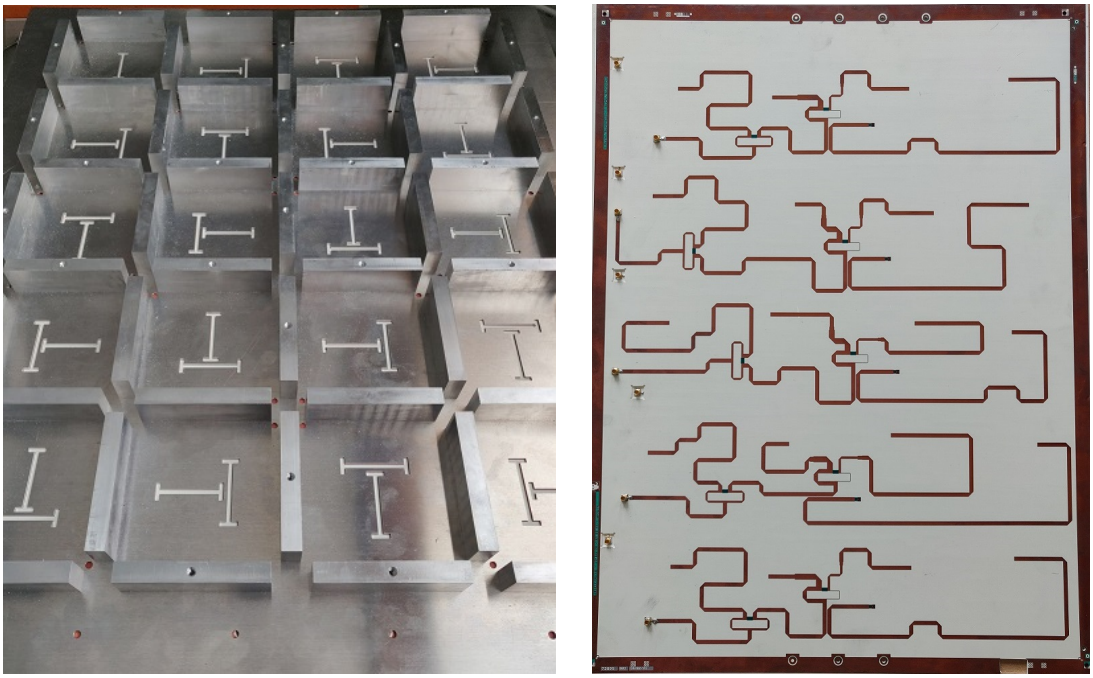

(a) (b)

Figure 5.34.: Manufactured subarray 5×4 prototype. (a) Aluminum structure. (b) Azimuth feeding network with soldered SMP connectors.

The final constructed prototype, installed on the CTR positioner for its measurement, is shown in Figure 5.35a. The elevation network is implemented in the same way as for the linear array, by means of 1:6 power dividers, attenuators and custom made cables. The side view of the antenna, depicted in Figure 5.35b, shows the assembled elevation network.

In order to fully characterize the peformance of the manufactured subarray prototype, the S-parameters at the azimuth feeding network, as well as the radiation pattern are measured, and the results are discussed next.

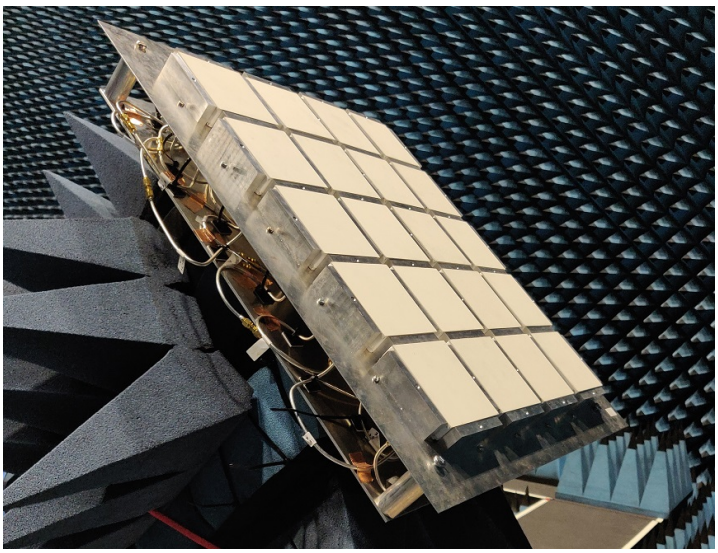

(a)

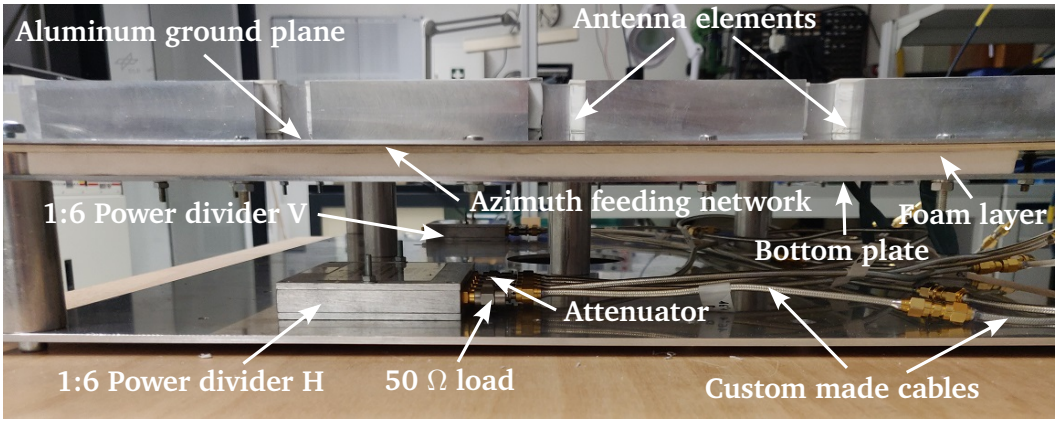

(b)

Figure 5.35.: Prototype subarray 5×4. (a) Installed on the CTR positioner. (b) Side view.

Measurement of the S-parameters

The measured S-parameters at the input of each azimuth feeding row are shown in Figure 5.36. Measurements show a consistent good machting level $|S(H_\mathrm{i}, H_\mathrm{i})|, |S(V_\mathrm{i}, V_\mathrm{i})|$ for both polarization networks, with values better than 10 dB within the antenna bandwidth and higher than 15 dB at the center frequency of operation. The coupling levels between

two closely located feeding rows of the same polarization network $|S(H_{i+1}, H_i)|$, $|S(V_{i+1}, V_i)|$ are mainly better than -20 dB for the center frequency band, despite the proximity of array elements. The measured polarization isolation levels $|S(H_i, V_i)|$ are greater than 25 dB.

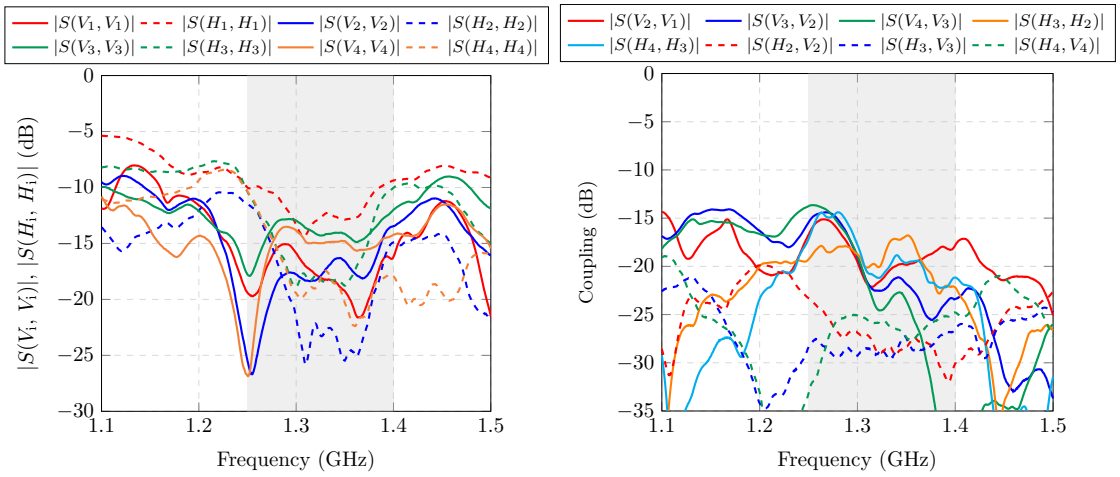

(a) (b)

Figure 5.36.: Measured S-parameters of the manufactured subarray. (a) Reflection factor. (b) Coupling and polarization isolation values.

Measurement of the radiation pattern

The radiation pattern of the manufactured subarray is measured in the CTR. In order to avoid the interaction of the radiated fields with the sharp edges of the aluminum ground plane, an absorber collar is placed around the ground plane, as shown in Figure 5.37. Thus, a direct comparison with the simulated model of Figure 5.32 can be performed.

The measured radiation pattern in elevation, at the center frequency of operation, is plotted in Figure 5.38. It can be noted the good agreement between measurement and simulation for both polarizations, especially regarding the main beam. The influence of the absorber collar is more visible for the vertical polarization, since the beamforming takes place along the E-plane, by which the radiation at lower elevation angles ($90° \leq \theta \leq 270°$) is reduced. On the other side, the nadir suppression for the horizontal polarization is replaced by a side lobe level of approximately 20 dB, probably due to a phase innacuracy in the elevation feeding network. The measured directivities are 15.82 dBi and 15.52 dBi

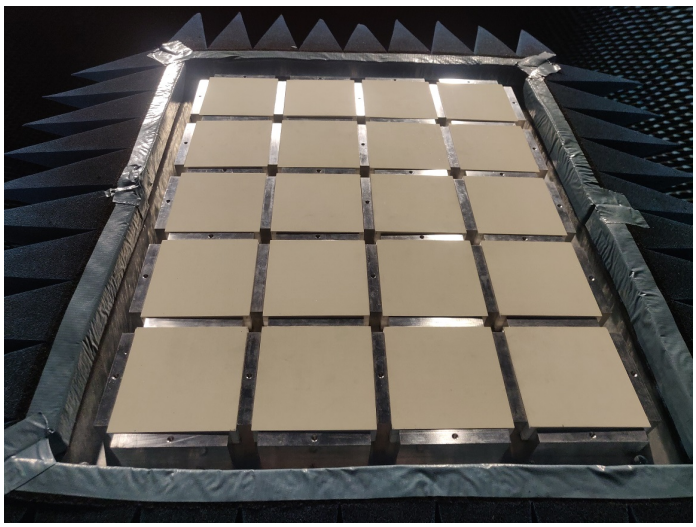

Figure 5.37.: Measurement of the subarray with absorber collar around the ground plane.

for the vertical and horizontal polarization, respectively, which are approximately 1 dB and 0.2 dB higher than the simulated values.

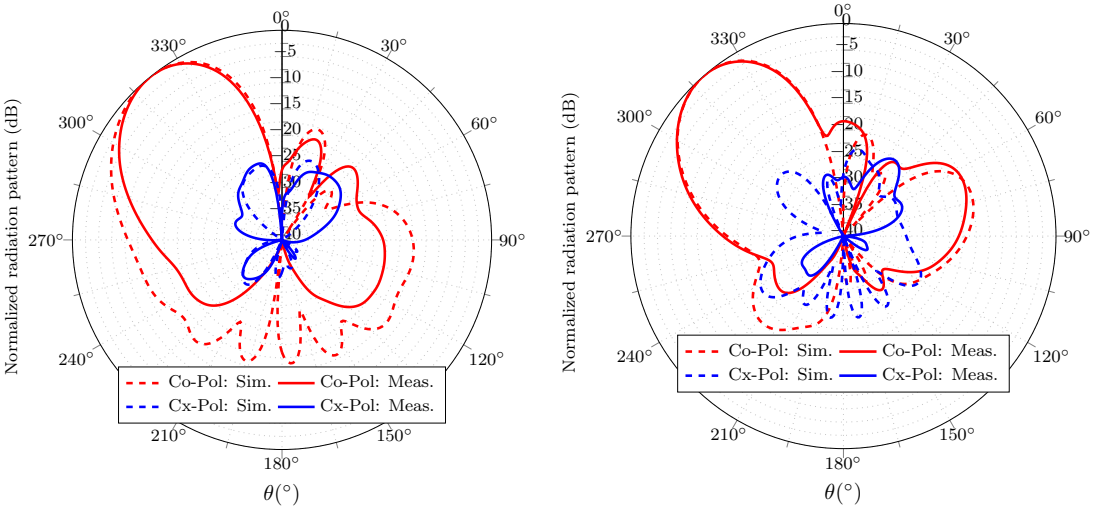

Figure 5.38.: Measured radiation pattern in elevation. (a) Vertical pol. (b) Horizontal pol.

The measured radiation pattern in azimuth is depicted in Figure 5.39. The pattern is not entirely symmetric due to the amplitude tapering in azimuth. This pattern asymmetry will be compensated adding the second mirrored subarray, when the final antenna is built. Despite that the effect of the absorber is also visible in the measurement of the vertical polarization, an overall good agreement with the simulation is achieved. The cross-polarization levels in azimuth are higher than in elevation, since in the azimuth plane, which corresponds to the plane YZ tilted by the maximum in elevation ($\theta = -42°$), is near to $\theta = \pm 45°$, where the cross-polarization levels are the highest ones.

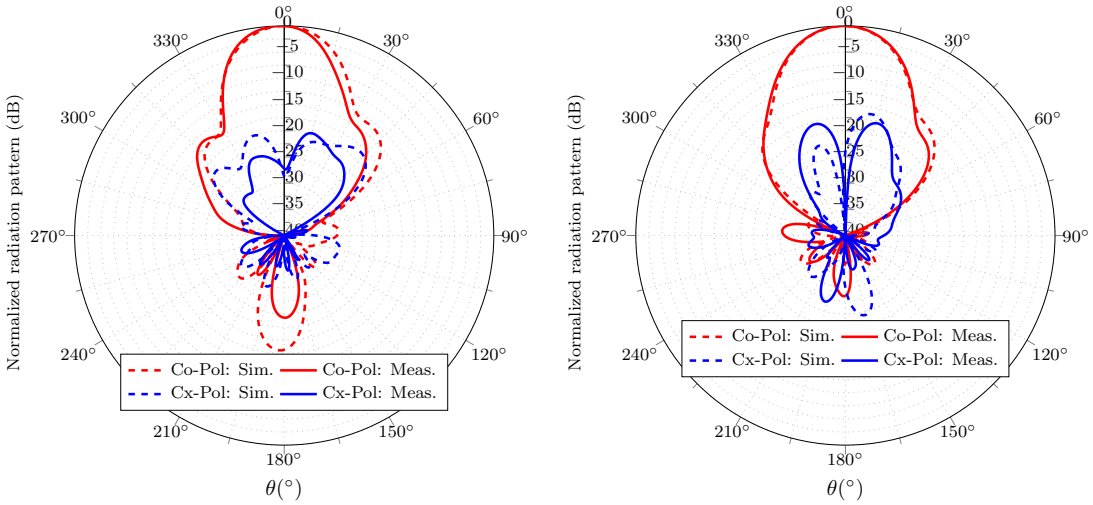

Figure 5.39.: Measured radiation pattern in azimuth (a) Vertical pol. (b) Horizontal pol.

Finally, a comparison of the measured elevation patterns for different frequencies, within the operational bandwidth, are plotted in Figure 5.40. The vertical polarization is slighty more sensitive to the frequency variation, especially regarding the main beamwidth. This can also be explained due to the effect of the absorber collar. Nevertheless, measurements show a good frequency stability of the radiation pattern in elevation for both polarizations.

After validating the electrical performance of the subarray 5×4, the final antenna array 5×8 can be designed by means of two mirrored subarrays. In this final development phase, the feeding network in elevation is also designed and integrated within the antenna housing, as it is presented next.

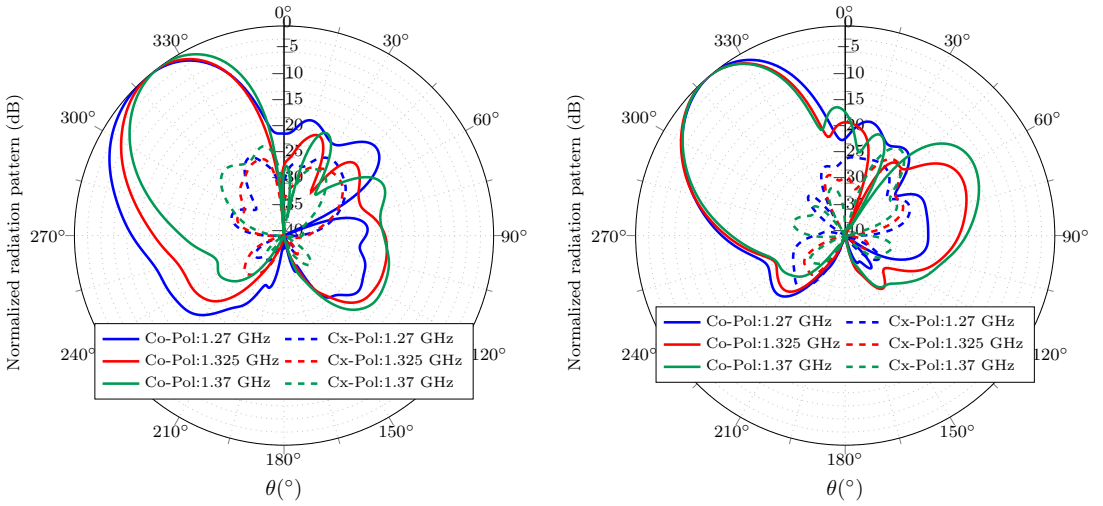

(a) (b)

Figure 5.40.: Measured radiation pattern in elevation for 1.27 GHz, 1.325 GHz and 1.37 GHz. (a) Vertical polarization. (b) Horizontal polarization.

5.3. Design of the final planar phased array 5×8

The final planar phased array 5×8 can now be arranged, combining two mirrored electrical identical subarrays 5×4. Thereby, the previous subarray concept can be extended to build the final phased array antenna without an additional azimuth feeding network redesign.

The feeding scheme of the final antenna is depicted in Figure 5.41. As it is seen, the final antenna is composed of subarray A and subarray B, that is an electrical equivalent subarray A but mirrored, thus leading to a symmetric triangular amplitude distribution along azimuth. The feeding inputs of the azimuth network for the excitation of each subarray row are identified as $H_{1\text{-}5}, V_{1\text{-}5}$ and $H_{\text{A-E}}, V_{\text{A-E}}$ for the subarray A and B, respectively. The same beamforming configuration in elevation is applied, thereby providing equal amplitude $E_{1\text{-}5}, E_{\text{A-E}}$ and phase distribution $\varphi_{1\text{-}5}^{\text{H,V}}, \varphi_{\text{A-E}}^{\text{H,V}}$ to each subarray.

The array factor can be thus described by:

$$\begin{aligned} AF(\psi)^{\text{H,V}} &= AF(\psi_{\text{x}})^{\text{H,V}}\, AF(\psi_{\text{y}})^{\text{H,V}} = \\ &= \sum_{m=1}^{5} E_{\text{m}} e^{j(m-1)(kd_{\text{x}}\sin\theta\cos\varphi+\alpha_{\text{i}}^{\text{H,V}})} \sum_{n=1}^{8} A_{\text{n}}^{\text{H,V}} e^{j(n-1)(kd_{\text{y}}\sin\theta\sin\varphi)} \end{aligned} \tag{5.4}$$

where, due to the antenna symmetry:

$$A^{\mathrm{H,V}}_{(\mathrm{i}+4)} = A^{\mathrm{H,V}}_{(5\text{-}\mathrm{i})}\,, i \in [1,4] \text{ and } E_{\mathrm{A}} = E_1,\ E_{\mathrm{B}} = E_2,\ E_{\mathrm{C}} = E_3,\ E_{\mathrm{D}} = E_4,\ E_{\mathrm{E}} = E_5$$

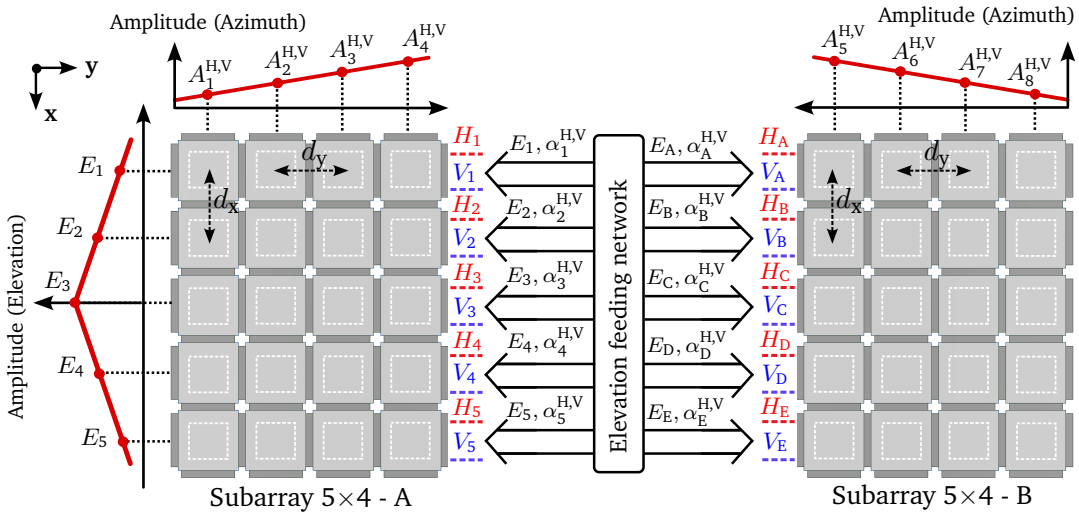

Figure 5.41.: Feeding configuration of the final array 5×8.

5.3.1. Simulation results

The first simulated HFSS model of the final antenna, based on two mirorred subarrays as it has been shown in Figure 5.32a, is depicted in Figure 5.42. The azimuth feeding network of both subarrays is shown in Figure 5.43. Due to manufacturing constraints, the connector position of each feeding row has been slightly shifted to assure a safe distance to the edge of the substrate panel. Due to the subarray mirroring, the slots of the horizontal polarization for the subarray B are excited from the opposite direction in comparison with the subarray A. Thus, the resulting out of phase has to be compensated adding 180°.

The final amplitude and phase distribution in elevation for each polarization and subarray is listed in Table 5.12.

The simulated radiation pattern in elevation is shown in Figure 5.44. The gain values for the vertical and horizontal polarization are 16.42 dBi and 17.31 dBi respectively, becoming 3 dB higher in comparison with the case of a single subarray, due to the addition of the second mirrored one. It can be noted the good nadir suppression, with values higher than 30 dB, and the side lobe level better than 20 dB for both polarizations.

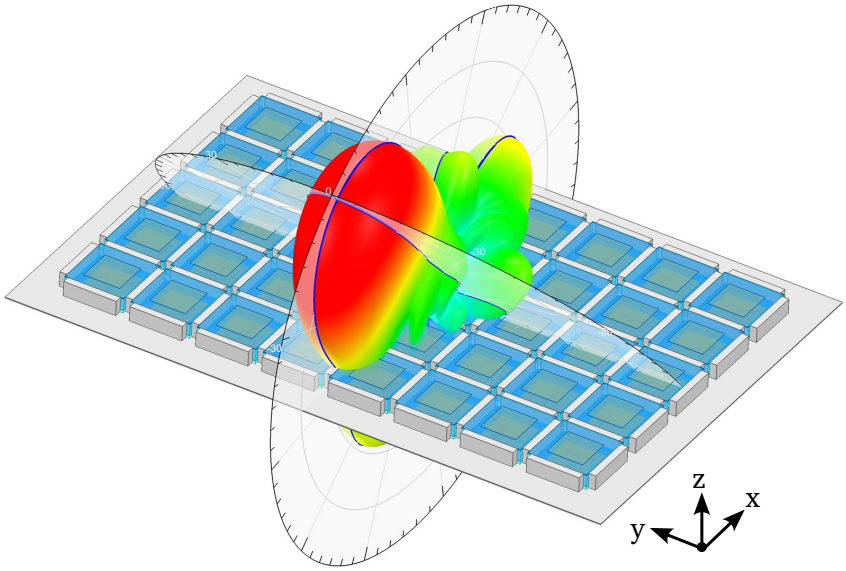

Figure 5.42.: Simulated HFSS model of the final array 5×8. 3D radiation pattern with two principal cuts.

Vertical polarization						**Horizontal polarization**					
V_1	E_1	α_1^V	V_A	E_A	α_A^V	H_1	E_1	α_1^H	H_A	E_A	α_A^H
	0.1 W	0°		0.1 W	0°		0.1 W	0°		0.1 W	0°+180°
V_2	E_2	α_2^V	V_B	E_B	α_B^V	H_2	E_2	α_2^H	H_B	E_B	α_B^H
	0.5 W	140°		0.5 W	140°		0.5 W	105°		0.5 W	105°+180°
V_3	E_3	α_3^V	V_C	E_C	α_C^V	H_3	E_3	α_3^H	H_C	E_C	α_C^H
	1 W	260°		1 W	260°		1 W	220°		1 W	220°+180°
V_4	E_4	α_4^V	V_D	E_D	α_D^V	H_4	E_4	α_4^H	H_D	E_D	α_D^H
	0.5 W	25°		0.5 W	25°		0.5 W	-5°		0.5 W	-5°+180°
V_5	E_5	α_5^V	V_E	E_E	α_E^V	H_5	E_5	α_5^H	H_E	E_E	α_E^H
	0.1 W	145°		0.1 W	145°		0.1 W	115°		0.1 W	115°+180°

Table 5.12.: Normalized amplitude and phase coefficients in elevation for each polarization and subarray.

Due to the low cross-polarization levels achieved and for the clarity of representation, the co-polar and cross-polar patterns in elevation of Figure 5.45 are plotted in cartesian

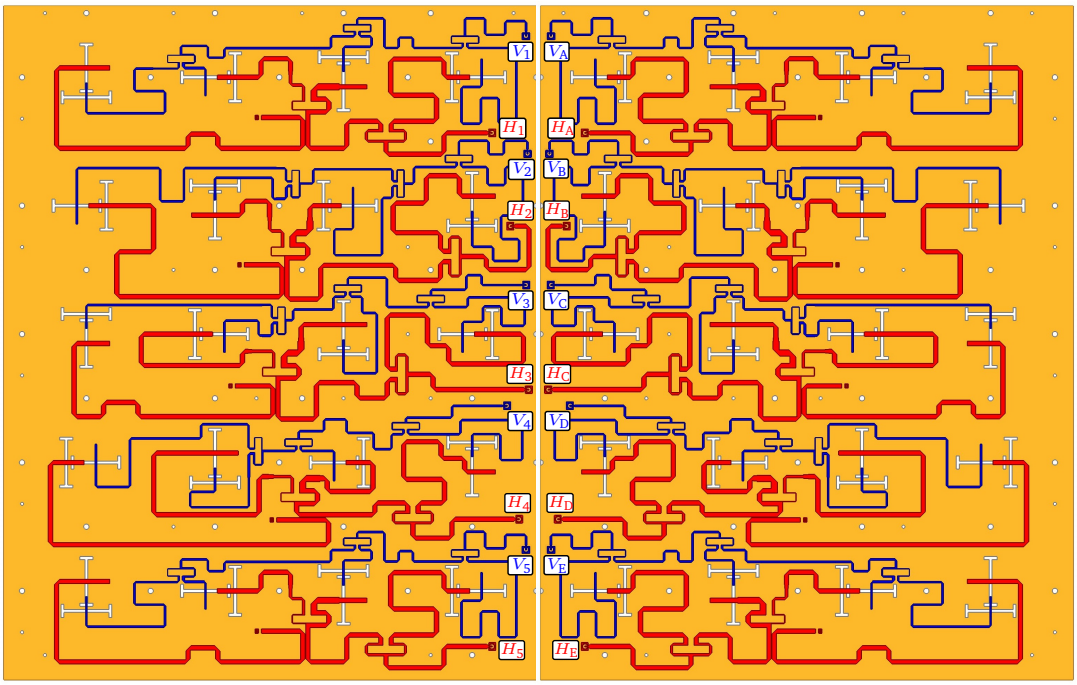

Azimuth feeding network subarray A Azimuth feeding network subarray B

Figure 5.43.: Azimuth feeding network for subarray A and B.

representation. It can be seen that the cross-polarization levels are considerably better than 40 dB, achieving excellent cross-polarization suppression values beyond 50 dB.

Figure 5.46 plots the simulated azimuth pattern for both polarizations. It can be noted the symmetry of the azimuth pattern in comparison with the case of the subarray 5×4.

5.3.2. Design of the elevation feeding network

The elevation feeding network is designed in order to provide the amplitude and phase excitation according to Table 5.12. The feeding network is implemented in microstrip technology on a substrate Rogers RO4360G2 ($\varepsilon_\mathrm{r} = 6.15, \tan\delta = 0.0038$), and with a thickness $h = 1.22$ mm.

The power distribution is achieved by means of a different Wilkinson dividers, working as power splitters and combiners, along with 10 dB coupling lines, as depicted in Figure 5.47. Due to the lack of space and the physical separation of the two subarray azimuth feeding networks, the excitation of the feeding rows for each subarray $H_{1\text{-}5}/H_{\text{A-E}}$ and $V_{1\text{-}5}/V_{\text{A-E}}$ are

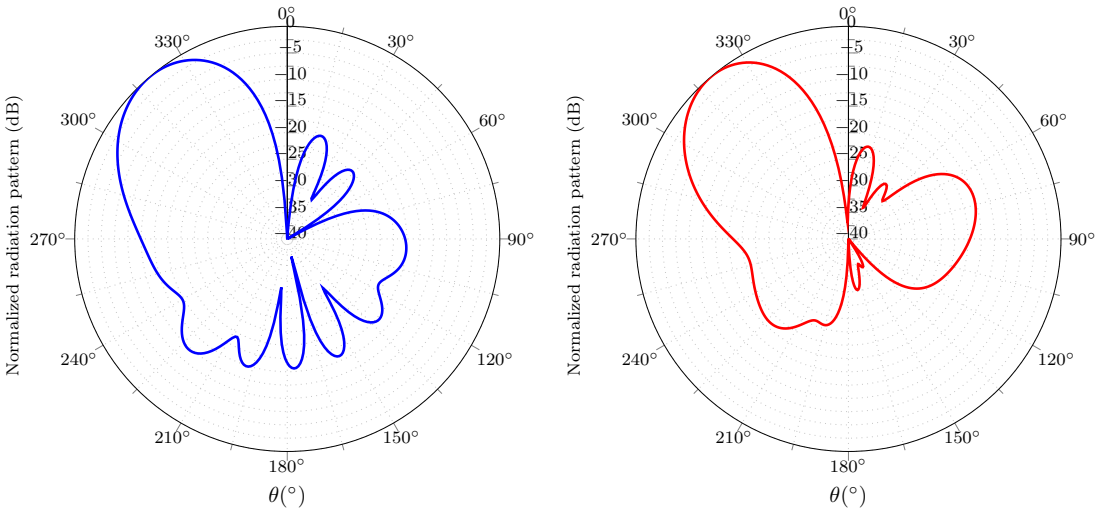

(a) (b)

Figure 5.44.: Simulated radiation pattern in elevation of the final array 5×8. (a) Vertical polarization. (b) Horizontal polarization.

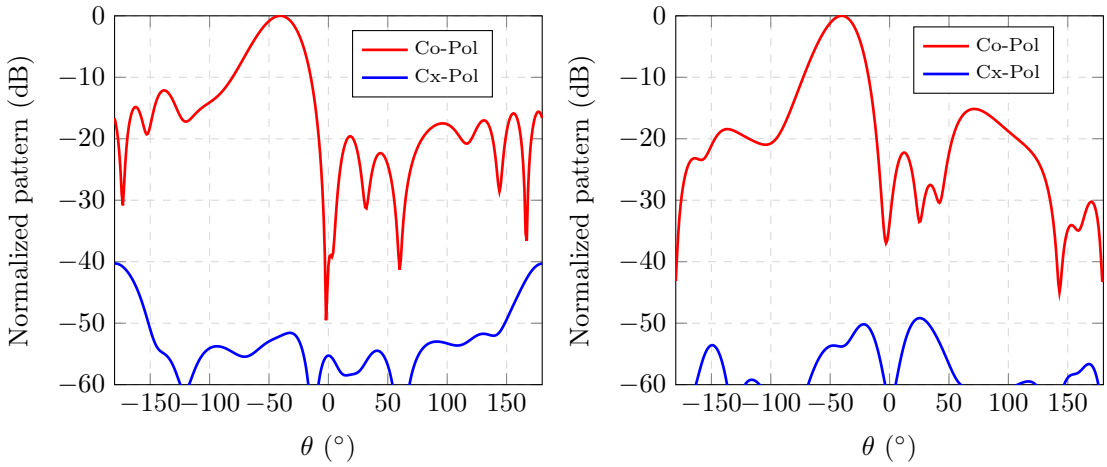

(a) (b)

Figure 5.45.: Normalized co-polar and cross-polar patterns in elevation of the final array 5×8. (a) Vertical polarization. (b) Horizontal polarization.

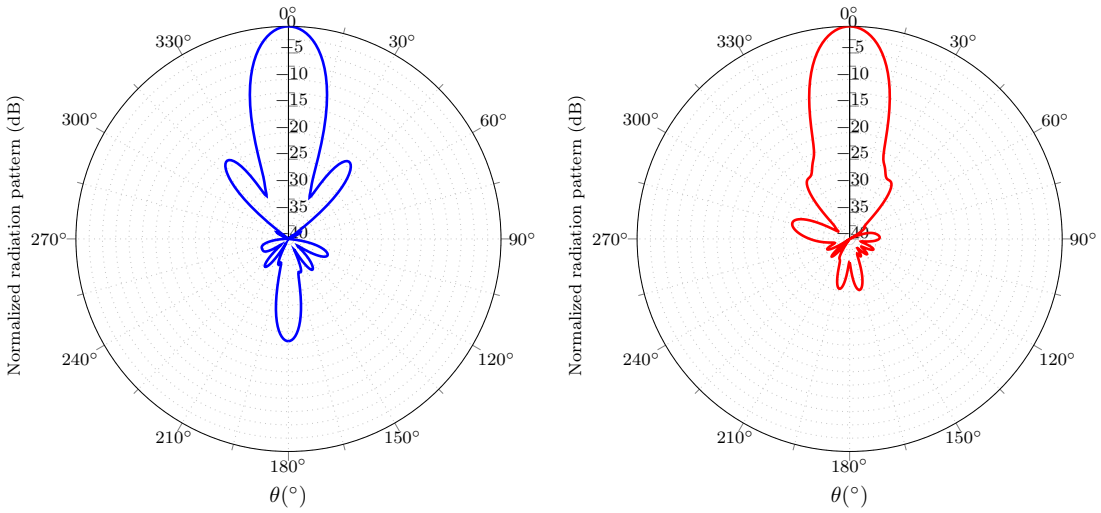

Figure 5.46.: Simulated radiation pattern in azimuth of the final array 5×8. (a) Vertical polarization. (b) Horizontal polarization.

performed in the last phase of the elevation network. A 180° phase difference is applied between the ports of each subarray for the horizontal polarization $H_{1\text{-}5} - H_{\text{A-E}}$ due to the mirrored symmetry of the array excitation.

It can be noted that the resistors of the Wilkinson dividers are not implemented by means of resistive thin films, but by discrete resistors. The reason for this decision is the power levels that the elevation feeding network has to endure, with pulse peak power of 1 kW, and the power handling capabilites of the resistor films. More information about this topic can be found in Appendix C. Precisely, for this reason, connectors type N model 864L1 are used to excite the elevation feeding network, due to their increased power handling in comparison with standard SMA connectors.

The interconnection between the azimuth and elevation feeding networks is performed using adjustable SMP adapters. The spring mechanism of the SMP adapters allows to firmly connect the SMP connectors of the elevation network, that are located on the same level, with those of the azimuth feeding network, that are placed on different substrate positions. Thus, a higher degree of integration can be achieved, preventing the use of internal cables.

The amplitude and phase values obtained at each output port of the elevation feeding network are listed in Table 5.13. It can be noted that the power amplitude at each

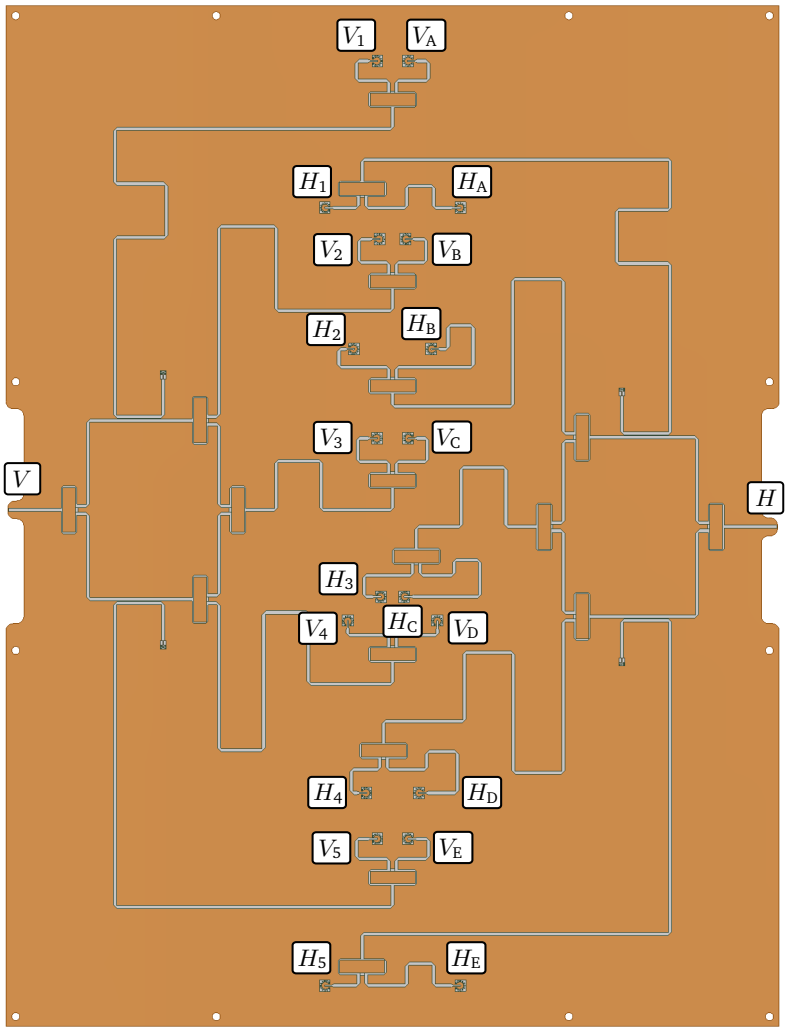

Figure 5.47.: Layout elevation feeding network.

port is not the same value as shown in Table 5.12, considering its equivalent in linear or logarithmic scale, but it does have the same normalized power distribution. This is explained since the elevation feeding network is a passive network, by which the feeding input power is necessarily distributed along the circuit, leading to negative power values in logarithmic scala at the output ports. On the other side, the phase difference values between ports $|\alpha_{i+1}^{H,V} - \alpha_{i}^{H,V}|$ coincide with the phase values listed in Table 5.12.

Vertical polarization			Horizontal polarization		
V_1	E_1	α_1^{V}	H_1	E_1	α_1^{H}
	-17.27 dB	-124.17°		-17.24 dB	-101.93°
V_{A}	E_{A}	$\alpha_{\mathrm{A}}^{\mathrm{V}}$	H_{A}	E_{A}	$\alpha_{\mathrm{A}}^{\mathrm{H}}$
	-17.24 dB	-124.11°		-17.34 dB	-78.6°
V_2	E_2	α_2^{V}	H_2	E_2	α_2^{H}
	-10.07 dB	15.88°		-10.04 dB	2.79°
V_{B}	E_{B}	$\alpha_{\mathrm{B}}^{\mathrm{V}}$	H_{B}	E_{B}	$\alpha_{\mathrm{B}}^{\mathrm{H}}$
	-10.04 dB	15.94°		-10.15 dB	-176.94°
V_3	E_3	α_3^{V}	H_3	E_3	α_3^{H}
	-7.04 dB	135.7°		-6.98 dB	118.45°
V_{C}	E_{C}	$\alpha_{\mathrm{C}}^{\mathrm{V}}$	H_{C}	E_{C}	$\alpha_{\mathrm{C}}^{\mathrm{H}}$
	-7.01 dB	135.66°		-7.11	-61.27°
V_4	E_4	α_4^{V}	H_4	E_4	α_4^{H}
	-10.1 dB	-99.23°		-10.07 dB	-106.44°
V_{D}	E_{D}	$\alpha_{\mathrm{D}}^{\mathrm{V}}$	H_{D}	E_{D}	$\alpha_{\mathrm{D}}^{\mathrm{H}}$
	-10.07 dB	-99.22°		-10.19 dB	72.82°
V_5	E_5	α_5^{V}	H_5	E_5	α_5^{H}
	-17.21 dB	20.88°		-17.17 dB	2.73°
V_{E}	E_{E}	$\alpha_{\mathrm{E}}^{\mathrm{V}}$	H_{E}	E_{E}	α_5^{H}
	-17.18 dB	20.93°		-17.26 dB	-176.83°

Table 5.13.: Amplitude and phase values at each output of the elevation feeding network.

5.3.3. Antenna mechanical assembly

The antenna and the different feeding networks are integrated within a flight-certified aluminum housing, that allows its installment on the antenna carrier. The antenna assembly is mechanically attached by means of screws, whose position is set to fulfill the airworthiness requirements and to avoid a possible interference with the feeding lines of the azimuth networks. The SMP adjustable adapters, that interconnect the azimuth and elevation feeding networks, go through the back side of the antenna housing. An additional grid cover is used for the mechanical stability of the array elements. The gap between the back side of the antenna casing and the azimuth feeding network is filled with a foam layer, in order to avoid the air condensation that can occur at high aircraft altitudes. The complete mechanical assembly is depicted in Figure 5.48.

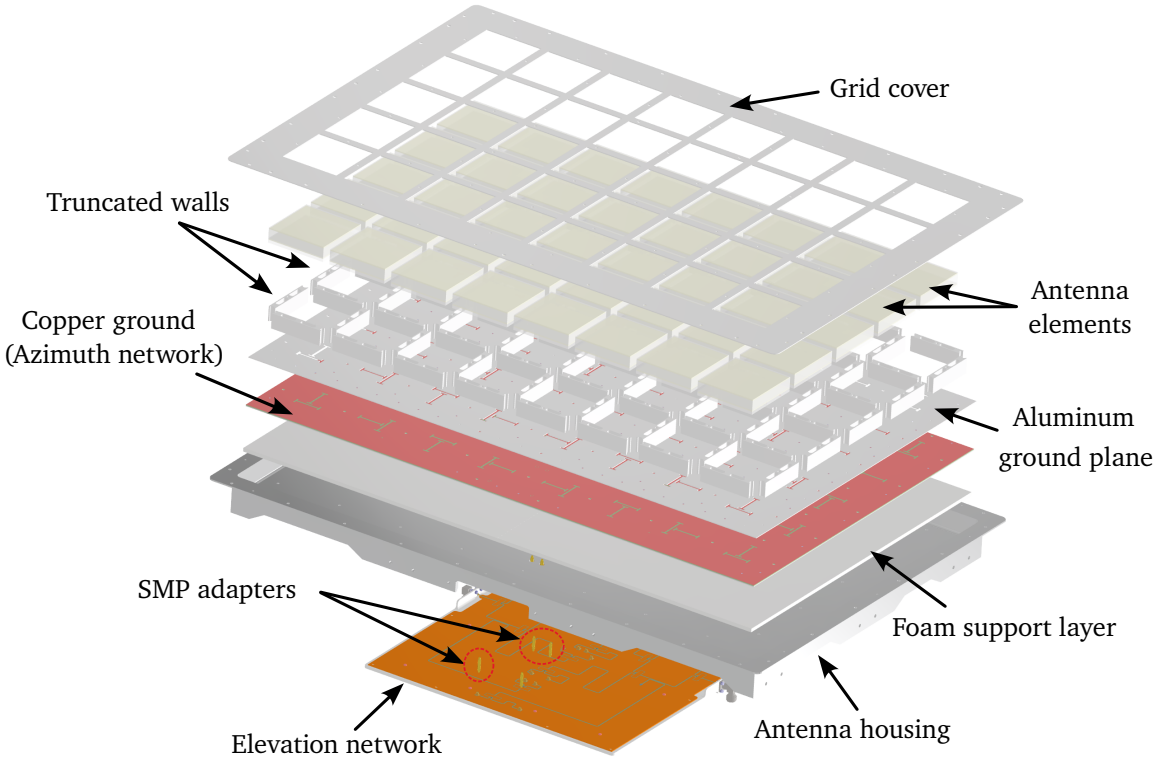

Figure 5.48.: Antenna mechanical assembly.

5.3.4. Simulation results

The antenna with the complete housing structure is simulated in HFSS, since the constructed prototype will be measured in this configuration before it is installed on the antenna carrier. Thus, the antenna with the mechanical assembly is analyzed for further comparisons. The simulated model is depicted in Figure 5.49.

The simulated pattern in elevation is shown in Figure 5.50, along with a comparison with the simulated results of the previous model depicted in Figure 5.42. For the current analysis, the amplitude and phase values of the designed elevation network, shown in Table 5.13, have been applied, and considering a normalized input power of 0 dBm for each polarization.

The antenna gain is 15.9 dBi and 16.62 dBi for the vertical and horizontal polarization, respectively. It can be noted the gain reduction of approximately 0.5∼0.7 dB in comparison with the case when the elevation coefficients, that are listed in Table 5.12, are applied. This

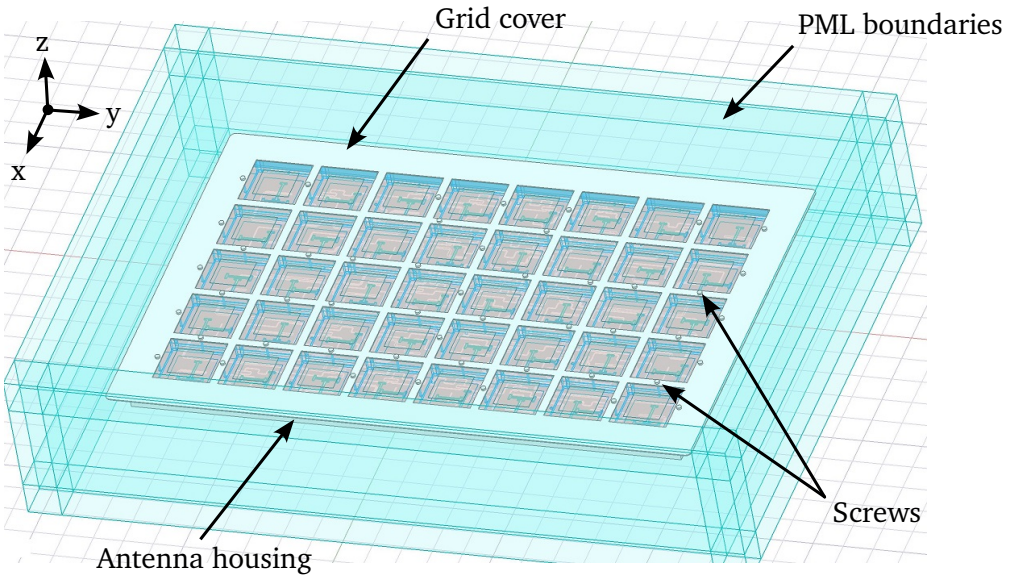

Figure 5.49.: HFSS model of the final array with the antenna housing and the grid cover.

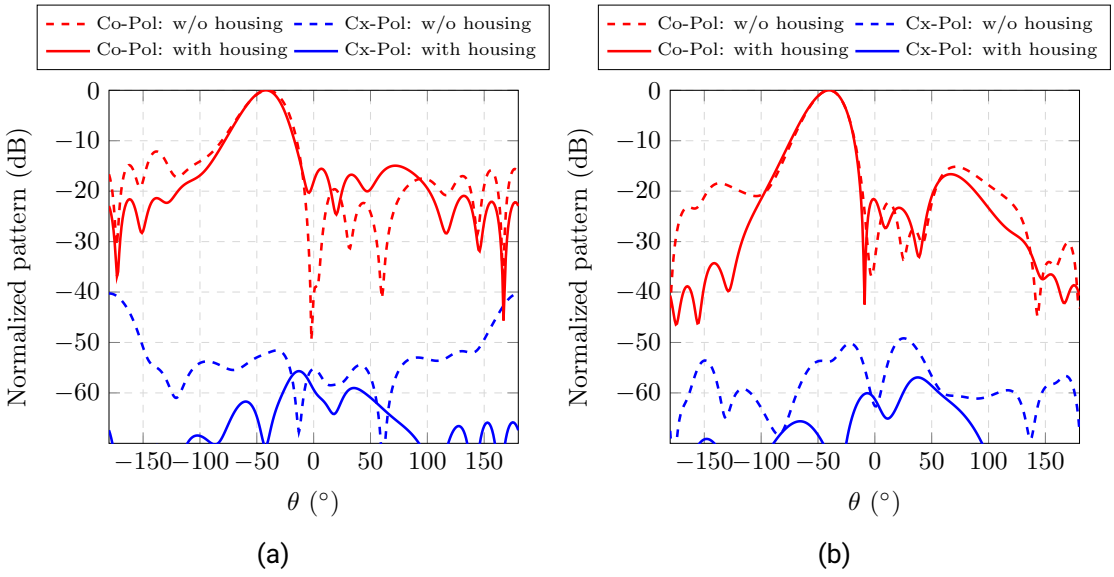

Figure 5.50.: Simulated co-polar and cross-polar patterns in elevation with and without the complete antenna structure. (a) Vertical pol. (b) Horizontal pol.

disagreement is explained since not all the power delivered at the input of the elevation feeding network is distributed to the corresponding outputs, due to the substrate losses, as well as the unavoidable insertion losses of each Wilkinson power divider and combiner.

The simulated co-polar patterns show a similar main beam but a visible difference regarding the side lobe level, nadir suppression and backward radiation, especially for the vertical polarization. The reasons that explain this slight disagreement in the co-polar pattern are the following ones:

- On the one hand, the radiated electric fields of the vertical polarization interact with the edges of the antenna housing. On the other hand, the fields of the horizontal polarization remain unaltered. This can be explained since the E-plane of the vertical polarization (plane XZ) coincides with the elevation plane, by which due to the beam steering and the orientation of the fields, the radiated fields interact with the forward and backward edges of the cover grid. This effect can be more visible in angular directions with higher sensitivity such as side lobe levels, radiation minimums or the back lobe. The polarization dependency of the field interaction is depicted in Figure 5.51, in which the magnitude of the electric field in elevation plane is represented for both polarizations.

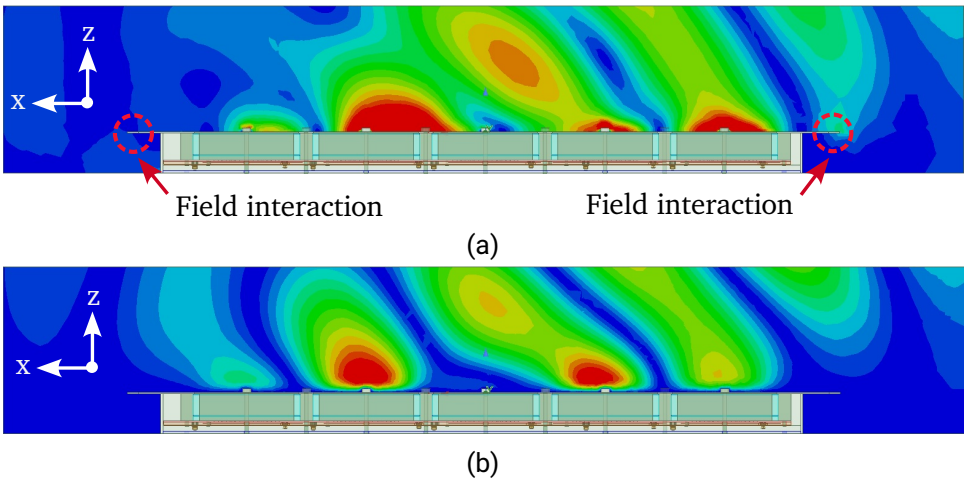

Figure 5.51.: Interaction of the radiated electric field with the edges of the antenna housing. (a) Vertical polarization. (b) Horizontal polarization.

- The simulation analysis also shows a slight interference of the electric fields, that are excited by the microstrip feeding lines, with the vertical screws that are needed to

attach the antenna mechanical assembly. This effect is more visible for the feeding network of the vertical polarization. Figure 5.52 shows the intensity of the electric field when the vertical polarization is excited. Despite that the position of the screws are set to avoid its proximity with the feeding lines, the propagation of the electric fields causes its interaction with the conductive surface of the screws. This interference can lead to a slight variation in the amplitude or phase that is applied to each antenna element. Despite this effect, the use of screws can not be avoided, since its geometrical arrangement has been calculated to fulfill the airworthiness requirements, and to assure the mechanical stability of the antenna assembly.

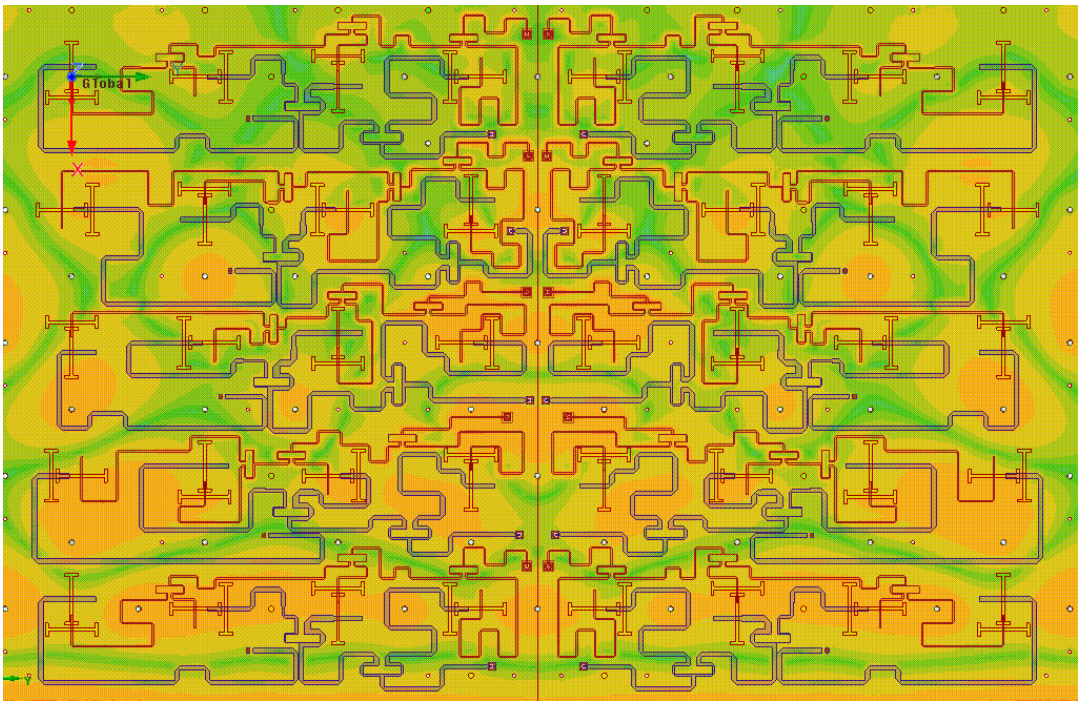

Figure 5.52.: Intensity of the electric field when the vertical polarization is excited. Red areas around the screws position show the electric field interaction

Regarding the cross-polarization performance, simulation results of the final assembled antenna show better cross-polarization suppression levels, with values beyond 50 dB. However, this improvement is not relevant, since due to the extremely low cross-polarization levels of the antenna, any slight modification can lead to an improvement or deterioration of several dBs.

5.3.5. Measurements of a manufactured array 5×8 prototype

The 40 array elements, along with the elevation and azimuth feeding networks and the antenna housing have been manufactured, assembled and measured. Since the antenna has been constructed in different stages, the electrical performance of each integration phase has been tested to assure an accurate assembly process.

Measurement of the elevation feeding network

The S-parameters of the elevation feeding network has been measured before its integration in the complete antenna assembly. The measured return loss levels for both polarizations are depicted in Figure 5.53, and show matching values better than 20 dB for the frequency band of operation, leading to a good agreement with the simulated data.

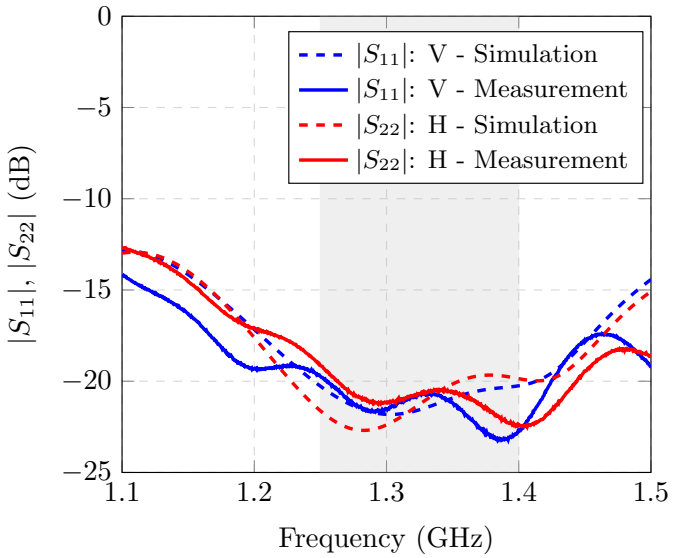

Figure 5.53.: Measured and simulated reflection factor of the elevation network.

The measured power amplitude at each output for both polarizations, along with the corresponding simulated value, previously shown in Table 5.13, are listed in Table 5.14.

The difference between simulation and measurement is approximately 0.9 dB for the center output ports (H_3, H_C and V_3, V_C), while for the outer ports this variation is slightly higher than 1 dB. This is due to the substrate losses, by which electrical larger paths between the input H, V and the output ports H_i, V_i lead to a higher dielectric material

Vertical polarization			Horizontal polarization		
V_1	Simulation	-17.27 dB	H_1	Simulation	-17.24 dB
	Measurement	-18.5 dB		Measurement	-18.5 dB
V_A	Simulation	-17.24 dB	H_A	Simulation	-17.34 dB
	Measurement	-18.5 dB		Measurement	-18.6 dB
V_2	Simulation	-10.07 dB	H_2	Simulation	-10.04 dB
	Measurement	-11 dB		Measurement	-10.9 dB
V_B	Simulation	-10.04 dB	H_B	Simulation	-10.15 dB
	Measurement	-11 dB		Measurement	-11.1 dB
V_3	Simulation	-7.04 dB	H_3	Simulation	-6.98 dB
	Measurement	-7.95 dB		Measurement	-7.8 dB
V_C	Simulation	-7.01 dB	H_C	Simulation	-7.11 dB
	Measurement	-7.95 dB		Measurement	-8 dB
V_4	Simulation	-10.1 dB	H_4	Simulation	-10.07 dB
	Measurement	-11.07 dB		Measurement	-10.8 dB
V_D	Simulation	-10.07 dB	H_D	Simulation	-10.19 dB
	Measurement	-11.08 dB		Measurement	-11 dB
V_5	Simulation	-17.21 dB	H_5	Simulation	-17.17 dB
	Measurement	-18.5 dB		Measurement	-18.4 dB
V_E	Simulation	-17.18 dB	H_E	Simulation	-17.26 dB
	Measurement	-18.49 dB		Measurement	-18.5 dB

Table 5.14.: Simulated and measured amplitude power of the elevation feeding network.

attenuation.

Even though the simulation values are calculated considering substrate losses, there is still a slight discrepancy between the value for the dielectric losses $tan\delta$ considered in the simulation and the real value. In addition, the measured values also include the insertion loss contributions of the connectors, power splitters, as well as conductor and ohmic losses. Furthermore, the insertion losses of the SMA-SMP adapters are also included in the measurement, since they are not considered in the calibration process of the network analyzer. Nevertheless, the measured phase and amplitude values, as well as the return loss and the port isolation, agree pretty well with the simulated data.

Measurement of the antenna with integrated azimuth feeding network

In this construction phase, the array with the azimuth feeding network is assembled and only the integration of the elevation feeding network is missing. The installment process of the azimuth feeding network is shown in Figure 5.54a.

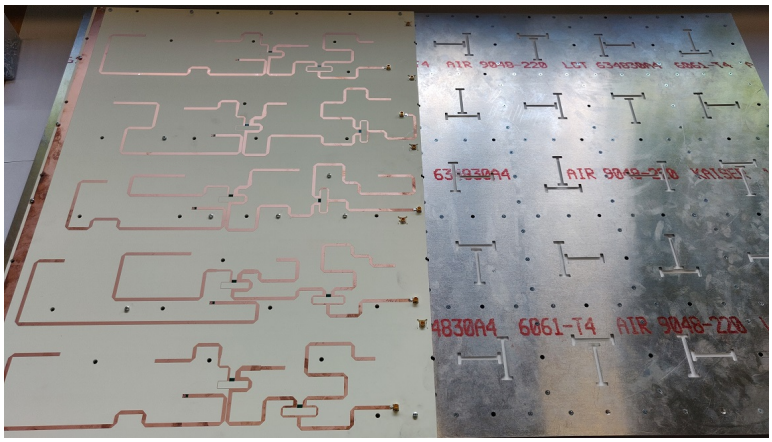

(a)

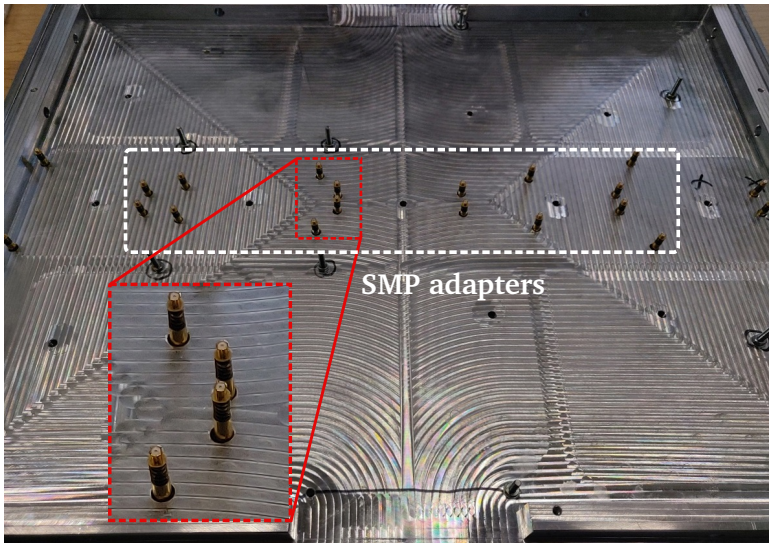

(b)

Figure 5.54.: (a) Attachment of the azimuth feeding network. (b) Back side of the antenna housing. View of the SMP adapters.

The measurement of the S-parameters is performed through the back side of the antenna housing by means of bores, through which the SMP adapters go through, thus allowing to access each azimuth feeding port, as shown in Figure 5.54b. Since all possible combinations of S-parameters can not be plotted, only a few examples of the measured return loss, coupling levels and polarization isolation values are presented.

Figure 5.55a shows the measured return loss levels $|S(H_\mathrm{i}, H_\mathrm{i})|, |S(V_\mathrm{i}, V_\mathrm{i})|$ at different array rows for both polarizations. Measurements show matching levels mainly better than 10 dB for the operational bandwidth, with values beyond 20 dB at the center frequency of operation. In addition, it can be noted that the matching levels of the same feeding row and polarization for different subarrays are quite comparable, since they are electrically identical.

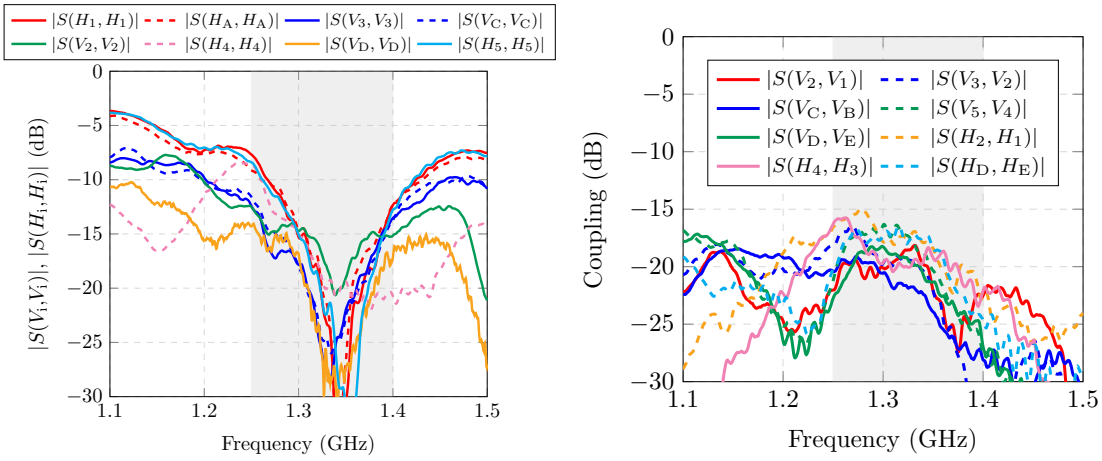

Figure 5.55.: Measured S-parameters of the final array 5×8 prototype at the azimuth feeding network. (a) Reflection factor. (b) Coupling.

The coupling levels $|S(H_{\mathrm{i}+1}, H_\mathrm{i})|, |S(V_{\mathrm{i}+1}, V_\mathrm{i})|$, between two closely located polarization feeding rows are shown in Figure 5.55b. Despite the close proximity of array elements, the isolation values mainly vary from 16 dB up to levels better than 20 dB, for the lowest and highest frquency bands of operation, respectively.

The coupling between polarizations at the same azimuth feeding row $|S(H_\mathrm{i}, V_\mathrm{i})|$ are plotted in Figure 5.56. The measured coupling levels between different feeding rows are mainly better than -20 dB for the operational bandwidth, and lower than -25 dB at the center frequency of operation.

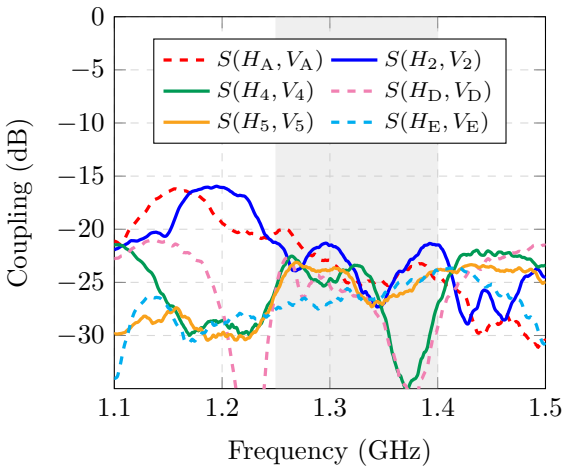

Figure 5.56.: Measured coupling between polarizations at the same azimuth feeding network row.

Measurement of the final assembled antenna

The final antenna is completely assembled and measured in the CTR. Figure 5.57a and 5.57b show the aluminum antenna housing, and a view of the connection between the azimuth and elevation feeding network using adjustable SMP adapters. The interconnection between feeding network demands an extremely accurate alignment of the top and bottom SMP connectors, and the adaptors adjustment can only be achieved within a narrow aperture. The final assembled antenna is depicted in Figure 5.58.

The measured return loss is depicted in Figure 5.59, and it shows a matching level practically higher than 15 dB for the entire operational bandwidth, as well as values better than 20 dB at the center frequency of operation. Furthermore, the polarization isolation is beyond 25 dB for the frequency range of operation.

The measured patterns in elevation and azimuth, along with a comparison with the simulated data, are plotted in Figures 5.60a and 5.60b respectively. Measurements show excellent agreement with the simulations. The measured cross-polarization levels are higher than the simulated data, since the sensitivity required to measure cross-polarization suppression values around 50 dB is difficult to achieve. However, the measured antenna cross-polarization suppression levels are still better than 35 dB, being 10 dB beyond the system specifications. The side lobe level in both antenna planes is better than 20 dB with a slight asymetry in azimuth of the vertical polarization, certainly due to fabrication or construction tolerances.

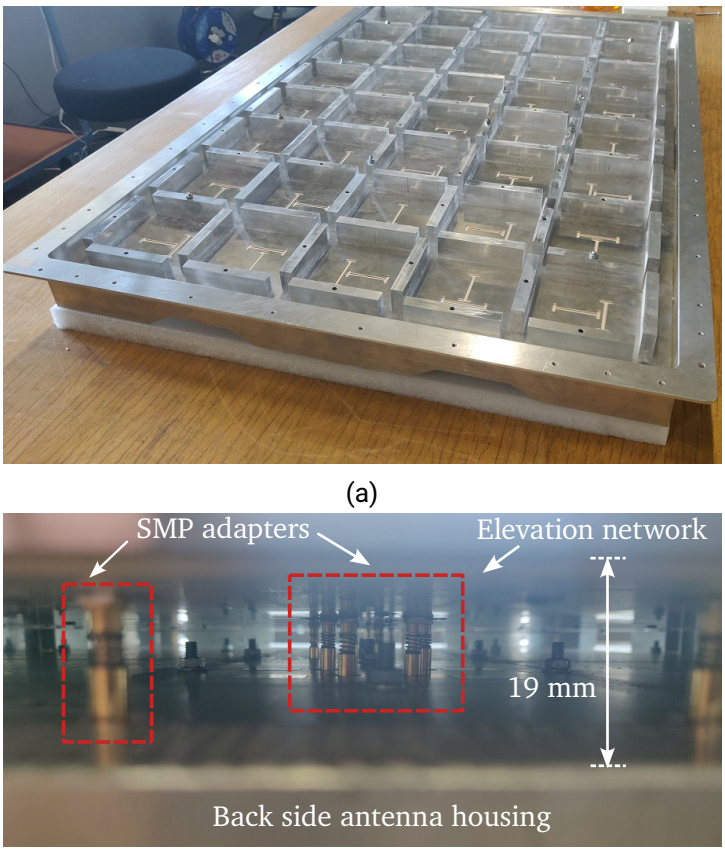

(a)

(b)

Figure 5.57.: (a) Antenna housing without array elements. (b) View of the SMP adapters.

The measured antenna gain values are 14.2 dBi and 15.1 dBi for the vertical and horizontal polarization, respectively. The gain reduction in comparison with previous simulations, is explained due to the following reasons. First of all, it can be seen from Table 5.14, that the measured amplitude weighting in the elevation feeding network differs from the simulated values around 0.9 dB∼1.2 dB. This is directly related to the dielectric losses and the electrical size of the elevation feeding network, leading to unavoidable power losses. In addition, the substrate material considered in the simulation, Rogers RT/Duroid 6006 ($\varepsilon_\mathrm{r} = 6.15, \tan\delta = 0.0019$) diposes of a slightly lower dielectric losses, than the actual substrate used in the manufacturing process, Rogers RO4360G2 ($\varepsilon_\mathrm{r} = 6.15, \tan\delta = 0.0038$). Thus, the simulated values does not consider the real dielectric

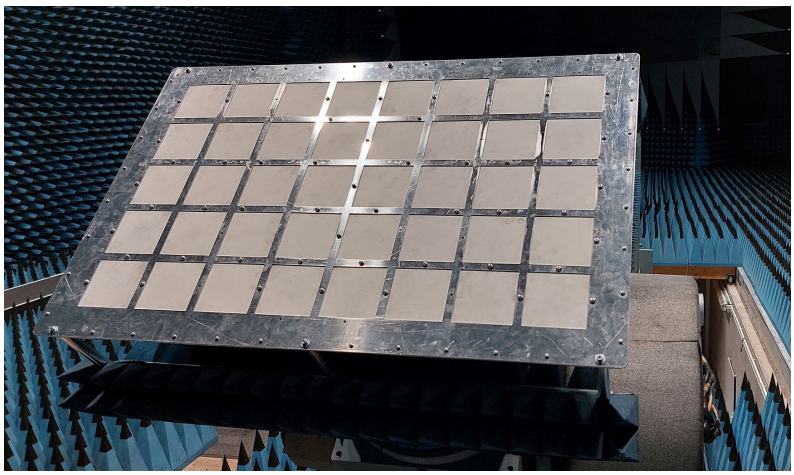

Figure 5.58.: Final assembled antenna in the DLR's Compact Test Range.

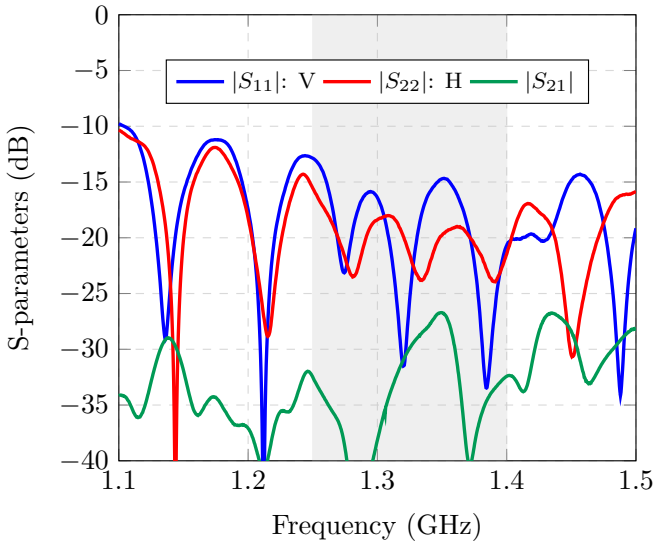

Figure 5.59.: Measured S-parameters of the final assembled antenna.

losses. The use of the substrate Rogers RO4360G2 was mandatory in order to implement the resistor film technology, that is required in the azimuth feeding network. Thus, for simplicity in the manufacturing process, the same substrate is also considered for the elevation feeding network. Nevertheless, the dielectric loss value given by the manufacturer

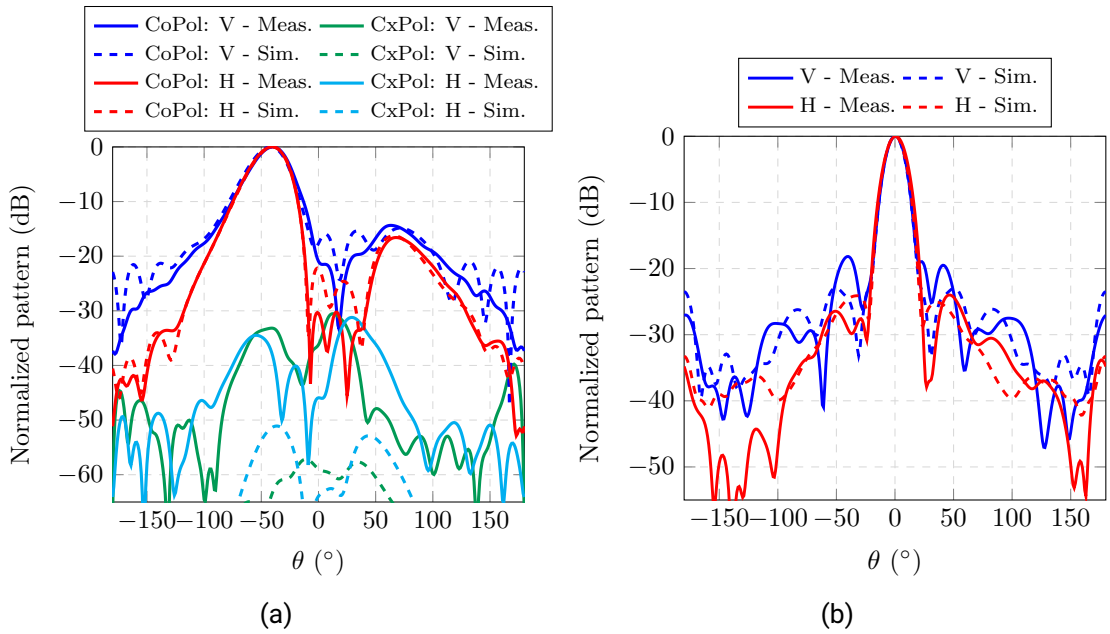

(a) (b)

Figure 5.60.: Measured normalized patterns of the final constructed array 5×8 prototype. (a) Elevation. (b) Azimuth.

is calculated at one frequency, by which a variation is also expected. Besides the substrate losses, the insertion losses of the SMP adjustable adapters (that are not considered in the simulation), as well as the connectors, also contribute to the overall power losses.

Table 5.15 shows the directivity and gain values of the measured antenna and the simulated model depicted in Figure 5.49. To provide a more realistic comparison, the simulation analysis considers the measured amplitude and phase values of the elevation feeding network, as well as the real dielectric loss values of the feeding substrate used in the azimuth network. It can be noted the good agreement between measured and simulated values. The antenna directivity is approximately 3 dB higher than the gain, yielding an antenna efficiency around 50%. This efficiency value is directly associated to the use of passive feeding networks and their related power losses. Nevertheless, the achieved antenna efficency values are satisfactory considering the design complexity of the planar phased array of 5×8 elements, as well as the electrical size of the feeding networks.

The measured half-power beamwidth in elevation Θ_e and azimuth Θ_a for both polarizations is also shown in Table 5.16.

Vertical polarization			Horizontal polarization		
Gain	Simulation	14.57 dBi	**Gain**	Simulation	15.49 dBi
	Measurement	14.22 dBi		Measurement	15.1 dBi
Directivity	Simulation	17.87 dBi	**Directivity**	Simulation	18.22 dBi
	Measurement	17.82 dBi		Measurement	17.84 dBi

Table 5.15.: Simulated and measured directivity and gain values of the final antenna.

Vertical polarization				Horizontal polarization			
HPBW in elevation: Θ_e	33°	HPBW in azimuth: Θ_a	16°	HPBW in elevation: Θ_e	33°	HPBW in azimuth: Θ_a	16°

Table 5.16.: Measured half-power beamwidth in elevation and azimuth at 1.325 GHz.

A further analysis is performed in Figure 5.61a, by which the radiation pattern in elevation is plotted for different frequencies. It can be noted the excellent beam steering stability over the operational bandwidth, and the measured low levels of cross-polarization.

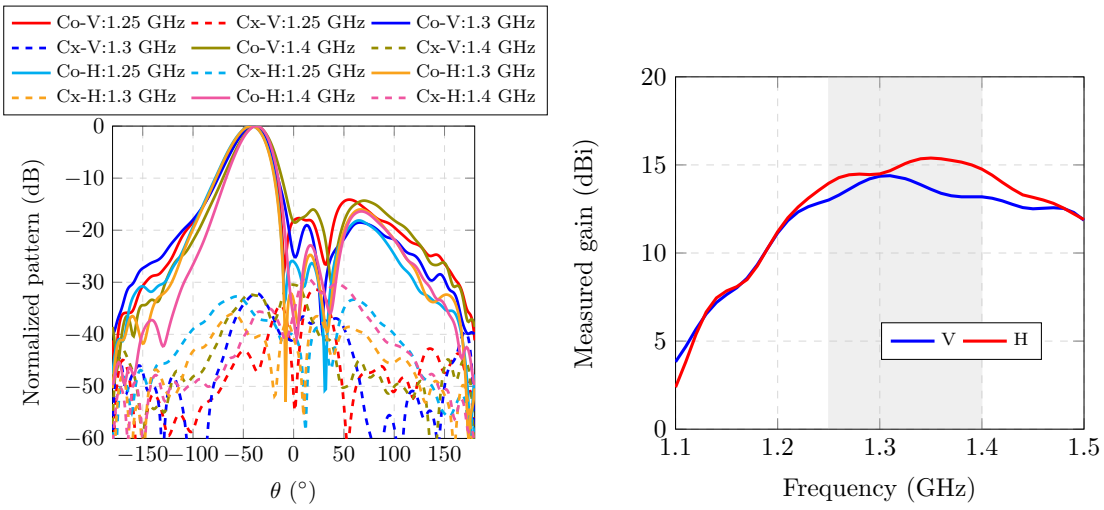

(a) (b)

Figure 5.61.: (a) Measured normalized radiation pattern in elevation for different frequencies. (b) Measured gain over frequency.

The gain variation over frequency is depicted in Figure 5.61b. It can be seen that the

maximum gain is slightly shifted in frequency for both polarizations, and a steady gain is achieved over the frequency range of operation.

5.3.6. Comparison with other works

In order to get an overview of the level of compaction achieved with the proposed work, a comparison with other L-band antennas for SAR applications is shown in Table 5.17. It can be noted the degree of integration obtained with the presented design, which even though a considerable miniaturization has been achieved, an antenna bandwidth of almost 20% is reached.

Reference	**Array elements**	**Size (λ_0^2)**	**Interelement spacing**	**Density (Elements/Size)**	**Polariz.**	**Relative BW.**
[37]	4×6	2.34×3.77	$0.66\lambda_0 \times 0.44\lambda_0$	2.77	Dual lin.	12%
[27]	2×6	1.37×3.43	$0.55\lambda_0$	2.55	Dual circ.	6.1%
[28]	2×6	1.59×4.57	$0.75\lambda_0$	1.65	Dual lin.	35%
[29]	2×2	1.38×1.46	$0.7\lambda_0$	1.98	Single lin.	6.5%
[23]	4×3	2.08×1.54	$0.53\lambda_0$	3.74	Dual lin.	8%
[30]	8×8	5.6×5.6	$0.7\lambda_0$	2.04	Dual lin.	8%
This work	**5×8**	**2.34×3.77**	$\mathbf{0.48\lambda_0}$	**4.53**	**Dual lin.**	**18%**

Table 5.17.: Comparison of the proposed work with other L-band planar antennas for SAR applications.

A further comparison can be performed with the current L-band antenna of the DLR's operative monostatic multifrequency airborne SAR sensor, F-SAR. Since the next generation bistatic airborne SAR sensor and the actual F-SAR system are mounted on the same aircraft, the available antenna aperture size for both L-band antennas is the same.

Figure 5.62 shows a comparison in terms of array elements between the current L-band array antenna (4×6 elements) and the proposed antenna (5×8 elements). The electrical performance of both antennas is compared in Table 5.18. It can be seen that the presented solution provides 16 additional array elements, which leads to an increase of 66% more antenna elements in the exact same antenna aperture size. In addition, considering that both antennas are excited with a triangular amplitude distribution, the new solution also provides more antenna gain, due to the improved element isolation. Furthermore, the gain increase should be also considered twice in the system performance, since due to the two way operation of SAR systems, the same antenna is used for both transmission and reception purposes.

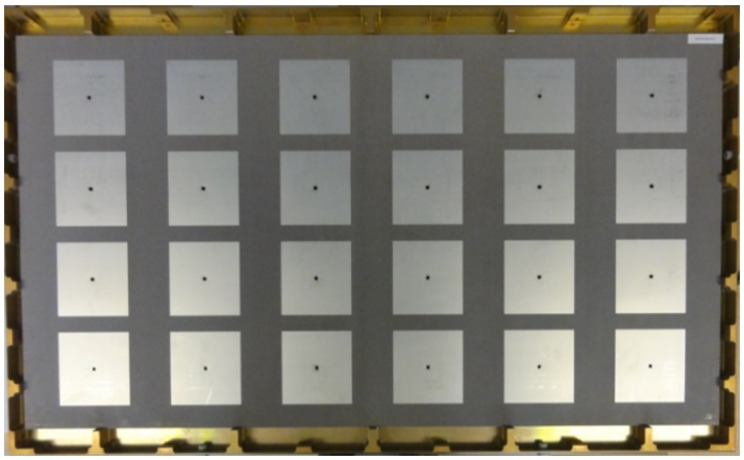

(a)

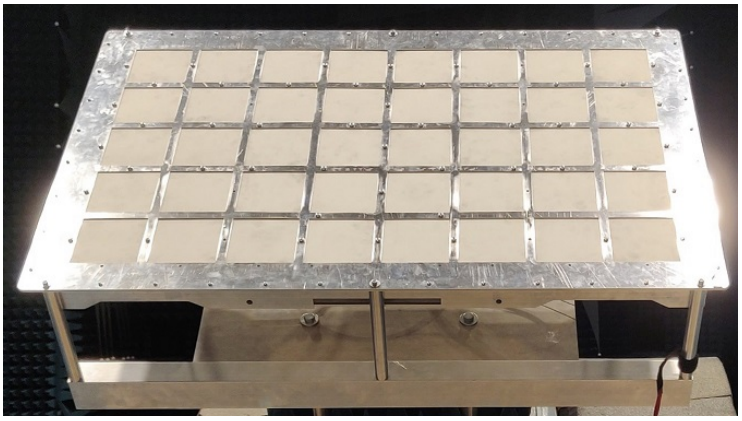

(b)

Figure 5.62.: Comparison between the DLR's airborne SAR L-band antennas with the same aperture size. (a) F-SAR system. (b) This work.

L-band SAR antenna	Array elements	Bandwidth	Measured gain	
			Vertical	Horizontal
Current F-SAR	4×6	150 MHz	12.3 dBi	13.8 dBi
This work	5×8	210 MHz	14.2 dBi	15.1 dBi
Improvement	16 (66%)	60 MHz	1.9 dB	1.3 dB

Table 5.18.: Performance comparison with the current DLR's L-band F-SAR antenna.

6. Mitigation of External Antenna Interactions

In this chapter, practical scenarios where the antenna interacts with its environment, and how this leads to a potential radiation performance degradation, are presented. Consequently, the polarization dependent edge diffration effects due to the antenna interaction with the carrier are analyzed. Finally, the application of Electromagnetic Bandgaps (EBGs) as a solution to deal with the previous cases, and thus to mitigate the impact of the field interactions, is proposed and validated.

6.1. Antenna external interactions

So far in this thesis, different designs have been presented to overcome the internal antenna interactions. These are inherent to any antenna system, and usually lead to trade-off decisions that can limit the antenna performance. Some of the main contributions of the proposed work in this field are:

- Robust excitation against feeding tolerances, and extremely compact solution of a feeding network implemented in GCPW and SIW technologies.
- Reduction of the array interelement spacing while keeping reasonable low coupling levels, thus increasing number of array elements. This way, the limited antenna aperture size can be efficiently exploited.
- Dual-polarized antennas with reduced cross-polarization levels and enhanced polarization isolation.
- Broadband antenna performance with compact implementation.

However, the antenna is not isolated but it is part of a given environment, and it irremediably interacts with its surroundings due to the propagation nature of the radiated fields, resulting in external antenna interactions.

Usually, airborne antennas are installed or surrounded by metallic structures such as platforms, the antenna carrier or the aircraft. Thus, currents are induced on these surfaces,

due to the propagation of the radiated fields along such conductive structures. The wave interactions with the antenna environment can lead to scattering effects, edge diffraction due to discontinuities on the surrounding geometry or multipath interference, causing signal distortion as a result of the contribution of different waves that propagate along distinct paths.

Thus, the interaction of the antenna with its environment can lead to a modification of its electrical performance, leading to a distortion of the radiation pattern. Some well-known effects, among others, are:

- Distortion of the antenna main beam. Amplitude and phase ripple.
- Radiation increment at undesired directions (back lobe, side lobe level) and distortion of the radiation suppression due to constructive and destructive interferences.
- Increase of cross-polarization levels.
- Due to coupling enhancement, interference with nearby antenna systems.

Some well-known approaches make use of choke rings [102], or metamaterial absorbers [103] to mitigate the multipath effect in navigation applications, or as an antenna shielding [104]. However, choke rings can become bulky solutions, and the use of microwave absorbers can lead to pattern distortion or loss of desired radiated energy, especially if they are placed too close to the antenna. Other approaches take advantage of the stop band properties of Electromagnetic Bandgaps (EBGs), to synthesize a high impedance surface ground, thus enhancing the radiation properties of the antenna [105], or to reduce the interference between antenna elements [106, 107]. Due to its miniaturization and integration capabilities, as well as its low-profile characteristic, EBGs become a suitable solution in order to mitigate the antenna external interactions in airborne applications, thus achieving a more independent radiation performance regardless of the antenna environment.

Next, some realistic scenarios are presented, where the impact of the antenna external interactions can be analyzed and, consequently, how these effects can be mitigated by means of EBGs.

6.2. Practical examples in airborne SAR applications

Some practical examples of antenna external interactions in airborne applications, and how these can impact the antenna performance, are presented next.

6.2.1. Interaction with the antenna housing edges

As already mentioned in chapter 5, the radiated fields of the vertical polarization interacts with the antenna housing edges, unlike the horizonal one, that remain unaltered, as shown in Figure 6.1. This is explained since the beam steering in elevation coincides with the E-Plane for this polarization, thus being more sensitive to geometrical discontinuities in this plane due to the field orientation. The steeper the inclination of the main beam, the higher the interaction, which leads to some distortion of the radiation pattern, especially in sensitive areas such as the side lobe level, back lobe radiation or nadir suppression.

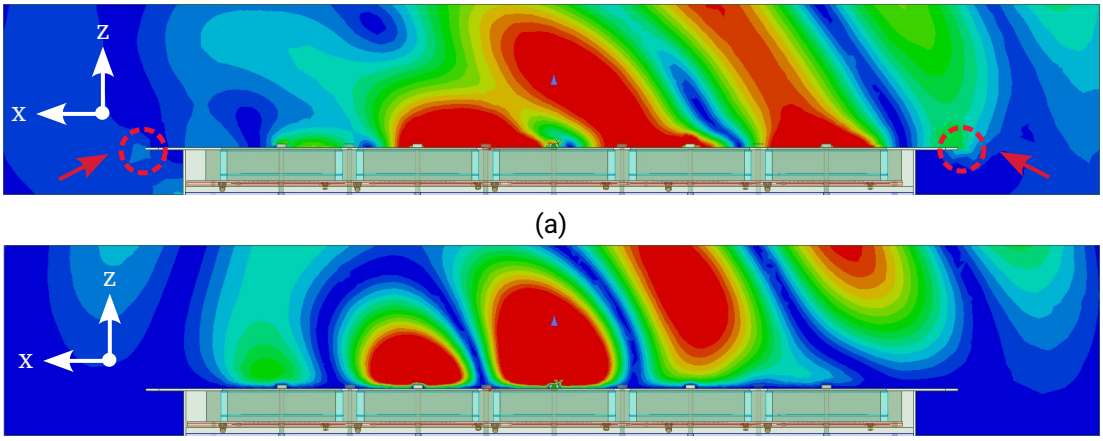

Figure 6.1.: Polarization dependent interaction with the edges of the antenna housing. (a) Vertical polarization. (b) Horizontal polarization.

A direct approach to avoid the field interaction with the edges is placing an absorber around the antenna housing, thus covering the casing borders, as depicted in Figure 6.2.

This antenna configuration is measured in the CTR and compared with the case without absorber, that was already shown in Figure 5.58. The measured patterns in elevation for both polarizations are depicted in Figure 6.3. It can be seen that the use of the absorber has a visible impact on the vertical polarization, by which the main beam is smoothed, the nadir suppression is enhanced, and the back lobe is reduced. In addition, the measured gain is around 0.8 dB lower, due to the absorbing properties of the absorber collar. On the other side, the elevation pattern of the horizontal polarization practically remains unchanged, since the radiated fields are not sensitive to the edge discontinuities, as can be seen in the electric field propagation plotted in Figure 6.1b.

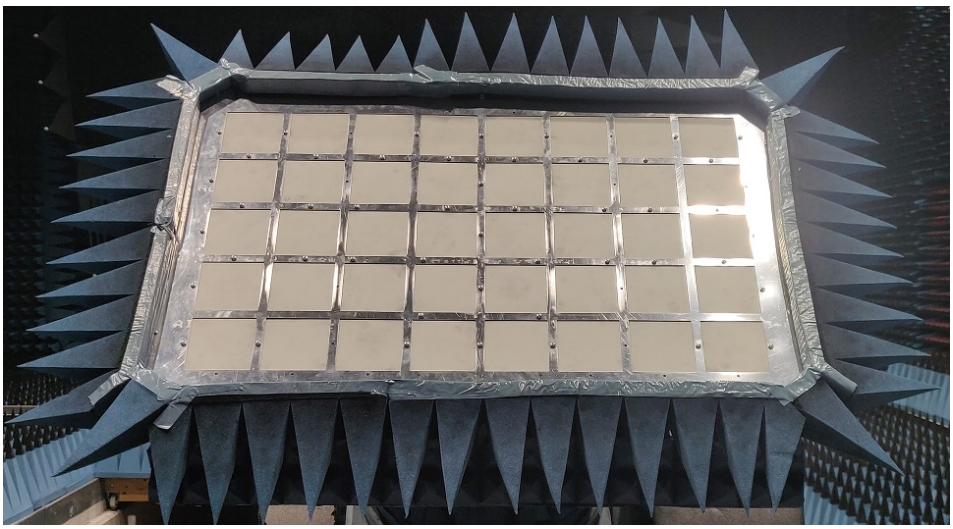

Figure 6.2.: Final antenna with absorber covering the housing edges.

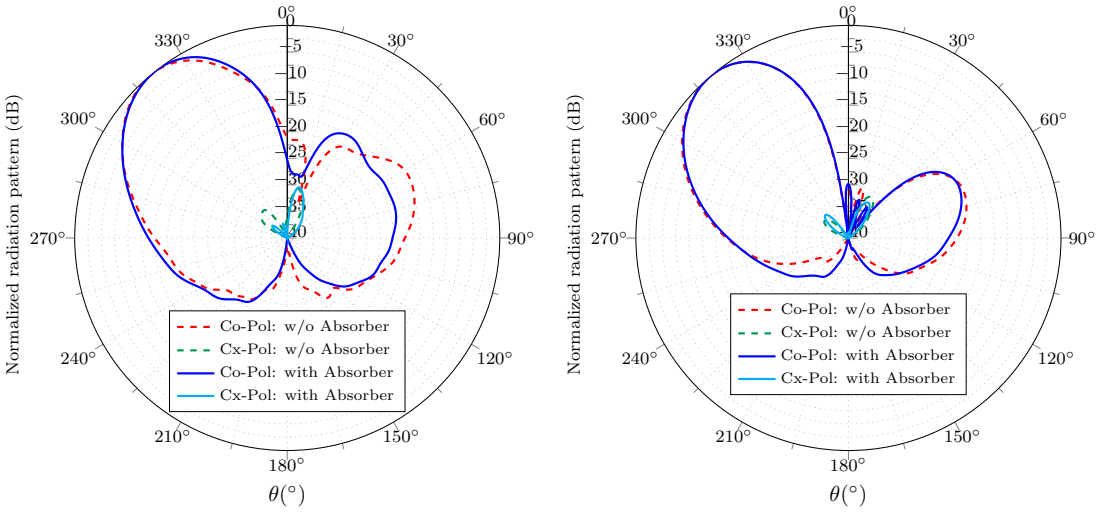

Figure 6.3.: Measured normalized radiation pattern in elevation of the final antenna with and w/o absorber around the antenna housing. (a) Vertical polarization. (b) Horizontal polarization.

6.2.2. Interaction with the antenna carrier

In airborne SAR applications, the antenna irremediably interacts with the antenna carrier, an aerodynamic attachment structure that allows the antenna installment on the aircraft. This flight-certified platform is especially designed to carry the antennas, and it is essential to fulfill the airworthiness requirements.

Figure 2.12 depicts the antenna carrier of the F-SAR, that is mounted sideways on the aircraft, as shown in Figure 1.4. As a multifrequency airborne SAR system, different antennas are installed on the same F-SAR carrier. For across-track interferometric purposes, the X-band antennas are mounted on the upper and bottom side.

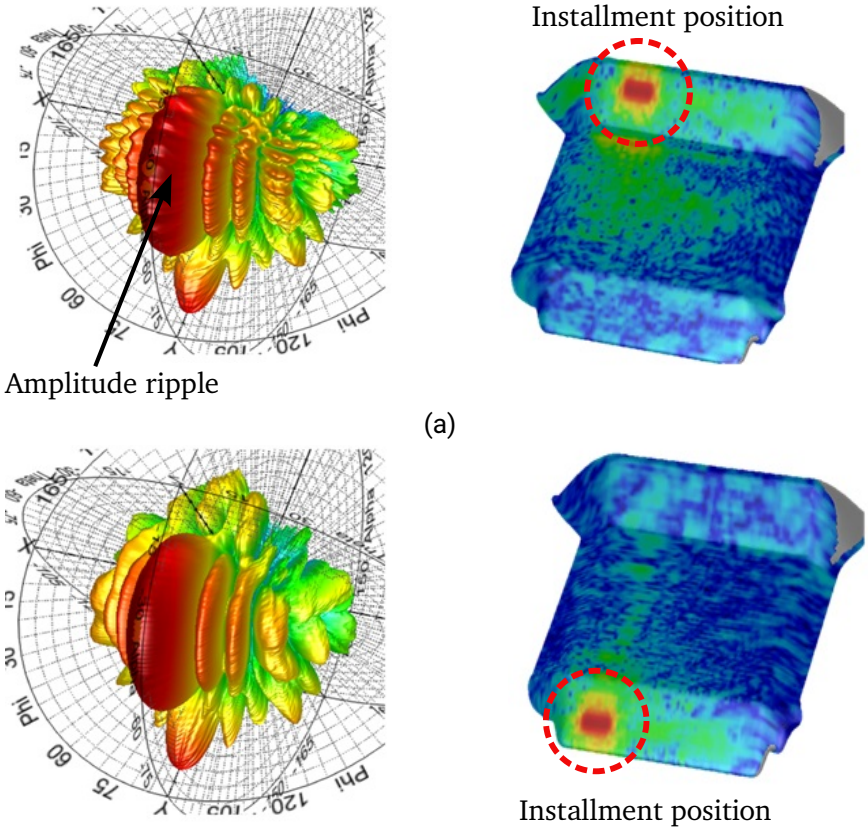

Figure 6.4.: Measured interaction with the carrier depending on the antenna installment position. F-SAR system. (a) Top side. (b) Bottom side.

Figure 6.4 shows the performance of the X-band antennas, represented by the magnitude of the electric fields on the carrier surface and the 3D spherical radiation pattern, for two different installment positions on the carrier. For this analysis, the same identical electrical antenna is considered, by which the orientation of the polarized fields is orthogonal to the flight path. It can be noted that the sitting position on the top clearly influences the interaction of the antenna with the carrier, due to its slanted geometry and electrical size. This impact can be seen as an amplitude ripple of the radiation pattern, especially visible in elevation direction. On the other side, installing the antenna on the lower side of the carrier does not visibly affect its performance.

Another example can be found when the planar phased array antenna 5×8, that has been presented in the last chapter, is mounted on the DuoLIM carrier. The antenna carrier is a Carbon-Fiber Reinforced Polymer (CFRP) circular plate with diameter 120 cm, thickness 1.27 cm, and covered with a metal mesh, that is placed underneath the aircraft, as shown in Figure 6.5. The installment position under the aircraft, along with the rotation platform, allows several swath illumination configurations under different looking angles, unlike other airborne SAR systems, where the antenna is attached sideways.

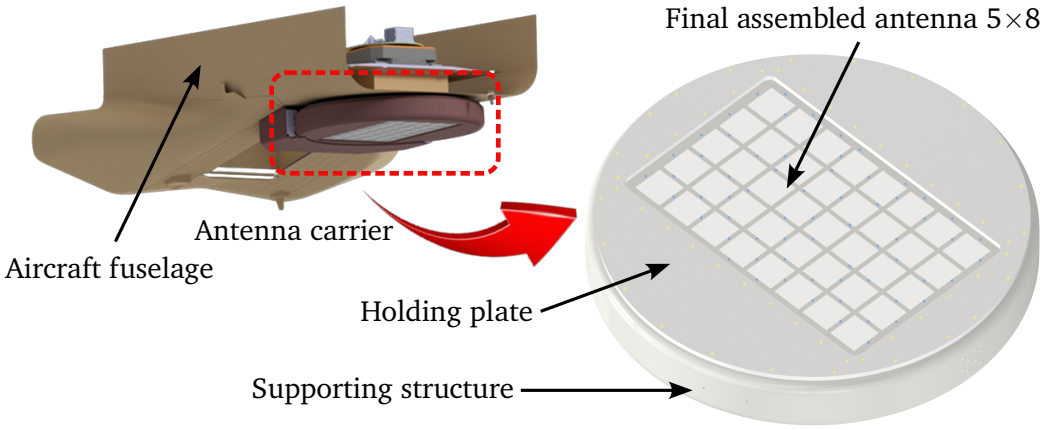

Figure 6.5.: The antenna carrier is placed beneath the aircraft.

The antenna, mounted on the circular platform structure, is simulated in HFSS. The plate is coated by a copper mesh, thus being the carrier a conducting surface. Figure 6.6 depicts the magnitude of the surface currents that are induced on the carrier, due to the propagation of the radiated fields. It can be clearly seen that the intensity of the induced currents, for the vertical polarization, is stronger than for the horizontal one. This can be explained by analyzing the propagation of the electric field in elevation for both polarizations, that is represented in Figure 6.7.

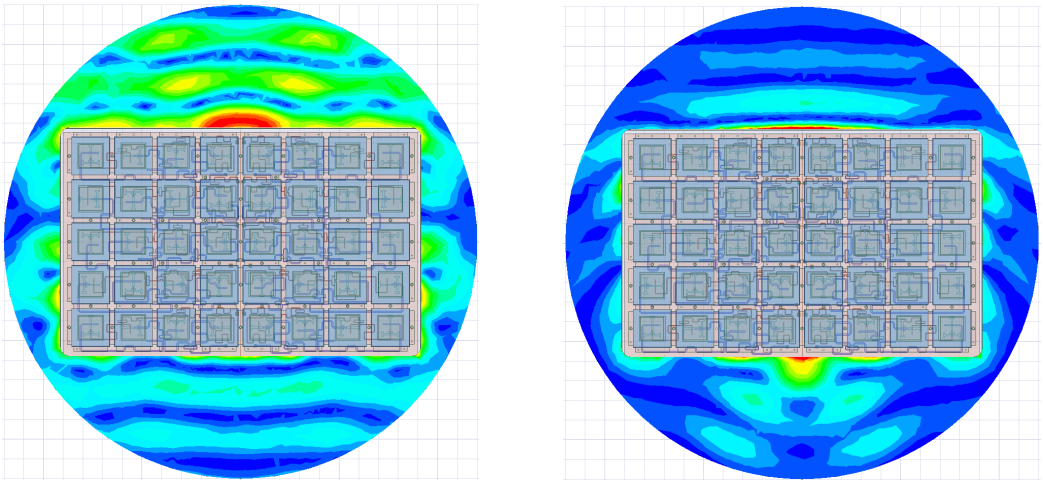

(a) (b)

Figure 6.6.: Intensity of the surface currents induced on the antenna carrier. (a) Vertical polarization. (b) Horizontal polarization.

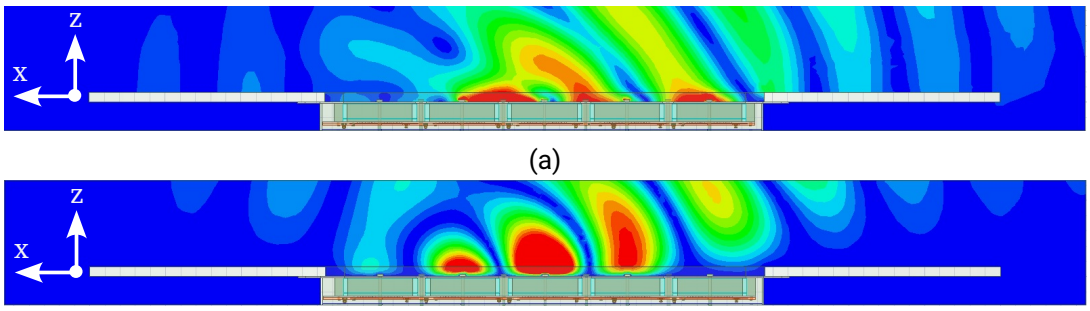

(a)

(b)

Figure 6.7.: Propagation of the electric fields in elevation with the antenna carrier. (a) Vertical polarization. (b) Horizontal polarization.

It can be noted that, for the vertical polarization, the radiated electric fields propagate along the conductive surface of the antenna carrier, unlike the horizontal one, onto which surface currents are generated. The interaction of the propagating surface waves with geometrical discontinuities or edges lead to edge diffraction effects that can cause a distortion of the radiation pattern. Thus, the analysis and suppression of surface waves becomes essential in order to mitigate the antenna interaction with the carrier.

Surface waves

Surface waves propagate on the interface between two materials such as dielectric and metal, or free space and metal. Since surface waves exponentially decay or attenuate away from the surface, they can be considered as a type of guided waves that are bounded to the surface or interface between these two mediums. In addition, surface waves can extend many wavelengths along the surrounding space, and they are usually described as surface currents that are induced on conductors [108, 109]. Let us consider a surface wave propagating in +z direction with propagation constant β, and the fields decaying exponential in the +x direction with attenuation constant α, as depicted in Figure 6.8.

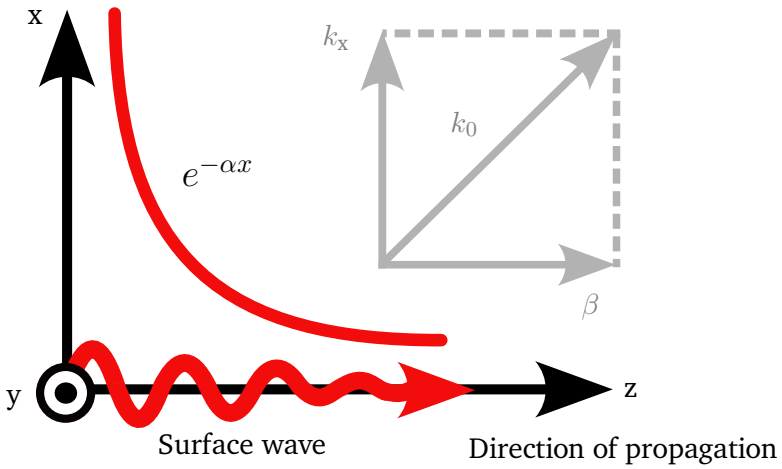

Figure 6.8.: Surface wave propagation along a surface placed on the plane YZ.

The surface wave can be described as:

$$E(x,z) = E_0 e^{-jk_x x} e^{-j\beta z} \tag{6.1}$$

by which k_x is the component of the wavenumber in the x-axis, related to the propagation constant β through $k_x = \sqrt{k_0^2 - \beta^2}$, being k_0 the wavenumber in free-space $k_0 = \frac{2\pi f}{c_0} = \frac{2\pi}{\lambda_0}$.

Surface waves are characterized by $|\beta| > k_0$, by which the phase velocity is slower than the speed of light $v_{ph} = \frac{2\pi f}{\beta} < c_0$, which is why surface waves are known as slow waves. This condition leads to a purely imaginary wavenumber in the x-axis k_x, since:

$$|\beta| > k_0 \rightarrow k_x = \sqrt{k_0^2 - \beta^2} = \pm j\alpha \tag{6.2}$$

Since the solution $+j\alpha$ implies an exponential increasing wave that is not physically possible, then $k_x = -j\alpha$. Therefore $e^{-jk_x x} \rightarrow e^{-\alpha x}$ that leads to an exponential power decay in x-axis away from the surface. Thus, radiation does not exist, the solution is guided and this is the reason why a surface wave can be considered as a guided wave.

Surface waves can be characterized as TE (Transversal Electric) or TM (Transversal Magnetic) waves, depending if only magnetic field or electric field exists along the direction of propagation, respectively.

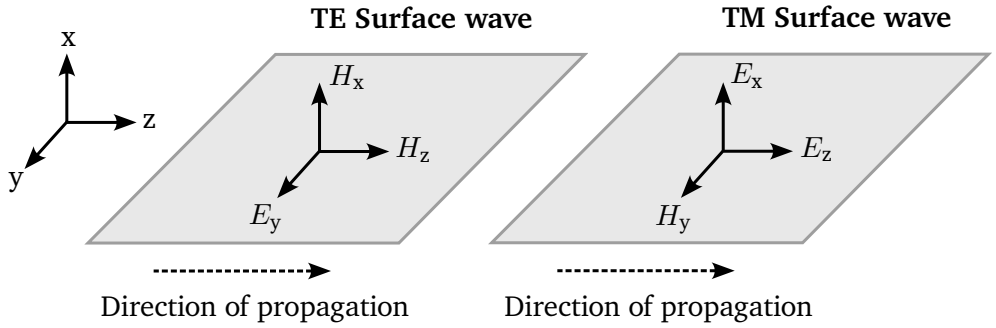

Figure 6.9.: TE and TM suface waves.

Thus, a surface impedance value Z_s can be derived for each type of surface wave:

$$Z_s^{TE} = -\frac{E_y}{H_z} = -\frac{j\omega\mu_{eff}}{\alpha}$$
$$Z_s^{TM} = \frac{E_z}{H_y} = \frac{j\alpha}{\omega\varepsilon_{eff}} \tag{6.3}$$

being respectively ε_{eff} and μ_{eff} the effective dielectric permittivity and magnetic permeability of the surface, and $\omega = 2\pi f$ the angular frequency.

In many practical airborne applications, the antenna is placed or surrounded by metal or conductive surfaces, such as the ground plane, the antenna carrier or the aircraft. It is known that the surface impedance of a flat sheet of metal is given by [108]:

$$Z_s = \frac{1+j}{\sigma\delta_{sd}} \tag{6.4}$$

being σ the metal conductivity, and δ_{sd} the skin depth that measures the degree of penetration of the surface currents into the metal, given by $\delta_{sd} = \sqrt{1/(\sigma\mu\pi f)}$.

It can be noted the inductive nature of the surface impedance of metal, since $Im(Z_s)$>0, proving that metal planes only support the propagation of TM surface waves. This can be

also explained since, due to boundary conditions, the tangential electric field in conducting surfaces must be zero and thus, TE waves cannot exist, as depicted in Figure 6.9.

In real applications, the metal structures around the antenna have a finite size, by which the induced surface waves on them interact with their edges or discontinuities, leading to edge diffraction effects. The resulting field scattering from the edges and corners is added to the direct antenna radiated fields, producing constructively or destructively interferences that can distort the radiation pattern [47, 110]. This impact is especially visible in angular regions of low field intensity such as backward radiation, side lobe level or radiation nulls, as well as it also increases the cross-polarization levels of the antenna [111].

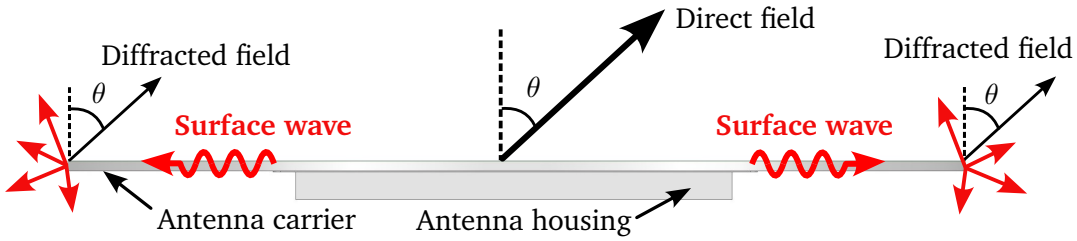

Figure 6.10.: Surface waves induced on the antenna carrier surface.

Furthermore, the main beam of the antenna pattern in E-plane can be considerably affected for electrically large ground planes or metal structures (in terms of wavelengths), by which the diffracted fields can cause an amplitude ripple, as it is seen in Figure 6.4. This effect is especially relevant for operation at higher frequencies, since the metal structures surrounding the antenna certainly become electrically large.

Experimental verification of edge diffraction effects

The phased array antenna 5×8 is installed on the antenna carrier, as depicted in Figure 6.11, and measured in the CTR. The circular plate has a diameter of 120 cm and thickness 1.27 cm. Figure 6.12 plots a comparison between simulation and measurement of the radiation pattern for both polarizations considering the antenna carrier. At the same time, the measured pattern without the carrier is also plotted to analyze the carrier effect.

Be noted that the following measurements are performed with the final flight model antenna. This design differs from the prototype, presented in the last chapter, in the number of vertical screws that are used to assure the mechanical stability of the complete antenna assembly. Therefore, small differences can be expected in the radiation pattern

regarding the side lobe level or radiation nulls, due to the unavoidable slight field distortion of the feeding network produced by the screws, that can lead to small innacuracies in the amplitude and phase excitation of some array elements, as already shown in Figure 5.52.

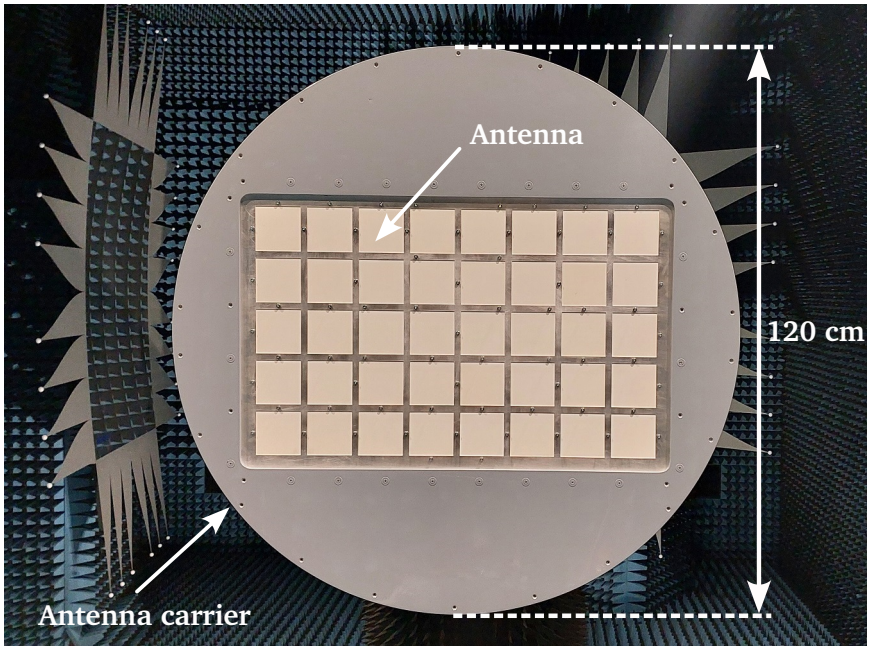

Figure 6.11.: Antenna installed on the carrier during CTR measurements.

It can be noted from Figure 6.12a that the antenna carrier widens the main beamwidth for the vertical polarization, leading to a measured gain reduction of approximately 1 dB, in comparison with the case without the carrier. The simulated results of the antenna with the carrier structure agree well with the measurement, being the simulated gain slightly higher than the measured value. On the other side, the radiation pattern of the horizontal polarization remains practically unchanged, as shown in Figure 6.12b. This can be explained from Figure 6.7, where the radiated electric fields of the vertical polarization propagate along the surface carrier, unlike the horizontal one, by which surface currents are induced. This effect is clearly visible for the vertical polarization, since the beam steering in elevation coincides with the E-plane, thus being more sensitive to edge diffraction effects.

Further analysis is performed in Figure 6.13, where the effect of the antenna carrier is investigated for different circular plate diameters. The simulated radiation pattern in elevation, considering an increment of the the antenna carrier size of 50% and 100%,

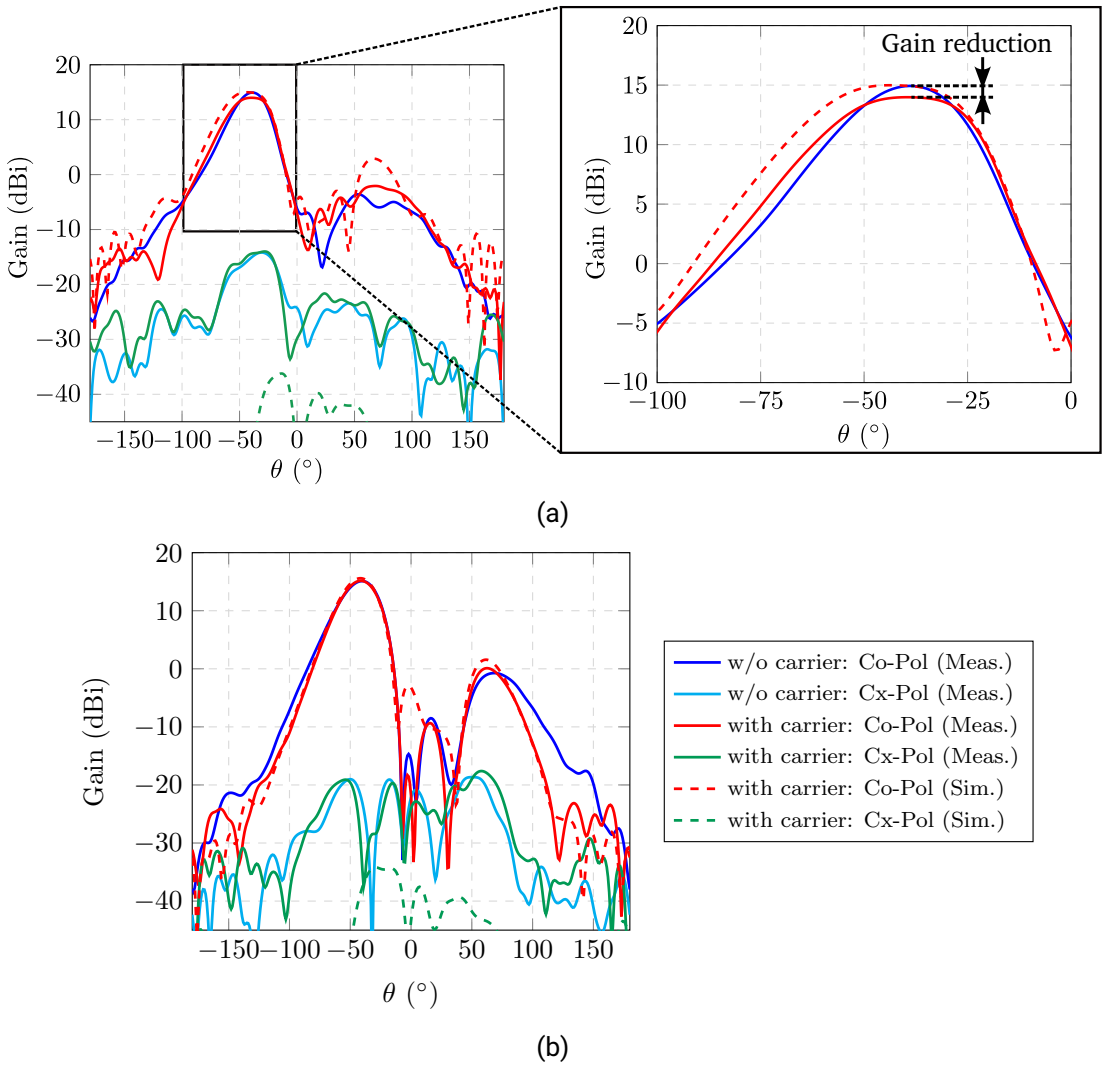

Figure 6.12.: Measured radiation pattern in elevation with and w/o antenna carrier and comparison with the simulation. (a) Vertical pol. (b) Horizontal pol.

corresponding with radius values of 90 cm and 180 cm, respectively, is plotted and compared with the measurement of the original carrier of radius 60 cm. Once again, the polarization-dependency of the edge diffraction effects become visible for the vertical polarization, when electrically large carrier structures are considered, leading to a visible

amplitude ripple. The cross-polarization levels are also slightly increased, but since the cross-polarization performance of the antenna is extremely low, it is less noticeable. The radiation performance of the horizontal polarization in elevation is unchanged, regardless of the electrical size of the antenna carrier.

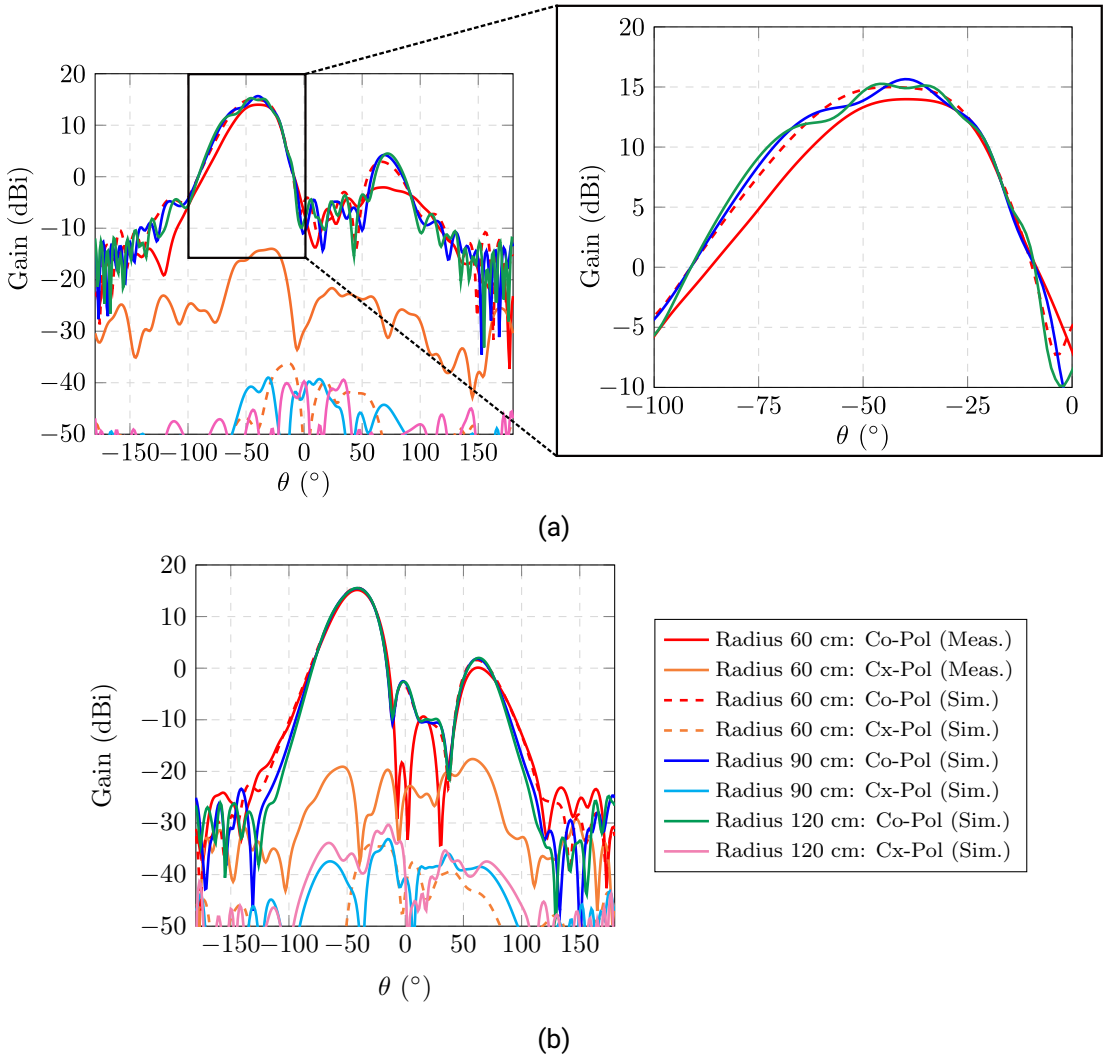

Figure 6.13.: Analysis radiation pattern in elevation for different values of the carrier radius. (a) Vertical polarization. (b) Horizontal polarization.

A possible approach to deal with the aforementioned carrier effects comprises the use of Electrogmanetic Bandgaps (EBGs), by which the propagation of surface waves can be suppressed. Thus, a more independent antenna electrical performance can be achieved, regardless of its environment.

6.3. Electromagnetic Bandgaps (EBGs)

The Electromagnetic Bandgaps (EBGs) are a type of metamaterial, an artificial periodic structure that exhibits unique electromagnetic properties. EBGs suppress the propagation of surface waves for any incident angle and polarization state within a given frequency band, also known as stop-band. Despite that they can be also arranged as 3D structures, 2D or planar EBGs, also known as metasurfaces, allow a higher degree of integration, thus becoming a compact and low-profile solution for antenna design and airborne applications [31, 112].

EBGs are metal-dielectric structures that are periodically arranged along a two dimensional pattern by the repetition of the same unit cell (UC). The periodicity is much less than the wavelength in free space, so the resulting geometry is seen as an homogeneous structure for the electromagnetic wave. By modifying the conductive geometry of the unit-cell and the electrical properties of the substrate, the overall periodic structure becomes a LC circuit with different capacitances and inductances values, by which at the frequency of resonance, no surface wave can propagate.

There are plenty of different EBG-UC types, that are designed to achieve a particular performance (broadband, multiband) or to reduce the fabrication complexity, for instance by preventing the use of vias. One of the most well-known EBG-UC is the mushroom type.

6.3.1. Mushroom-like EBG

The mushroom type EBG-UC is a metallic patch placed on a substrate and connected to the ground by means of a via, as depicted in Figure 6.14. Each square patch has a width W_p and it is separated to the neighbour element by a gap g, thus the UC periodicity p_g is given by $p_\mathrm{g} = W_\mathrm{p} + g$. The via stub has a radius r_via and its height is determined by the substrate thickness h. The electrical properties of the substrate are given by its dielectric permittivity ε_r and magnetic permeability μ_r.

The capacitance is given by the gap between patches, and the inductor results from the current loop generated among the patches and vias. The equivalent LC parallel resonant circuit for the mushroom-like EBG structure is depicted in Figure 6.15. According to [113], the edge capacitance and inductance can be calculated as follows:

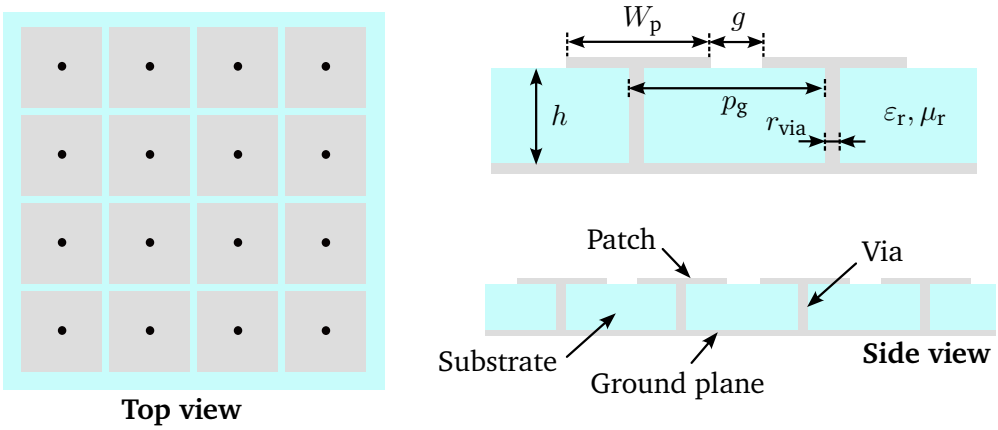

Figure 6.14.: Mushroom type EBG unit cell.

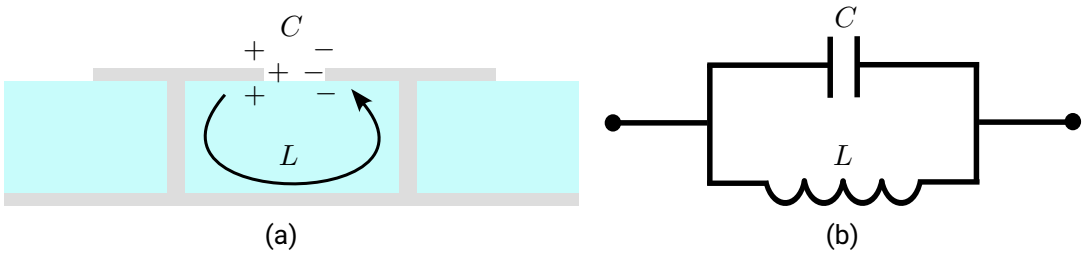

Figure 6.15.: (a) LC model of the EBG mushroom-like. (a) Equivalent parallel LC circuit.

$$C = \frac{W_p\,\varepsilon_0(1+\varepsilon_r)}{\pi}\cosh^{-1}\left(\frac{W_p+g}{g}\right) \qquad (6.5)$$
$$L = \mu_r h$$

It is well-known that the resonance frequency f_0 of the parallel LC circuit shown in Figure 6.15b is given by:

$$f_0 = \frac{1}{2\pi\sqrt{LC}} \qquad (6.6)$$

and the circuit impedance Z_s can be expressed as:

$$Z_s = \frac{j(2\pi f)L}{1-(2\pi f)^2 LC} = \frac{j\omega L}{1-\omega^2 LC} \qquad (6.7)$$

At the frequency of resonance $f = f_0 \rightarrow Z_s = \infty$ and the LC circuit shows infinite impedance, behaving like an open circuit, thus preventing the propagation of electromagnetic waves. It can be noted that for frequencies below the frequency of resonance ($f < f_0$) the impedance is inductive ($Im(Z_s) > 0$), by which the EBG supports TM surface waves. On the other side, for higher frequencies ($f > f_0$), the impedance is capacitive ($Im(Z_s) < 0$), thus supporting TE surface waves.

6.3.2. Characterization of Electromagnetic Bandgaps (EBGs)

There are several methods to analyze the EBGs in order to characterize the bandgap properties of these structures. These different approaches are described next and analyzed with HFSS.

Dispersion diagram

The dispersion diagram is the graphical representation of the wavenumber variation k, that describes the propagation property of electromagnetic waves, with frequency. The calculation of the wavenumber for surface waves is not always a trivial process, and usually, a full wave simulation is performed in order to determine it. This simulation analysis makes use of an eigenmode solver, by which the resonant frequency for a given wavenumber is calculated. There may exist several different solutions at the same frequency, and each one represents a specific propagating mode with its own phase velocity and field distribution.

Since the EBG is a periodic structure, the calculation of the wavenumber can be limited to the so-called irreducible Brillouin zone [113], that determines the range of wavenumbers that must be covered, making use of the structure symmetry. The stop-band or bandgap can be identified as those frequencies that do not yield any real wavenumber solution.

In addition, the dispersion diagram is graphically divided into two areas using a straight line, called light line, which represents the wavenumber in free space $k_0 = \frac{2\pi f}{c_0}$. These two parts correspond to the propagation of slow-waves (surface waves) or fast-waves (leaky-waves), depending if the phase velocity is slower than the speed of light ($v_{ph} < c_0$) or faster ($v_{ph} > c_0$), respectively. Thus, considering a wave propagating along the plane XY, the transverse propagation constant can be described by $\beta = \sqrt{(k_x)^2 + (k_y)^2}$, and the following classification shown in Table 6.1 can be established:

Surface wave (slow-wave)			**Leaky wave (fast-wave)**		
$\lvert\beta\rvert > k_0$	$v_{ph} < c_0$	k_z Imaginary	$\lvert\beta\rvert < k_0$	$v_{ph} > c_0$	k_z Real

Table 6.1.: Surface wave and leaky wave characteristics.

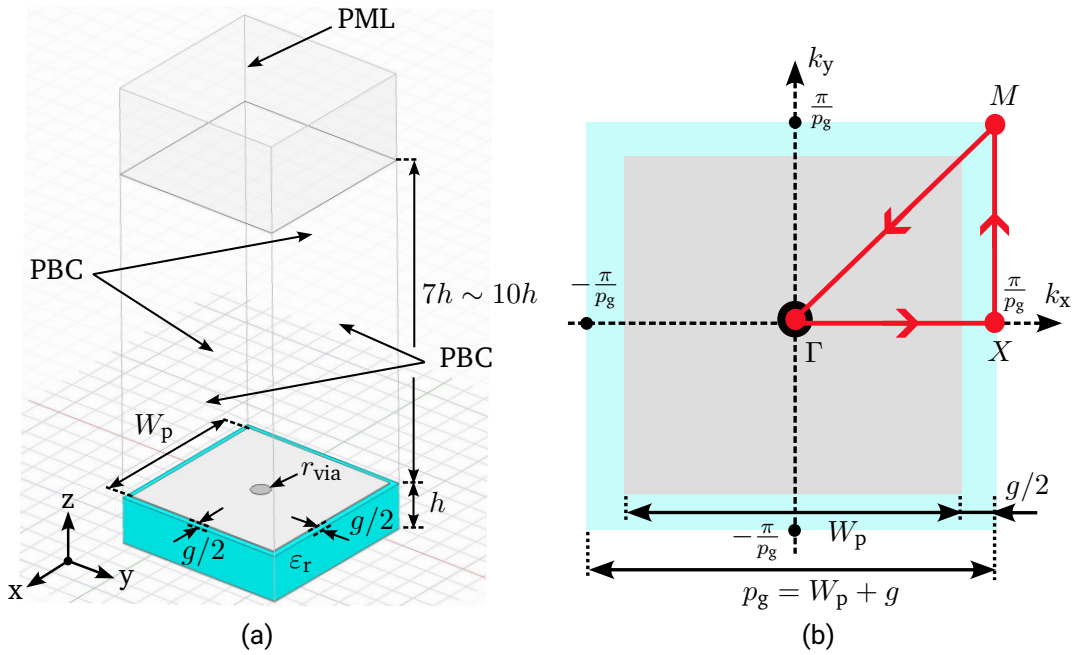

Figure 6.16.: (a) HFSS model of the UC-EBG structure with periodic boundaries using the eigenmode solver. (b) Brillouin zone.

The simulated unit cell model in HFSS is depicted in Figure 6.16a. The EBG structure is placed within an airbox of overall height $8h \sim 10h$, to assure no interference with the surface wave propagation, and terminated on top with an absorber layer PML (Perfect Matched Layer). A periodic boundary condition (PBC) is set on each pair of airbox faces corresponding to constant x and y values of $\big(\pm(W_p + g)/2\big)$.

The Brillouin zone is shown in Figure 6.16b. Due to the structure symmetry, the dispersion diagram can be fully characterized computing the wavenumber values along the branches $\Gamma - X, X - M, M - \Gamma$ defined by the Brillouin triangle. Since the phase difference of the surface wave after propagating along one unit cell is $2\pi/(W_p+g) = 2\pi/p_g$ and the transverse propagation constant is given by $\beta = \sqrt{(k_x)^2 + (k_y)^2}$, each vertex of the Brillouin triangle can be identified from the wavenumbers in x and y directions (k_x, k_y) as shown in Table 6.2

The dispersion diagram of a UC EBG mushroom type with a width $W = 35$ mm, via radius $r_{via} = 2.5$ mm and periodicity $p_g = W_p + g = 37.5$ mm is plotted in Figure 6.17. The unit cell is implemented using a substrate Arlon AD260A of thickness h=10 mm, dielectric permittivity of $\varepsilon_r = 2.65$ and dielectric losses given by $tan\delta = 0.0017$.

Brillouin points	k_x	k_y
Γ	0	0
X	π/p_g	0
M	π/p_g	π/p_g

Table 6.2.: Characterization of Brillouin vertex points.

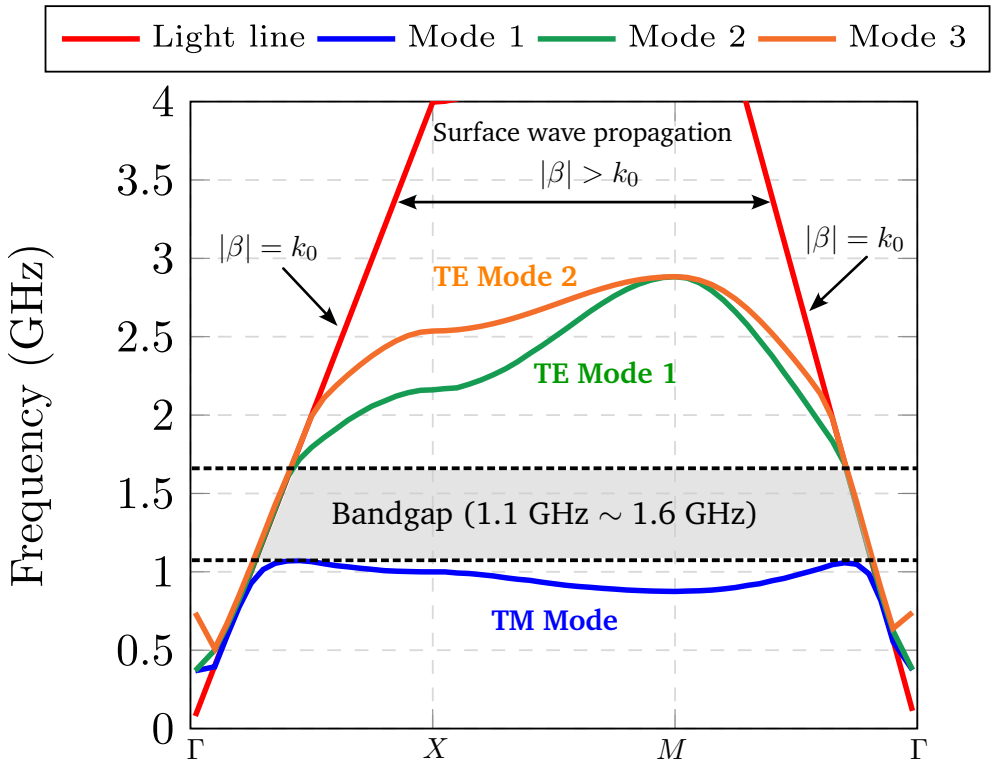

Figure 6.17.: Dispersion diagram.

It can be seen from the dispersion diagram that the propagation of surface waves is confined within the light lines given by $|\beta| = k_0$. Beyond these light lines ($|\beta| < k_0$), leaky waves propagate. Each plotted line represents the propagation of a surface wave at a given frequency, whose propagation direction is defined by the existence of a real wavenumber in x- or y-direction ($k_x \neq 0$, $k_y \neq 0$) or both ($k_x \neq 0$ and $k_y \neq 0$). The stop-band or bandgap can be identified as the frequency range where no surface wave propagates, by which

no real wavenumber solution exists. In the dispersion diagram depicted in Figure 6.17 it can be noted that the suppression band covers approximately the frequency range from 1.1 GH∼1.6 GHz. Below the resonance frequency, TM surface wave modes propagate since the impedance surface is inductive. For higher frequencies beyond the bandgap, the structure supports the propagation of TE surface waves, due to the capacitive nature of the impedance surface. The relative bandwidth of the bandgap BW is given by [108]:

$$BW = \frac{1}{\eta_0}\sqrt{\frac{L}{C}}\,(\%) \tag{6.8}$$

by which is proportional to the factor $\sqrt{L/C}$. Thus, from Eq. (6.5) it can be noted that thicker substrates increase the inductance, ($h \uparrow$, $L \uparrow$), as well as reducing the dielectric permittivity decreases the capacitance value ($\varepsilon_{\mathrm{r}} \downarrow$, $C \downarrow$), leading in both cases to a bandwidth enhancement ($BW \uparrow$).

Reflection phase

Another remarkable characteristic of EGBs is the property to behave as an Artificial Magnetic Conductor (AMC), that does not exist in nature. Hence, EBG structures can provide in-phase reflection to a normal incident plane wave, by which the reflected electric field by the EBG structure has the same phase (in-phase reflection) as the incident electric field, unlike flat metal surfaces or perfect electric conductors that yield a 180° reflection phase, as depicted in Figure 6.18.

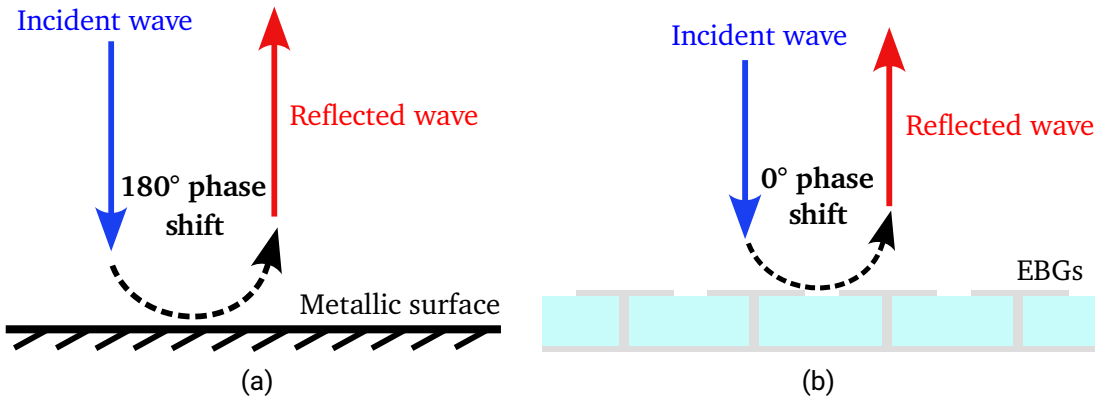

Figure 6.18.: Phase shift of the reflected wave. (a) 180°: metal surface. (b) 0°: EBGs acting as an artificial magnetic conductor.

The bandgap can be thus identified by the frequency range where the reflected phase varies from $\pm 90°$, by which the center frequency of resonance f_0 yields a 0° reflection phase [113]. It is important to point out that not always the in-phase reflection bandwidth coincides with the stopband suppression of surface waves [114].

The characterization of the in-phase reflection in HFSS is performed by simulating one unit-cell with periodic boundaries, and excited with a Floquet port placed on top of the airbox, as shown in Figure 6.19a.

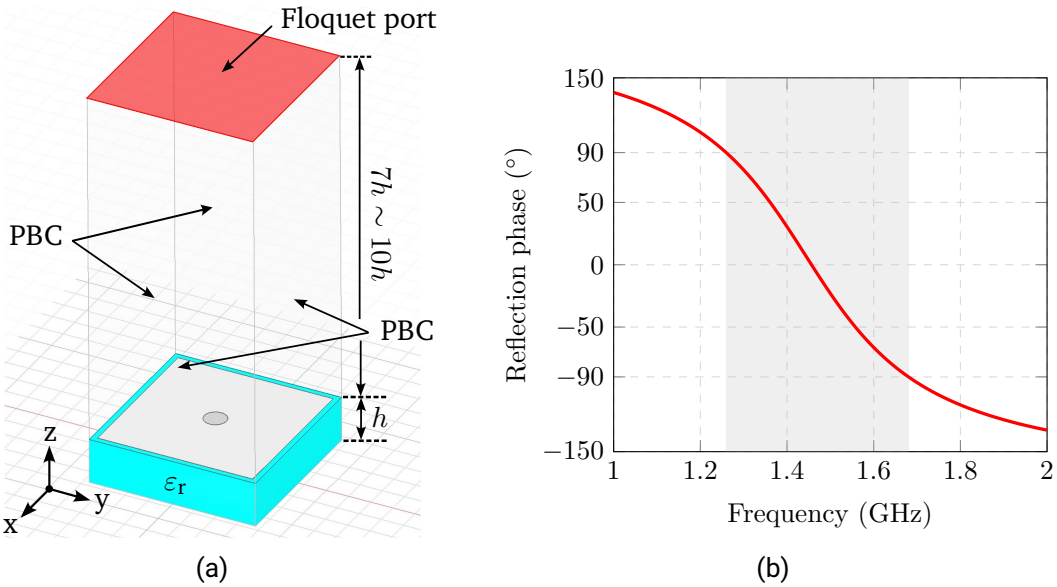

Figure 6.19.: Reflection phase characterization (a) Simulated UC model in HFSS with Floquet port. (b) Reflection phase value over frequency.

The simulated reflection phase is plotted in Figure 6.19b. The bandgap is approximately from 1.25 GHz to 1.68 GHz, and it is given by the frequency range where the reflection phase varies from 90° to -90°. The center frequency of resonance is f_0=1.46 GHz, at which an in-phase reflection of 0° is achieved. The calculated stopband agrees very well with the one extracted from the dispersion diagram, except the slight frequency shift at the beginning of the frequency band. It can be also noted, that for frequencies below the bandgap, the EBG structure behaves as a metallic surface, yielding a 180° phase shift of the reflected wave.

Nevertheless, the in-phase reflection property of the mushroom type EBG UC is less relevant for the proposed application, since the purpose to mitigate the antenna external

interactions is to make use of the surface wave suppression characteristic.

Waveguide transmission method

The EBG structures can be also characterized by means of a waveguide transmission method [115], as depicted in Figure 6.20. A given number of unit-cells are inserted within a waveguide whose top and bottom faces are set as perfect electric conductor (PEC), and the left and right sides as perfect magnetic conductor (PMC). Hence, the waveguide structure can be excited by a TEM vertical wave, that has no cut-off frequency and thus any frequency range can be analyzed, using waveports that are placed at least $\lambda_0/8$ apart from the structure to avoid the effect of higher order modes. The height of the waveguide is usually set as twice the thickness of the EBG structure.

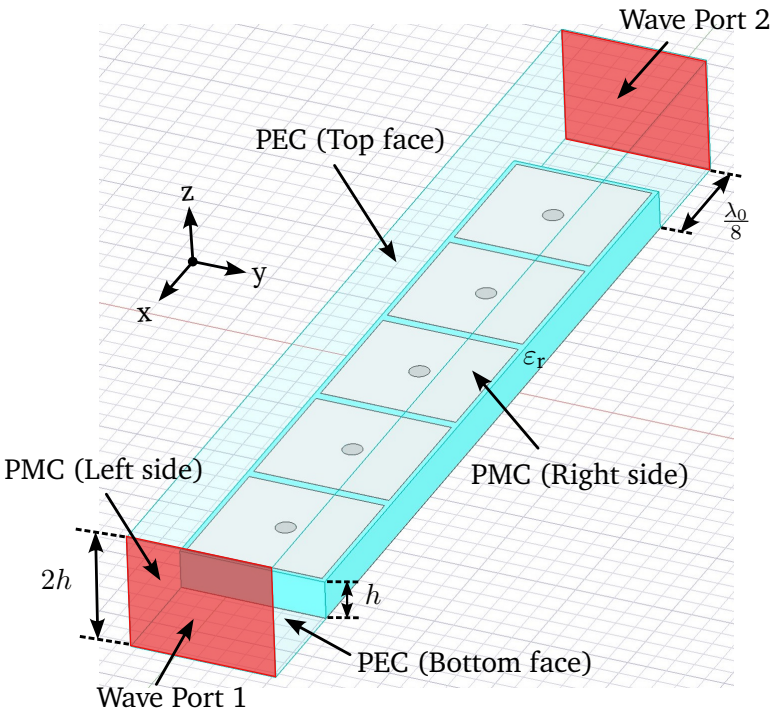

Figure 6.20.: Waveguide transmision model with EBGs.

The simulated S-parameters of the waveguide structure with EBGs are plotted in Figure 6.21. It can be clearly seen that in the bandgap, no transmission occurs since $|S_{21}| \leq -20$ dB and full reflection is achieved with $|S_{11}| \approx 0$ dB. Also in this analysis, the

stop-band begins at slightly lower frequencies than for the previous methods. Nevertheless, it can be noted the overall good agreement among the different approaches.

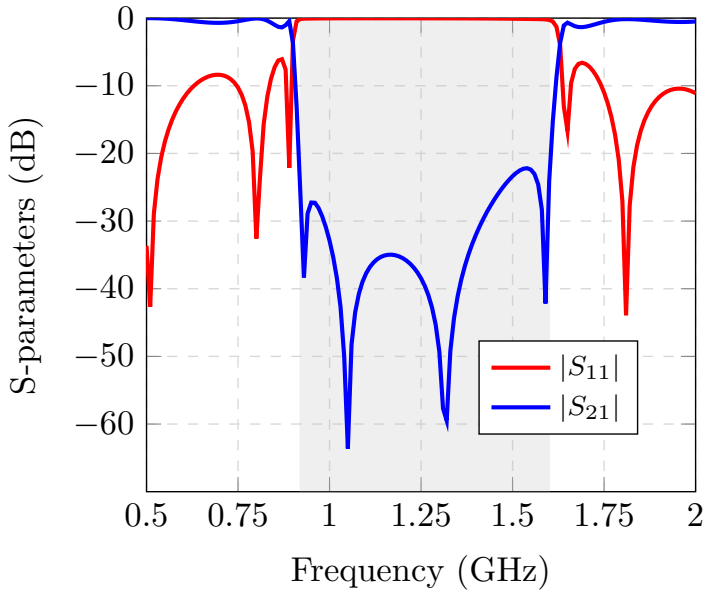

Figure 6.21.: Simulated S-parameters of the waveguide model with EBGs.

Unlike the previous methods, that are based on the simulation of the same unit-cell with periodic boundaries, the waveguide transmission method allows to analyze a EBG structure cascading different unit-cell designs.

Suspended transmission line method

Another method to analyze the stopband performance of the EBGs is exciting the arrangement of unit-cells using a suspended microstrip line [115]. As shown in Figure 6.22, a microstrip line is placed at a given distance d_line from the EBG structure.

However, the expected results might not be always accurate. This is explained due to the inherent capacitance that is added as a result of the coupling of the microstrip line placed above the EBGs, by which the bandgap is shifted to lower frequencies. In addition, this type of feeding technique can also interfere in the bandgap performance due to the interaction of the quasi-TEM fields of the microstrip line with the EBG structure, affecting the excitation of the surface wave modes.

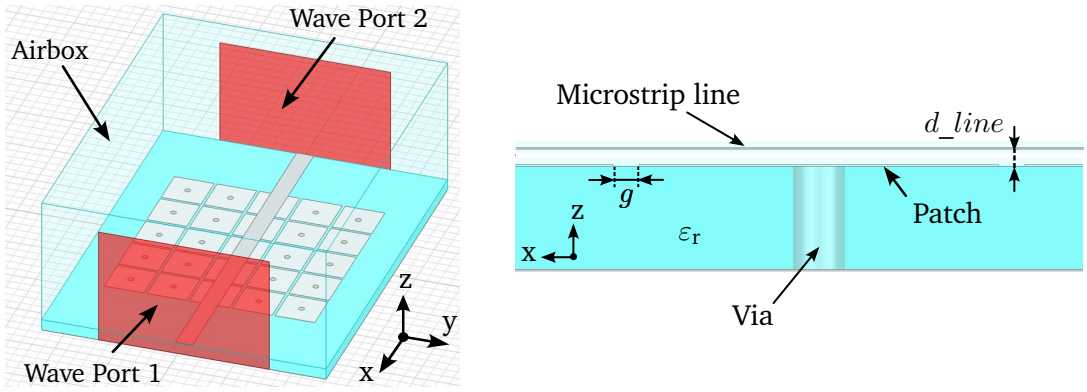

(a) (b)

Figure 6.22.: (a) Suspended transmission line model in HFSS. (b) Side view.

The simulated S-parameters of the suspended transmission line method, for $d\_line = 1$ mm, are plotted in Figure 6.23. It can be noted that the stop-band is shifted to lower frequencies, as depicted in Figure 6.23a. The influence of the microstrip line separation from the EBGs can be seen in Figure 6.23b, by which placing the feeding line closer to the structure yields to broader bandgap bandwidths, due to the higher coupling excitation.

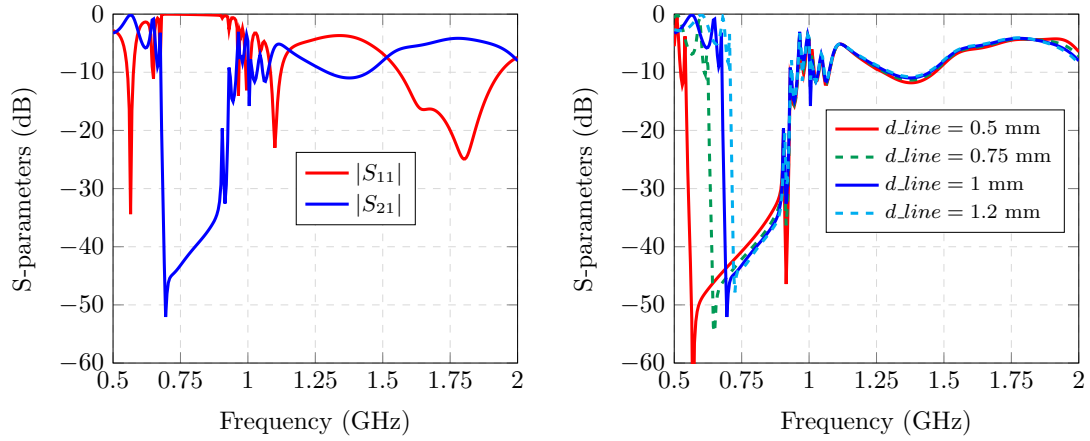

(a) (b)

Figure 6.23.: Simulation results transmission line model. (a) S-parameters. (b) Analysis $|S_{21}|$ for different d_line values.

6.4. Mitigation of the antenna carrier impact using EBGs

The edge diffraction effects, arisen by the interaction with the carrier, can be mitigated making use of the surface wave suppression characteristic of the EBGs. For this analysis, the unit cell EBG mushroom type, as presented previously, is placed on both sides of the the antenna carrier in a geometrical arrangement as depicted in Figure 6.24. This way, the induced currents on the carrier surface can be reduced, thus preventing the edge diffraction effects.

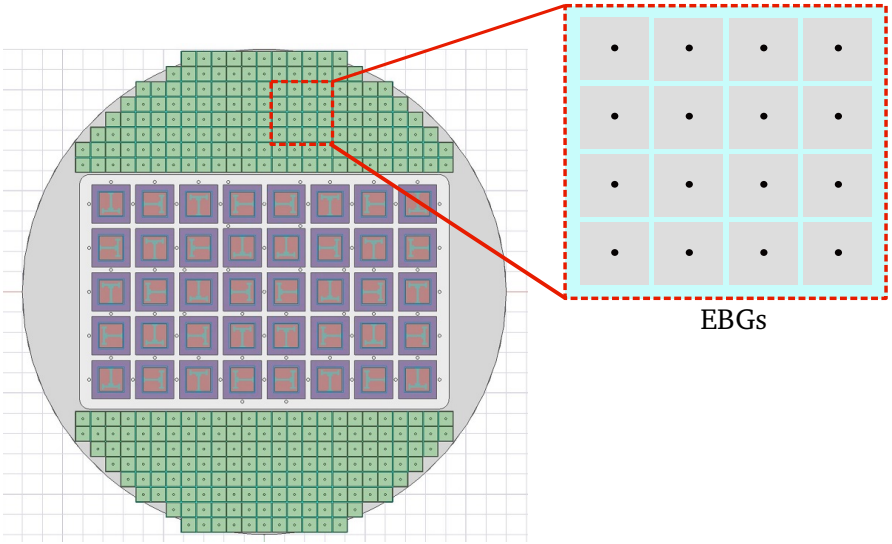

Figure 6.24.: EBGs placed on the surface carrier.

Figure 6.25 plots the surface currents for both polarizations. It can be noted that, in comparison with Figure 6.6 and for the vertical polarization, the magnitude of the induced currents on the carrier surface are strongly mitigated. For the horizontal polarization the surface currents are also reduced, especially around the antenna aperture, where they are more concentrated.

The impact of the EBGs in the radiated electric fields can be seen in Figure 6.26. For the vertical polarization, and in comparison with the Figure 6.7, the radiated fields do not propagate along the carrier, thus achieving a more comparable performance that is similar to the horizontal polarization, that remains practically unaltered.

The radiation pattern in elevation for both polarizations, and a comparison with the antenna carrier without EBGs, is plotted in Figure 6.27. It can be seen that, for the vertical polarization, no beam distortion occur, as well as the antenna gain is increased by 1 dB

approximately when compared with the simulated results with the antenna carrier. On the other side, the performance of the horizontal polarization is not altered. Thus, the use of EBGs allow to achieve a more comparable antenna performance for both polarizations, regardless not only the given antenna carrier geometry, but also for larger electrical carrier sizes. Further work will be to test the proposed solution with manufactured EBGs.

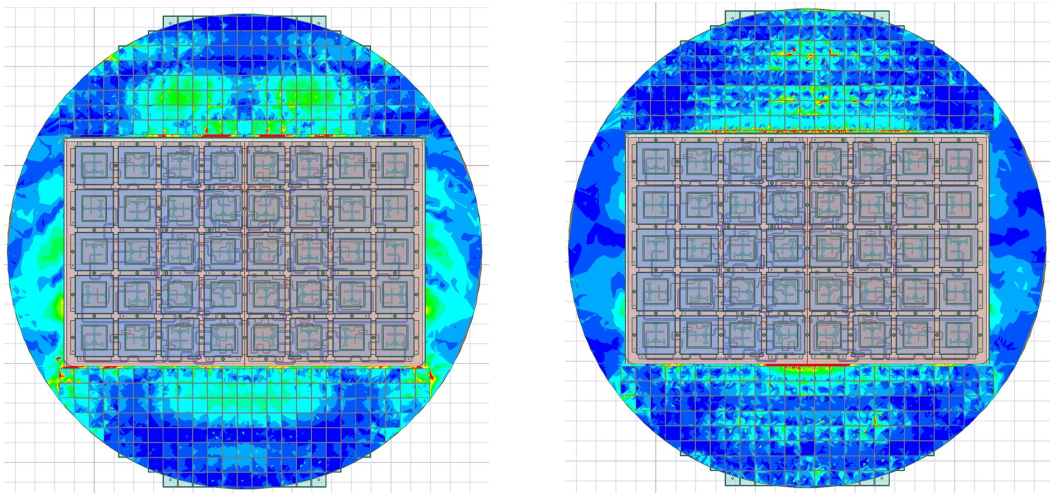

(a) (b)

Figure 6.25.: Intensity of the surface currents induced on the antenna carrier with EBGs. (a) Vertical polarization. (b) Horizontal polarization.

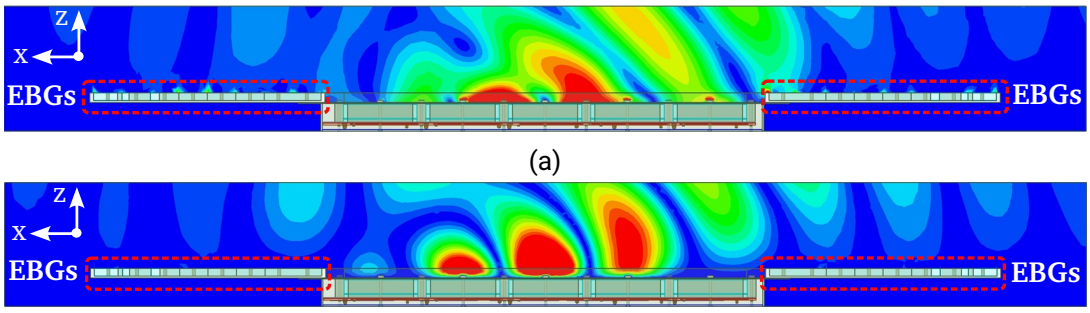

(a)

(b)

Figure 6.26.: Propagation of the electric fields in elevation with the antenna carrier and EBGs. (a) Vertical polarization. (b) Horizontal polarization.

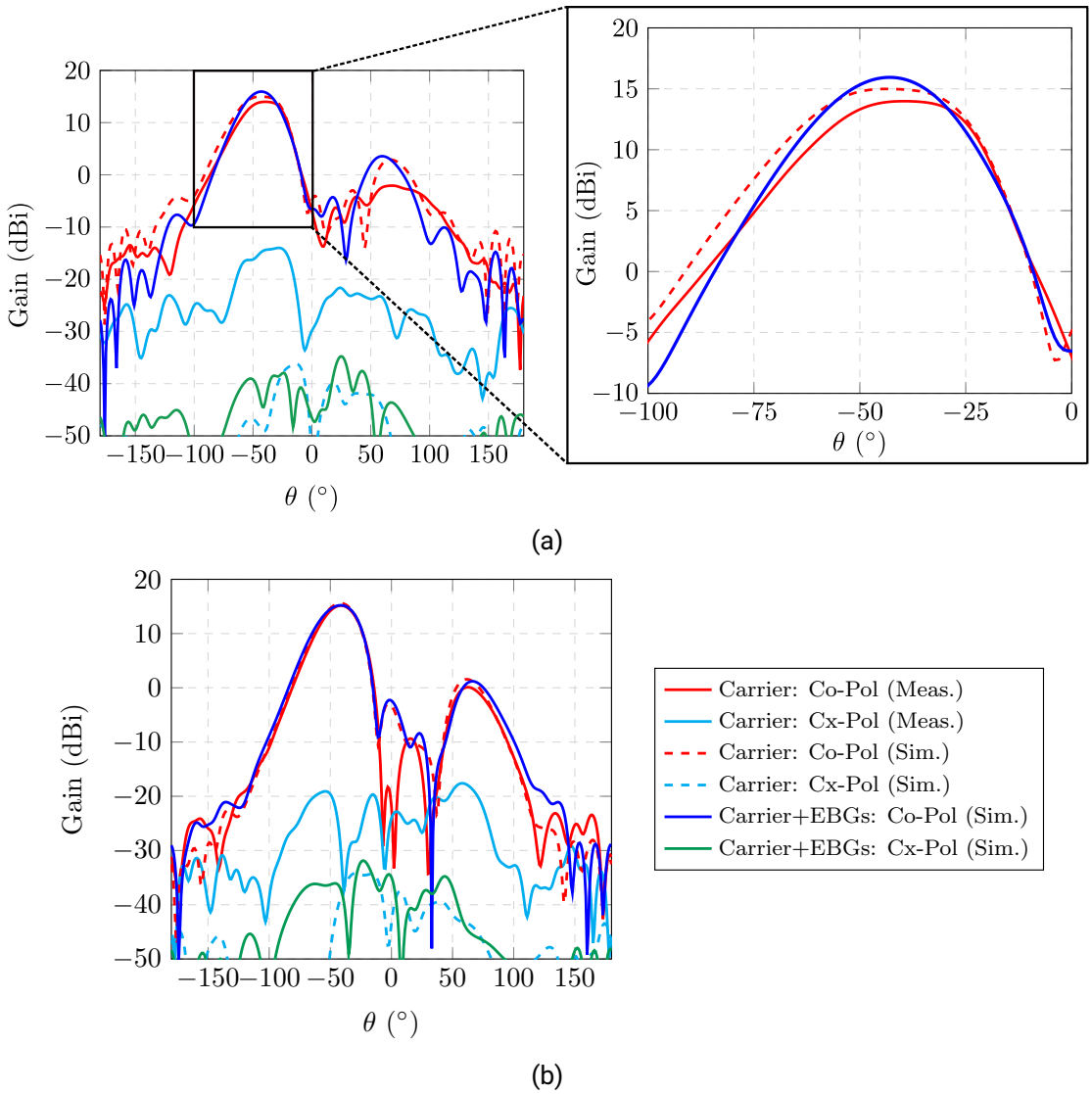

Figure 6.27.: Analysis radiation pattern in elevation with EBGs on the carrier. (a) Vertical polarization. (b) Horizontal polarization.

Last but not least, the previous study has shown the electrical advantages that EBG structures provide in order to mitigate the antenna external interactions. The proposed solution is optimized to achieve the suppression of surface waves in one single frequency

band, namely L-band, which is determined by the required application. The increase of multifrequency systems also leads to a rising interest of mutiband EBGs, that can provide bandgaps at different frequency bands.

For this reason, and in the scope of this work, a EBG multiband unit-cell has been designed that achieves simultaneosly surface wave suppression at the L-, S-, C- and X-band. The choice of these frequency bands is not trivial, since the goal is to mitigate the impact of the F-SAR antenna carrier, onto which several antennas, operating at different frequencies, are installed, as already shown in Figure 2.12.

However, since the patenting process has been initiated, no further information about the proposed solution can be provided.

7. Conclusions and Future Work

Synthetic Aperture Radar (SAR) provides high-resolution imaging data on a global scale, with day-and-night and weather-independent operational capabilities. Due to its versatility and wide scope of applications, SAR has become one of the most well-established Earth remote-sensing techniques in our time.

Making use of the penetrating properties of electromagnetic waves at lower frequencies, SAR allows for monitoring vegetation density or estimating forest height using tomography, as well as performing geological and glaciological studies with subsurface imaging, among other applications.

Precisely, the public concern about climate change and global warming has boosted the demand for spaceborne SAR sensors for environmental studies. Future SAR satellite missions reaffirm the rising interest in Earth surface dynamic monitoring systems.

Next-generation SAR sensors will be driven by the demand to achieve higher resolution imaging along wider swaths. Thereby, future SAR systems will make use of advanced imaging modes by means of digital beamforming techniques, along with bistatic and multistatic constellations. In order to support the development of upcoming spaceborne SAR systems, airborne sensors are employed. Due to their operational flexibility, they are used to test new radar concepts and novel signal processing methods, that is only possible with state-of-the-art hardware. Thus, airborne SAR sensors can be considered at the forefront of technological development.

The increasing complexity of future SAR systems also leads to a more demanding requirements that irremediably affects the antenna system design such as wider bandwidth to improve the range resolution, dual-linear polarized antennas to apply polarimetric techniques, compact hardware to be installed on platforms with limited size, and increasing number of array elements to enhance the digital beamforming capabilities. However, in order to fulfill the aforementioned requirements, the inherent limitations of antenna internal interactions have to be overcome. Thus, methods have to be investigated to achieve an efficient exploitation of the limited antenna aperture size by reducing the array interelement spacing while enhancing its isolation, to improve the bandwidth while keeping a higher degree of integration, or to come up with robust feeding techniques to deal with tolerances in low-profile and compact solutions. In addition, the antenna external

interactions have to be mitigated in order to achieve the desired antenna performance regardless its environment, especially relevant in airborne applications when the antenna is installed on an aerodynamic platform required to fulfill the airworthiness requirements.

Thus, the proposed work will enable the operation of future DLR's airborne SAR sensors, driven by the demand of higher degree of integration required for airborne applications and enhanced beamforming capabilities. In this thesis, the design of highly integrated SAR RF components, such as feeding networks and phased arrays antennas, have been presented and validated with measurements of hardware prototypes.

First, an extremely compact feeding network, based on power dividers in SIW technology and excited by a GCPW line to provide robustness against feeding tolerances, has been presented. In addition, the proposed solution allows to excite the dual-polarized subarray arrangements using stacked-up configurations to provide a higher degree of integration and excitation versatility for beamforming applications.

Secondly, a dual-polarized highly integrated multilayer L-band planar phased array antenna of 5x8 elements has been designed. The development process of the antenna covers several design steps in which the beamforming characteristics, the performance of half antenna, and the final array with integrated feeding networks, have been tested with constructed prototypes. The presented solution exploits efficiently the limited available antenna aperture on the aircraft, providing 66% more array elements than the L-band antenna of the DLR F-SAR system with the same aperture size, thus enhancing the beamforming capabilities of the system.

Last but not least, a method to mitigate the antenna external interaction with the carrier, making use of the stopband properties of Electromagnetic Bandgaps, has been proposed. Thus, the surface currents induced on the antenna carrier can be attenuated leading to a reduction of the edge diffraction effects. This way, a more balanced electrical performance of both polarizations can be achieved regardless the antenna carrier and its electrical size.

Some possible design aspects can be considered to enhance the electrical performance of the proposed solutions for future works. First of all, the five antenna elements in elevation of the phased array in L-band slightly limits the beamforming capabilities of the system in this direction, especially in the backward radiation, despite that the number of array elements have been considerable improved in comparison with the L-band antenna of the F-SAR system. Increasing the number of elements in elevation, that will also lead to a larger antenna aperture size, would yield more degrees of freedom to reduce the backlobe radiation, and thus to suppress the contribution of the opposite imaged area, also known as opposite swath.

As a passive phased array antenna, the unavoidable contribution of the dielectric losses due to the electrical large size of the different feeding networks, especially the elevation network, leads to a reduction of the antenna efficiency, and thus a gain loss. This could be

compensated by using a substrate with less dielectric losses or to implement the elevation feeding network in other technology. However, both options would lead to a larger size of the feeding network that has to be considered if a compact and low-profile solution has to be achieved.

Finally, the proposed method to reduce the edge diffraction effect by means of a EBGs can be extended to multifrequency airborne SAR systems. For instance, in the DLR F-SAR airborne system, and in order to exploit interferometry, several antennas operating at different frequencies are installed on the same carrier structure on the aircraft. Thus, a multiband unit cell EBG that provides the suppression of the surface waves for different frequencies, namely L-band, S-band, C-band and X-band would allow to mitigate the edge diffraction effects using only one unit cell design, regardless the frequency band of operation and the antenna installment position.

A. Doppler Effect

In this section, a theoretical analysis of the Doppler phenomenon, as well as how Synthetic Aperture Radar makes use of the Doppler effect, are described.

The Doppler effect or Doppler shift, named after the physicist Christian Doppler who described it for the first time, is the change of the frequency regarding the observer when it is moving relative to the wave source.

Physical description

Given the scenario depicted in Figure A.1 where a radiofrequency source transmits periodically pulses with a temporal separation Δt_s:

$$\Delta t_s = t_{i+1} - t_i \tag{A.1}$$

From pulse to pulse, the distance between the source and observer increases:

$$\Delta r = r_{i+1} - r_i \tag{A.2}$$

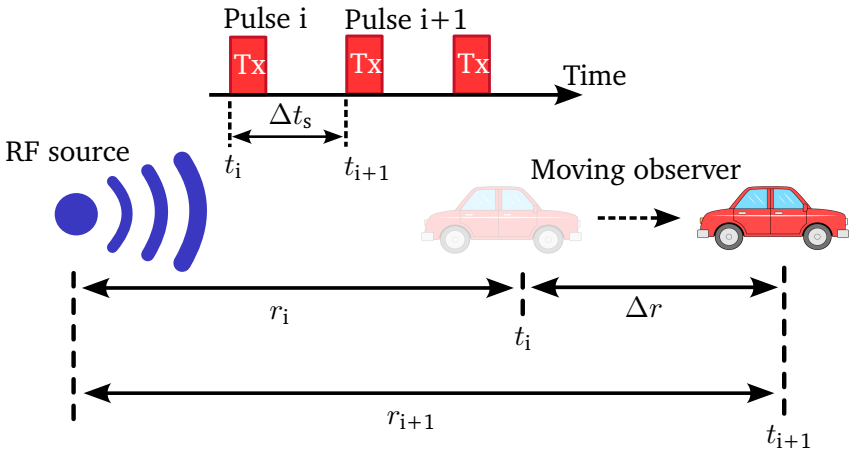

Figure A.1.: Source transmits periodically pulses that are received by a moving observer.

Then, two consecutive pulses arrive at the moving observer at a delayed time interval Δt_{e}:

$$\Delta t_{\mathrm{e}} = \left(t_{\mathrm{i}+1} + \frac{r_{\mathrm{i}+1}}{c}\right) - \left(t_{\mathrm{i}} + \frac{r_{\mathrm{i}}}{c}\right) = (t_{\mathrm{i}+1} - t_{\mathrm{i}}) + \left(\frac{r_{\mathrm{i}+1} - r_{\mathrm{i}}}{c}\right) = \Delta t_{\mathrm{s}} + \frac{\Delta r}{c} \tag{A.3}$$

Dividing by Δt_{s}:

$$\frac{\Delta t_{\mathrm{e}}}{\Delta t_{\mathrm{s}}} = 1 + \frac{1}{c}\frac{\Delta r}{\Delta t_{\mathrm{s}}} \tag{A.4}$$

Considering $f_{\mathrm{s}} = \frac{1}{\Delta t_{\mathrm{s}}}$ and $f_{\mathrm{e}} = \frac{1}{\Delta t_{\mathrm{e}}}$ then:

$$\frac{f_{\mathrm{s}}}{f_{\mathrm{e}}} = 1 + \frac{1}{c}\frac{\Delta r}{\Delta t_{\mathrm{s}}} \Rightarrow f_{\mathrm{e}} = \frac{f_{\mathrm{s}}}{1 + \frac{1}{c}\frac{\Delta r}{\Delta t_{\mathrm{s}}}} \tag{A.5}$$

Since $\frac{1}{1+x} \approx 1 - x$ if $x << 1$ and given that $\frac{\Delta r}{\Delta t_{\mathrm{s}}} << c$ it can be approximated as:

$$f_{\mathrm{e}} \approx f_{\mathrm{s}}\left(1 - \frac{1}{c}\frac{\Delta r}{\Delta t_{\mathrm{s}}}\right) \Rightarrow f_{\mathrm{e}} = f_s - \frac{f_{\mathrm{s}}}{c}\frac{\Delta r}{\Delta t_{\mathrm{s}}} \tag{A.6}$$

The definition of the Doppler shift is the difference between the frequency of the transmitted pulse and the frequency received by the moving observer. Thus, approximating $\frac{\Delta r}{\Delta t_{\mathrm{s}}}$ as the partial derivative in time of the distance $\frac{\Delta r}{\Delta t_{\mathrm{s}}} \Rightarrow \frac{\partial r}{\partial t}$, then:

$$f_{\mathrm{D}} = f_{\mathrm{e}} - f_{\mathrm{s}} \Rightarrow f_{\mathrm{D}} = -\frac{f_{\mathrm{s}}}{c_0}\frac{\partial r}{\partial t} \tag{A.7}$$

Which can be also expressed in terms of the transmitted wavelength:

$$f_{\mathrm{D}} = -\frac{1}{\lambda}\frac{\partial r}{\partial t} \tag{A.8}$$

Doppler shift of a moving radar

As it is depicted in Figure A.2, considering r_0 as the distance of the closest approach between the target and the radar platform at $t = 0$, the instantaneous distance between the point target and the radar that moves at a velocity v_{p} is given by:

$$r(t) = \sqrt{r_0^2 + (v_{\mathrm{p}}\, t)^2} \tag{A.9}$$

Then, applying equation (A.9), the Doppler shift can be calculated as it follows:

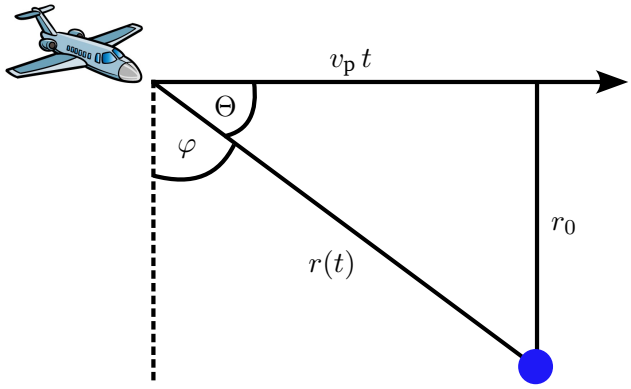

Figure A.2.: Coordinate system of a moving radar.

$$f_D = -\frac{2}{\lambda}\frac{\partial r}{\partial t} = -\frac{2}{\lambda}\frac{v_\mathrm{p}^2 t}{\sqrt{r_0^2 + (v_\mathrm{p}\,t)^2}} \tag{A.10}$$

where the factor 2 comes from the forward and backward propagation.

From Figure A.2 it can be seen that $\sin\varphi = \cos\Theta = -\frac{v_\mathrm{p}\,t}{r(t)}$ (where the negative sign comes from $t < 0$), which leads to:

$$f_D = -\frac{2}{\lambda}\frac{v_\mathrm{p}^2 t}{r(t)} \Rightarrow f_D = \frac{2\,v_\mathrm{p}}{\lambda}\sin\varphi = \frac{2\,v_\mathrm{p}}{\lambda}\cos\Theta \tag{A.11}$$

Iso-Doppler lines

Considering stationary targets distributed in space, all the targets that are seen by the radar at the same time with the same velocity form a cone, whose tip is at the radar and the axis is given by the flight direction. The intersection of such cone with the flat Earth (i.e horizontal plane) forms hyperbolas or iso-Doppler lines, where all the points along the same line have equal Doppler shift. This result is depicted in Figure A.3.

The iso-range lines with constant range, result from the intersection between an sphere, centered in the radar with radio $r = \frac{c\,\tau_\mathrm{p}}{2}$, and the horizontal plane. Two different objects can be separated by its Doppler frequency, as it is seen in Figure A.4. Thus, the capability of distinguishing them is given by the Doppler frequency variation Δf_D, than can be also expressed in terms of the observation time:

$$\Delta f_\mathrm{D} = f_{\mathrm{D}1} - f_{\mathrm{D}2} = \frac{1}{T_\mathrm{obs}} \tag{A.12}$$

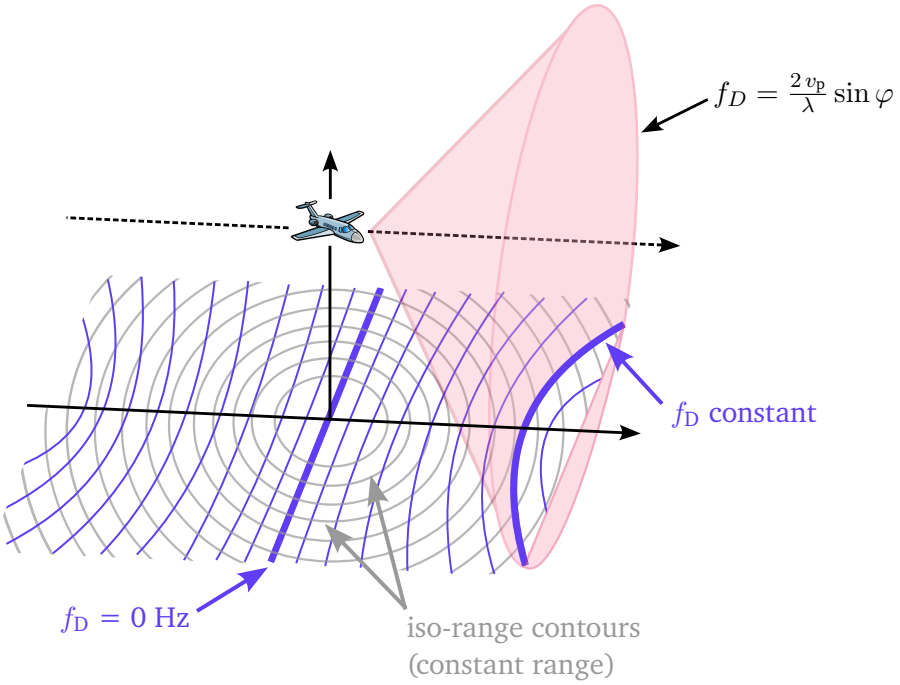

Figure A.3.: Constant Doppler frequency lines.

For small angle variations, equations (A.11) and (A.12) can be approximated by:

$$f_D = \frac{2\,v_p}{\lambda} \sin\varphi \approx \frac{2\,v_p}{\lambda}\varphi \Rightarrow \Delta f_D = \frac{2\,v_p}{\lambda}\Delta\varphi \tag{A.13}$$

And considering equation (A.12), it leads to the following angular resolution:

$$\Delta\varphi = \frac{\lambda}{2\,v_p}\frac{1}{T_{obs}} \tag{A.14}$$

Considering $\Delta\varphi$ as the halfpower beamwidth of the antenna in azimuth and r the range distance, then applying equation (2.6), the azimuth resolution can be expressed as:

$$\delta_{sa} = r\,\Delta\varphi = \frac{\lambda\,r}{2\,v_p}\frac{1}{T_{obs}} \tag{A.15}$$

Which yields the azimuth resolution in SAR systems considering the definition of T_{obs} given in equation (2.13) and assuming $r = r_0$:

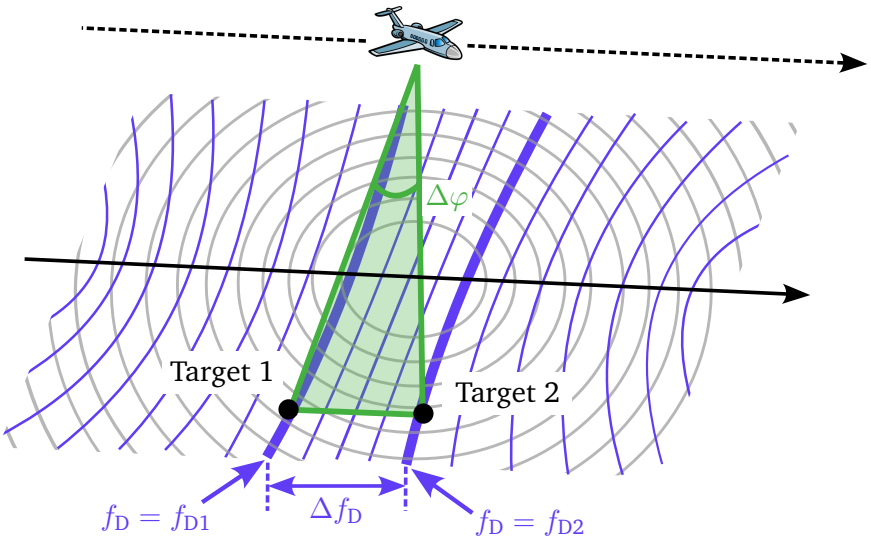

Figure A.4.: Angular resolution based on different Doppler frequency of targets.

$$T_{obs} = \frac{\lambda\, r_0}{d_a\, v_p} \Rightarrow \delta_{sa} = \frac{\lambda\, r_0}{2\, v_p} \frac{1}{T_{obs}} = \frac{d_{az}}{2} \tag{A.16}$$

Being d_{az} the antenna aperture length in azimuth. Thus, a finer spatial resolution in azimuth can be achieved regardless distance and frequency, being only dependent on the antenna size, which becomes the key principle of Synthetic Aperture Radar operation.

B. Antenna Theory

In this appendix, the basics of antenna theory are summarized in order to provide a better understanding of the SAR antenna development presented in chapters 4 and 5 of this work.

B.1. Radiation mechanism of electromagnetic waves

Electromagnetic radiation is created by currents that are generated from the accelerated movement of charges. In order to accomplish radiation, these currents have to follow an oscillating or time-variation distribution. The radiation mechanism is usually produced when these currents interact with discontinuities such as apertures, slots or edges.

The antenna can be considered as a transition interface between a guiding device or transmission line, usually connected to a circuit that provides the antenna excitation, and the free-space where the radiation of electromagnetic waves occurs. Thus, an antenna can be seen as a transducer which converts electrical currents and voltages into electromagnetic waves that are transmitted into free-space. Due to its reciprocity, the antenna can be also used for reception purposes when the opposite mechanism takes place, the received waves are converted into electrical signals such as currents and voltages.

An antenna radiates spherical waves that propagate in the radial direction r, as it is depicted in Figure B.1, considering a spherical coordinate system with angular directions φ, θ where the antenna is located in the center.

Far-field region

The space surrounding the antenna is divided into three different regions where the electromagnetic fields propagate (see Figure B.2). These field areas are given by the proximity to the radiation source and are known as reactive near-field region, radiating near-field or Fresnel region and far-field or Fraunhofer region. For many applications, such as communications, radar or remote-sensing the distance between the source and the receiver (observer, target, etc.) is many wavelengths apart, which means that the propagation of the electromagnetic fields can be characterized in the far-field region.

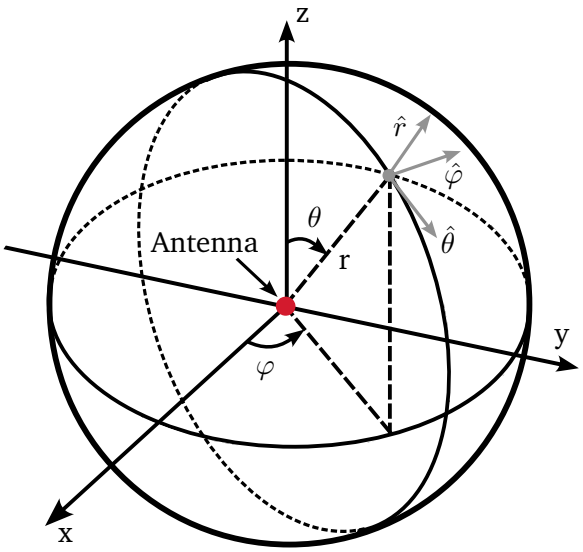

Figure B.1.: Spherical coordinate system.

Typically, the far-field region exists at radial distances from the antenna $R_{\mathrm{F}} > \frac{2D^2}{\lambda}$, being D the largest antenna dimension and λ the wavelength of operation.

Electric and magnetic fields

As a spherical wave, the radiated electric field amplitude E can be expressed as a function of r, φ and θ coordinates:

$$E = f(r, \theta, \varphi) \tag{B.1}$$

At greater distances from the antenna (far-field region) the field distribution only has angular components. The radiated spherical wave can be approximated as a uniform plane wave, since the spherical wave front can be approximated to a planar wave front (the wave energy tends to spread out over a bigger spherical surface area). The electric field vector can be thus expressed as:

$$\vec{E} = [E_\theta(\theta, \varphi)\hat{\theta} + E_\varphi(\theta, \varphi)\hat{\varphi}] \, \frac{e^{-jkr}}{r} \, \left(\frac{V}{m}\right) \tag{B.2}$$

being E_θ and E_φ the phasor componentes of the electric field in the direction of the unit vectors $\hat{\theta}$ and $\hat{\varphi}$.

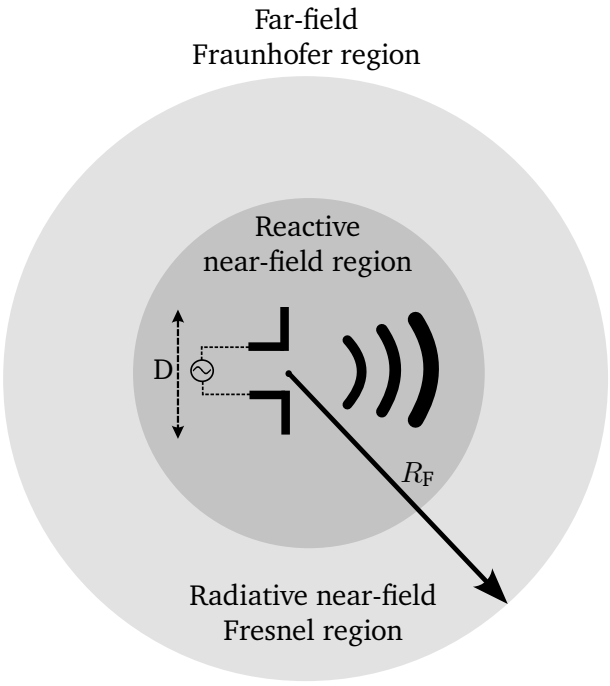

Figure B.2.: Propagation of the electromagnetic waves into different space regions.

As a transversal electromagnetic wave (TEM), the electric $\vec{E}$ and magnetic field component $\vec{H}$ are orthogonal to each other, transverse to the radial direction of propagation and related by means of the intrinsic impedance of the medium η.

$$\vec{E} = \eta\,(\vec{H} \times \hat{r}) \tag{B.3}$$

In free-space propagation this impedance is $\eta = \eta_0 = 120\pi\,\Omega$, and the electric and magnetic field components are given by:

$$\begin{aligned} H_\theta &= -\frac{E_\varphi}{\eta}\ \left(\frac{A}{m}\right) \\ H_\varphi &= \frac{E_\theta}{\eta}\ \left(\frac{A}{m}\right) \end{aligned} \tag{B.4}$$

Polarization

The polarization is a wave property related to plane waves at far-field, by which the phase of the wave is constant over a plane that is perpendicular to the direction of propagation.

The wave polarization can be considered as the direction of the electromagnetic fields while they propagate through a medium. By definition, it is characterized by the orientation of the figure traced by the electric field oscillation or instantaneous electric field vector observed towards the direction of propagation.

If the electric field oscillation is confined in a single plane, and thus the electric field vector variation can be represented along a single line, the electromagnetic wave has a linear polarization. Linear polarized waves are usually defined as horizontal or vertical polarized, in which the plane where the electric field vector oscillates, is orthogonal to each other. For instance, Figure B.3 depicts a linear polarized electromagnetic wave in x direction that propagates along the z direction.

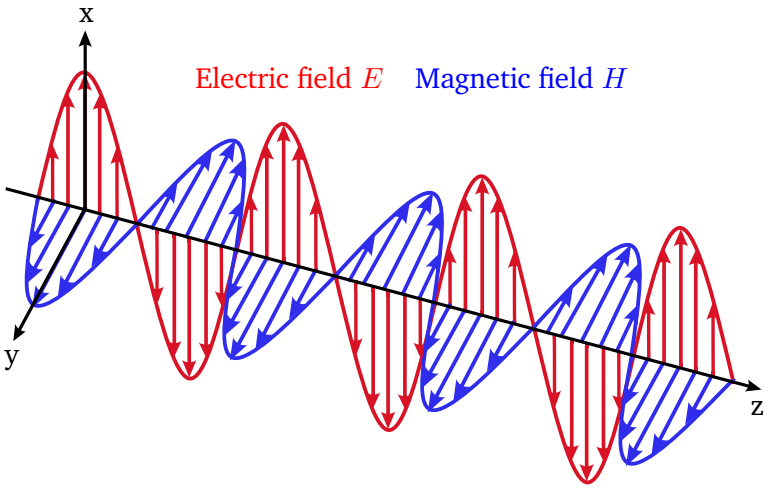

Figure B.3.: Linear polarized electromagnetic wave.

A wave has a circular polarization when the direction of the electric field rotates with time and with a constant magnitude. From the transmitter point of view, circular polarized waves can be classified as right hand (RHCP) or left hand (LHCP) depending on the electric field oscillation if it is clockwise or counterclockwise, respectively. Circular polarized waves can be seen as a combination of two polarized linear waves with a phase shift of 90° between them.

The direction of the electric field of elliptical polarized waves rotates with time and varying magnitude. Linear and circular polarization can be considered as a special case of elliptical polarization.

In SAR polarimetric applications, linear polarized electromagnetic waves are used in order to enhance the retrieval of information, due to the different scattering response

depending on the transmitted polarization. Thus, the scope of this thesis is focused on dual-linear polarized antennas.

In reality, electromagnetic waves are not purely polarized, that means that their polarization state can be divided in two orthogonal polarization components: co-polarization and cross-polarization. Co-polarization or co-pol is the intended polarization to be radiated or received, while the cross-polarization or cross-pol is the undesired orthogonal polarization.

B.2. Antenna parameters

Radiation pattern

In the far-field region, the antenna focuses the transmission or reception of electromagnetic waves in a given angular direction. This characteristic is described by means of the radiation pattern $d(\theta, \phi)$, that measures the ratio of the field strength in a given direction to the maximum field strength at a constant radial distance from the antenna.

The radiation pattern is as a mathematical function by which the radiation properties of the antenna can be graphically represented, as a function of the angular coordinates, and it is independent on the distance to the antenna. Thus, it can be expressed for a given radial distance as:

$$d(\theta,\varphi) = \left.\frac{|E(r,\theta,\varphi)|}{|E(r,\theta,\varphi)|_{max}}\right|_{r=const\to\infty} = \frac{|E(\theta,\varphi)|}{|E(\theta,\varphi)|_{max}} \quad \text{being } |E(\theta,\varphi)| = \sqrt{|E_\theta|^2 + |E_\varphi|^2} \tag{B.5}$$

The radiation pattern is usually plotted in cartesian or polar coordinates, a two-dimensional logarithmical representation that represents a cut in the three-dimensional radiation pattern, as it is depicted in Figure B.4.

The antenna pattern is typically characterized by a main beam that determines the angular direction where the radiation is enhanced, as well as some additional minor lobes that represent radiation in unwanted directions, as it is shown in Figure B.5.

Another important antenna parameter is the half-power beamwidth HPBW, that is the angular separation within two identical points of the main beam at opposite sides that yield values $\frac{1}{\sqrt{2}}$ of the maximum E-field level.

Alternatively, the radiation pattern in terms of power can be expressed by means of:

$$t(\theta,\varphi) = d(\theta,\varphi)^2 = \left[\frac{|E(\theta,\varphi)|}{|E(\theta,\varphi)|_{max}}\right]^2 \tag{B.6}$$

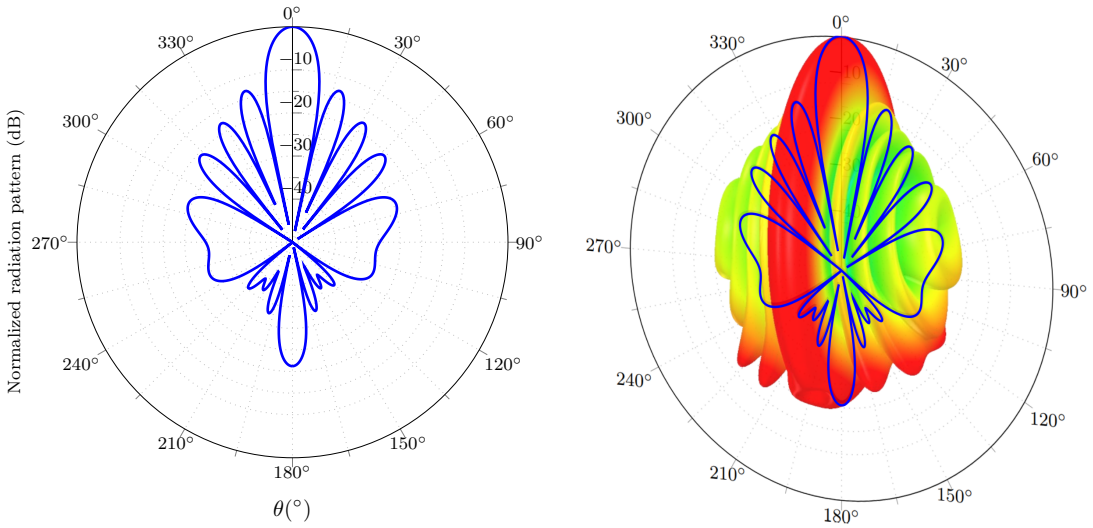

(a) (b)

Figure B.4.: Antenna radiation pattern (a) Polar representation (b) Equivalent cut in 3D radiation pattern.

that also leads to a more common definition of the half-power beamwidth HPBW, defined by the angular separation given by the values of the power radiation pattern that are 3 dB (half-power) below the maximum level, as it is seen in Figure B.5.

Other parameters such as the side lobe level (SLL) and Forward to Backward ratio (FWBR), measure the amplitude difference between the main beam and the first minor lobe, and between the main beam and the back lobe, respectively.

Radiated power

The power density of an electromagnetic wave can be described by means of its Poynting vector:

$$\vec{P}(\theta,\varphi) = \Re[\vec{E} \times \vec{H}^*] \left(\frac{W}{m^2}\right) \tag{B.7}$$

by which $\times$ is the vector cross product and H^* the complex conjugate of the magnetic field phasor. Considering equation (B.3). it can be expressed by:

$$P(\theta,\varphi) = \frac{|E(\theta,\varphi)|^2}{\eta} = \frac{|E_\theta|^2 + |E_\varphi|^2}{\eta} \left(\frac{W}{m^2}\right) \tag{B.8}$$

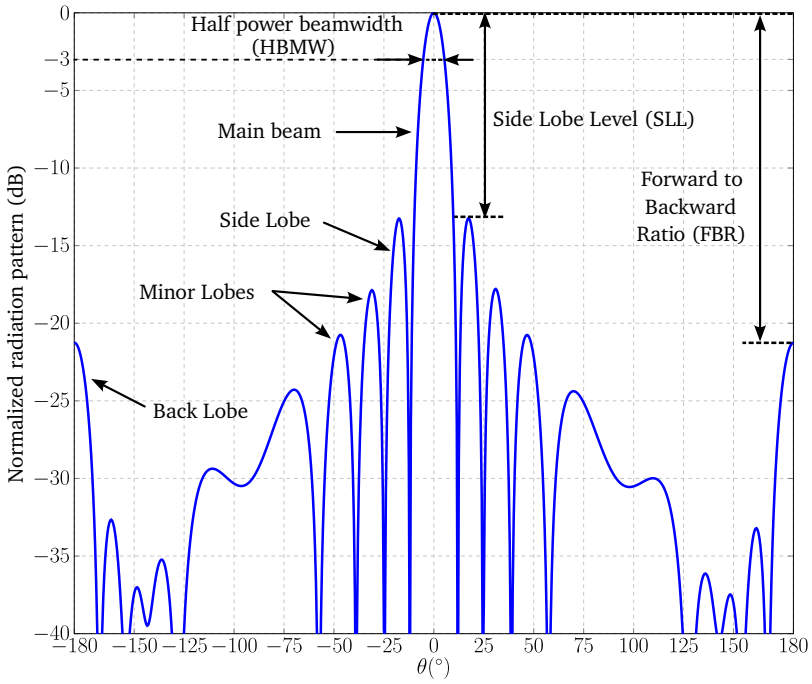

Figure B.5.: Cartesian representation of the radiation pattern.

and decreases over distance as $\frac{1}{r^2}$.

Alternatively, the radiation intensity $K(\theta, \varphi)$ measures the power radiated from an antenna per unit solid angle, in order to remove the dependency on the radial distance. Thus, the radiation intensity remains the same at all distances and it is defined by:

$$K(\theta, \varphi) = r^2 \, P(\theta, \varphi) \, \left(\frac{W}{sr} \right) \tag{B.9}$$

The total radiated power over a spherical surface is given by:

$$W_{\text{rad}} = \iint_S P(\theta, \varphi) \, ds = \iint_S P(\theta, \varphi) \, r^2 \, \sin\theta \, d\theta \, d\varphi \, (W) \tag{B.10}$$

All antennas radiate with different intensities in different directions. An antenna that radiates equally in all angular directions is called an isotropic radiator. An isotropic antenna is an ideal source and it does not exist in practice, but it is used as a mathematical model or reference to compare the radiation properties of real antennas.

Since an isotropic antenna radiates with the same intensity in all directions regardless the spherical coordinates θ and φ, the radiated power of an isotropic radiator, considering a power density P_{iso} uniformly distributed over the surface of a sphere of radius r, can be expressed as:

$$W_{\text{rad}}^{\text{iso}} = \iint_S P_{\text{s}}\, ds = \iint_S = 4\pi r^2\, P_{\text{iso}} \tag{B.11}$$

Directivity

The directivity measures the ability of the antenna to transmit or receive in a particular angular direction. It is expressed by the ratio between the radiation intensity of the given antenna and an isotropic antenna that radiates the same power:

$$D(\theta,\varphi) = \frac{P(\theta,\varphi)}{P_{\text{iso}}} = \frac{P(\theta,\varphi)}{\left(\frac{W_{\text{rad}}^{\text{iso}}}{4\pi r^2}\right)} = D_{\text{max}}\, d(\theta,\varphi)^2 \tag{B.12}$$

The directivity describes only the directional capabilities of the antenna, and thus it is only dependent on the antenna radiation pattern $d(\theta,\varphi)$.

Gain and antenna efficiency

The antenna gain is related to the directivity by means of the antenna efficiency η_{eff}:

$$G(\theta,\varphi) = \eta_{\text{eff}}\, D(\theta,\varphi) \tag{B.13}$$

The antenna gain measures the capability of the antenna to radiate the power delivered to it. Thereby, the antenna gain is the ratio between the radiation intensity of the antenna and the radiation intensity of an isotropic antenna having the same input power W_{in}.

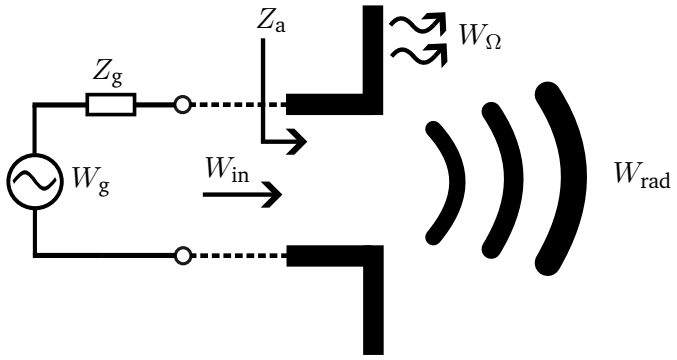

Figure B.6.: Antenna efficiency.

Considering a generator that is connected to the antenna with an impedance Z_g which delivers a power W_g, and an input antenna impedance at its terminals given by:

$$Z_a = R_a + jX_a \tag{B.14}$$

where R_a and X_a are the antenna resistance and reactance respectively. In order to maximize the power delivered to the antenna, then:

$$Z_g = Z_a^* \tag{B.15}$$

However, a real antenna is not ideal but a lossy radiator, and it does not radiate all the power delivered to it due to the inherent conductor and dielectric losses. Thus, the antenna resistance can be expressed as:

$$R_a = R_r + R_\Omega \tag{B.16}$$

by which R_r represents the antenna radiation resistance, and R_Ω accounts the internal antenna losses that causes a power dissipation W_Ω. Thereby, the antenna efficiency η_{eff} can be defined as the ratio of the power delivered to the radiation resistance R_r to the power delivered to R_r and R_Ω:

$$\eta_{eff} = \frac{R_r}{R_r + R_\Omega} \tag{B.17}$$

by which the radiated power of the antenna can be expressed as a function to the power delivered to it:

$$W_{rad} = \eta_{eff} W_{in} \tag{B.18}$$

where the power delivered to the antenna W_{in} is the sum of the radiated and dissipated powers (W_{rad} and W_Ω):

$$W_{in} = W_{rad} + W_\Omega \tag{B.19}$$

Effective Aperture

The antenna effective aperture or effective area describes, in reception, how much power is captured from the antenna (in the direction of the maximum radiation) and delivered to the antenna terminals. Being P_{in} the power density of the received plane wave and W_{rx} the received power, then the effective aperture can be expressed as:

$$W_{\text{rx}} = P_{\text{in}}\, A_{\text{eff}} \quad (W)$$
$$A_{\text{eff}} = \frac{G_{\text{max}}\lambda^2}{4\pi} = \frac{D_{\text{max}}\,\eta_{\text{eff}}\,\lambda^2}{4\pi} \quad (m^2) \tag{B.20}$$

Since the antenna is reciprocal, in transmission, the effective aperture represents the area that the antenna would have if such area would deliver all the power to the antenna. The effective area can be related to the actual physical area of the antenna A_{s} by means of the aperture efficiency η_{ap}.

$$A_{\text{eff}} = \eta_{ap}\, A_{\text{s}} \quad (m^2) \tag{B.21}$$

Bandwidth

The antenna bandwidth is defined as the range of frequencies in which the antenna operates within a certain performance. This operational stability in the frequency band can be measured referring to different antenna parameters, such as input impedance or return loss level, pattern, beamwidth, polarization, gain, etc.

Usually, the antenna bandwidth is described in relative terms (BW), which is defined as follows. Considering f_{min}, f_{max} and f_0 the lower, higher and center frequency of operation respectively, then:

$$BW = \frac{(f_{\text{max}} - f_{\text{min}})}{f_0} \quad (\%) \tag{B.22}$$

B.3. Antenna array

An array is a group of antennas that are spatially separated along one direction (linear array) or two directions (planar array). These antennas are excited with a different amplitude and phase in order to enhance the radiation properties that, otherwise, cannot be achieved with a single radiator. The array arrangement makes use of the wave interferences, by which the radiation characteristics of the antenna group can be shaped in order to achieve higher directivity, to control the angular direction of the main beam or to reduce the side lobe level, among other applications.

Linear array

Considering N antennas equispaced a distance d along z-axis, the total electric field at the observation point P will be the sum of the electric field contribution of each antenna:

$$E_{\text{total}}(\theta,\varphi) = E_1(\theta,\varphi) + E_2(\theta,\varphi) + E_3(\theta,\varphi) + ... + E_{\text{N}}(\theta,\varphi) \tag{B.23}$$

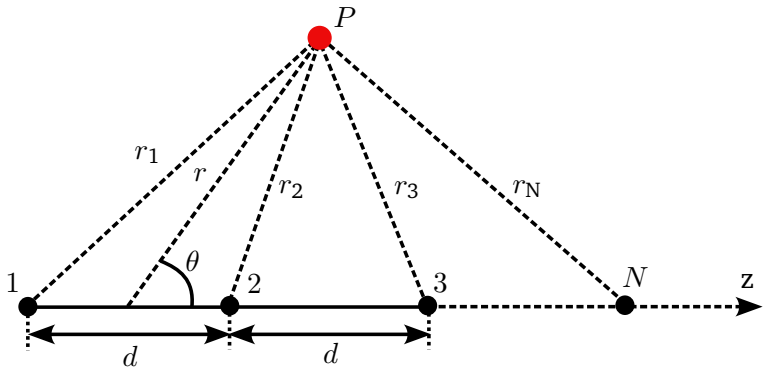

Figure B.7.: Linear array of N antennas.

Considering that all the antennas have the same pattern and radiate the electric field as described in (B.2), we will have:

$$E_{\text{total}}(\theta,\varphi) = \left[E_\theta(\theta,\varphi)\hat{\theta} + E_\varphi(\theta,\varphi)\hat{\varphi}\right]\left(\frac{e^{-jkr_1}}{r_1} + \frac{e^{-jkr_2}}{r_2} + \frac{e^{-jkr_3}}{r_3} + ... + \frac{e^{-jkr_N}}{r_N}\right) \tag{B.24}$$

Assuming far-field observations (the point P is located very far away from the antenna array), the approach of parallel paths can be applied, which leads to $r_1 = r_2 = r_3 = ...r_N$ and thus, to consider the same electrical amplitude of each antenna contribution.

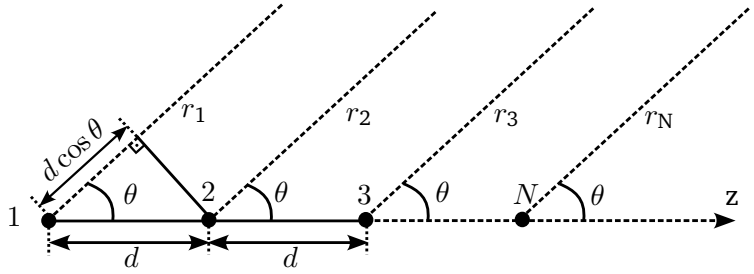

Figure B.8.: Approach of parallel paths.

Regarding the phase variation of the electric field from each path contribution, from Figure B.8 we can easily inferred that:

$$
\begin{aligned}
r_2 &= r_1 - d\cos\theta \\
r_3 &= r_2 - d\cos\theta = r_1 - 2d\cos\theta \\
r_N &= r_1 - (N-1)\,d\cos\theta
\end{aligned}
\tag{B.25}
$$

Thus equation (B.20) can be written as:

$$
\begin{aligned}
E_{\text{total}} &= E(\theta,\phi)\left(\frac{e^{-jkr}}{r} + \frac{e^{-jk(r-d\cos\theta)}}{r} + \frac{e^{-jk(r-2d\cos\theta)}}{r} + ... + \frac{e^{-jk(r-(N-1)\cos\theta)}}{r}\right) = \\
&= E(\theta,\phi)\,\frac{e^{-jkr}}{r}\left(1 + e^{jkd\cos\theta} + e^{j2kd\cos\theta} + ... + e^{j(N-1)kd\cos\theta}\right) = \\
&= E(\theta,\phi)\,\frac{e^{-jkr}}{r}\sum_{n=0}^{N-1} e^{jknd\cos\theta} = E(\theta,\phi)\,\frac{e^{-jkr}}{r}\,(AF)
\end{aligned}
\tag{B.26}
$$

Thus, the total electric field can be expressed as the electric field of the antenna element multiplied by the array factor AF. In addition, defining $\psi = kd\cos\theta$, the array factor becomes:

$$
AF(\psi) = \sum_{n=0}^{N-1} e^{jn\psi} \tag{B.27}
$$

Multiplying by $e^{j\psi}$ and substracting equation (B.27), the array factor can be rewritten as:

$$
AF(\psi) = \frac{e^{jN\psi} - 1}{e^{j\psi} - 1} = e^{j\left(\frac{N-1}{2}\psi\right)}\left[\frac{\sin\left(N\frac{\psi}{2}\right)}{\sin\left(\frac{\psi}{2}\right)}\right] \tag{B.28}
$$

and then the amplitude of the array factor can be expressed as:

$$
|AF(\psi)| = \left|\frac{\sin\left(N\frac{\psi}{2}\right)}{\sin\left(\frac{\psi}{2}\right)}\right| \tag{B.29}
$$

Linear arrays with amplitude weighting and linear phase difference between elements

The antenna radiation pattern can be further optimized providing a given amplitude and phase to each array element.

Applying an amplitude tapering allows to reduce the side lobe level to minimize radiation in undesired directions, as well as to broaden the half-power beamwidth at the expense of losing directivity or to reduce the number of side lobes, among other possibilites.

On the other side, exciting the array elements with a progressive phase difference enables to control the angular direction of the main beam or maximum radiation, which leads to the concept of phased array antenna.

Considering a linear phased array with equispaced elements, the excitation I_{n} of each array element can be described by:

$$I_{\mathrm{n}} = A_{\mathrm{n}} e^{jn\alpha} \tag{B.30}$$

where A_{n} and $n\alpha$ are the amplitude weighting and phase respectively of each element. Thus, if a progressive phase difference among the array elements is considered (α, 2α, 3α...), the array factor can be expressed by:

$$AF(\psi) = \sum_{n=0}^{N-1} A_{\mathrm{n}} e^{jn(kd\cos\theta+\alpha)} = \sum_{n=0}^{N-1} A_{\mathrm{n}} e^{jn\psi} \tag{B.31}$$

redefining $\psi = kd\cos\theta + \alpha$. From this expression, it can be obtained the value of α to choose a particular value for the angular direction of the main beam.

The previous array analysis is considered when the antenna elements are placed along the z-axis. A more generalized array factor can be expressed for any axis as follows:

$$AF(\psi_{\mathrm{a}}) = \sum_{n=0}^{N-1} A_{\mathrm{n}} e^{jn\psi_{\mathrm{a}}} \tag{B.32}$$

where ψ_{a} depends on the axis where the array elements are aligned:

$$\begin{aligned} &\text{x-axis} \rightarrow \psi_{\mathrm{a}} = \psi_{\mathrm{x}} = kd\sin\theta\cos\varphi + \alpha \\ &\text{y-axis} \rightarrow \psi_{\mathrm{a}} = \psi_{\mathrm{y}} = kd\sin\theta\sin\varphi + \alpha \\ &\text{z-axis} \rightarrow \psi_{\mathrm{a}} = \psi_{\mathrm{z}} = kd\cos\theta + \alpha \end{aligned} \tag{B.33}$$

Planar array

A planar array is a two-dimensional arrangement of antennas spatially separated along two directions. Considering a group of $M \times N$ antennas on the XY plane with an element

spacing d_{x} in the x-axis and d_{y} in the y-axis, the excitation I_{mn} of the array element mn can be divided into the amplitude and phase variation along each axis direction:

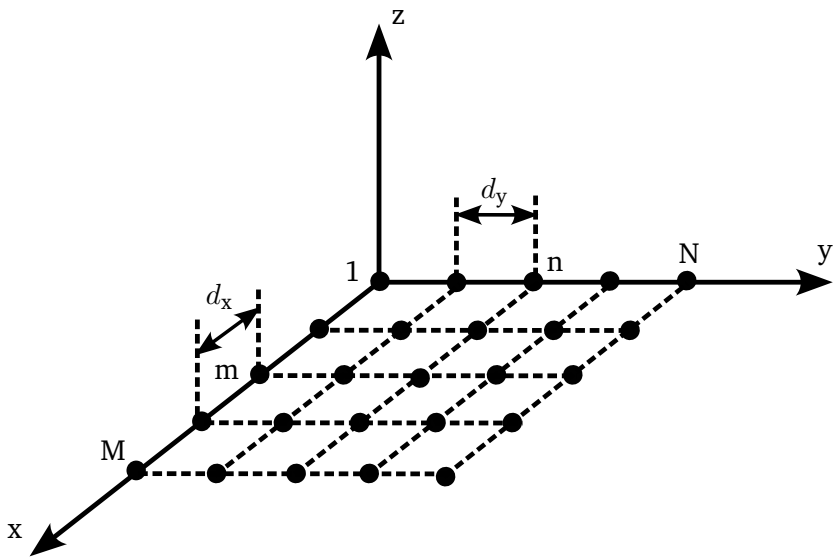

Figure B.9.: Planar array of $M \times N$ antennas.

$$\begin{aligned} I_{\mathrm{mn}} &= I_{\mathrm{m}}^{\mathrm{x}}\, I_{\mathrm{n}}^{\mathrm{y}} \\ I_{\mathrm{m}}^{\mathrm{x}} &= A_{\mathrm{m}} e^{jm\alpha_{\mathrm{x}}} \\ I_{\mathrm{n}}^{\mathrm{y}} &= A_{\mathrm{n}} e^{jn\beta_{\mathrm{y}}} \end{aligned} \tag{B.34}$$

where A_{m}, $m\alpha$ and A_{n}, $n\beta$ are the pair of amplitude and phase values for each element in the x and y direction, respectively.

Thus, considering equation (B.29), $\psi_{\mathrm{x}} = kd_{\mathrm{x}} \sin\theta \cos\varphi + \alpha_{\mathrm{x}}$ and $\psi_{\mathrm{y}} = kd_{\mathrm{y}} \sin\theta \sin\varphi + \beta_{\mathrm{y}}$, the planar array factor AF(ψ) can be expressed as follows:

$$\begin{aligned} AF(\psi) = AF(\psi_{\mathrm{x}})\, AF(\psi_{\mathrm{y}}) &= \sum_{m=0}^{M-1} A_{\mathrm{m}} e^{jm(kd_{\mathrm{x}} \sin\theta \cos\varphi + \alpha_{\mathrm{x}})} \sum_{n=0}^{N-1} A_{\mathrm{n}} e^{jn(kd_{\mathrm{y}} \sin\theta \sin\varphi + \beta_{\mathrm{y}})} \\ &= \sum_{m=0}^{M-1} A_{\mathrm{m}} e^{jm\psi_{\mathrm{x}}} \sum_{n=0}^{N-1} A_{\mathrm{n}} e^{jn\psi_{\mathrm{y}}} \end{aligned} \tag{B.35}$$

C. Fundamentals of Microstrip Technology and Design of Passive Components

In this chapter the basics of microstrip, as well as the design of different components implemented in this technology, are presented.

C.1. Microstrip transmission line

A microstrip line is a type of transmission line based on a metallic strip or signal trace, that is separated from the ground plane using a slab of a dielectric material.

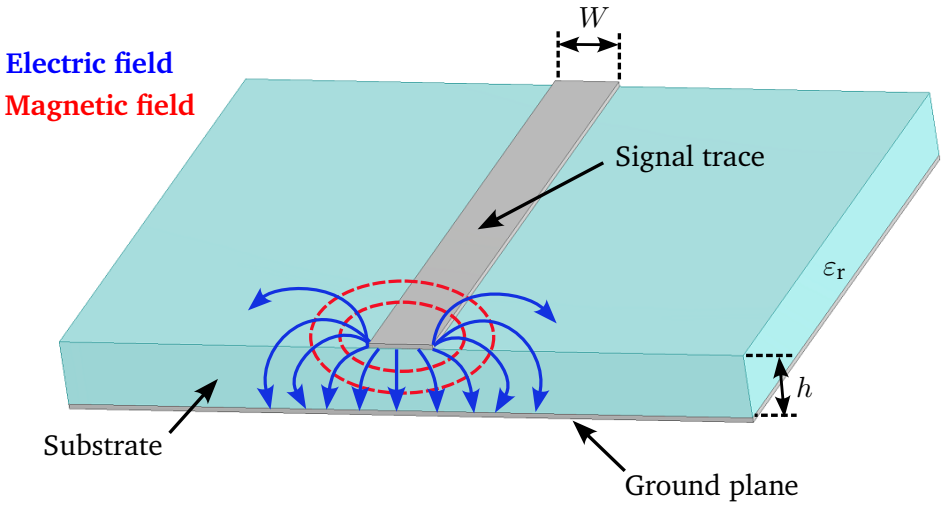

Figure C.1.: Microstrip line.

The microstrip line supports the propagation of a quasi-TEM mode, where the fields propagate in air and within the substrate, as seen in Figure C.1. Thus, this air-dielectric interface leads to the definition of an effective dielectric permittivity ε_{eff}.

The width line W determines the value of the line impedance characteristic Z_0, where greater width values yield lower impedances, and on the other way around.

According to [116], the ε_{eff} and Z_0 values of a microstrip line are given by the following expressions, depending on the ratio between width and substrate thickness W/h:

$$\left.\begin{aligned} \varepsilon_{\text{eff}} &= \frac{\varepsilon_{\text{r}}+1}{2} + \frac{\varepsilon_{\text{r}}-1}{2}\left[\frac{1}{\sqrt{1+12\left(\frac{h}{W}\right)}} + 0.04\left(1-\left(\frac{W}{h}\right)\right)^2\right] \\ Z_0 &= \frac{60}{\sqrt{\varepsilon_{\text{eff}}}}\ln\left(8\left(\frac{h}{W}\right)+0.25\left(\frac{W}{h}\right)\right) \end{aligned}\right\} \quad \left(\frac{W}{h}\right) < 1 \tag{C.1}$$

$$\left.\begin{aligned} \varepsilon_{\text{eff}} &= \frac{\varepsilon_{\text{r}}+1}{2} + \frac{\varepsilon_{\text{r}}-1}{2}\left[\frac{1}{\sqrt{1+12\left(\frac{h}{W}\right)}}\right] \\ Z_0 &= \frac{120\pi}{\sqrt{\varepsilon_{\text{eff}}}\left[\frac{W}{h}+1.393+\frac{2}{3}\ln\left(\frac{W}{h}+1.444\right)\right]} \end{aligned}\right\} \quad \left(\frac{W}{h}\right) \geq 1 \tag{C.2}$$

Thus, being f_0 the center frequency of operation, the guided wavelength λ_{g} of the microstrip transmission line can be expressed by:

$$\lambda_{\text{g}} = \frac{c_0}{\sqrt{\varepsilon_{\text{eff}}}\, f_0} \tag{C.3}$$

C.1.1. Microstrip line excitation in HFSS. Wave ports and lumped ports

Microstrip lines can be excited in HFSS using wave ports and lumped ports. Usually, wave ports provide a higher degree of accuracy, but they have to be placed on a perfect conductor material (PEC) exactly at the limit of the airbox or boundary condition, as depicted in Figure C.2. On the other side, lumped ports can be used as internal ports which provide more flexibility to excite the microstrip lines placing them wherever they are required.

In this work, both types of excitation ports are used depending on the design geometry and complexity. Usually, the first preliminary design stages are simulated using lumped ports. Wave ports are also used to excite waveguides or coaxial connectors, such as SMA or SMP ones, that are considered in the final design, since a more realistic model is required to enhance the accuracy of the simulation results.

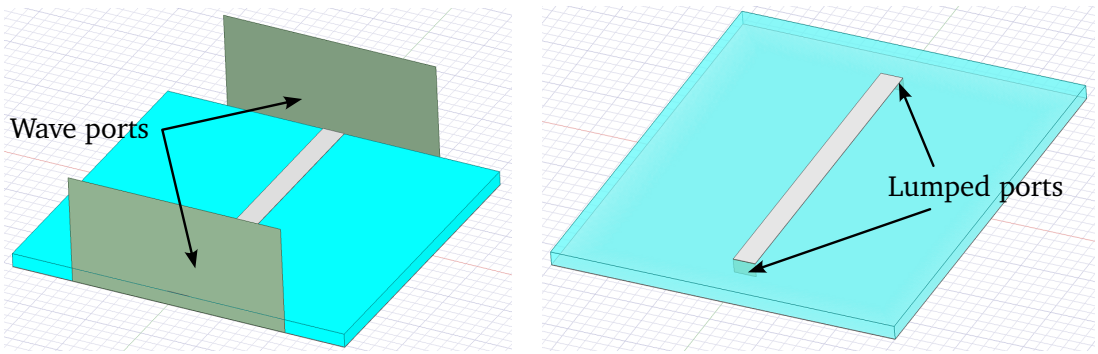

Figure C.2.: Microstrip excitation modeling in HFSS (a) Wave ports. (b) Lumped ports.

Port sizing

As shown in Figure C.2b, the width and height of the lumped ports has to match the line width and substrate thickness respectively. The wave port sizing depends on the ratio W/h, as shown in Table C.1.

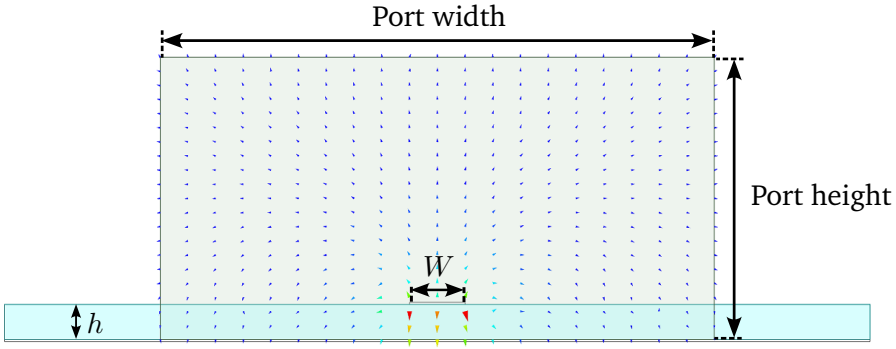

Figure C.3.: Excitation of Quasi-TEM mode. Wave port sizing.

$W \geq h$	**Port width**	**Port height**	$W < h$	**Port width**	**Port height**
	$10W$	$6h \sim 10h$		$5W$ or $3h \sim 4h$	$6h \sim 10h$

Table C.1.: Wave port sizing guidelines.

C.1.2. Phase shift slope variation

Figure C.4 depicts the phase variation of the transmission factor $|S_{21}|$ of a microstrip line for different lengths that are proportional to a guided wavelength λ_g. Considering a substrate with a dielectric permittivity of $\varepsilon_r = 6.15$, thickness $h = 1.22$ mm, and a line width $W = 1.92$ mm, that yields an impedance of $Z_0 = 50\,\Omega$, the calculated guided wavelength for the center frequency of operation $f_0 = 1.325$ GHz is $\lambda_g = 10.8$ cm.

Thus, a microstrip line with a physical length of 10.8 cm does not produce any phase shift, since its electrical length corresponds to a guided wavelength λ_g, as shown in Figure C.4. Thus, the phase variation of the transmission factor at 1.325 GHz is approximately 0°. Increasing the electrical length of the microstrip line in factors of a guided wavelength ($2\lambda_g, 3\lambda_g, 4\lambda_g$) does not affect the value of the phase shift for the center frequency of operation, due to the cyclic phase repetition, but it does change the slope of the phase variation, which impacts the phase shift for other frequencies.

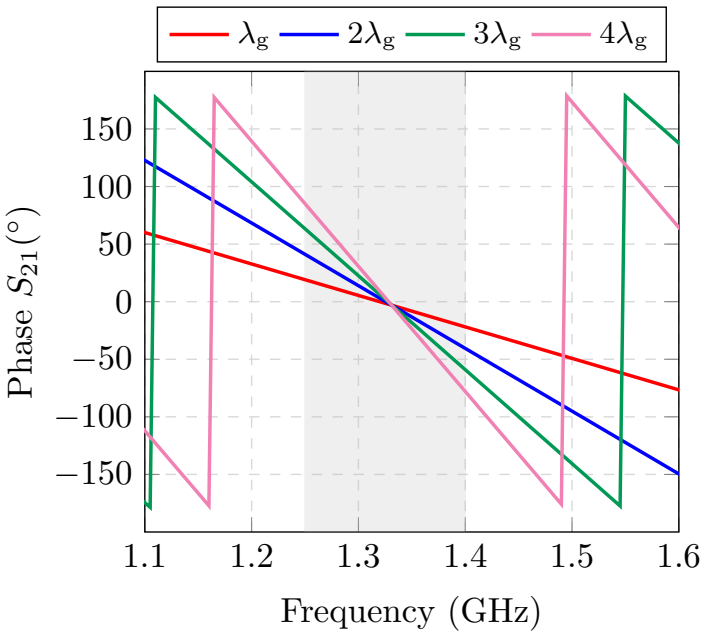

Figure C.4.: Variation slope of the phase shift for different electrical lengths of the microstrip line.

The slope change of the phase variation is considered in the design of the azimuth feeding network. Thus, in order to have a similar phase variation slope, within the

operational bandwidth 1.2 GHz-1.4 GHz, for the excitation of each antenna element along azimuth, a comparable electrical path (in terms of guided wavelengths) between the feeding network input and the position of each slot has been set.

C.1.3. Design of microstrip bend lines

In this work, microstrip bend lines are used to reduce unwanted signal reflections. The optimized design of 90° bend transmission lines, according to Figure C.5, is based on equation C.4:

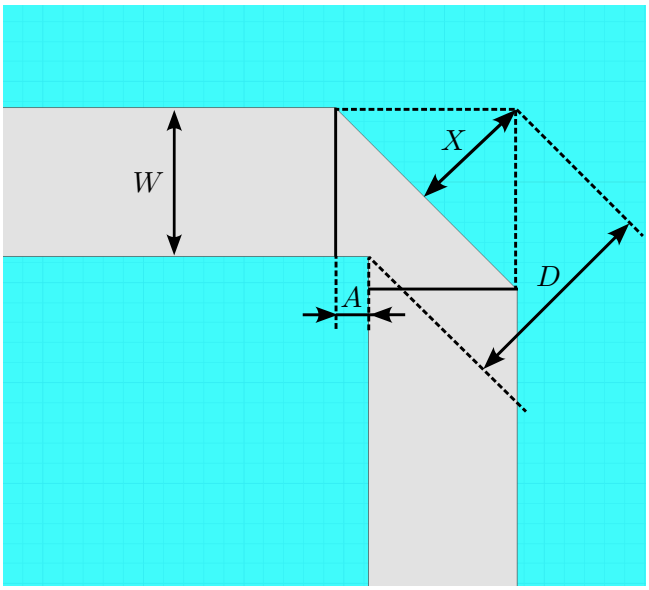

Figure C.5.: 90° bend microstrip transmission line.

$$\begin{aligned} D &= W\sqrt{2} \\ X &= D\left(0.52 + 0.65e^{\left(-1.35\frac{W}{h}\right)}\right) \\ A &= X\sqrt{2} - W \end{aligned} \tag{C.4}$$

C.2. Wilkinson power dividers

In this section, the design of balanced and unbalanced Wilkinson power dividers in microstrip technology is described.

Due to its reciprocity, Wilkinson dividers can be used as power splitters for transmission, and unlike T-Junctions, also as power combiners for receving purposes. The resistance placed between the divider outputs enhances the isolation among them.

C.2.1. Balanced power divider

A balanced Wilkinson power divider equally splits the power at their outputs. Being the input port 1 and the outputs 2 and 3, then $|S_{21}| = |S_{31}| \approx -3\,\text{dB}$, by which half of the power is transmitted to each output. An schematic and the HFSS model are shown in Figures C.6a and C.6b respectively.

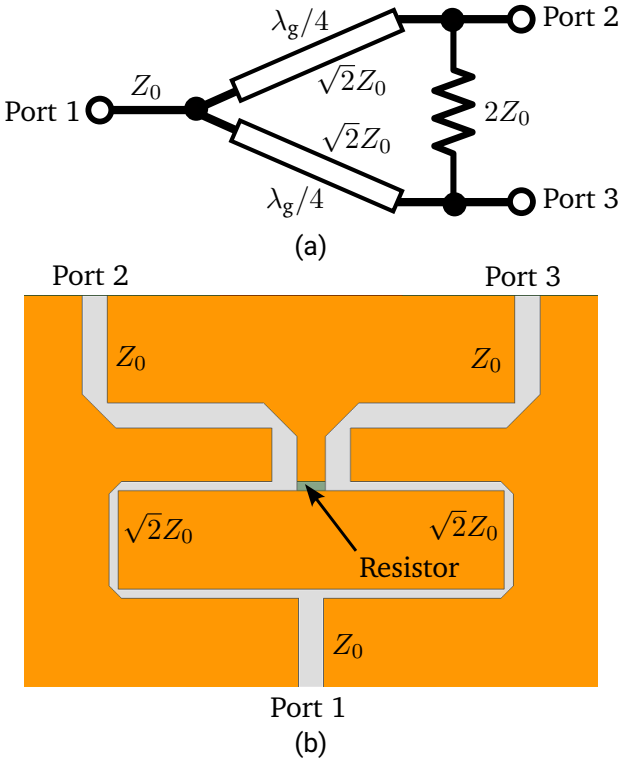

Figure C.6.: Wilkinson power divider (a) Schematic. (b) HFSS model.

C.2.2. Unbalanced power divider

Wilkinson power dividers can be also designed to provide an unequal or asymmetric power distribution at their outputs, by which $|S_{21}| \neq |S_{31}|$. Considering a power ratio between outputs 2 and 3, P_2, P_3 given by $K^2 = \frac{P_3}{P_2}$ and different branch lines impedances of Z_{02} and Z_{03}, then:

$$\begin{aligned} Z_{03} &= Z_0\sqrt{\frac{1+K^2}{K^3}} \\ Z_{02} &= Z_0\sqrt{K(1+K^2)} = K^2 Z_{03} \\ R &= Z_0(K + \frac{1}{K}) \end{aligned} \tag{C.5}$$

being Z_2, Z_3 the impedance at the output of the branches 2 and 3 respectively:

$$\begin{aligned} Z_2 &= Z_0 K \\ Z_3 &= \frac{Z_0}{K} \end{aligned} \tag{C.6}$$

An schematic of the unbalanced Wilkinson power divider is depicted in Figure C.7. The balanced power divider can be considered as a particular case of the unequal power splitter by which $K = 1$.

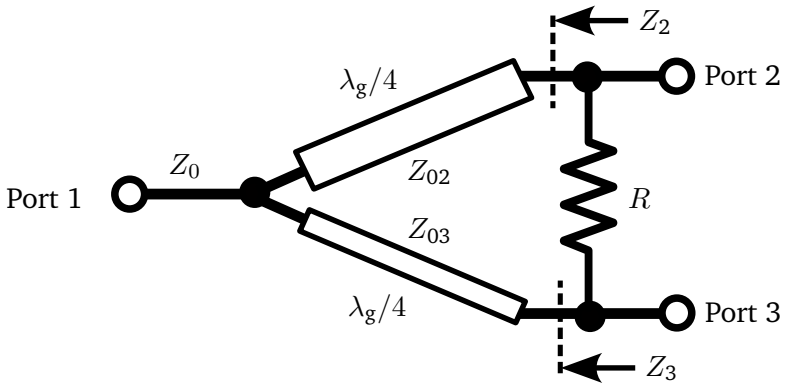

Figure C.7.: Schematic of the unbalanced Wilkinson power divider.

The HFSS model of the unbalanced Wilkinson power divider is shown in Figure C.8.

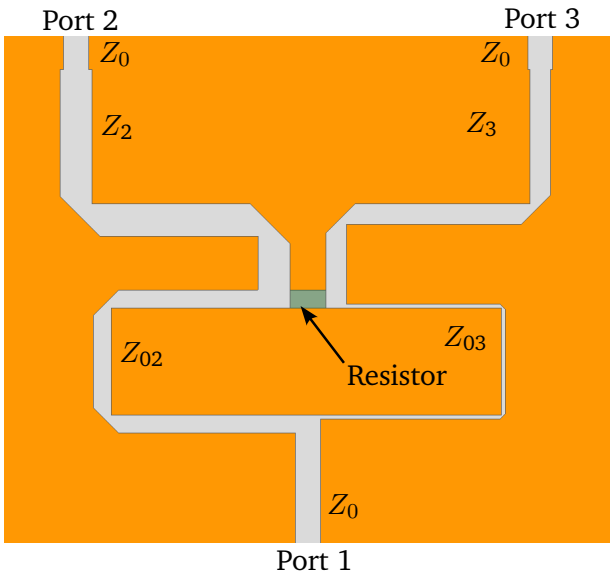

Figure C.8.: HFSS model of the unbalanced Wilkinson power divider.

Ticer resistive films

In the design of the azimuth feeding network, the resistors of the power dividers have been implemented by means of resistive thin foils [101]. Combining resistive square films of a given ohmic value per square (Ω/sq), different resistors can be built. For instance, for a terminal load of 50 Ω one square (of 50 Ω/sq) can be used, as well as using two squares a 100 Ω resistor can be achieved. This technology is extremely useful for multilayer designs since it enables a more homogeneous electrical performance, avoiding to solder individually lumped resistors.

In order to use this technology, a special substrate that allows its manufacturing must be used.

C.3. 10-dB directional coupler

For the implementation of the azimuth and elevation feeding networks, 10-dB directional coupling lines have been employed. They are used to couple a small fraction of the power (10 dB) from the direct transmission line, thus enabling to use the coupled power to excite further array elements.

Figure C.9 depicts a 10-dB coupling line model in HFSS, with the corresponding ports

numeration. Almost all the energy is transmitted to the second port, by which $|S_{21}| \approx 0.5$ dB, that accounts for the insertion losses. The coupled power is directed to the output 3 with $|S_{31}| \approx -10$ dB, and the minimum remaining power is absorbed by the terminal load, that is short circuited to the ground by means of vias. The length of the coupling line is approximately $\lambda_g/4$, and it is located very close to the main line so it can be electromagnetically coupled.

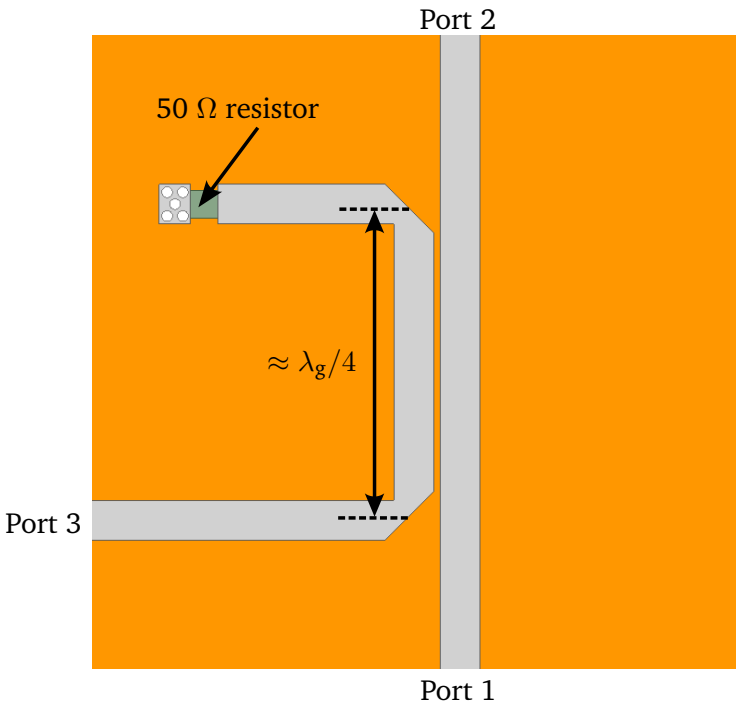

Figure C.9.: HFSS model of the 10-dB directional coupling line.

C.4. PCB Test Wilkinson dividers

In order to assess the suitability of the Ticer resistive films, a multilayer PCB for testing purposes has been prepared with the layout depicted in Figure C.10. Thus, the performance of the microstrip components required in the implementation of the azimuth feeding network, namely Wilkinson power dividers and directional couplers, can be tested before its application. The PCB is designed using two layers of the substrate Rogers RO4360G2

($\varepsilon_r = 6.15, \tan\delta = 0.0038$), each of them with a thickness $h = 1.22$ mm, as it will be used later for the manufacturing of the azimuth feeding network.

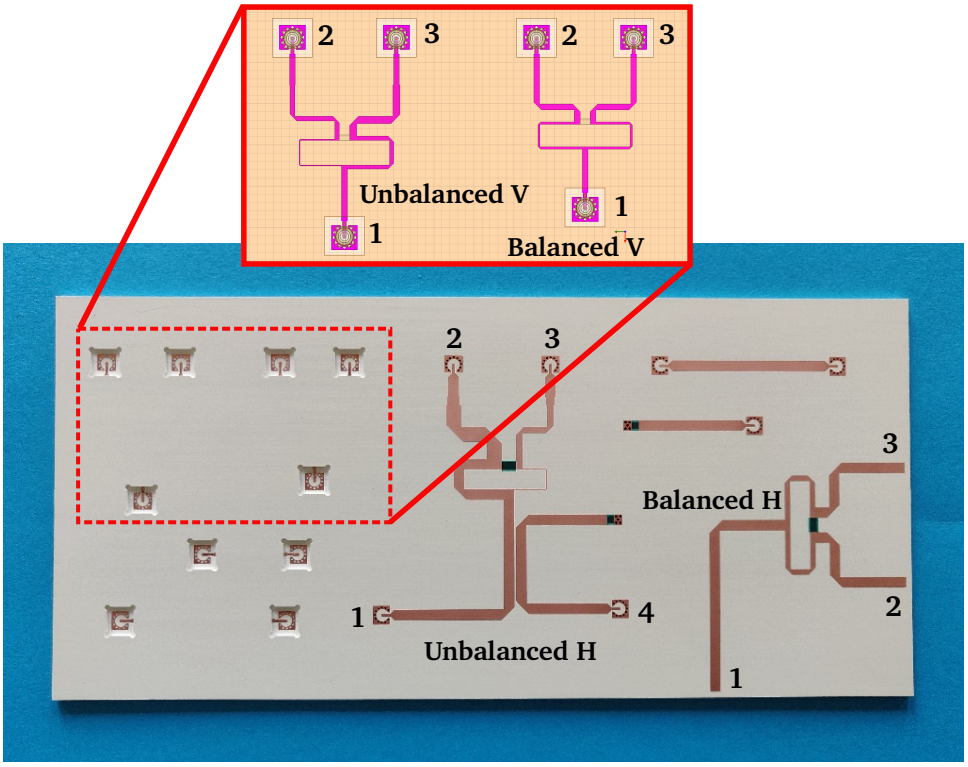

Figure C.10.: Prepared PCB multilayer for testing purposes.

All the components are excited by SMP connectors except the balanced power divider H, that is fed by SMA connectors. The S-parameters of each Wilkinson splitter are measured and compared with the simulation. The port numeration can be found in Figure C.10.

C.4.1. Measurements of the power dividers V

The Wilkinson power dividers V are placed in the intermediate layer, and they are used to excite the vertical polarization in the azimuth feeding network. The use of resistive thin films in multilayer structures prevent the substrate milling in order to allow the soldering of the lumped resistor, becoming the application of this technology extremely convenient.

The return loss level and the transmission factor at each output of the balanced and unbalanced power dividers V are plotted, respectively, in Figures C.11 and C.12.

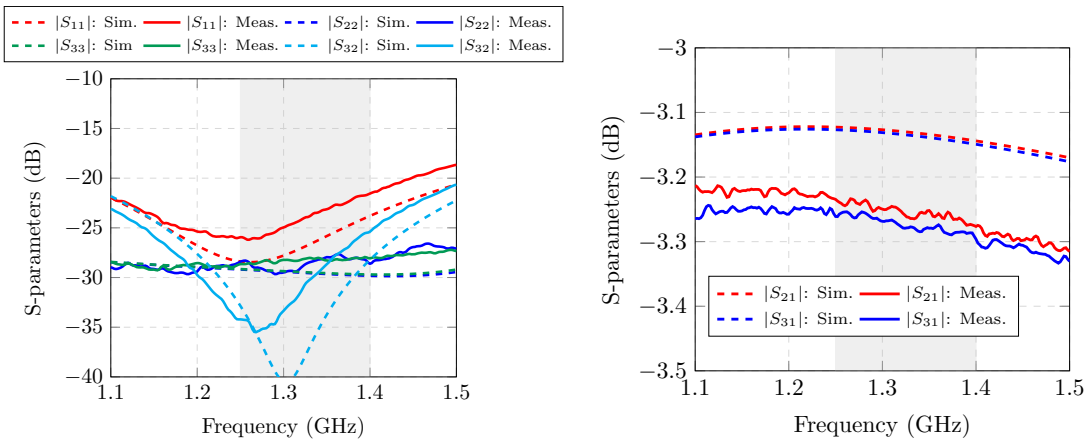

(a) (b)

Figure C.11.: Measured S-parameters of the balanced Wilkinson divider V. (a) Reflection factor and output ports isolation. (b) Transmission factor.

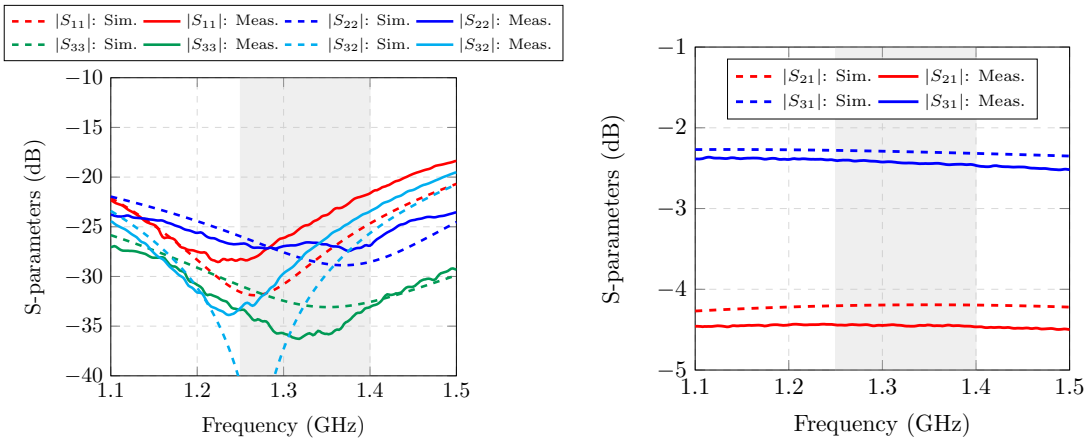

(a) (b)

Figure C.12.: Measured S-parameters of the unbalanced Wilkinson divider V. (a) Reflection factor and output ports isolation. (b) Transmission factor.

It can be seen that the measurements of both power dividers meet really good the simulation results. The insertion losses are slightly higher since the SMA-SMP adapters required for the measurement are not included in the calibration of the network analyzer.

C.4.2. Measurements of the power dividers H

The same measurements are performed with the power dividers H. Figure C.13 shows the measured S-parameters of the balanced power divider. It can be noted that, despite that the return loss at the input is better than 15 dB, measurements show a slight performance shift to lower frequencies. This can be explained due to the SMA connectors, since their unstable position at the edge of the PCB board prevent a clean soldering process. Nevertheless, the measured results are satisfactory.

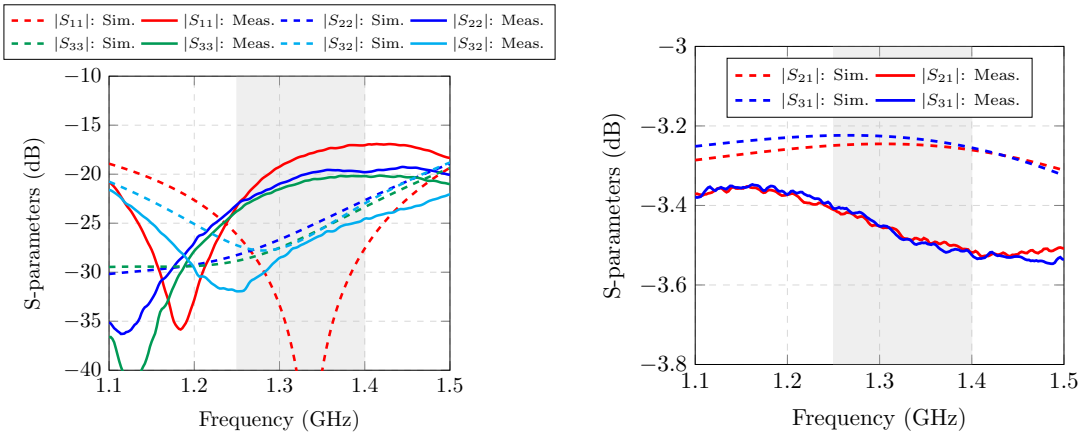

(a) (b)

Figure C.13.: Measured S-parameters of the balanced Wilkinson divider H. (a) Reflection factor and output ports isolation. (b) Transmission factor.

The measured S-parameters of the unbalanced power divider are plotted in Figure C.14. Unlike the previous power divider, it can be noted that the measurements of the unbalanced divider, and the coupling line, agree extremely well with the simulation results.

Thus, after performing the measurements of the PCB board test, it can be confirmed the suitability of the resistive thin film technology to implement the resistors of the Wilkinson dividers.

C.4.3. Power handling measurements

Additionally, further measurements are performed in order to evaluate the power handling capabilities of the Ticer thin film resistors. This analysis is specially relevant for the design of the elevation feeding network, due to the power level that this feeding network must handle, specially at the first layout stages.

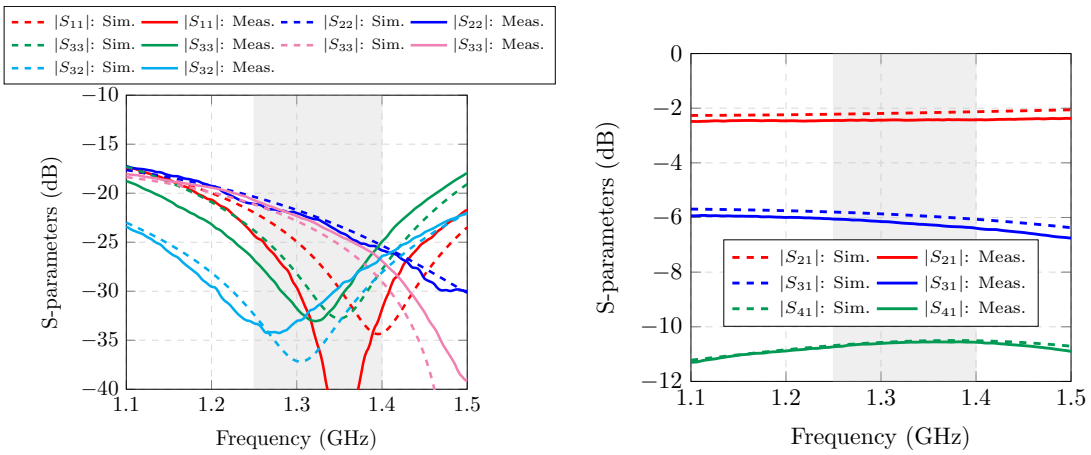

(a) (b)

Figure C.14.: Measured S-parameters of the unbalanced Wilkinson divider H. (a) Reflection factor and output ports isolation. (b) Transmission factor.

For this measurement purpose, the different power dividers and lines of the PCB board are excited by an RF pulse with a peak power of 1 kW, and varying gradually the average power until 100 W, which corresponds to the operation conditions of the F-SAR system in L-band. For each measurement, the temperature on the resistive film has been measured using an infrared camera.

The measurement setup uses a pulse generator and a high power amplifier. The outputs of the power dividers are connected to high power 50 Ω loads to dissipate the power.

Varying the pulse repetition frequency ($PRF = 1/T$) for a determined peak power ($P_{\text{peak}} = 1$ kW), and pulse duration ($\tau_{\text{p}} = 10\,\mu$s), different values of average power P_{avg} can be achieved, as depicted in Figure C.15.

$$\frac{P_{\text{avg}}}{P_{\text{peak}}} = \frac{\tau_{\text{p}}}{T} = \tau_{\text{p}}\, PRF = \text{Duty cycle} \tag{C.7}$$

Thus, the PCB board can be excited with a pulse having an average power from 10 W to 100 W modifying the duty cicle from 1% to 10 %, corresponding to PRF values from 1 KHz to 10 KHz. The measurement process is shown in Figure C.16.

After performing the power handling measurements, the following conclusions are summarized next:

- All power dividers for both polarizations have handled 100 W average power excita-

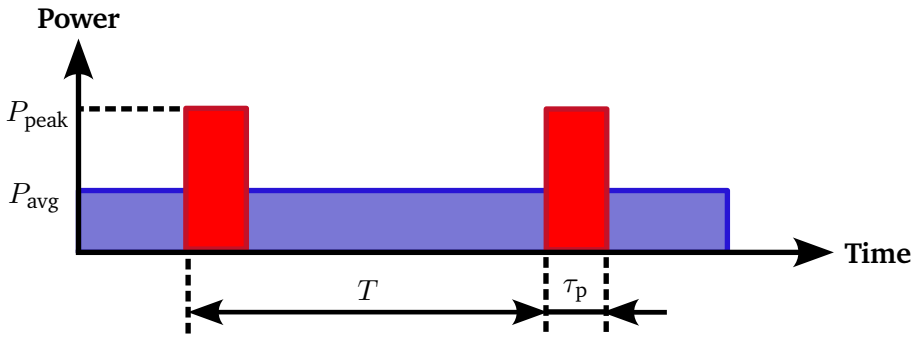

Figure C.15.: Pulse power peak and power average.

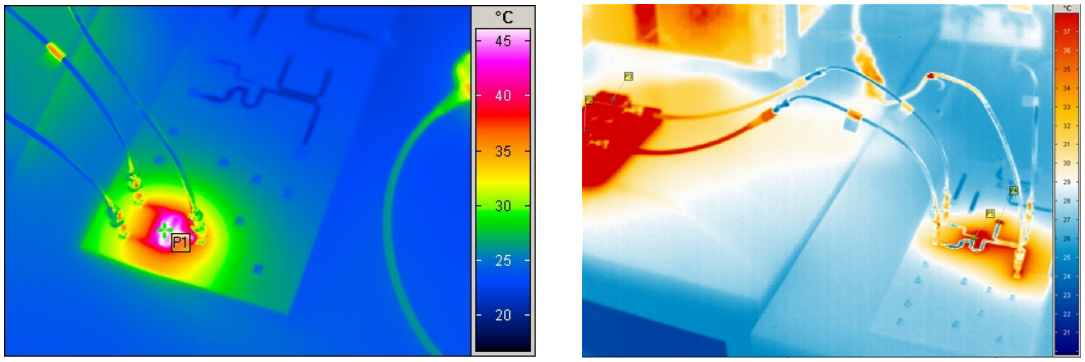

(a) (b)

Figure C.16.: Power handling measurements. (a) Unbalanced power divider V (b) Unbalanced power divider H.

tion. After measurements, the S-parameters of the power dividers were measured again in order to confirm its normal operation.

- The thin film resistor of the unbalanced power divider H has achieved a maximal temperature of approximately 90°. For the balanced divider, a temperature value of around 60° has been achieved. This can be explained due to the asymmetric power output distribution at the outputs of the unbalanced divider, which can be more critical for the film resistor.

- The same temperature behaviour is seen for the power dividers V. However, the measured temperatures are lower, since the measurement is performed on the

substrate surface due to the multilayer structure.

- The 50 Ω thin film resistors, that are used as an output line termination resistance, have been broken when a power average of 10 W has been applied. Nevertheless, only microstrip lines with a termination resistance are used at the output of the 10 dB coupling lines, where the power absorbed by the thin film is considerably lower.

Thus, it can be noted that these power measurements show a good power handling capabilites of the thin film resistors. However, this technology is not applied in the elevation feeding network, even though the maximal power average excitation at each input will be 50 W, that comes from the peak power pulse of 1 kW along with a duty cycle of 10% and the subsequent equally power distribution to each output branch.

Bibliography

[1] C. Hülsmeyer. *Verfahren, um entfernte metallische Gegenstände mittels elektrischer Wellen einem Beobachter zu melden*. German Patent 165546, 1904.

[2] R. K. Moore. *Imaging Radar Systems*. 2nd ed. Vol. 1. American Society of Photogrammetry, 1983.

[3] C.A. Wiley. "Synthetic aperture radars: a paradigm for technology evolution". In: *IEEE Transactions on Aerospace and Electronic Systems* vol. 3 (1985), pp. 440–443.

[4] P. Rizzoli, M. Martone, C. Gonzalez, C. Wecklich, D. Borla Tridon, B. Bräutigam, M. Bachmann, D. Schulze, T. Fritz, M. Huber, B. Wessel, G. Krieger, M. Zink, and A. Moreira. "Generation and performance assessment of the global TanDEM-X digital elevation model". In: *ISPRS Journal of Photogrammetry and Remote Sensing* vol. 132 (2017), pp. 119–139.

[5] T. Jagdhuber, I. Hajnsek, A. Bronstert, and K. P. Papathanassiou. "Soil moisture estimation under low vegetation cover using a multi-angular polarimetric decomposition". In: *IEEE Transactions on Geoscience and Remote Sensing* 51.4 (2013), pp. 2201–2215.

[6] M. Bernier, J. Dedieu, Y. Duguay, and G. Seguin. "Snow water equivalent estimation using high resolution SAR data". In: *2017 IEEE International Geoscience and Remote Sensing Symposium (IGARSS)*. 2017, pp. 1351–1354.

[7] M. Martone, P. Rizzoli, C. Wecklich, C. González, J. Bueso-Bello, P. Valdo, D. Schulze, M. Zink, G. Krieger, and A. Moreira. "The global forest/non-forest map from TanDEM-X interferometric SAR data". In: *Remote Sensing of Environment* 205 (2018), pp. 352–373.

[8] Y. Huang, Q. Zhang, and L. Ferro-Famil. "Forest height estimation using a single-pass airborne L-band polarimetric and interferometric SAR system and tomographic techniques". In: *Remote Sensing* 13.3 (2021).

[9] P. Paillou, S. Lopez, T. Farr, and A. Rosenqvist. “Mapping subsurface geology in sahara using L-band SAR: first results from the ALOS/PALSAR imaging radar”. In: *IEEE Journal of Selected Topics in Applied Earth Observations and Remote Sensing* 3.4 (2010), pp. 632–636.

[10] M. Eineder, A. Moreira, and A. Roth. “Ten years of TerraSAR-X—scientific results”. In: *Remote Sensing* 11.3 (2019).

[11] A. Rucci, A. Ferretti, A. Monti Guarnieri, and F. Rocca. “Sentinel 1 SAR interferometry applications: The outlook for sub millimeter measurements”. In: *Remote Sensing of Environment* 120 (2012), pp. 156–163.

[12] J. Sanchez Palma, A. Solana Gonzalez, I. Martin Hervas, F. Monjas Sanz, M. Labriola, J. Martinez Cengotitabengoa, F. M. Garcia Molleda, S. Moreno Aguado, P. Saameno Perez, J. Closa Soteras, and V. Bautista Juzgado. “SAR panel design and performance for the PAZ mission”. In: *8th European Conference on Synthetic Aperture Radar*. 2010, pp. 1–4.

[13] M. Sedehi, A. Carbone, E. Imbembo, F. Heliere, B. Rommen, M. Fehringer, K. Scipal, A. Leanza, T. Simon, and P. Willemsen. “Biomass - A fully polarimetric P-band SAR ESA mission”. In: *EUSAR 2021; 13th European Conference on Synthetic Aperture Radar*. 2021, pp. 1–5.

[14] S. Huber, F.Q. de Almeida, M. Villano, M. Younis, G. Krieger, and A. Moreira. “Tandem-L: A technical perspective on future spaceborne SAR sensors for earth observation”. In: *IEEE Transactions on Geoscience and Remote Sensing* 56.8 (2018), pp. 4792–4807.

[15] M. Younis, C. Fischer, and W. Wiesbeck. “Digital beamforming in SAR systems”. In: *IEEE Transactions on Geoscience and Remote Sensing* 41.7 (2003), pp. 1735–1739.

[16] G. Krieger, M. Younis, S. Huber, F. Bordoni, A. Patyuchenko, J. Kim, P. Laskowski, M. Villano, T. Rommel, P. Lopez-Dekker, and A. Moreira. “Digital beamforming and MIMO SAR: Review and new concepts”. In: *EUSAR 2012; 9th European Conference on Synthetic Aperture Radar*. 2012, pp. 11–14.

[17] G. Krieger, M. Zonno, M. Rodriguez-Cassola, P. Lopez-Dekker, J. Mittermayer, M. Younis, S. Huber, M. Villano, F.Q. de Almeida, P. Prats-Iraola, and A. Moreira. “MirrorSAR: A fractionated space radar for bistatic, multistatic and high-resolution wide-swath SAR imaging”. In: *2017 IEEE International Geoscience and Remote Sensing Symposium (IGARSS)*. 2017, pp. 149–152.

[18] A. Reigber, R. Scheiber, M. Jager, P. Prats-Iraola, I. Hajnsek, T. Jagdhuber, K. P. Papathanassiou, M. Nannini, E. Aguilera, S. Baumgartner, R. Horn, A. Nottensteiner, and A. Moreira. “Very-High-Resolution airborne synthetic aperture radar imaging: signal processing and applications”. In: *Proceedings of the IEEE* 101.3 (2013), pp. 759–783.

[19] A. Reigber, A. Nottensteiner, M. Limbach, M. Jäger, A. Kosc, R. Scheiber, J. Fischer, A. Di Maria, G. Müller, R. Que, M. Künemund, K. Trappschuh, S. Pasch, D. Geßwein, D. Höflmayr, B. Gabler, M. Keller, R. Horn, and A. Moreira. “DBFSAR: An airborne very high-resolution digital beamforming SAR system”. In: *2017 European Radar Conference (EURAD)*. 2017, pp. 175–178.

[20] M. Eineder, N. Adam, R. Bamler, N. Yague-Martinez, and H. Breit. “Spaceborne Spotlight SAR interferometry with TerraSAR-X”. In: *IEEE Transactions on Geoscience and Remote Sensing* 47.5 (2009), pp. 1524–1535.

[21] J. Li, J. Chen, P. Wang, and C. Li. “Sensor-Oriented path planning for multiregion surveillance with a single lightweight UAV SAR”. In: *Sensors* 18.2 (2018).

[22] A. Kość, A. Di Maria, M. Limbach, R. Horn, and A. Reigber. “A 5 way lumped-elements Wilkinson power divider”. In: *2013 7th European Conference on Antennas and Propagation (EuCAP)*. 2013, pp. 357–360.

[23] Y. Chen and R. G. Vaughan. “Dual-Polarized L -Band and Single-Polarized X -Band Shared-Aperture SAR Array”. In: *IEEE Transactions on Antennas and Propagation* 66.7 (2018), pp. 3391–3400.

[24] A. Reigber, E. Schreiber, K. Trappschuh, S. Pasch, G. Müller, D. Kirchner, S. Geßwein D.and Schewe, A. Nottensteiner, M. Limbach, A. Schreiber, T. Rommel, R. Horn, M. Jäger, R. Scheiber, S.V. Baumgartner, S.K. Joshi, A. Barros Cardoso da Silva, and A. Moreira. “The High-Resolution digital-beamforming airborne SAR system DBFSAR”. In: *Remote Sensing* 12.11 (2020).

[25] V.K. Kothapudi and V. Kumar. “A 6-Port two-dimensional 3×3 series-fed planar array antenna for dual-polarized X-band airborne synthetic aperture radar applications”. In: *IEEE Access* 6 (2018), pp. 12001–12007.

[26] R. Di Bari, T. Brown, S. Gao, M. Notter, D. Hall, and C. Underwood. “Dual-polarized printed S-band radar array antenna for spacecraft applications”. In: *IEEE Antennas and Wireless Propagation Letters* 10 (2011), pp. 987–990.

[27] Yohandri, V. Wissan, I. Firmansyah, P. Rizki Akbar, J.T. Sri Sumantyo, and H. Kuze. “Development of circularly polarized array antenna for synthetic aperture radar sensor installed on UAV”. In: *Progress In Electromagnetics Research* 19 (2011), pp. 119–133.

[28] D.K. Sharma, B.K. Pandey, S. Kulshrestha, S.B. Chakrabarty, and R. Jyoti. “Design of wideband microstrip antenna array at L-band for synthetic aperture radar applications”. In: *Microwave and Optical Technology Letters* 55.4 (2013), pp. 903–908.

[29] T. Dong, K. Li, Z. Xia, and X. Li. “A low-profile shared-aperture dual-band broadband antenna array for SAR applications”. In: *2020 50th European Microwave Conference (EuMC)*. 2021, pp. 37–40.

[30] L.L. Shafai, W.A. Chamma, M. Barakat, P.C. Strickland, and G. Seguin. “Dual-band dual-polarized perforated microstrip antennas for SAR applications”. In: *IEEE Transactions on Antennas and Propagation* 48.1 (2000), pp. 58–66.

[31] Md. Shahidul A., N. Misran, B. Yatim, and M. Tariqul Islam. “Development of electromagnetic band gap structures in the perspective of microstrip antenna design”. In: *International Journal of Antennas and Propagation* 2013 (2013).

[32] M.K. Khandelwal, B.K. Kanaujia, and Kumar S. “Defected ground structure: fundamentals, analysis, and applications in modern wireless trends”. In: *International Journal of Antennas and Propagation* 2017 (2017).

[33] M. Limbach, B. Gabler, R. Horn, A. Kosc, A. Di Maria, and R. Scheiber. “P-band antenna array for airborne SAR application and DBF SAR demonstration”. In: *2015 9th European Conference on Antennas and Propagation (EuCAP)*. 2015, pp. 1–5.

[34] K. Woelders and J. Granholm. “Cross-polarization and sidelobe suppression in dual linear polarization antenna arrays”. In: *IEEE Transactions on Antennas and Propagation* 45.12 (1997), pp. 1727–1740.

[35] J. Granholm and K. Woelders. “Dual polarization stacked microstrip patch antenna array with very low cross-polarization”. In: *IEEE Transactions on Antennas and Propagation* 49.10 (2001), pp. 1393–1402.

[36] H. Saeidi-Manesh and G. Zhang. “High-isolation, low cross-polarization, dual-polarization, hybrid feed microstrip patch array antenna for MPAR application”. In: *IEEE Transactions on Antennas and Propagation* 66.5 (2018), pp. 2326–2332.

[37] R. Horn, M. Jaeger, M. Keller, M. Limbach, A. Nottensteiner, M. Pardini, A. Reigber, and R. Scheiber. “F-SAR - recent upgrades and campaign activities”. In: *2017 18th International Radar Symposium (IRS)*. 2017, pp. 1–10.

[38] M.K. Emara, K. Madhoun, R. Madhoun, and S. Gupta. “A Low-cost light-weight 3D-printed choke ring for multipath mitigation for GNSS antennas”. In: *2019 IEEE International Symposium on Antennas and Propagation and USNC-URSI Radio Science Meeting*. 2019, pp. 721–722.

[39] D. Sievenpiper, R. Broas, and E. Yablonovitch. “Antennas on high-impedance ground planes”. In: *1999 IEEE MTT-S International Microwave Symposium Digest (Cat. No.99CH36282)*. Vol. 3. 1999, pp. 1245–1248.

[40] J. Tak and J. Choi. “A wearable metamaterial microwave absorber”. In: *IEEE Antennas and Wireless Propagation Letters* 16 (2017), pp. 784–787.

[41] K.A.C de Macedo, S. Placidi, and A. Meta. “Bistatic and monostatic InSAR results with the MetaSensing airborne SAR System”. In: *2019 6th Asia-Pacific Conference on Synthetic Aperture Radar (APSAR)*. 2019, pp. 1–5.

[42] *SMP Connectors*. URL: https://www.rosenberger.com/fileadmin/content/headquarter/Products_Services/COM/SMP/Chapter_SMP.pdf.

[43] *ARCS Analysis Manual v1.74*. March Microwave Systems.

[44] M. Limbach, B. Gabler, A. Di Maria, R. Horn, and A. Reigber. “DLR compact test range facility”. In: *2012 6th European Conference on Antennas and Propagation (EUCAP)*. 2012, pp. 1276–1280.

[45] D. Reale, G. Fornaro, A. Pauciullo, X. Zhu, and R. Bamler. “Tomographic imaging and monitoring of buildings with very high resolution SAR data”. In: *IEEE Geoscience and Remote Sensing Letters* 8.4 (2011), pp. 661–665.

[46] M. Davidson, L. Iannini, R. Torres, and D. Geudtner. “New perspectives for applications and services provided by future spaceborne sar missions at the European Space Agency”. In: *IGARSS 2022 - 2022 IEEE International Geoscience and Remote Sensing Symposium*. 2022, pp. 4720–4723.

[47] Constantine A. Balanis. *Antenna Theory: Analysis and Design*. Wiley, 1982.

[48] Thomas A. Milligan. *Modern Antenna Design*. Wiley, 2005.

[49] A. Patyuchenko, M. Younis, S. Huber, F. Bordoni, and G. Krieger. “Design aspects and performance estimation of the reflector based digital beam-forming SAR system”. In: *International Radar Symposium (IRS)*. 2009.

[50] F. Meyer. *The SAR Handbook: Comprehensive Methodologies for Forest Monitoring and Biomass Estimation*. NASA, 2019.

[51] J. Lee and E. Pottier. *Polarimetric Radar Imaging*. CRC Press, 2009.

[52] Y. Huang, J. Levy-Vehel, L. Ferro-Famil, and A. Reigber. “3D imaging for underfoliage targets using L-band multi-baseline PolInSAR data and sparse estimation methods”. In: *2016 IEEE International Geoscience and Remote Sensing Symposium (IGARSS)*. 2016.

[53] W. Yang, Y. Li, W. Liu, J. Chen, C. Li, and Z. Men. “Scalloping suppression for ScanSAR images based on modified kalman filter with preprocessing”. In: *IEEE Transactions on Geoscience and Remote Sensing* 59.9 (2021), pp. 7535–7546.

[54] W. Xu, L. Zhang, C. Fang, P. Huang, W. Tan, and Y. Qi. “Staring spotlight SAR with nonlinear frequency modulation signal and azimuth non-uniform sampling for low sidelobe imaging”. In: *Sensors* 21.19 (2021).

[55] V. Akshay Pandit, A. Kesarkar, Y. Sahu, A. Rohada, J. Rao, P. K. Nath, R. Bhan, Ch. V. N. Rao, and R. Jyoti. “Design of small SAR constellation for minimizing revisit time”. In: *Computer Aided Constellation Management and Communication Satellites*. 2023.

[56] C. Roemer. “Introduction to a new wide area sar mode using the F-SCAN principle”. In: *2017 IEEE International Geoscience and Remote Sensing Symposium (IGARSS)*. 2017, pp. 3844–3847.

[57] G. Krieger, M. Zonno M.and Rodriguez-Cassola, P. Lopez-Dekker, J. Mittermayer, M. Younis, S. Huber, M. Villano, P. de Almeida F.and Prats-Iraola, and A. Moreira. “MirrorSAR: A fractionated space radar for bistatic, multistatic and high-resolution wide-swath SAR imaging”. In: *2017 IEEE International Geoscience and Remote Sensing Symposium (IGARSS)*. 2017, pp. 149–152.

[58] S. Dill, E. Schreiber, A. Engel M.and Heinzel, and M. Peichl. “A drone carried multichannel Synthetic Aperture Radar for advanced buried object detection”. In: *2019 IEEE Radar Conference (RadarConf)*. 2019, pp. 1–6.

[59] Ke Wu, D. Deslandes, and Y. Cassivi. “The substrate integrated circuits - a new concept for high-frequency electronics and optoelectronics”. In: *6th International Conference on Telecommunications in Modern Satellite, Cable and Broadcasting Service, 2003. TELSIKS 2003.* Vol. 1. 2003.

[60] M. Bozzi, A. Georgiadis, and Ke Wu. “Review of substrate-integrated waveguide circuits and antennas”. In: *Microwaves, Antennas and Propagation, IET* 5 (July 2011), pp. 909–920.

[61] D. Deslandes and Ke Wu. “Accurate modeling, wave mechanisms, and design considerations of a substrate integrated waveguide”. In: *IEEE Transactions on Microwave Theory and Techniques* 54.6 (2006), pp. 2516–2526.

[62] A. Belenguer, H. Esteban, A. Borja, J.. Ballesteros, M. Fernández, J.. Morro, C. de Dios J.and Bachiller, and V. Boria. “Empty Substrate-Integrated Waveguides: a low-cost and low-profile alternative for high-performance microwave devices”. In: *Wiley Encyclopedia of Electrical and Electronics Engineering*. John Wiley and Sons, Ltd, 2020, pp. 1–23.

[63] J. Hirokawa, K. Sakurai, M. Ando, and N. Goto. “An analysis of a waveguide T junction with an inductive post”. In: *IEEE Transactions on Microwave Theory and Techniques* 39.3 (1991), pp. 563–566.

[64] EIA RS-261-B. *Rectangular waveguides (WR3 to WR2300)*. Standard of the Electronic Industries Association of the United States of America, May 1979.

[65] *Rogers TMM Laminates*. Aug. 11, 2023. URL: https://www.rogerscorp.com/-/media/project/rogerscorp/documents/advanced-electronics-solutions/english/data-sheets/tmm-thermoset-laminate-data-sheet-tmm3----tmm4----tmm6----tmm10----tmm10i----tmm13i.pdf.

[66] David M. Pozar. *Microwave Engineering*. Wiley, 2011.

[67] Dominic Deslandes. “Design equations for tapered microstrip-to-Substrate Integrated Waveguide transitions”. In: *2010 IEEE MTT-S International Microwave Symposium*. 2010, pp. 704–707.

[68] R. Kazemi, A. E. Fathy, S. Yang, and R. A. Sadeghzadeh. “Development of an ultra wide band GCPW to SIW transition”. In: *2012 IEEE Radio and Wireless Symposium*. 2012, pp. 171–174.

[69] R. Simons. *Coplanar Waveguide Circuits, Components, and Systems*. Wiley, 2001.

[70] D. Deslandes and K. Wu. “Analysis and design of current probe transition from grounded coplanar to substrate integrated rectangular waveguides”. In: *IEEE Transactions on Microwave Theory and Techniques* 53.8 (2005), pp. 2487–2494.

[71] A. Patrovsky, M. Daigle, and K. Wu. “Millimeter-wave wideband transition from CPW to substrate integrated waveguide on electrically thick high-permittivity substrates”. In: *2007 European Microwave Conference*. 2007, pp. 138–141.

[72] G. Gentile, B. Rejaei, V. Jovanovic, L.K. Nanver, L.C.N. de Vreede, and M. Spirito. “Ultra-wide band CPW to substrate integrated waveguide (SIW) transition based on a U-shaped slot antenna”. In: *2013 European Microwave Integrated Circuit Conference*. 2013, pp. 25–28.

[73] R. Fang, C. Liu, and C. Wang. “Compact and broadband CB-CPW-to-SIW Transition using stepped-impedance resonator With 90°-bent slot”. In: *IEEE Transactions on Components, Packaging and Manufacturing Technology* 3.2 (2013), pp. 247–252.

[74] C. Liu, Y. Lu, and C. Wang. “GCPW-to-SIW transition using tapered slot”. In: *Proceedings of the 5th World Congress on Electrical Engineering and Computer Systems and Sciences (EECSS’19)* (2019).

[75] F. Taringou, D. Dousset, J. Bornemann, and K. Wu. “Substrate-integrated waveguide transitions to planar transmission-line technologies”. In: *2012 IEEE/MTT-S International Microwave Symposium Digest*. 2012, pp. 1–3.

[76] S. Lee, S. Jung, and H. Lee. “Ultra-wideband CPW-to-substrate integrated waveguide transition using an elevated-CPW section”. In: *IEEE Microwave and Wireless Components Letters* 18.11 (2008), pp. 746–748.

[77] R. Kazemi and A.E. Fathy. “Design of single-ridge SIW power dividers with over 75% bandwidth”. In: *2014 IEEE MTT-S International Microwave Symposium (IMS2014)*. 2014, pp. 1–3.

[78] K. B. Kumar and T. Shanmuganantham. “3-Port T-junction SIW power divider for 60 GHz applications”. In: *2017 IEEE International Conference on Antenna Innovations and Modern Technologies for Ground, Aircraft and Satellite Applications (iAIM)*. 2017, pp. 1–4.

[79] E. Setijadi and A. Pandu W. “Ultrawide band power divider based on substrate integrated waveguide (SIW) for S-band applications”. In: *ARPN Journal of Engineering and Applied Sciences* 13.1 (2018).

[80] K. Güvenli, S. Yenikaya, and M. Seçmen. “Design and implementation of substrate integrated waveguide filter to work on X-band and Ku-band”. In: *2018 9th International Conference on Ultrawideband and Ultrashort Impulse Signals (UWBUSIS)*. 2018, pp. 198–200.

[81] A. R. Akbarzadeh and Z. Shen. “Waveguide power dividers using multiple posts”. In: *Microwave and Optical Technology Letters* 50.4 (2008), pp. 981–984.

[82] G.F. Engen and C.A. Hoer. “Thru-Reflect-Line: an improved technique for calibrating the dual six-port automatic network analyzer”. In: *IEEE Transactions on Microwave Theory and Techniques* 27.12 (1979), pp. 987–993.

[83] E. Diaz Caballero, A. Belenguer, H. Esteban, and V.E. Boria. “Thru-reflect-line calibration for substrate integrated waveguide devices with tapered microstrip transitions”. In: *Electronics Letters* 49.2 (2013), pp. 132–133.

[84] *Microstrip (Patch) Antennas*. Apr. 26, 2024. URL: https://https://www.antenna-theory.com/antennas/patches/antenna.php.

[85] W.S.T Rowe, R.B. Waterhouse, and C. Caloz. "Investigation into the performance of proximity coupled stacked patches". In: *IEEE Transactions on Antennas and Propagation* 54.6 (2006), pp. 1693–1698.

[86] M. Bugaj and M. Wnuk. "Bandwidth optimization of aperture-coupled stacked patch antenna". In: *Advancements in Microstrip Antennas with Recent Applications*. IntechOpen, 2013, pp. 1–23.

[87] V. Rathi, G. Kumar, and K.P. Ray. "Improved coupling for aperture coupled microstrip antennas". In: *IEEE Transactions on Antennas and Propagation* 44.8 (1996), pp. 1196–1198.

[88] David M. Pozar. *A Review of Aperture Coupled Microstrip Antennas: History, Operation, Development, and Applications*. 1996. URL: https://people.umass.edu/dpozar/miscfiles/aperture.pdf.

[89] M. Limbach, B. Gabler, R. Horn, A. Kosc, and A Di Maria. "New cavity backed capacitively coupled stacked element for P-Band SAR application". In: *2014 8th European Conference on Antennas and Propagation (EuCAP)*. 2014, pp. 2030–2033.

[90] H. Saeidi-Manesh, S. Karimkashi, G. Zhang, and R. Doviak. "High-isolation low cross-polarization phased-array antenna for MPAR application". In: *Radio Science* 52.12 (2017), pp. 1544–1557.

[91] H. Saeidi-Manesh and G. Zhang. "Challenges and limitations of the cross-polarization suppression in dual-polarization antenna arrays using identical subarrays". In: *IEEE Transactions on Antennas and Propagation* 68.4 (2019), pp. 2853–2866.

[92] R. Florencio, J.A. Encinar, R.R. Boix, G. Pérez-Palomino, and G. Toso. "Cross-polar reduction in reflectarray antennas by means of element rotation". In: *2016 10th European Conference on Antennas and Propagation (EuCAP)* (2016), pp. 1–5.

[93] Y. Weishuang, L. Xiuye, C. Ang, Z. Zhe, S. Lei, G. Fang, L. Xiaohan, and Z. Jian. "Cross-polarization suppression for patch array antennas via generalized Kerker effects". In: *Optics Express* 28.1 (2020), pp. 40–47.

[94] F. Fan, Z. Yan, P. Xu, and K. Tan. "Sequential rotation feeds microstrip array". In: *Microwaves & RF* 52 (2013), pp. 55–58.

[95] L.A. Greda and A. Dreher. "Tx-terminal phased array for satellite communication at Ka-band". In: *2007 European Microwave Conference*. 2007, pp. 266–269.

[96] W. Hu, G. Wen, D. Inserra, Y. Huang, J. Li, and Z Chen. “A circularly polarized antenna array with gain enhancement for long-range UHF RFID systems”. In: *Electronics* 8.4 (2019).

[97] L. Baggen, S. Holzwarth, W. Simon, and O. Litschke. “Phased array using the sequential rotation principle: analysis of coupling effects”. In: *IEEE International Symposium on Phased Array Systems and Technology, 2003.* 2003, pp. 571–576.

[98] C. Deng, Y. Li, Z. Zhang, and Z. Feng. “A wideband sequential-phase Fed circularly polarized patch array”. In: *IEEE Transactions on Antennas and Propagation* 62.7 (2014), pp. 3890–3893.

[99] Q. Garcia-Garcia. “Linear arrays of sequentially rotated circularly polarized patch radiators”. In: *Microwave and optical technology letters* 25.6 (2000), pp. 387–390.

[100] Q. Garcia-Garcia. “Scanning properties of sequential rotated linear arrays of circularly polarized patch”. In: *Microwave and optical technology letters* 30.5 (2001), pp. 343–350.

[101] *High-performance, thin-film embedded resistor copper foil*. Aug. 7, 2024. URL: `https://ticertechnologies.com/`.

[102] M. K. Emara, K. Madhoun, and S. Madhoun R.and Gupta. “A low-cost light-weight 3D-printed choke ring for multipath mitigation for GNSS antennas”. In: *2019 IEEE International Symposium on Antennas and Propagation and USNC-URSI Radio Science Meeting*. 2019, pp. 721–722.

[103] S. Caizzone, R.A. Gerguis, E.O. Addo, S.P. Hehenberger, and W. Elmarissi. “Spatial filtering of multipath at GNSS reference stations through metamaterial-based absorbers”. In: *IEEE Transactions on Aerospace and Electronic Systems* 59.6 (2023), pp. 7764–7771.

[104] M. I. Hossain, N. Nguyen-Trong, K. H. Sayidmarie, and A. M. Abbosh. “Equivalent circuit design method for wideband nonmagnetic absorbers at low microwave frequencies”. In: *IEEE Transactions on Antennas and Propagation* 68.12 (2020), pp. 8215–8220.

[105] N.M. Mohamed-Hicho, E. Antonino-Daviu, M. Cabedo-Fabrés, and M. Ferrando-Bataller. “A novel low-profile high-gain UHF antenna using high-impedance surfaces”. In: *IEEE Antennas and Wireless Propagation Letters* 14 (2015), pp. 1014–1017.

[106] A.C. Durgun, C.A. Balanis, C.R. Birtcher, H. Huang, and H. Yu. “High-impedance surfaces with periodically perforated ground planes”. In: *IEEE Transactions on Antennas and Propagation* 62.9 (2014), pp. 4510–4517.

[107] A.K. Oladeinde, E. Aryafar, and B. Pejcinovic. “MmWave Tx-Rx self-interference suppression through a high impedance surface stacked EBG”. In: *Electronics* 13.15 (2024).

[108] D. Sievenpiper, L. Zhang, R.F.J. Broas, N.G. Alexopolous, and E. Yablonovitch. “High-impedance electromagnetic surfaces with a forbidden frequency band”. In: *IEEE Transactions on Microwave Theory and Techniques* 47.11 (1999), pp. 2059–2074.

[109] P. Kovács and T. Urbanec. “Electromagnetic Band Gap Structures: Practical Tips and Advice for Antenna Engineers”. In: *Radioengineering* 21 (Apr. 2012).

[110] N.A. Aboserwal, C. Balanis, and C.R. Birtcher. “Impact of finite ground plane edge diffraction on radiation patterns of aperture antennas”. In: *Progress In Electromagnetics Research B* 55 (2013), pp. 1–21.

[111] J. L. Salazar, N. Aboserwal, J. D. Díaz, J. A. Ortiz, and C. Fulton. “Edge diffractions impact on the cross polarization performance of active phased array antennas”. In: *2016 IEEE International Symposium on Phased Array Systems and Technology (PAST)*. 2016, pp. 1–5.

[112] S. Peddakrishna, T. Khan, and A. De. “Electromagnetic band-gap structured printed antennas: A feature-oriented survey”. In: *International Journal of RF and Microwave Computer-Aided Engineering* 27.7 (2017).

[113] F. Yang and Y. Rahmat-Samii. *Electromagnetic Band Gap Structures in Antenna Engineering*. Cambridge University Press, 2009.

[114] A. Aminian, F. Yang, and Y. Rahmat-Samii. “In-phase reflection and EM wave suppression characteristics of electromagnetic band gap ground planes”. In: *IEEE Antennas and Propagation Society International Symposium*. Vol. 4. 2003, pp. 430–433.

[115] L. Li, Y. Shi, and T.J. Cui. *Electromagnetic Metamaterials and Metasurfaces: From Theory to Applications*. Springer, 2024.

[116] I.J. Bahl and D.K. Trivedi. “A Designer’s Guide to Microstrip Line”. In: *Microwaves*. 1977, pp. 174–182.

List of Publications

The following articles have been published during the development of this thesis.

- **D. Lorente**, M. Limbach and B. Gabler, "L-Band Antenna Array for Next Generation DLR Airborne SAR Sensor," *2019 12th German Microwave Conference (GeMiC)*, Stuttgart, Germany, 2019, pp. 182-185.
- **D. Lorente**, M. Limbach, H. Esteban and V. Boria, "Compact Ultrawideband Grounded Coplanar Waveguide to Substrate Integrated Waveguide Tapered V-Slot Transition," *IEEE Microwave and Wireless Components Letters*, vol. 30, no. 12, pp. 1137-1140, Dec. 2020.
- **D. Lorente**, A. Schreiber, M. Limbach, H. Esteban and V. E. Boria, "High Permittivity CPW-SIW Power Divider for Antenna Feed Networks in Airborne Phased Arrays Applications," 2020 *17th European Radar Conference (EuRAD)*, Utrecht, Netherlands, 2021, pp. 254-257.
- **D. Lorente**, M. Limbach, B. Gabler, H. Esteban and V. Boria, "Sequential 90° Rotation of Dual-Polarized Antenna Elements in Linear Phased Arrays with Improved Cross-Polarization Level for Airborne Synthetic Aperture Radar Applications," *Remote Sensing*, 13(8), 1430, 2021.
- **D. Lorente**, M. Limbach, B. Gabler, H. Esteban and V. E. Boria, "Dual-Polarized Multilayer L-Band Asymmetric Subarray with Truncated Electric Walls Separation for Airborne SAR Applications," *2021 18th European Radar Conference (EuRAD)*, London, United Kingdom, 2022, pp. 133-136.
- B. Gabler, **D. Lorente** and L. G. T. van de Coevering, "Synthesis of a Phased Array with Planar Near-Field Techniques Based on Far-Field Measurements of a Sub-Array in a CATR," *2021 Antenna Measurement Techniques Association Symposium (AMTA)*, Daytona Beach, FL, USA, 2021, pp. 1-5.
- **D. Lorente**, M. Limbach, B. Gabler, H. Esteban and V. E. Boria, "Highly Integrated Low-Profile Multilayer Dual-Polarized Phased Array Antenna With Truncated Cavities

for First Pulsed Bistatic L-Band Airborne SAR Sensor," *IEEE Access*, vol. 12, pp. 435-449, 2024.

- **D. Lorente**, M. Limbach, B. Gabler, H. Esteban and V. E. Boria, "Mitigation of the Antenna Carrier Impact in Dual-Polarized Phased Arrays with Electromagnetic Bandgaps for Airborne SAR Sensors," *2025 19th European Conference on Antennas and Propagation (EuCAP)*, Stockholm, Sweden, 2025.

Besides the aforementioned works, two additional scientific outputs are currently ongoing:

- Related to the previous publication, an invitation to submit an extended version in the *Review of Electromagnetics (RoE) - EuCAP Journal Special Issue* has been received. For this reason, a journal article is planned to be submitted soon.
- A German patenting process has been initiated about the design of a multiband EBG unit-cell that provides the suppression of surface waves at the L-, S-, C- and X-band simultaneously.